ABSTRACT

MEASUREMENT OF THE HADRONIC CHARM PRODUCTION CROSS SECTION IN A HIGH RESOLUTION STREAMER CHAMBER EXPERIMENT

Liang Tzeng

Yale University, 1984

Hadronic production of charmed particles in association with muons from semileptonic decay of these short lived particles has been observed in a high resolution streamer chamber experiment performed at Fermi National Accelerator Laboratory in 1982. The incident beam was a collimated high energy neutron beam with an average energy of 280 Gev. The streamer chamber was triggered on the detection of the prompt muon from the charm decay. Two toroids were installed at the downstream end of the muon spectrometer for analyzing the muon momentum. In the operation of the streamer chamber, we achieved a streamer size of 50 μm and a full track width of 120μm in space. The streamer chamber optical system had a demagnification factor of about 1.5 from space to film. The minimum separation between two measurable tracks was about 150 μm on the film. With a special miss-distance analysis of the streamer chamber pictures, 17.32$\pm$4.73 charm signal events were obtained. Using the assumption of $A^{2/3}$ dependence for the production cross section and several different D-$\bar{D}$ production models, the nucleon-nucleon charm production cross section, averaged over the neutron spectrum, is estimated to be between 13 to 20 μb (with the average value equal to 17.69 $\pm$ 6.80 μb).

MEASUREMENT OF THE HADRONIC CHARM PRODUCTION CROSS SECTION IN A HIGH RESOLUTION STREAMER CHAMBER EXPERIMENT

A Dissertation

Presented to the Faculty of the Graduate School

of

Yale University

in Candidacy for the Degree of

Doctor of Philosophy

by

Liang Tzeng

April, 1984

Acknowledgements

I would like to express my appreciation to my advisor, Professor Jack Sandweiss, for his continuous support , guidance, understanding, encouragement and help throughout the course of my graduate school education. Most importantly, his sincere, dedicate attitude in research and his deep insight in physics have been and will always be the greatest inspiration to me.

I wish to thank Dr. Jean A. Slaughter and Dr. Richard D. Majka, two of my best teachers and best friends. Without them, the streamer chamber experiments could not have been done. I am grateful to Professor Peter Némethy for his continuous interest in this experiment. His advice, help and encouragement throughout the course of this experiment were invaluable.

I would also like to thank Dr. Marvin Johnson of Fermilab and my fellow student Ms. Patricia McBride. They built the three cathode readout PWC's and helped considerably in putting the whole experiment together.

To Mr. Peter J. Martin go my appreciation. His resourceful support and, in particular, his gracious friendship have made the austerity (of the past eight years) endurable.

The late Professor Horace D. Taft, who helped us in designing the neutron beam line, running the experiment and setting up the Vanguard film measurement machine, will always be remembered.

Thanks go to Professor Peter S. Cooper who set up the on-line software and a major portion of the off-line analysis program for this experiment. Thanks go to Professor Lucien J. Teig who set up the toroid magnetic field measurement device and the muon reconstruction program. Thanks go to Dr. Richard Kellogg. In the early part of 1978,

Dr. Kellogg and I spent most of the time in assembling and disassembling the streamer chamber. Thanks also go to Dr. Yan-San Li from the People's Republic of China. From 1979 to 1981, Dr. Li and I worked together on the laser triggered Blumlein system and updating the strteamer chamber for the E-630 experiment.

I also wish to thank Professor Robert E. Beringer for allowing me to include many of his elegent work in my thesis. Professor Van Altena of the Department of Astromy is acknowledged for allowing me to measure the 3-D grid pictures on their Photometric-Data-System (Yale-PDS). Thanks go to Mr. Andy Disco, Mr. Stainley Ladzinsky and Mr. Anthony Massioni of the Yale Gibbs Instrumentation Lab. Their skillful technique created the streamer chamber and made many other almost imaginary requests come true.

I wish to thank Ms. Catherine Bettega for her dedication in operating the Vanguard measurement machine at Yale. Thanks go to the crews of the Fermilab film analysis facility for scanning and measuring the streamer chamber pictures. Thanks also go to Mr. James Welch, Mr. John Welch and Mr. Gregg Granberg for their help in setting up the experiment. I wish to thank Ms. Jean Ahern, Ms. Sara Batter, Mr. Charles Green, Ms. Rochelle Lauer, Mr. Osborne Murphy, Mr. Dennis Petrillo and Ms. Irene Polard for their countless assistance and friendship.

Many people helped me in preparing this thesis. I am particularily grateful to Professor Sandweiss, Dr. Slaughter, Dr. Majka and Professor Némethy for reading the drafts and suggesting many valuable corrections.

Finally I would like to thank my parents, my wife and the members of my family for their patience, tolerance and encourgement.

Table of Contents

List of Figures vii

List of Tables x

Chapter 1: INTRODUCTION 1
- 1.1 A BRIEF REVIEW OF THE CURRENT STATUS OF THE CHARMED PARTICLES 1
- 1.2 EXPERIMENTAL METHODS 7

Chapter 2: THE STREAMER CHAMBER 14
- 2.1 ELECTRON AVALANCHES, STREAMER FORMATION AND THE YALE STREAMER CHAMBER. 15
- 2.2 THE MARX GENERATOR 26
- 2.3 THE BLUMLEIN PULSE SHAPING SYSTEM 32
- 2.4 THE WIRE ELECTRODES AND THE TERMINATOR 57
- 2.5 THE PERFORMANCE OF THE YALE HIGH PRESSURE STREAMER CHAMBER 68

Chapter 3: THE NEUTRON BEAM LINE, THE MUON SPECTROMETER AND THE TRIGGERS 84
- 3.1 THE NEUTRON BEAM LINE 84
- 3.2 THE MUON SPECTROMETER AND THE TRIGGERS 96

Chapter 4: MUON RECONSTRUCTION AND PICTURE MEASUREMENT 102
- 4.1 MUON TRACK RECONSTRUCTION 103
- 4.2 FILM MEASUREMENT 108
- 4.3 THREE DIMENSIONAL RECONSTRUCTION AND THE ALIGNMENT OF THE APPARATUS 118

Chapter 5: THE MISS-DISTANCE ANALYSIS 130

Chapter 6: RESULTS AND DISCUSSIONS 144
- 6.1 CALCULATION OF THE CHARM PRODUCTION CROSS SECTION . . 144
- 6.2 DISCUSSIONS AND CONCLUSIONS 155

Appendix I: MONTE-CARLOS. 163
- 1.1 THE CHARM MONTE-CARLO - <MONTED> 163

I.2 STRANGE PARTICLE MONTE-CARLO - <STRNGE> 168

Appendix II: THE WEDGE-SHAPED TERMINATOR 175

References 177

List of Figures

Figure 1-1:	Weak decay of charmed particles	3
Figure 1-2:	Quark-quark and gluon-gluon fusion diagrams	8
Figure 1-3:	Order-α_s^2 diagrams for charm excitation	8
Figure 1-4:	Charm excitation	8
Figure 1-5:	Hadronic production cross-section	9
Figure 2-1:	Stages in the growth of a streamer	17
Figure 2-2:	Spark chamber	18
Figure 2-3:	Operational scheme of streamer chamber	18
Figure 2-4:	Scaling principle of avalanche formation	20
Figure 2-5:	A cutaway view of the Yale High Resolution Streamer Chamber	24
Figure 2-6:	Example of an MARX GENERATOR circuit	27
Figure 2-7:	Equivalent circuit for the MARX-RESISTOR-BLUMLEIN system	27
Figure 2-8:	Equivalent circuit for the resistive divider monitor	27
Figure 2-9:	The coupling resistor and the resistive divider monitor	28
Figure 2-10:	Computer calculated Marx monitor pulse	31
Figure 2-11:	Oscilloscope trace of the Marx monitor pulse	31
Figure 2-12:	Marx output pulses from the resistive divider monitor	31
Figure 2-13:	The Blumlein lines	33
Figure 2-14:	Ideal Blumlein-line output pulse	33
Figure 2-15:	Cutaway and cross section views of the Blumlein Box	35
Figure 2-16:	Impedance of parallel plate transmission line	36
Figure 2-17:	Sampling scope picture of the Blumlein pulse	39
Figure 2-18:	Tektronic 7904 scope picture of the Blumlein pulse	39
Figure 2-19:	N_2 laser pulse	41
Figure 2-20:	The output pulse from the prototype laser triggered Blumlein	41
Figure 2-21:	Standing wave inside a uniform transmission line	43
Figure 2-22:	Radial line transmission line	44
Figure 2-23:	Plots of Z_0, G_0, G_1, ψ and θ as functions of kr	45
Figure 2-24:	Plot of $Z_i(r)/Z_0(r)$ vs kr and the list of poles in $Z_i(r)$	46
Figure 2-25:	The single gap Blumlein output pulse	48
Figure 2-26:	Lumped R−L−C circuit	48
Figure 2-27:	Marx output pulse	50
Figure 2-28:	Blumlein output pulse	50
Figure 2-29:	Transmission line	52
Figure 2-30:	Blumlein-line system	52
Figure 2-31:	Calculated output pulse shape from a Blumlein system with inductive switch	55
Figure 2-32:	The Yale High Resolution Streamer Chamber	58
Figure 2-33:	The wire electrode section of the Streamer Chamber	60

Figure 2-34:	The wedge-shaped terminator	62
Figure 2-35:	8 thick film resistors are used to make up the terminator	62
Figure 2-36:	Blumlein output pulse; terminator functions normally	63
Figure 2-37:	Blumlein output pulse; terminator damaged	63
Figure 2-38:	U-pickoff response to a square pulse from mercury pulser	66
Figure 2-39:	Pulse shape at T-pickoff monitor	66
Figure 2-40:	Pulse shape at DC-pickoff when the terminator was damaged	67
Figure 2-41:	Pulse shape at T-pickoff when the terminator was damaged	67
Figure 2-42:	Streamer chamber picture was taken without image intensifier	69
Figure 2-43:	200 Gev/c π^- interaction at 250 psia 90%Ne+10%He	69
Figure 2-44:	350 Gev/c P^+ interaction at 370 psia 90%Ne+10%He	70
Figure 2-45:	350 Gev/c P^+ interaction at 370 psia 90%Ne+10%He	70
Figure 2-46:	350 Gev/c P^+ beam tracks	72
Figure 2-47:	The elastic scattering cross section for electron in Ne	73
Figure 2-48:	The elastic scattering cross section for electron in Xe	73
Figure 2-49:	Ru^{106} β source track at 600 psia 99%(Ne−He)+1%Xe	74
Figure 2-50:	Emission spectra for helium and neon	75
Figure 2-51:	Absorption coefficients of UV light in the heavy noble gases	76
Figure 2-52:	Absorption coefficients k and photo ionization coefficient k_i of UV light in CO_2	76
Figure 2-53:	Electron elastic and inelastic scattering cross section in CO_2	78
Figure 2-54:	Ru^{106} β source track at 600 psia 97.5%(Ne−He)+2.5%CO_2	78
Figure 2-55:	Electron attachment cross section in CO_2	80
Figure 2-56:	Diffusion and memory time study	80
Figure 2-57:	Picture from E-630	82
Figure 2-58:	Picture from E-630	82
Figure 3-1:	E-630 neutron beam line	86
Figure 3-2:	Neutron beam line (horizontal section)	87
Figure 3-3:	Neutron beam line (vertical section)	88
Figure 3-4:	Neutron beam profile in front of the streamer chamber	89
Figure 3-5:	Neutron spectrum from Run-642	95
Figure 3-6:	Interaction hodoscope	96
Figure 3-7:	E-630 muon spectrometer	97
Figure 3-8:	E-630 triggers	101
Figure 4-1:	$\delta\phi$ of muon track	104
Figure 4-2:	Distribution of $\delta\phi$	104
Figure 4-3:	Centroid measurement	112
Figure 4-4:	Track fitting residue	113
Figure 4-5:	Distribution of the vertex chi-squared per degree of freedom	116
Figure 4-6:	Illustration of the streamer chamber optical system	118
Figure 4-7:	3-D grid for the space reconstruction	121
Figure 4-8:	Definition of the projection angle and the dip-angle	126
Figure 4-9:	Estimation of the effective field region of the streamer chamber	126
Figure 4-10:	Alignment of the streamer chamber and the muon spectrometer	129
Figure 5-1:	Definition of event topology parameters	131
Figure 5-2:	S and θ_B distributions	132
Figure 5-3:	S/DS distributions	136

Figure 5-4:	An event picked up by the miss-distance analysis	139
Figure 5-5:	Graphic display of the measurement output for the event in figure 5-4	140
Figure 5-6:	Histogram of S/DS for events with S/DS $\geq$ 3	143
Figure 6-1:	Charm production cross section and the distribution of the center of mass energy (see text)	160
Figure 7-1:	Comparison of the monte-carlo film measurement procedure with a real event from E-630 data	171
Figure 7-2:	Distribution of fitted vertices	172
Figure 7-3:	*Measurable track length* distribution and *measurable track angle* distribution	173
Figure 7-4:	Number of measurable tracks per event	174

List of Tables

Table 1-1:	R & D history of the Yale high resolution streamer chamber	13
Table 2-1:	Operating parameters of the Yale high resolution streamer chamber	83
Table 3-1:	E-630 neutron beam line and muon spectrometer setup	90
Table 4-1:	E-630 data summary	111
Table 4-2:	Optical constants of the E-630 streamer chamber	123
Table 5-1:	Summary of the miss-distance analysis	143
Table 6-1:	Estimation of charm production cross sections versus various production models	154
Table 6-2:	Values of R_i, P_o and P_{sum} for different production models	158

Chapter 1

INTRODUCTION

1.1 A BRIEF REVIEW OF THE CURRENT STATUS OF THE CHARMED PARTICLES

Since the discovery of the J/Ψ particle in 1974, the study of the hadronic production of charmed particles [1, 47] has been actively pursued. It is believed that a better understanding of the production characteristics of these heavy particles will contribute fruitful inputs to our understanding of QCD [10, 11, 15] which at present is the only framework available for us for handling problems in the strong interactions.

The observation of an open charm (i.e. charm quantum number not equal to 0) state was first reported in 1975 by a BNL bubble chamber experiment [2] with a (ν_μ+p$\rightarrow$ $\mu^-+\Lambda+\pi^++\pi^++\pi^++\pi^-$) event which was interpreted as the production of either a Σ_c^{++} or a Λ_c^+. In 1976 a clear signal for the production of D^+ particles was reported by an e^+e^- experiment at SPEAR, SLAC. [3] Since then, data on charmed particles has been rapidly accumulated. By the time of the 1979 Lepton-Photon Conference at Fermilab, experimental results on the observation of charmed particle production were contributed by more than 17 experimental groups (Ref. [4] to [9]) including 3 ISR (pp) colliding beam experiments [5], a CERN π^-p-interaction bubble chamber experiment (LEBC), a Fermilab pN-interaction streamer chamber experiment [28] and a Fermilab pN beam dump

experiment [6, 7, 20]. By that time, evidence for the D, $\bar{D}$, D^* and $\bar{D}^*$ mesons, the F_c^+ ($c\bar{s}$) meson and the Λ_c^+ (c[ud]) baryon had been reported. The masses of D, $\bar{D}$, D^* and $\bar{D}^*$ were also measured by e^+e^- experiments [4]. The results of hadronic experiments were still in a very primitive stage and the mass of Λ_c^+ was estimated to be about 2.25 to 2.29 Gev/c^2 from the ISR experiments. Results from SPEAR (the DELCO experiment [4]) and the Fermilab emulsion experiment [8], however, gave surprising results on the lifetimes of the charmed particles.

According to the *spectator* pictures as discussed in the classical paper of Gaillard, Lee and Rosner [47], the decay of a charmed particle proceeds via the elementary processes of the charm quark and the other quark ($\bar{q}$) remains essentially as a spectator (figure 1-1 (a)). Comparing with the μ decay diagram (figure 1-1 (b), $\mu \rightarrow e\nu\nu$), the decay rate of the charmed particle can be roughly estimated as

$$\Gamma_c/\Gamma_\mu \sim 5(m_c/m_\mu)^5 \tag{1-1}$$

where the first factor 5 includes the three colors of the quark and the contributions from $e\nu$ and $\mu\nu$. m_c is the mass of the charm quark ($\sim$1.5 Gev) and m_μ is the mass of muon($\sim$ 0.1 Gev). Therefore one would expect that the lifetimes of D^+ and D^0 are approximately equal ($\sim 6 \times 10^{-13}$ sec.). Moreover, the semileptonic decay rates for both D^+ and D^0 are also expected to be equal since the Cabibbo-favored semileptonic Lagrangian has the form

$$\mathcal{L} \sim \cos\theta_c[\,\bar{c}\gamma_\mu(1-\gamma_5)s\,][\,\bar{l}\gamma^\mu(1-\gamma_5)\nu\,] \tag{1-2}$$

where θ_c is the Cabibbo angle, c and s represent the charm and strange quark respectively, l represents the lepton (e or μ) and ν represents the neutrino. This Lagrangian carries zero isotopic spin hence

$$\Gamma(D^+ \rightarrow l^+ + \nu + X^0) = \Gamma(D^0 \rightarrow l^+ + \nu + X^-) \tag{1-3}$$

where X^0 and X^- are isospin $\frac{1}{2}$ hadronic states. Therefore one would expect that the

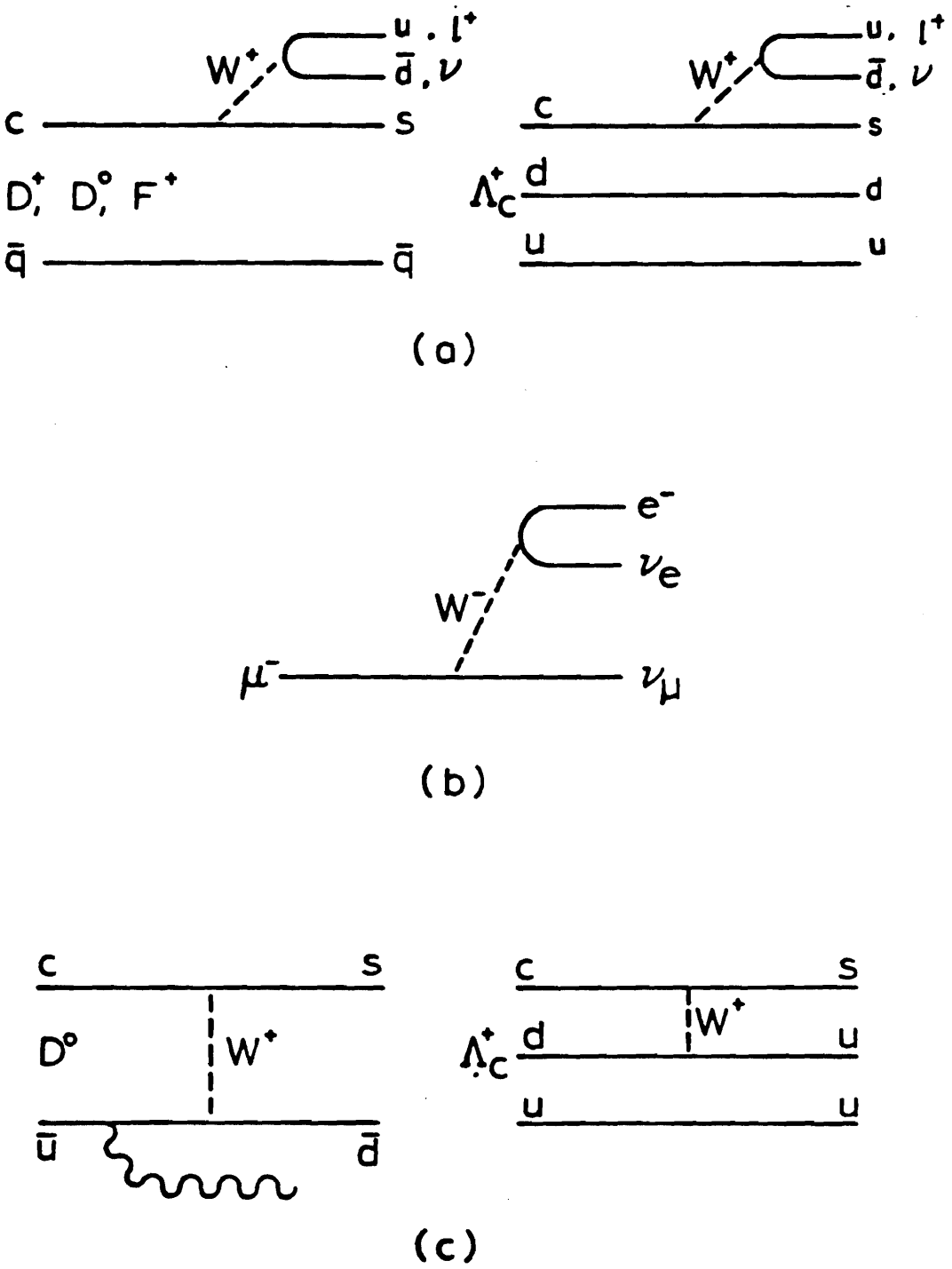

Figure 1-1: Weak decay of charmed particles

(a)The spectator pictures. (b)Muon decay diagram. (c)W-exchange diagrams.

semileptonic decay branching ratios for D^+ and D^0 are the same and

$$BR(D^+ \to l+X)/BR(D^0 \to l+X) = \tau(D^+)/\tau(D^0) \tag{1-4}$$

Contrary to the expectation from the spectator model, the lifetimes reported by the emulsion experiment [8] were $\tau(D^+) \sim 8 \times 10^{-13}$ sec. and $\tau(D^0) \sim 0.66 \times 10^{-13}$ sec. On the other hand, the e^+e^- experiment reported measurements on the semileptonic branching ratios [4]

$$BR(D^+ \to e+X)/BR(D^0 \to e+X) > 4 \tag{1-5}$$

By that time (1979), it was clear that something was missing from the original predictions concerning the weak decay of the charmed particles.

The most recently published summarized results on the lifetimes and semileptonic branching ratios of the charmed particles are listed below: [12, 50]

$$\tau(D^0) = 3.9 \begin{smallmatrix} +0.4 \\ -0.4 \end{smallmatrix} \times 10^{-13} \text{ sec.} \tag{1-6}$$

$$\tau(D^+) = 8.2 \begin{smallmatrix} +1.1 \\ -0.9 \end{smallmatrix} \times 10^{-13} \text{ sec.} \tag{1-7}$$

$$\tau(F_c^+) = 2.5 \begin{smallmatrix} +1.2 \\ -0.7 \end{smallmatrix} \times 10^{-13} \text{ sec.} \tag{1-8}$$

$$\tau(\Lambda_c^+) = 2.2 \begin{smallmatrix} +0.7 \\ -0.4 \end{smallmatrix} \times 10^{-13} \text{ sec.} \tag{1-9}$$

$$BR(D^+ \to e\nu X) = 16.8 \pm 6.4\% \quad \text{(MARK II)} \tag{1-10}$$

$$BR(D^0 \to e\nu X) = 5.5 \pm 3.7\% \quad \text{(MARK II)} \tag{1-11}$$

The ratio $\tau(D^+)/\tau(D^0)$ is approximately equal to 2 instead of 1. An attempt to answer this problem includes other decay mechanisms which contribute preferentially to D^0 hadronic decay such as the non-spectator W-exchange diagram for the D^0 meson in figure 1-1 (c). The extra gluon is necessary to bypass the helicity suppression. Detailed discussions on the issue of charm decay can be found in references [12], [16], [18], [19], [62]

and [63]. The current situation on the weak decay of charmed particles is that a lot of progress has been made on the experimental study of the lifetimes of charmed particles during the past 6-7 years. Better data on the measurements of semileptonic branching ratios are however still needed to obtain absolute semileptonic decay rates and compare to the standard model.

Questions also exist when one turns to the subject of the production mechanism(s) of the open-charm particles. Perturbative QCD calculations based on the gluon-gluon fusion and "Drell-Yan like" quark-quark fusion mechanisms (figure 1-2) have been remarkably successful in interpreting experimental data on the hadronic production of the J/Ψ particle (see references [10, 49, 50, 51, 57, 58]). Using these fusion models, the original theoretical predictions [54, 55, 56, 57, 58] for the total charm production cross-section were on the order of few microbarns at Fermilab or SPS energies ($\sim$ 60 μb at ISR energy) and the charm-anticharm pair were produced *centrally* (i.e. the distribution of the produced charm can be expressed by the function $(1-|X_F|)^n$ with $n\sim5$; where $X_F=P_{||}/P_{max}$). However, several measurements of the hadronic charm production cross-section from earlier Fermilab or SPS beam dump experiments (for example, [20, 22, 28, 29]) indicated that the cross-section ($\sigma(D\bar{D})\sim$20-30μb) is much bigger than the original predictions.

The differences between the fusion model predictions and the experimental measurements gets even worse if we include data from the ISR. The three experiments [21, 25, 26] discussed in reference [5] detected a large mass peak in the $\Lambda_c^+ \rightarrow k^-p\pi^+$ decay channel and an abundance of the Λ_c^+ were observed at large X_F. The total inclusive cross-section was estimated to be about 200-400 μb. These results, later supported by another ISR experiment [32, 33, 34], displayed *diffractive* production phenomenon of charmed particles (especially the leading Λ_c^+ baryon). The word *diffractive* here means *forward* production and is associated with a *much flatter* X_F distribution. According to the definitions of reference [15], with a proton or neutron beam, Λ_c^+ or $\bar{D}^0$ are diffractively produced with the X_F distribution proportional to $(1-X_F)^1$ and $(1-X_F)^3$ respectively. With a π meson beam, D^0 will be diffractively

produced with a $(1-X_F)^1$ distribution. Centrally produced particles follow a $(1-X_F)^5$ distribution.

In order to accommodate the data, several alternative approaches have been pursued to improve the theoretical understanding in the problem of heavy flavoured particle production. It is possible to obtain a bigger cross-section under the framework of the fusion model by varying the parameters used in the calculation (such the mass of the c-quark [55, 58]). It has been suggested by some authors (for example, reference [57]) that collective nuclear effects might enhance the charm production cross-section and that non-perturbative effects might turn out to be important for the charm production process. Generally speaking, the fusion model tends to give centrally produced charmed particles and the calculated production cross-section is well below 200 μb at ISR energy.

Another attempt to answer these questions is the *intrinsic charm* model proposed by Brodsky et al. [64, 65]. The basic idea of this model starts with the observation that all of the constituents inside the proton (hadron) must have the same velocity in order to keep the proton together. If *intrinsic* charm quarks are included in the proton wave function with ~(1-2)% probability then these heavy constituents will carry most of the momentum of the parent proton. The consequences are that the produced Λ_c^+ or D particles have flatter X_F distribution and 200-400 μb diffractive production cross-section of the charmed particles at ISR energy is hence understandable.

This *intrinsic* charm model is, however, argued against by some theorists (for example, reference [15]) on the standpoint that valence-like $c\bar{c}$ components in the proton wave function are not a feature of QCD. The point is, according to reference [15], intrinsic charm could be generated through the process where a soft gluon produces a soft $c\bar{c}$ pair that eventually shares the momentum of the valence quarks after multiple interactions with the valence quarks. These c-quarks are far off-shell and subject to short-time scale fluctuation in contradiction to the long-time scale intrinsic charm picture. Most importantly, results from a Fermilab beam dump experiment (see references [11, 13, 74, 76]) and the CERN EMC experiment (reference [73]) do not seem to support

this intrinsic charm model.

The flatter X_F distribution of the charmed particles at ISR energies could also come from valence quarks (u, d) of the proton combined with a charm quark excited from the sea of the other hadron. This is the so-called charm excitation model [15, 59, 67, 68, 69, 73] (see figure 1-3 and figure 1-4). However, there are two major difficulties associated with the calculation of the excitation diagrams. The first one is the lack of knowledge of the structure function of the charmed sea quarks. The second difficulty is the determination of the $\hat{t}_{min}$ cutoff (i.e. the minimum momentum transfer needed to excite a charmed sea quark) which is necessary in the calculation since the diagrams diverge as $\hat{t}$ approaches 0.

Given these difficulties, Odorico [69] used a Monte-Carlo technique to generate the charm structure function from QCD evolution and obtained a rather hard X_F distribution for the produced charmed particles. Figure 1-5 shows the results of this calculation compared with result from the fusion model calculation. From this figure we can see that the output of the calculation depends sensitively on the choice of the parameters. At present, I think it is fair to say that the current theoretical status on the subject of hadronic production of charmed particles is still very primitive. To improve the situation, experimental groups have to provide better data. Unfortunately, even though the study of charmed particle physics has almost 8 years of history, high statistics and precise experimental data (especially on the hadronic production) are still very scarce.

1.2 EXPERIMENTAL METHODS

Let us now look at two important properties of the charmed particles that cause the study of charm physics to be not a simple matter. First, the smallness of the production cross-section sets a certain level of difficulty for the experiments. In a Fermilab fixed target experiment for example, the 20-50 μb production cross-section of charmed particles is about 3 orders of magnitude smaller than the total hadronic inelastic interaction cross section. Therefore event triggeribility for the experimental apparatus is naturally

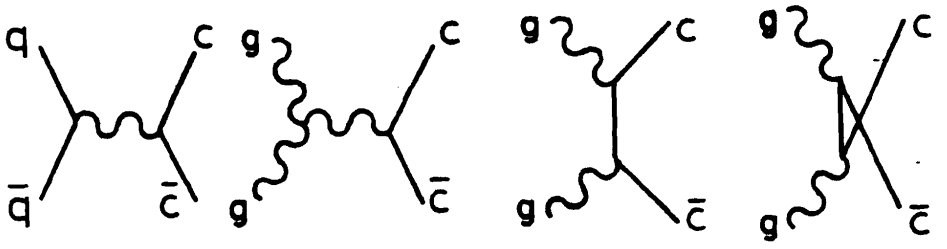

Figure 1-2: Quark-quark and gluon-gluon fusion diagrams

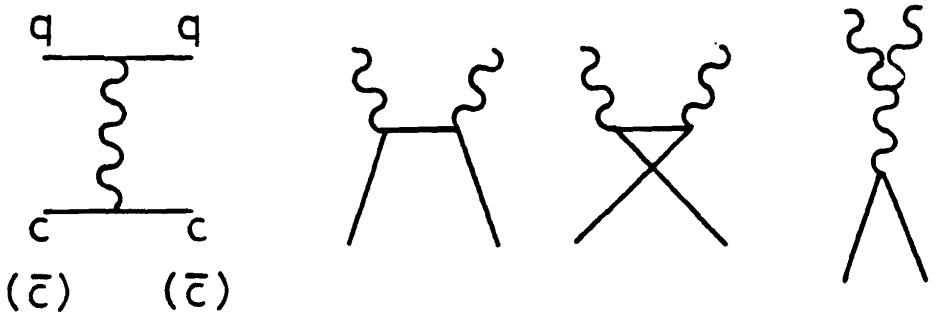

Figure 1-3: Order-α_s^2 diagrams for charm excitation

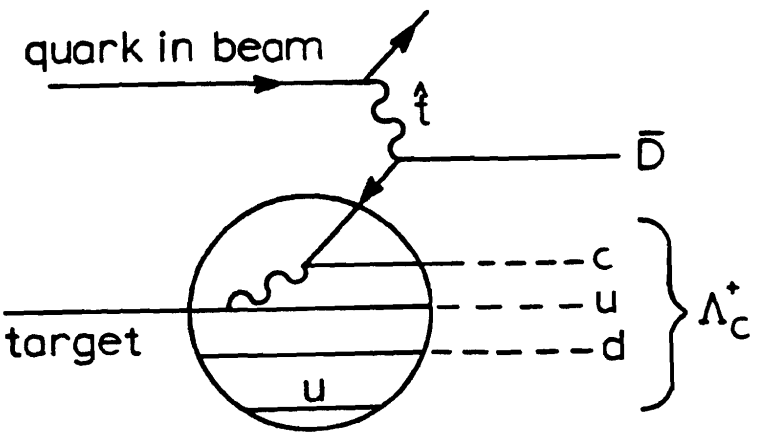

Figure 1-4: Charm excitation

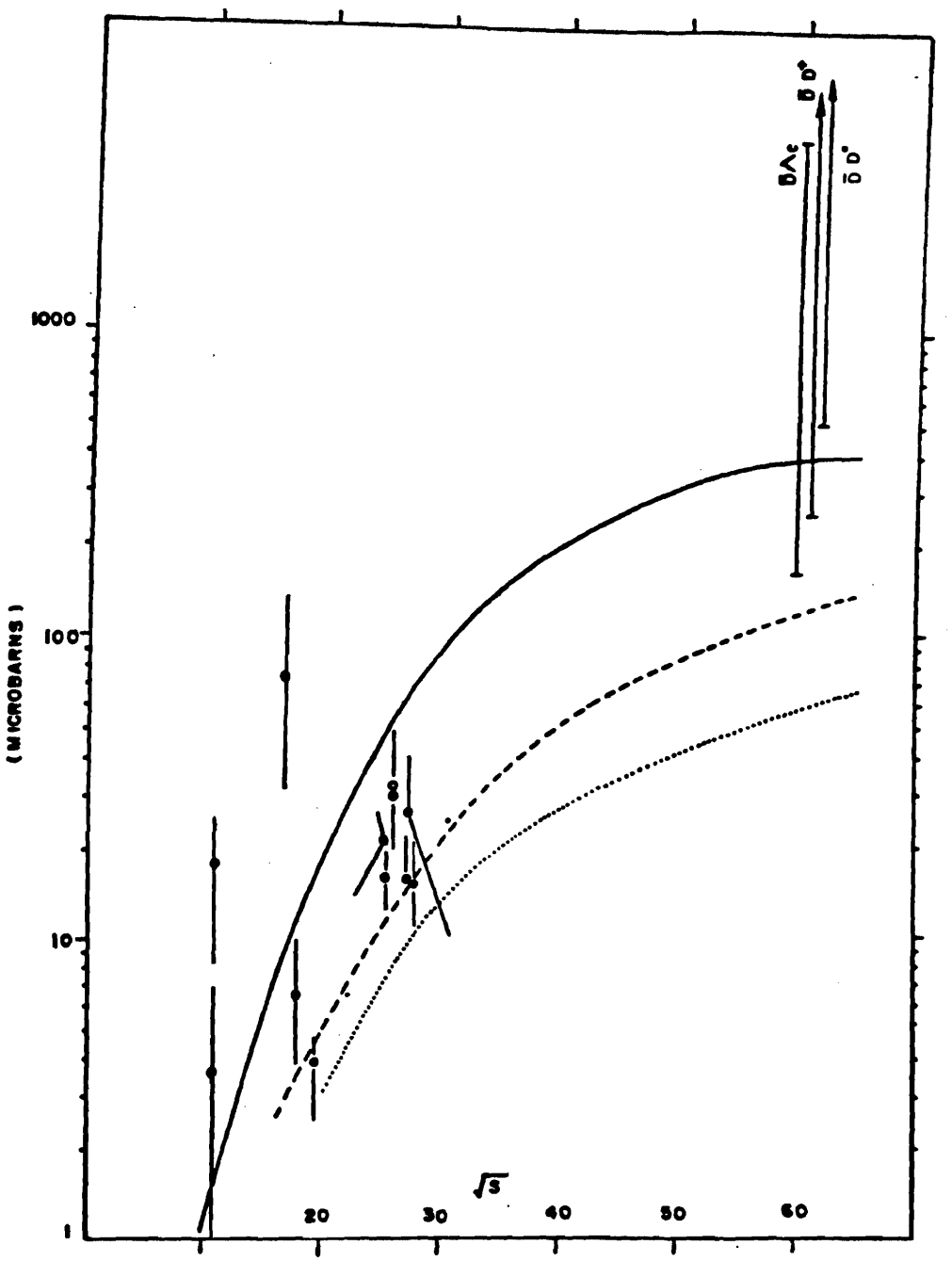

Figure 1-5: Hadronic production cross-section

(1)$\sqrt{S}$=C.M. energy. (2)Solid line: Monte-Carlo charm excitation calculation with $t_{min}=m_c^2/4$. (3)Dashed line: Same as (1), $\hat{t}_{min}=m_c^2/2$. (4) Dotted line: Fusion model calculation. (see references [69, 11])

required. Most of the spectrometer experiments, without a vertex detector, select special decay channels of the charmed particles as a means of detecting the charm signal. For example, the CERN ACCMOR collaboration at CERN [42, 43] is designed to look for the production of charmed particles in π-Be interactions such as

$$\pi^- \text{Be} \rightarrow D^0 + D^- + X \tag{1-12}$$

A charm event is identified by tagging the electron from the semileptonic decay of one of the D particles and measuring the hadronic decay mode of the other D particle (such as $D^0 \rightarrow K^-\pi^+$). At Fermilab or SPS energies ($\sim$ 400 Gev), the mean charged multiplicity per hadronic inelastic interaction event is about 12-15 (total number of secondary particles is about 18-22). In order to establish the D^0 signal as mentioned above, one has to loop through all possible combinations for all of the particles detected. This kind of *combinatorial background* together with the fact that most of the spectrometer experiments have limited acceptance are the two major disadvantages for this type of experiment.

Second, as listed in Eq. 1-6 to Eq. 1-9, the lifetimes of the charmed particles are very short ($\sim 10^{-13}$ to 10^{-12} sec.). In a fixed target experiment, with 300 Gev/c incident hadrons the decay distance is about 400 μm (assuming central production, $X_F \sim 0$ and $\tau_D \sim 10^{-13}$ sec.). The average *distance*, s, between a decay track from a short lived particle and the primary vertex can be estimated (in the relativistic limit) as [77]

$$<s/\beta c\tau>_{av} = \pi/2 \tag{1-13}$$

$$\Rightarrow s \sim 40\ \mu\text{m}$$

Experimentally, the best way to measure the lifetimes is with a 4π acceptance visual vertex detector. Visual detection of the charmed particles can also avoid the dependence of detection on a specific decay mode (like the $D^0 \rightarrow k^-\pi^+$ mode mentioned above). However, to obtain 40 μm resolution for a visual detector is not a simple task. So far, there are three kinds of visual detectors performing experiments to study the charm

physics. They are the *emulsion experiments*, the *bubble chamber experiments* and the *streamer chamber experiment*.

The emulsion technique can provide excellent resolution ($\sim$ 1 μm). However, a considerable *scanning* effort is required since the emulsion stacks are not triggerable (see for example references [8, 9, 24, 40, 35]). A typical example for the high resolution bubble chamber experiment is the CERN LEBC collaboration [31, 14, 36, 37, 38]. This bubble chamber has been exposed to both pion and proton beams and the resolution is reported to be about 30-40 μm. The bubble chamber technique shares the same disadvantage as the emulsion experiment, namely, it can not be triggered and therefore the *charm-event yield per picture* is still of the order of 10^{-3}.

The streamer chamber, a triggerable visual detector, provides a means to vastly improve the charm yield per picture. To detect charmed particle decays however, the streamer size (typically 1-2 mm for conventional chambers) must be significantly reduced. (As we will discuss in chapter 2, the *streamer size* can indeed be gotten down to the range of 40-50 μm). Based on this strategy (triggerablity + visual detector), starting in 1975, a high resolution streamer chamber has been proposed, designed and constructed by an experimental high energy physics group at Yale University under the leadership of Professor Jack Sandweiss. Table 1-1 lists a brief history of the R & D of this streamer chamber. All of the items included in this table will be discussed in detail in the following chapters.

Two experiments, Fermilab E-490 and E-630, have been performed with this streamer chamber. For both experiments, the streamer chamber was triggered on the detection of the prompt muon from a charmed particle (i.e. utilize the weak muonic decay of the charm quark as a signature of the hadronic production of the charmed particles. See figure 1-1-(a)). The prompt muons were required to be produced in an angle between 30 mr and 250 mr with respect to the beam direction and a minimum energy of 3.5 Gev and 6 Gev for the E-490 experiment and E-630 experiment respectively.

The E-490 experiment was set up in the M-1 beam line of the Meson Laboratory,

Fermilab in 1978. This was actually a test run for the chamber and the result has been published in 1980 [28]. In this experiment, 350 Gev protons were focused and directed into the chamber where interactions between the protons and the chamber gas (90%Ne-10%He, 300 psia) occurred. The production of charmed particles was signaled by energetic muons (> 3.5 Gev) from the semileptonic decay of the charmed particles. This energy selection was achieved by requiring the muons to travel through several *hadron shields* which were stacks of steel to filter out hadrons generated by the primary interactions. The events were recorded on film which was then developed, measured and analyzed.

In the E-630 experiment, which was set up in the Proton-Center experimental area of Fermilab with a high energy (~330 Gev average energy) collimated neutron beam instead of a proton beam. The trigger and apparatus were essentially the same as the E-490 experiment with the exception that two iron toroidal magnets were added at the end of the hadron filter to provide measurement on the muon momentum. The minimum muon energy was raised to 6 Gev with the addition of these toroids. The streamer chamber was also upgraded for this experiment. The reason that a neutron beam was selected for E-630 was to elliminate the presence of the beam tracks in the pictures[1]. From the experience of E-490, the charged particle beam tracks will often obscure the vertex region and make the forward jet area even more complicated (sometimes generating extra confusion when measuring the events). In the following chapters of this thesis, I will concentrate on describing the E-630 experiment. Chapter 2 includes detailed descriptions of the streamer chamber and the related high voltage devices. Chapter 3 describes the neutron beam line and the experiment. (A more detailed discussion of the muon spectrometer and the proportional wire chambers will be given in another thesis [78].) Chapter 4 discusses the data acquisition and film measurement. In chapter 5, the miss-distance calculation used in analyzing the pictures will be discussed. Finally in the last

[1]The disadvantage of using neutron beam is that it is very difficult to construct a *monochromatic* neutron beam line therefore it will be much harder to extract information on the C.M. energy of the interactions

chapter I will summarize and discuss the results of the calculation of the production cross-section.

YEAR	ACTIVITIES
1975	Design and proposal of the Yale streamer chamber.
1976-1978	Construction and tests.
1978	E-490 experiment; M-1, Fermilab; 350 Gev proton beam.
1980	Test of laser triggered Blumlein spark gaps.
1981	E-630 set up; Proton-Center, Fermilab; Neutron beam.
1982	E-630 experiment.

Table 1-1: R & D history of the Yale high resolution streamer chamber

Chapter 2

THE STREAMER CHAMBER

In this chapter, I will discuss the operational principles and the related high voltage pulsing technology associated with the Yale high pressure streamer chamber. In the first section, before we discuss the structure of the Yale high pressure streamer chamber, I will try to review briefly the theory of electron avalanche and the streamer formation. This is actually one of the subjects of gaseous discharge. A great deal of theoretical and experimental studies on gaseous discharge, avalanche, streamer and spark formation have been done over the past decades and many instructive descriptions on these subjects can be found in the literature (e.g. references [79] to [89] and [102]).

The high frequency high voltage pulsing technology (such as the Marx generator, the Blumlein system, the capacitive pulse monitors etc.) used in association with the streamer chamber will be described in section 2.2, section 2.3 and section 2.4. The overall performance of this streamer chamber and the related studies of various gas mixtures will be reported in section 2.5.

2.1 ELECTRON AVALANCHES, STREAMER FORMATION AND THE YALE STREAMER CHAMBER

When a charged particle passes through a gas, a trail of ions, electrons and excited atoms (molecules) are created along its path (Ref. [79]; Chapter 1). If an intense electric field is applied across the gas, the electrons will be quickly accelerated while the ions are relatively stationary. As they accelerate, the electrons (or ions) will collide with the gas atoms. For the case of isotropic scattering, the average fractional energy loss due to an elastic collision of an electron with mass m_e with an atom with mass M is

$$\Delta = \frac{2m_e M}{(m_e + M)^2} \tag{2-1}$$

Δ is approximately equal to $\frac{2m_e}{M}(\ll 1)$ for $m_e \ll M$.

Hence, the electron gains energy until the average energy gained between collisions equals to the average energy loss per collision. For sufficiently large electric field, some of the electrons will have energy high enough to generate secondary ionization by colliding with a gas atom. The number of electrons multiplies and the phenomena of electron avalanche sets in.

Townsend's first ionization coefficient, α, is defined as the number of electrons produced by a primary electron in traveling 1 cm along the electric field direction. Therefore the number of electrons produced by n electrons in a distance dx (cm) will be

$$dn = n\,\alpha\,dx \tag{2-2}$$

and the number of electrons produced by single electron in a distance x (cm) is

$$n = e^{\alpha x} \tag{2-3}$$

It can be shown by simple kinetic theory [79] that

$$\alpha = \frac{1}{l}\, e^{-V_{ion}/lE} \tag{2-4}$$

where l is the collision mean free path of the electron, V_{ion} is the ionization potential of the gas atom and E is the applied electric field intensity. Using the relationship $l \propto \frac{1}{P}$ where P is the pressure of the gas, equation 2-4 can be written as

$$\alpha = A \cdot P\ e^{-APV_{ion}/E}$$

or

$$\frac{\alpha}{P} = Ae^{-BP/E} \tag{2-5}$$

where A and B are constants.

The length of the avalanche along the field direction can be estimated as a function of the time t

$$x \approx v_t = \mu_E\ t$$

where v_ is the electron drift velocity and μ_ is the electron mobility.

The lateral size of the avalanche is determined by the diffusion of electrons transverse to the electric field. Let us concentrate on the plane perpendicular to the field direction and let r be the radial distance of an electron from its original position after time t. It can be shown by kinetic and statistical arguments [79] that the mean square of r is

$$<r^2>_{av} = 4D_t \tag{2-6}$$

where D_ is the diffusion coefficient which is proportional to the thermal energy (3kT/2) at zero field and $D_ \propto E^{1/2}$, approximately [86], at constant pressure.

As the avalanche grows, at some point the mechanism of the electron multiplication changes from the avalanche phase to the streamer phase. A rapid longitudinal extension of the avalanche (the ***streamer***) occurs, at both the cathode and anode ends, which can no longer be explained by the simple electron ionization collision process.

A commonly accepted model for the streamer formation was proposed by Lozanskii in 1969 [82]. In this model, the photo-ionization process is considered as the dominant mechanism for the growth of the streamer. When the number of electrons inside a single avalanche approaches 10^8 [86], the space-charge field of the electrons and positive ions becomes important and practically cancels the applied field at the middle of the avalanche. (At this point, the whole avalanche acts like a dipole). Within the avalanche, recombinations between the electrons and the ions emit photons which photoionize other gas atoms. At either the cathode end or the anode end of the avalanche, the local field is

so much enhanced that a secondary avalanche is quickly developed. At the cathode end, the newly created electron cloud merges into the positive tip of the primary avalanche and neutralizes it, leaving behind positive ions with about the same density as that of the primary avalanche. A similar process takes place at the anode side. This phénomenon is usually called ***self-sustaining*** streamer.

The avalanches quickly merge, leaveing the central body of the streamer as a neutral plasma. The transition between the avalanche phase and the streamer phase occurs when the number of electrons in the primary avalanche reaches about 10^8. According to equation 2-3, $e^{\alpha X_M} \approx 10^8$ or

$$\alpha X_M \approx 20 \tag{2-7}$$

Equation 2-7 is usually called the ***Raether Criterion*** and $X_M \approx 20/\alpha$ is the ***Meek Length***. Figure 2-1, which is reproduced from Ref. [79], shows a simplified sequence for the streamer formation.

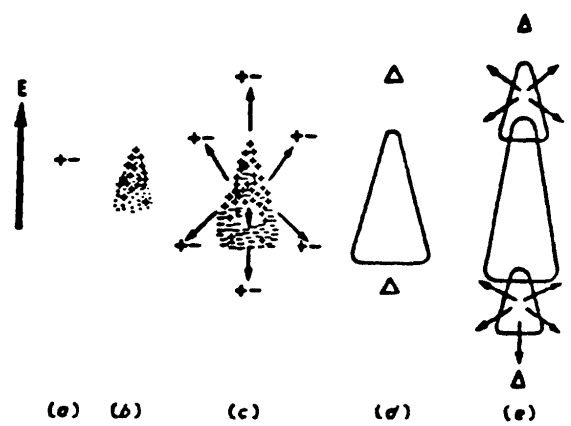

Figure 2-1: Stages in the growth of a streamer

(a)Creation of seed electrons and positive ions. (b)Formation of an avalanche. (c)Photons from recombinations produce more ion pairs. (d)New avalanches produced at the head and tail of the initial avalanche. (e)avalanches merge into a streamer.

After the transition from *avalanche* to *streamer*, if we keep supplying the electric field, the streamer will keep growing until a strip of conductive plasma between the two electrodes is established and electric breakdown occurs (a spark). A spark chamber

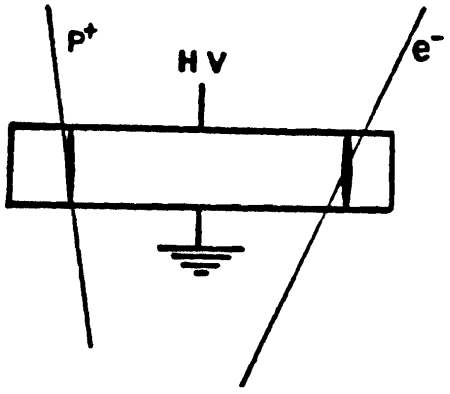

Figure 2-2: Spark chamber

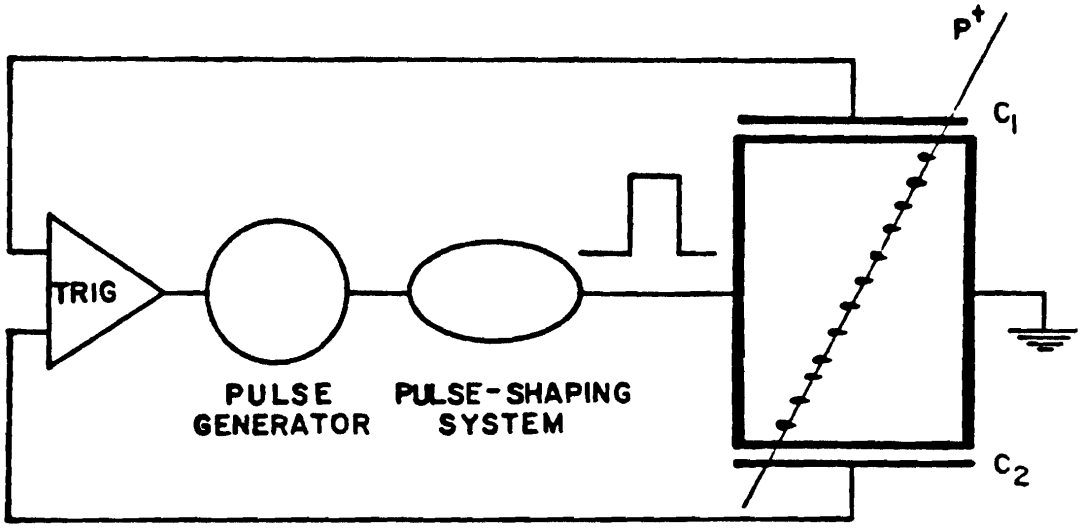

Figure 2-3: Operational scheme of streamer chamber

operates in this mode (Figure 2-2). For a streamer chamber, if however the high voltage across the chamber electrodes is terminated before the streamers develop into sparks, the primary seed electrons along the paths of the charged particles transfer into *localized* streamers which are self-luminous and can be photographed. Figure 2-3 is a schematic diagram of the streamer chamber. C_1 and C_2 stand for the charged particle detectors which provide the trigger signal for the generation of high voltage pulses. When viewed along the electric field direction, the pictures of charged particle tracks taken from a streamer chamber are similar to the pictures taken from a bubble chamber. A great advantage of the streamer chamber over the bubble chamber is that the streamer chamber is triggerable. (It is possible to operate the streamer chamber with a memory time of few microseconds.) The major limitations on the track resolution of the streamer chamber come from the thermal diffusion of the seed electrons during the unavoidable time delay between the passage of the particle and the arrival of the high voltage pulse. The track width depends on both the streamer size and the area of diffusion of the primary electrons. (A new *trick* to bypass the problem of thermal diffusion is to store the track information on negative ions or excited molecular states which have negligible diffusion. At the time this thesis is written, tests on these schemes are in progress at Yale).

The streamer chamber was first used as a particle detector by the Russian scientists G. E. Chikovani et al. [87, 88] and B. A. Dolgoshien et al. [89] in the early sixties. Later on, a great deal of pioneer work on the streamer chamber was done at SLAC [95]. Conventional streamer chambers operate at a pressure of about one atmosphere with field intensity in the order of 15 KV/cm and high voltage pulse duration of about 10 ns. The streamer size (transverse to the electric field) is on the order of few millimeters [118, 119] which is much bigger than the required resolution for the detection of the charmed particles (see the discussion in chapter 1, equation 1-13 for example).

The basic idea of the Yale high pressure high resolution streamer chamber is to apply a very high field on a high pressure chamber for a very short time (see also references [108] to [110]). Figure 2-4-(a) illustrates an avalanche in which the gas pressure is P_0.

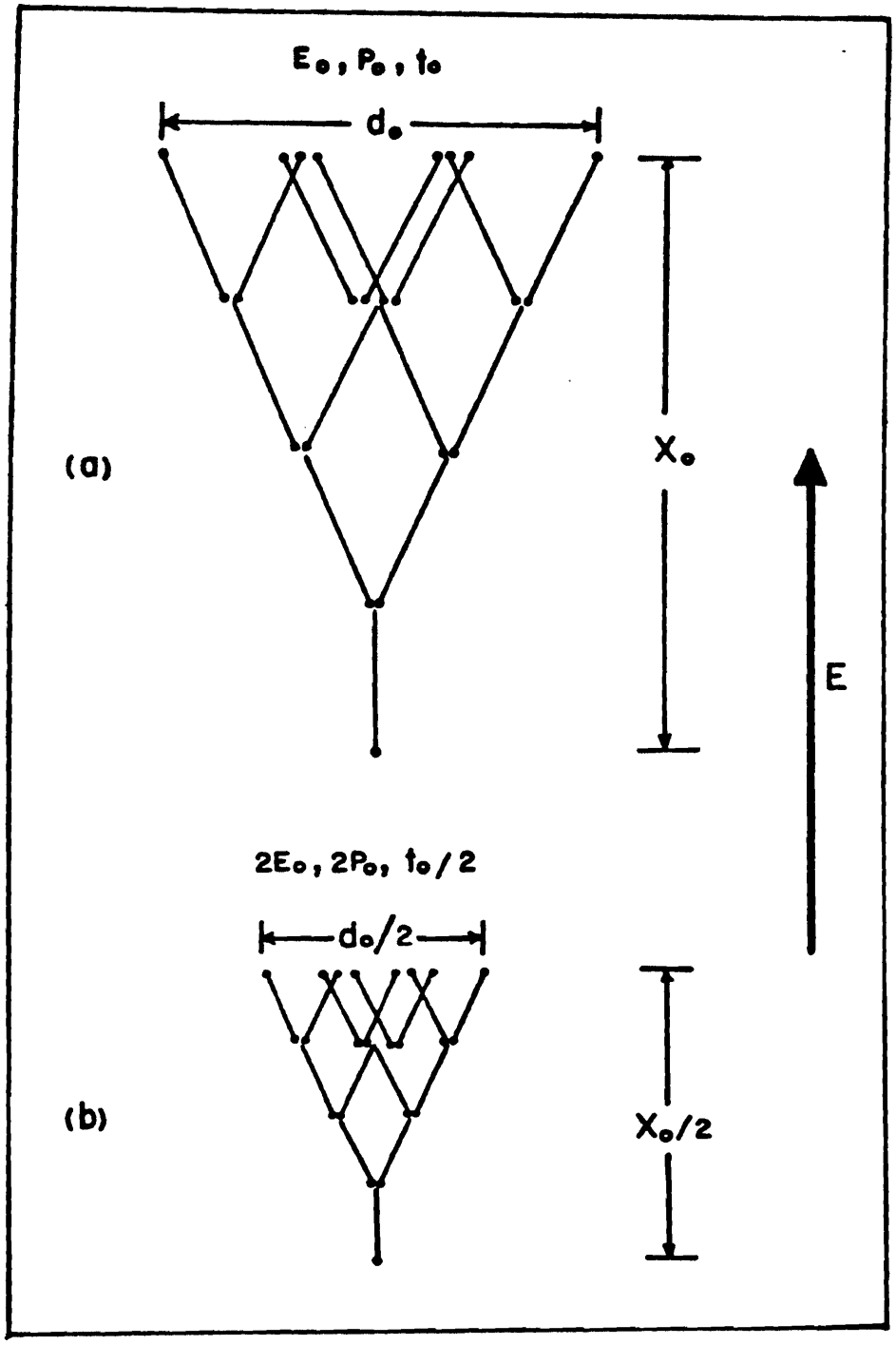

Figure 2-4: Scaling principle of avalanche formation

electric field intensity is E_0, the pulse duration is t_0 and the avalanche length is X_0. Figure 2-4-(b) shows another avalanche with pressure equal to $2P_0$, field intensity equal to $2E_0$, pulse duration equal to $2t_0$ and the avalanche length equal to $X_0/2$. The distance required for an electron to be accelerated to a certain value of energy in (b) is about 1/2 of the distance required in (a). On the other hand, the mean free path of ionization collision in (b) is also about 1/2 of the mean free path in (a). Therefore one would expect that the total number of electrons in (a) and (b) are the same. Let us take the situation with the same gas temperature for both cases. This implies that the electron drift velocity will be the same[1] for both (a) and (b). Thus the time required for the avalanche in (b) to develop is about 1/2 of the time required in (a).

We may also look at this scaling principle using the simple kinetic formulas. According to equation 2-5, $\alpha \propto P$ when E/P is constant. From equation 2-7 we thus have the Meek length $X_M \propto 1/P$. The lateral size of the avalanche in figure 2-4-(b) is also expected to be smaller than that of figure 2-4(a). The diffusion coefficient of electron under an electric field can be approximately expressed as (Ref. [79]; P.53)

$$D_ \propto \frac{E^{1/2}}{P^{3/2}} \tag{2-8}$$

since $E \propto P$, $D_ \propto 1/P$.

If t is proportional to 1/P then the avalanche radius (Eq. 2-6) is

$$\sqrt{<r^2>_{av}} = \sqrt{4D_t} \propto \frac{1}{P} \tag{2-9}$$

Now, let us apply this simple picture of the scaling principle to to our streamer chamber. At one atmosphere of 90%Ne–10%He, with an electric field of about 15 KV/cm and 10 ns pulse duration, the size of the avalanche in a conventional streamer chamber was of the order of 1 mm [86, 95]. The high voltage pulse of the Yale high pressure streamer chamber was designed to be in the order of 150 to 200 KV across a

---

[1] $v_ \propto \mu_E$ and $\mu_ \propto \frac{1}{P}$

chamber gap of $\sim$ 0.5 cm with $\sim$ 1 ns pulse duration. This amounts to an electric field of about 300 KV/cm, 20 times higher than the conventional chamber and a pulse duration 10 times shorter than the conventional chamber. The chamber pressure was designed to have a maximum pressure of 600 psia, 40 times higher than the conventional case. According to equation 2-9, we have:

$$D_{-\,(300KV/cm;\ 40atm)} \sim \frac{(20)^{1/2}}{(40)^{3/2}} D_{-\,(15KV/cm;\ 1atm)}$$

and the size of the avalanche

$$R_{(300KV/cm;\ 40atm)} \sim \sqrt{0.018 \times 0.1} \cdot R_{(15KV/cm;\ 1atm)} \sim 0.04 \text{ mm}$$

Therefore the *streamer* size should be $\sim$ 40 μm by operating the chamber in the avalanche mode.

Figure 2-5 shows the drawing of the assembly of the Yale streamer chamber. The *Blumlein box*, which contained the pulse shaping system[2] as illustrated in figure 2-3, was attached to two G-10 disks which were fixed inside a big G-10 cylinder. Extending from the Blumlein box was a parallel plate transmission line which carried the output HV pulses from the pulse shaping system to the chamber electrodes.[3] This transmission line was also mounted on G-10 supporting columns inside the same G-10 cylinder. The whole cylinder, as an integral unit, was inserted into a large stainless steel pressure vessel which was designed to have a maximum pressure of 40 atm. The size of this stainless steel vessel was about 274 cm long, 61 cm in diameter with 2.5 cm wall thickness. The front end of this vessel was covered by a 10 cm thick G-10 flange with a penetration hole at the center. An aluminum cylinder which carried the high voltage pulses from the Marx generator[4] (the HV pulse generator illustrated in figure 2-3) to the central electrode of the Blumlein system was inserted through this penetration hole and sealed against the G-10

---

[2]The Blumlein system will be discussed in detail in section 2.3

[3]The transmission line and the *transparent electrodes* will be discussed in detail in section 2.4

[4]The Marx generator will be discussed in section 2.2

flange with *O-rings*. One end of an aluminum vessel, which contained a coupling resistor between the Marx generator and the Blumlein system and a resistive monitor for monitoring the Marx output (see section 2.2), was attached to the surface of this G-10 cover flange and the other end was attached to the Marx generator (figure 2-9).

The beam ports were two symmetric stainless steel reentrant cones located at both sides of the transparent electrodes (figure 2-5). The beam windows on the tip surfaces of these two beam cones were made of 50 μm stainless steel with surface area of about 4 cm by 0.5 cm. The window and the beam cone were metal-sealed against each other. The edges of the openings on the beam cones were very carefully machined such that when the streamer chamber was pressurized (or evacuated), the deformation of the 50 μm windows followed smoothly the contour of the openings. This type of beam window structure was tested in the machine shop before it was applied to the streamer chamber. During the tests, the windows constantly broke at pressures higher than 1000 psia after more than 100 pressure-vacuum cycles. For more than 6 years operation of this streamer chamber, no damage (or leakage) on the beam windows was observed.

The optical system consisted of two lenses, one above and one below the *transparent* electrodes, viewing the streamers in the end to end direction. The two optical axes, which connected the centers of the lenses to the center of chamber, subtended an angle of (180−7) degrees. That is to say the optical system had a 7-degree stereo angle which provided information for the 3 dimensional reconstruction of the charged particle tracks. One of the lenses had a 4 inch focal length and the other had a 6 inch focal length. The reason for using two different focal lengths was simply that the two lenses were on hand (Perkin-Elmer lenses manufactured for the Yale PEPR system). The 6 inch Perkin-Elmer lens was later replaced with a Schnider Componon-S 150 mm lens. The two views were arranged such that they both had a demagnification factor of about 2/3. In this set up, both lenses had a resolution of about 30-40 μm with a depth of field around 2.5 mm[5].

[5]In the actual setup, we did not observe any noticable variation in the resolution of our optical system by adjusting the focal plane of the lenses through the 4.5 mm gap of the chamber electrodes

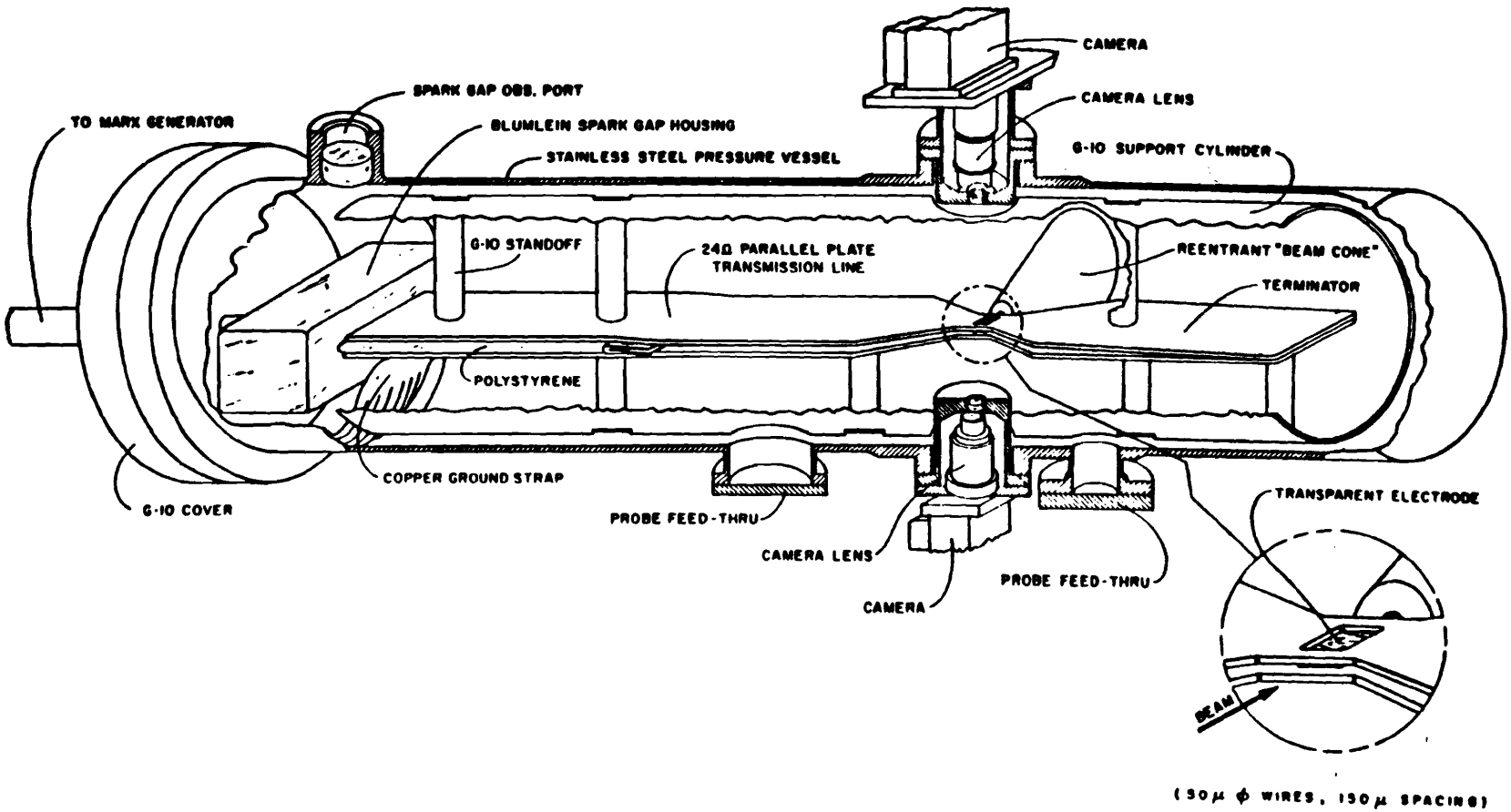

Figure 2-5:
A cutaway view of the Yale High Resolution Streamer Chamber

As will be explained in section 2.5, the pictures of the streamers were recorded through image intensifiers. The images of the streamers were actually focused on the photo-cathode of the image intensifiers and the cameras were mounted such that the film (35 mm Kodak S.O. 143 film) was pressed against the fiber optic output windows of the inage intensifiers. The cameras used in this experiment were originally used on the 21 inch and 30 inch bubble chambers at Brookhaven National Laboratory. Many mechanical and electrical modifications were required to make the cameras suitable for use on the streamer chamber. To ensure good contact between the film and the the fiber optic surface of the image intensifier, a rubber diaphragm was mounted in place of the vacuum platten. This rubber *balloon* was inflated by compressed air to push a layer of mylar forward which in turn pushed the film against the image intensifier. Before advancing the film, the rubber was flattened again (by vacuum) to allow the film to move smoothly. These cameras, as finally modified, were capable of being operated at about 6 frames per second without mechanical failure.

The most annoying problem caused by these cameras was the electrostatic discharge between the film and the metal body of the camera or between the film and the image intensifier. This electrostatic discharge caused tree-like images on the film. This problem was finally solved by increasing the humidity level in the *streamer chamber house* (the RF house) which served mainly as RF shielding cage to isolate the high frequency noise, generated by either the Marx generator or the Blumlein system, from interupting the electronic setups of the experiment and the beam line area. (The need for the shield cage was evident from the fact that the leakage RF noise from the streamer chamber would (unshielded) automatically trip off the fluorescent lamp outside the RF house and the CAMAC crate for the beam line electronics.)

By comparing figure 2-5 with figure 2-3, we can see that in order to have a *complete* streamer chamber system, it was necessary to incorporate a pulse generator. The type of pulse generator used in this experiment is a combination of a Marx generator and a spark gap switched Blumlein line. These components are discussed in the next sections.

2.2 THE MARX GENERATOR

As it is illustrated in figure 2-3, a complete streamer chamber system consists of the following parts: the trigger devices, the high voltage generator, the pulse shaping device and the chamber body. The trigger devices for this experiment will be described in chapter 3. In this chapter I will mainly concentrate on describing the streamer chamber itself. In the previous section, we estimated the required high voltage pulse for our streamer chamber is on the order of 150 KV to 200 KV with about 1 ns pulse width. In high voltage pulsing technology, this kind of fast, high voltage pulse is usually generated by coupling a pulse shaping system to a high voltage generator. First let us discuss the high voltage generator.

In principle, many kinds of high voltage pulse generators (or even a DC power supply) can be used to generate high voltage as the input to the pulse shaping device such as the Blumlein-line system. In practice (basically for *economic* reasons), the Marx generator is the most commonly chosen high voltage generator for this kind of application. The Marx generator is a triggerable device consisting of multiple stages of capacitors and low impedance switches. The capacitors are connected to a DC power supply and charged up in parallel to a high voltage, V_0. The output voltage of the Marx generator is obtained by discharging the capacitors in series through the switches. Therefore the peak output voltage of a Marx generator is approximately equal to the sum of the voltage across each stage of capacitors (i.e. $n \cdot V_0$ for the case of an n stage Marx generator). For most high voltage applications such as the streamer chamber pulse generator, spark gaps are used as the series switches of the Marx generator.

Figure 2-6 shows a simple 5 stage Marx generator circuit. Initially all of the capacitors are charged up to V_0. When the trigger pulse causes the breakdown of the first switch, S_1, the rest of the spark gaps are over stressed by the discharge of the first stage capacitor. These gaps are adjusted such that they will break down at this over voltage.

Since all of the spark gaps break down almost simultaneously, the risetime of the

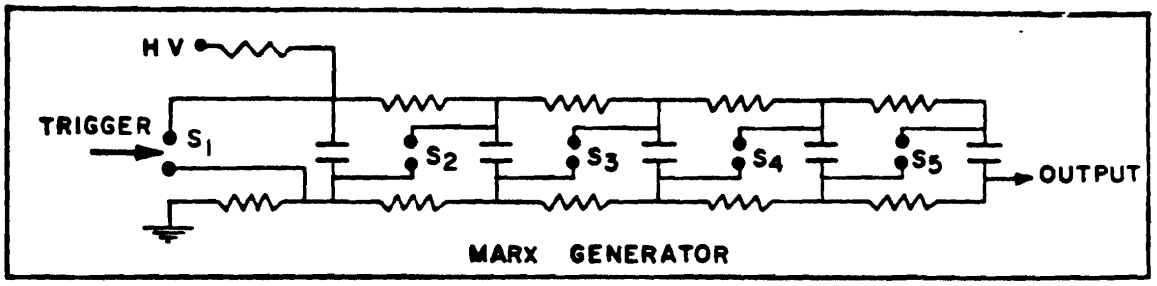

Figure 2-6: Example of an MARX GENERATOR circuit

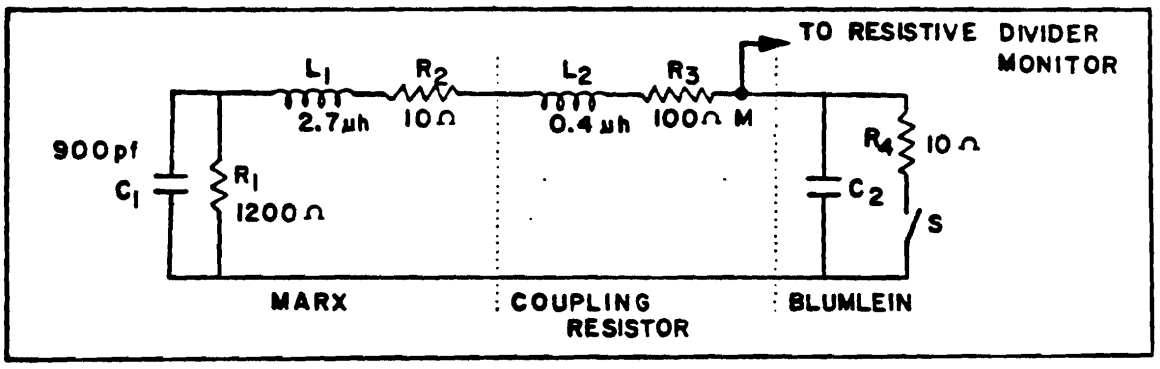

Figure 2-7: Equivalent circuit for the MARX-RESISTOR-BLUMLEIN system

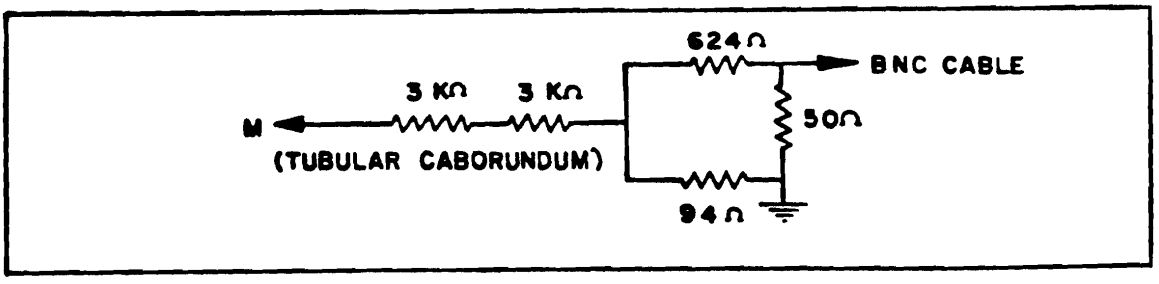

Figure 2-8: Equivalent circuit for the resistive divider monitor
Pickoff ratio ≈ 0.001

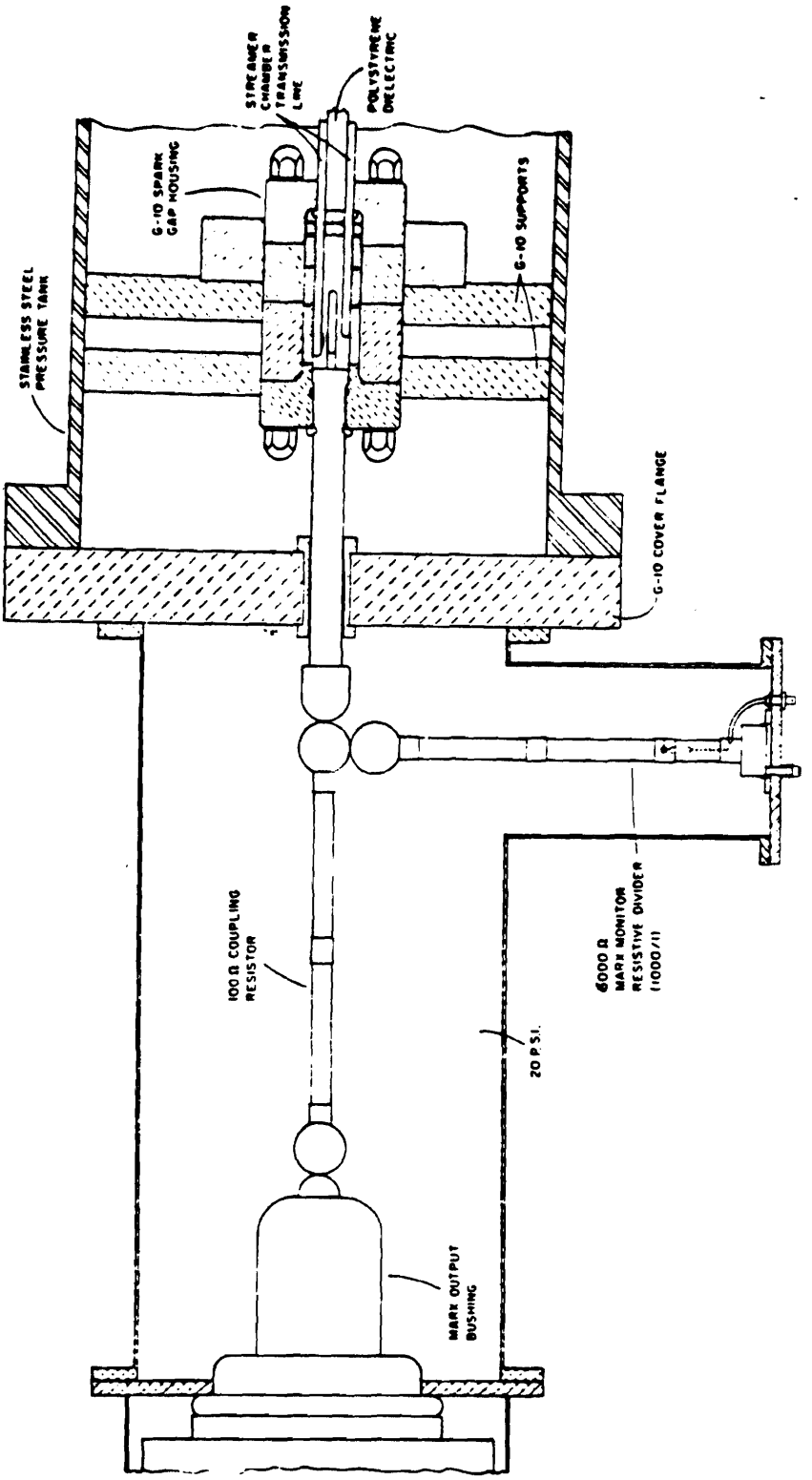

Figure 2-9: The coupling resistor and the resistive divider monitor, located as shown inside a 20 psia aluminum vessel which also acts as a ground return for the Marx charging current.

Marx output pulse depends mainly on the overall switching time of the spark gaps (this is usually negligible), the inductance of the Marx generator and the RC time constant between the series capacitace and the load resistance (assuming that the inductance and the impedance of the spark gaps and the load inductance are all negligible).

Generally speaking[6], the stability of the Marx output pulse depends strongly on the performance of the spark gaps. A conventional method of improving the simultaneity on the breakdown of the spark gaps is to let all spark gaps *see* the first trigger gap such that when the first gap *fires*, the UV generated will preload the rest of spark gaps and cause them break down easily under over voltage condition.

The Marx generator used for the Yale high resolution streamer chamber (during the EXP-630 period) was developed to our specification by the Pulsar Associate Inc.[7] (Pulsar model 400). Because we originally planed to incorporate the laser triggered switch technique with our Blumlein pulse shaping system (see section 2.3), the time jitter between the trigger signal and the Marx output pulse should be as small as possible. Figure 2-12 shows the oscilloscope traces of 30 Marx output pulses. The scope was triggered by the triggering signal for the Marx generator. The overall time jitter in the Marx output pulses was about 5 ns.

The output bushing of the Marx generator was connected to the Blumlein pulse shaping system (Sec.2.3) through a 100 Ω low inductance resistor. As will be discussed in detail in the next section, the Marx output pulse *sees* the Blumlein system as a capacitor shunted by a small resistor (few ohms; i.e. the spark). The effective impedance of the Blumlein was small compared to the 100 Ω coupling resistor. Therefore most of the energy was dissipated by the coupling resistor rather than by the *delicate* Blumlein system.

Figure 2-7 is an equivalent circuit for the Marx-resistor-Blumlein system, L_2 is the

---

[6]Detailed discussions on the Marx generator can be found in references [79, 90, 91, 95]

[7]A division of Physics International

estimated effective inductance for the section of the coupling resistor, C_2 is the capacitance of the Blumlein system and S represents the spark gap of the Blumlein with impedance R_4 when the Blumlein breaks down. At point M, a low inductance 6000 Ω resistive divider with about 8 ns rise time in response to a step pulse (see figure 1 of Ref. [99]) was used for monitoring the Marx output pulses. The pickoff ratio of this resistive monitor was about 1000:1.

Figure 2-8 shows the equivalent circuit for this monitor. Both the resistive divider and the coupling resistor were made of tubular carborundum and were shielded by an aluminum vessel (figure 2-9); this vessel was used as the ground return for the charging current and was pressurized to 20 psia with dry air to prevent HV breakdown between the resistors and the ground. The resistive monitor with its coaxial shield was essentially a resistive (lossy) transmission line with a coaxial return. As is mentioned in reference [99], this type of transmission line was the first transmission line problem to be solved analytically by Lord Kelvin in 1854, 20 years before Maxwell's ***Treatise on Electricity and Magnetism***. (The solution is also reproduced in [99].)

Figure 2-10 shows the calculated pulse shape at point M of figure 2-7 (with the condition that the Blumlein electrodes do not break down). The value of L_2 was estimated to be 0.4 μh and C_2 was taken as 100 pf. Figure 2-11 is a scope picture of the pulse from the resistive divider monitor. The similarity between these two pictures is very obvious. Figure 2-12 is a scope picture of the monitor pulses with the sharp traces indicate the breakdowns of the Blumlein spark gap. As can be seen from this picture, the Blumlein system was adjusted such that the switching spark gap in the Blumlein line broke down at the peak of the Marx output pulse.

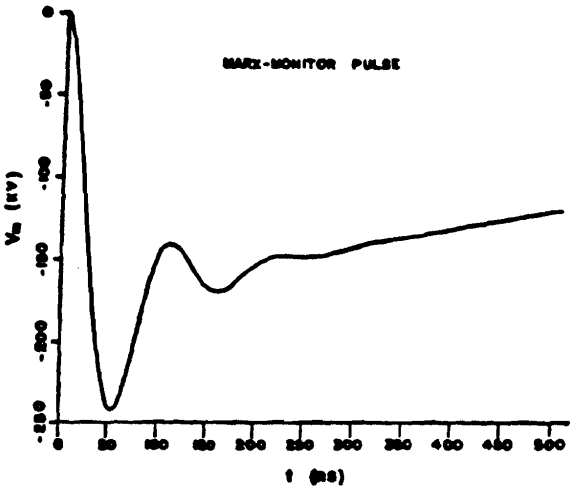

Figure 2-10: Computer calculated Marx monitor pulse

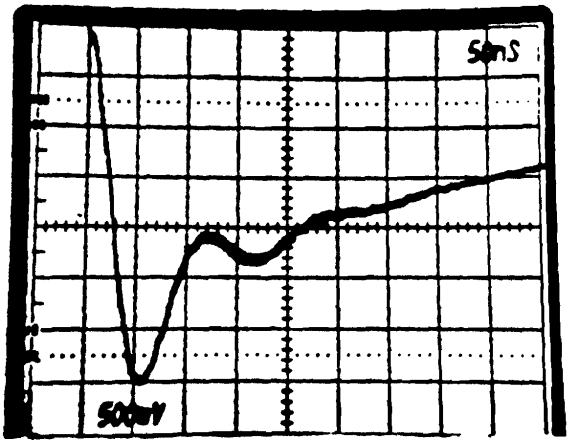

Figure 2-11: Oscilloscope trace of the Marx monitor pulse

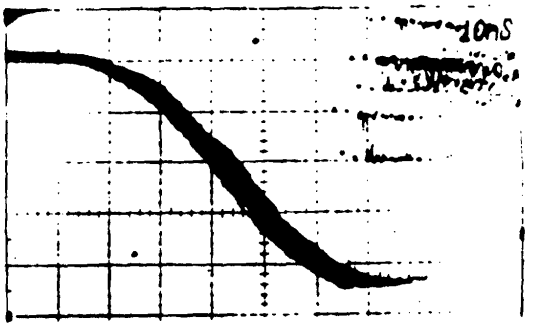

Figure 2-12: Marx output pulses from the resistive divider monitor

(30 shots; 10ns/Div.) Pulse amplitude is about 250 KV and the rise time is about 50 ns. The scope was triggered by the trigger signal for the Marx generator. The sharp switching traces are due to the break down of the Blumlein electrodes (Sec 2-3)

2.3 THE BLUMLEIN PULSE SHAPING SYSTEM

The output pulse from the Marx generator, as it is shown in figure 2-11, is certainly not suitable for our streamer chamber which requires a pulse voltage in the range 150 KV to 200 KV with pulse duration in the order of 0.5 to 1 ns. A Blumlein pulse shaping system is therefore added to *modify* the pulse shape from the Marx generator.

The way the ***Blumlein-line system*** works can be understood by considering the three-electrode diagram in figure 2-13. The two outer electrodes **A** and **C** extend to form a transmission line **c** and the front section of this line is separated into two equal lines, **a** and **b**. Let us assume that the line impedance of **a** and **b** are equal to Z_0 and the impedance of line **c** is equal to $2Z_0$. Electrode **A** is grounded and the central electrode, **B** is charged up by the Marx generator to $+V_0$. At time t=0, the switch **S** (spark gap) between electrodes **A** and **B** is closed. This will cause the charge on the central electrode to flow onto the electrode **A**. This is equivalent[8] to generating a wave with amplitude equal to $-V_0$ traveling to the right of line **a**. Let us label this wave as $V_a^{in}=-V_0$. At $t = \tau = L/c$, this wave reaches to the junction of the three lines where the wave *sees* a total impedance of $3Z_0$ across line **c** and line **b** (series sum). Part of the wave, $V_a^r = -V_0 \cdot [(3Z_0-Z_0) / (3Z_0+Z_0)] = -\frac{1}{2} V_0$, will be reflected back to the left of line **a** and the rest will be transmitted to the series composition of line **c** and line **b**. The total current must be conserved, therefore $I_t = I_{inc}-I_r = -\frac{1}{2}(V_0 / Z_0)$ and the total voltage across line **c** and line **b** will be $3Z_0 \cdot I_t = -\frac{3}{2} V_0$. Among this voltage, 2/3 of it will be distributed across line **c** and 1/3 of it goes to line **b** (electrode **B** relative to electrode **C**). Thus the part of wave transmitted to line **c** will have amplitude equal to V with the same polarity as the incident wave ($V_c=-V_0$).

If we label the part of wave *transmitted* to line **b** as $V_b^r=V_C-V_B$, then $V_b^r=-\frac{1}{3}(-\frac{3}{2} V_0)=\frac{1}{2} V_0$. We see already that the two *reflected* waves, V_a^r and V_b^r, are equal in amplitude yet opposite in polarity. At time $t=2\tau$, both reflected waves reach the

[8]Let us assume that the switch, S, is an ideal perfect switch (i.e. with 0 inductance and 0 impedance), and the closure of the switch will not affect the line impedance.

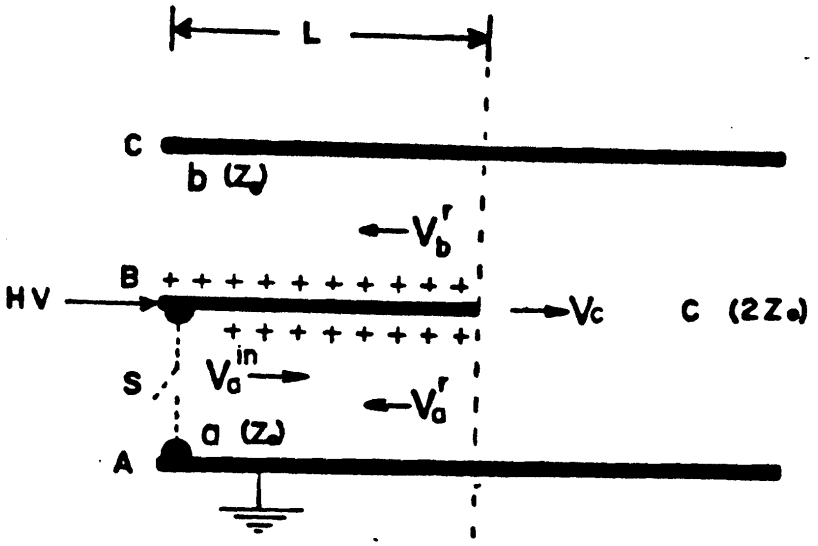

$V_a^{in} = -V_o$, $V_a^r = -V_o/2$, $V_b^r = V_o/2$

$V_c = -V_o$

Figure 2-13: The Blumlein lines

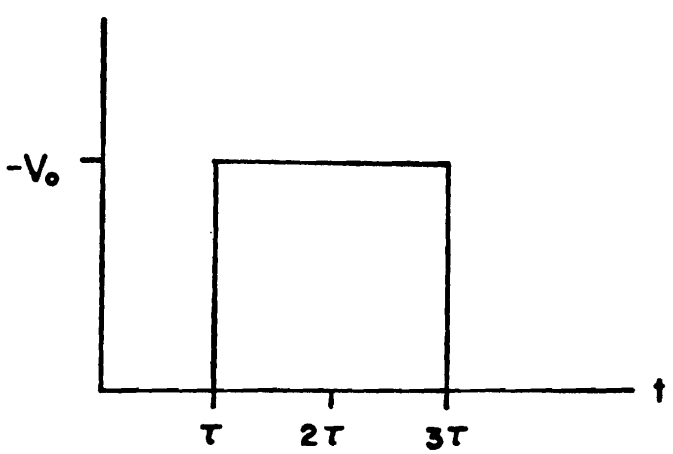

Figure 2-14: Ideal Blumlein-line output pulse

front end of line b and line a where they *see* opposite boundary conditions. The V_a^r encounter a shorted end whereas V_b^r sees an open end. Therefore upon reflection at the front end, the two ***doubly reflected*** waves will be equal in both amplitude and polarity ($\frac{1}{2}V_0$). At time t=3τ, these two waves travel back to the junction again and add up to a total voltage of $+V_0$ which cancels out the $-V_0$ wave on line c. The net result is a pulse (rectangular, for the ideal case) of 2τ duration, starting from time t=τ, propagating to the right in line c. The amplitude of this pulse is equal to the charging voltage from the Marx while the polarity is opposite (figure 2-14).

Many methods can be used to carry out the detailed calculation for the behavior of the Blumlein output pulse ([92] and [100], for example). The method of reference [100], which actually handles the transient behavior of the Blumlein pulse, will be described later on in this section.

Unlike most of the other streamer chambers which used a coaxial Blumlein lines, the Blumlein system of the Yale high resolution streamer chamber consisted of 3 parallel plates (figure 2-15(a) and figure 2-15(b)). The top and bottom electrodes extended to form the main transmission line which guided the high voltage pulses to the chamber. All three electrodes were made of aluminum 1 cm thick. The central electrode was a rectangular piece with dimension of 20.5 cm x 7 cm. The main reason for choosing a parallel plate configuration for the Blumlein system was to avoid the complex transition between a coaxial Blumlein system and the parallel plate transmission line. However, as will be described below, we essentially sacrificed the line uniformity for this mechanical simplicity.

In the original design (Fermilab EXP-490), there were 4 spark gaps between the central electrode plate and the grounded plate to provide effective switching along the input edge of the Blumlein. In the final operation mode (Fermilab EXP-630), only one spark gap was used. Again, we will talk about the reasons for this change below.

As it is shown in figure 2-15, the box housing the Blumlein was made of fiberglass (G-10) and the whole box was inserted inside two big G-10 disks (each about 60 cm in

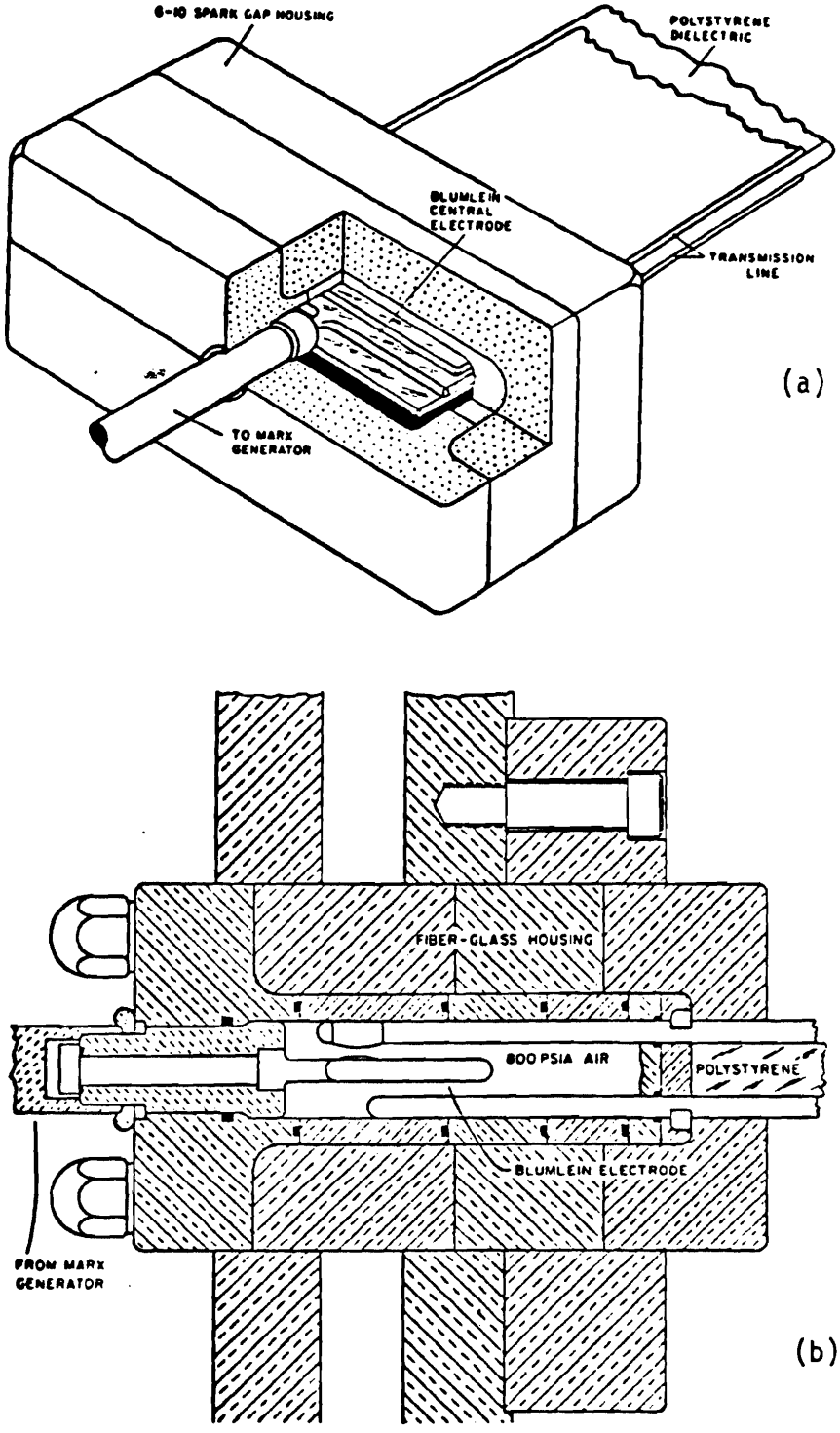

Figure 2-15: Cutaway and cross section views of the Blumlein Box

diameter and 5 cm thick).

The Blumlein box was pressurized to about 800 psia with dry air. (in the earlier Fermilab E-490 experiment, argon gas was used). Since the whole Blumlein box was inside the streamer chamber tank, which was pressurized to 600 psia (90%Ne-10%He), the differential pressure applied to the Blumlein box was only about 200 psia.

The impedance of the parallel plate transmission line can be estimated with the empirical formula [92]

$$Z = 120\pi \frac{s}{W+s+T} \Omega \tag{2-10}$$

where (figure 2-16) s is the spacing between the plates, W is the effective width of the plates and T is the thickness of the plates.

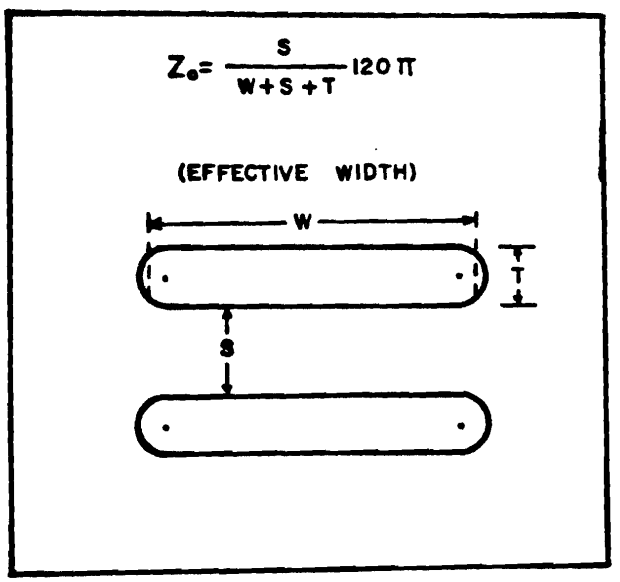

Figure 2-16: Impedance of parallel plate transmission line

Equation 2-10 is a modification to the formula used to calculate the characteristic impedance of the ideal parallel *plane* transmission line [93]

$$Z = \sqrt{\mu/\epsilon}\,\frac{s}{W} \tag{2-11}$$

$(\sqrt{\mu/\epsilon} = \sqrt{\mu_0/\epsilon_0} = 120\pi\ \Omega$ for free space)

The difference between equation 2-10 and equation 2-11 is that equation 2-10 takes into account the effect of the fringe field from the rounded edges of the plates.

Since the main transmission line of our Blumlein system had polystyrene ($\epsilon=2.25\epsilon_0$) as dielectric material, the impedance was etimated as

$$Z_m = \frac{120\pi}{\sqrt{2.25}} \frac{s}{W+s+T} = 26\ \Omega$$

$$(s = 2.5\ \text{cm},\ W = 20.5\ \text{cm},\ T = 1\ \text{cm})$$

For the two switching lines:

$$Z_s = 120\pi \frac{s}{W+s+T} = 13\ \Omega$$

$$(S = 0.77\ \text{cm},\ W = 20.5\ \text{cm},\ T = 1\ \text{cm})$$

Hence

$$Z_m = 2Z_s$$

To illustrate the properties of the parallel plate transmission line, take the function $e^{(j\omega t-\gamma z)}$ to describe the wave propagating along the $+\hat{s}$ direction and define $k^2 = \omega^2\mu\epsilon = (2\pi f)^2\mu\epsilon$. For waves in the TEM mode, $\gamma^2 = -k^2$ (for example, see Ref. [93]), so that the waves propagate with no attenuation. On the other hand, the situation is different for non-TEM waves. For example, consider TM waves and assume no variation in the $\hat{y}$ direction ($\hat{x}$ perpendicular to the conducting plane). The equations for the electric field intensity can then be written as

$$\frac{\partial^2 E_z}{\partial x^2} = -(\gamma^2 + k^2)\, E_z \tag{2-12}$$

$$\frac{\partial^2 E_y}{\partial x^2} = -(\gamma^2 + k^2)\, E_y \tag{2-13}$$

Define $k_c^2 = \gamma^2 + k^2$

In order to satisfy the boundary conditions, E_y and E_z must equal to 0 at x=0 and x=s (s is the spacing between the conducting plates). Therefore $k_c = n\pi/s$, n=integer and

$$\gamma = \sqrt{k_c^2 - k^2} = k\sqrt{(k_c/k)^2 - 1} = k\sqrt{(f_c/f)^2 - 1} \tag{2-14}$$

where f_c is the cut-off frequency. For a TM wave with frequency less than f_c, γ is real and the electric field intensity attenuates as the wave propagates. For the case of our Blumlein,

$$s = 0.77 \text{ cm and (take n=1)} \quad k_c = \frac{\pi}{0.77 \text{ cm}}$$

$$\Rightarrow$$

$$f_c = \frac{c \cdot k_c}{2\pi} = 19.5 \times 10^9 \text{ Hz}$$

Now, to conservatively estimate the maximum frequency of interest, we assume the risetime of the Blumlein pulse is 0.5 ns, which corresponds to a frequency (at 3 db point; Ref. [96], Sec 1-5, 2-7)

$$f = \frac{0.35}{0.5 \times 10^{-9}} = 0.7 \times 10^9 \text{ Hz}$$

and $k=0.147 \text{ cm}^{-1}$ for this frequency. This implies $\gamma=4.1 \text{ cm}^{-1}$. For a 7 cm Blumlein, $e^{-\gamma z}=3.4 \times 10^{-11}$. Hence we should feel safe to anticipate the dominance of TEM waves in our Blumlein design. It is also interesting to note that the smaller the spacing, s, between the two conducting plates, the higher the cut-off frequency. On the other hand, one would like to have a bigger spacing in order to withstand higher voltage. Therefore one would have to make compromises between these two factors when choosing the scale of the transmission line.

In the early stage of the development of this high pressure streamer chamber (E-490), the central electrode was supported from both sides and a small gap was kept between the central plate and the high voltage charging lead from the Marx generator. When the Marx *fired*, the voltage difference between the Marx lead and the central plate started to build up and eventually this gap broke down before the Marx output pulse reached to its peak voltage. The four spark gaps between the central plate and the grounded plate would thus be pre-loaded with photoelectrons (from the argon gas) generated by the UV from this breakdown. At this point, the central plate would also be charged up by the Marx output pulse. By carefully adjusting the four spark gaps, we could manage to make them switch *simultaneously* in some fraction of firings (about 50%). This operational

Figure 2-17: Sampling scope picture of the Blumlein pulse (see text) FWHM~0.5 ns

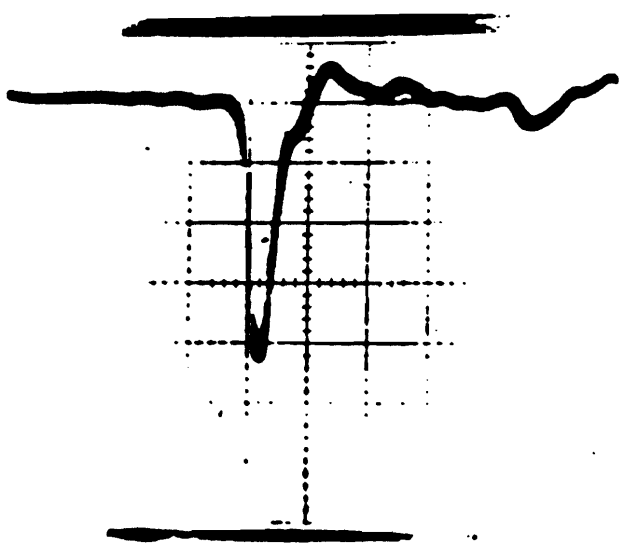

Figure 2-18: Tektronic 7904 scope picture of the Blumlein pulse. 50 shots overlapped; 2 ns/Div.

scheme has been used previously by a one atmosphere streamer chamber [94]. We operated the streamer chamber with this scheme for almost a whole year (Fermilab E-490 [28, 108, 109]).

Figure 2-17 shows a sampling scope picture of the Blumlein pulse when the Blumlein was operated with the scheme mentioned above[9]. The risetime of the sampling system was about 70 ps. The two peaks in figure 2-17 represent the same signal with time base displaced by 1.3 ns. The amplitude of the signal was about 90 KV and pulse width (FWHM) was about 0.5 ns. Figure 2-18 is a scope picture of the pulses with 50 shots overlapped. This picture was taken with a Tektronic 7904 oscilloscope which has a risetime of about 0.8 ns. The high voltage pulse amplitude was about 150 KV.

The trouble with operating the Blumlein in this scheme was the unsatisfactory stability of the Blumlein pulses due to the problem of syncronizing the four spark gaps. Since we were aiming at a pulse width of about 1 ns, the four spark gaps were required to switch synchronously at least within a few tenths of 1 ns. In order to improve the situation, we tried to trigger the spark gaps with a nitrogen UV laser (λ = 3370 nm, pulse energy about 3-4 millijoules and pulse width of about 5 ns FWHM; figure 2-19)

From the beginning of January 1980 to the end of March 1980, we set up a prototype with narrower Blumlein and only 1 spark gap to study the technique of the laser triggered Blumlein system. The time jitter between the laser beam and the Blumlein output pulse was measured. With careful alignment of the optical system, this time jitter can be worked down to about 1 ns (figure 2-19). Nevertheless when we tried this laser trigger scheme on the four spark gap system, we could just barely make two gaps fire together but were never be able to achieve four gap synchronism.

There are many experts in the subject of laser triggered switches (e.g. references [111] to [116]). Their studies indicate that the time jitter between the laser pulse and the breakdown of a spark gap depends strongly on the laser power density. As the power

---

[9]The Blumlein pulse *pickoff* will be described in Sec. 2.4

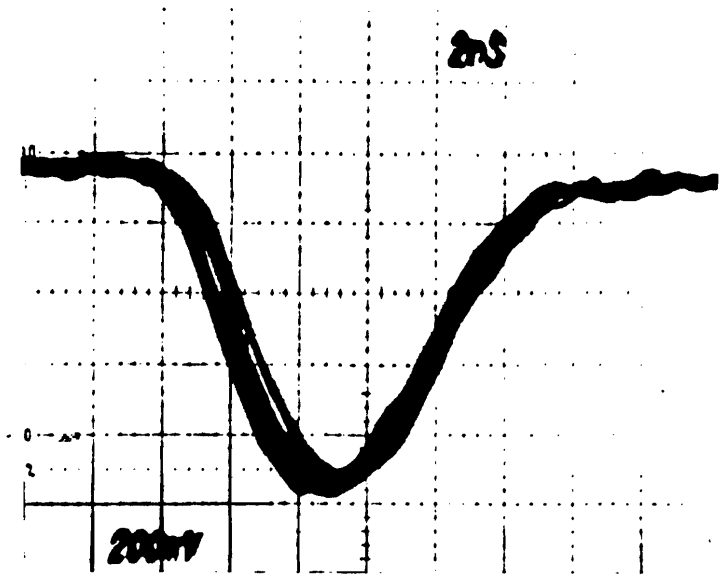

Figure 2-19: N_2 laser pulse; 2 ns/Div.

An EG&G FND-100 photo diode was used as the laser pulse monitor. The scope was triggered on the Blumlein output pulse (see the picture below). The signal traces were slightly contaminated by the RF noise generated by the Marx generator and the Blumlein spark gap.

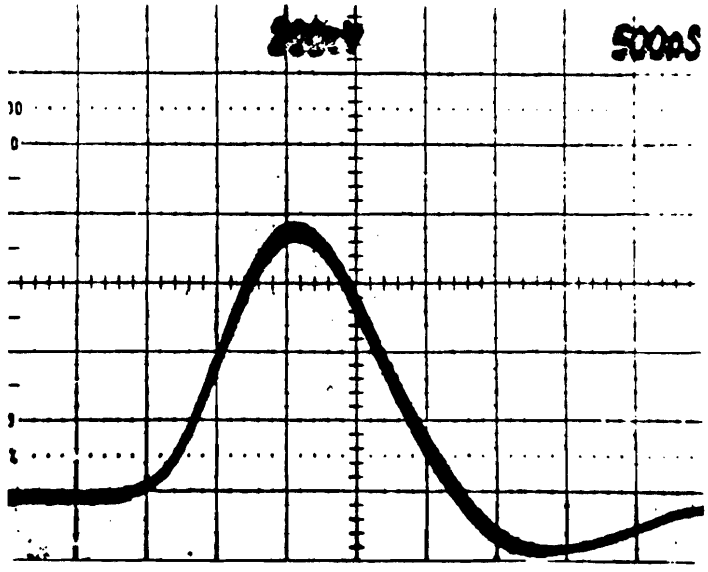

Figure 2-20: The output pulse from the prototype laser triggered Blumlein system 20 overlapped traces; scope scale: ~ 42.5 KV/Div and 500 ps/Div

density increases, the jitter decreases rapidly up to certain level ($\approx$ 0.1 ns; [111]). Beyond this level, the rate of decrease in the time jitter will decrease.

Insufficient laser power could only be one of the reasons why we failed to fire the four spark gaps simultaneously. There were some other factors which were also not negligible. For example, since the four spark were not electrically independent of each other, any small jitter in the spark formation time would cause most of the current to flow through whichever gap broke down first. Optical alignment was another serious problem in our setup. The whole Blumlein box unavoidably *moved* slightly after the box was pressurized. This mechanical instability caused the optical alignment to be extremely difficult. Any small amount of misalignment in one of the gaps had to be compensated by balancing the laser power (i.e. splitting the laser beam in different proportions). The net result was simply to make the total laser power available even smaller.

It was almost at the same time as we were struggling with the laser triggered Blumlein system that Professor R. Beringer at Yale made a series of elegant studies on the behavior of the Blumlein system and the characteristic properties of a spark gap (Ref. [97] to [101]). As is pointed out in these studies, the parallel plate Blumlein system suffers from the same problem as the radial line because appropriate frequency waves are not excited by the closure of the spark gap. This problem is actually rooted in the inductive property of a spark gap as has been reported in the SLAC-74 streamer chamber report (appendix A of reference [95]). The detailed mathematical arguments are included in reference [100]. I will simply summarize the results here:

[A] Uniform transmission line

For a uniform transmission line of length L with one end shorted (figure 2-21), from the consideration of standing waves, the normal mode spectrum can be expressed as

$$\lambda_n = \frac{4L}{2n+1} \qquad n = 0, 1, 2 \cdots \tag{2-15}$$

The corresponding wave frequencies are

$$\omega_n = (2n+1)\frac{\pi}{2\tau} \tag{2-16}$$

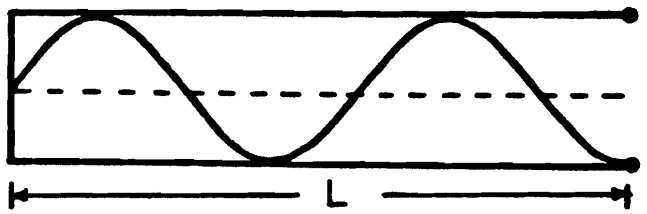

Figure 2-21: Standing wave inside a uniform transmission line

where $\tau = \frac{L}{c}$

We also remember that a square function, $V(t)=V_0$ for $0 < t < 2\tau$, can be represented by the Fourier series (e.g. Ref. [93], section 1.12)

$$V(t) = \frac{4V_0}{\pi}[sin(\frac{\pi}{2\tau}t) + \frac{1}{3}sin(\frac{3\pi}{2\tau}t) + \cdots] \tag{2-17}$$

we can immediately see that the component frequencies in the Fourier series is exactly the same as the standing wave frequencies. Therefore the *right* frequencies can be generated by shorting a *perfect* switch at one end of an uniform line. (We also recall that a step pulse is generated when the switch closes in an ideal Blumlein system as discussed in the beginning of this section.)

[B] Radial transmission line

For the case of the radial transmission line (figure 2-22; Also see Ref. [93], Sec. 8.12), if we define the input wave impedance as $Z_i=E_{zi}/H_{\phi i}$ and the load impedance $Z_L=E_{zL}/H_{\phi L}$ then the value of Z_i can be calculated according to the equation [93]

$$Z_i = Z_{0i}\left[\frac{Z_L cos(\theta_i-\psi_L) + jZ_{0L}sin(\theta_i-\theta_L)}{Z_{0L}cos(\psi_i-\theta_L) + jZ_L sin(\psi_i-\psi_L)}\right] \tag{2-18}$$

where

$$\theta(x) = tan^{-1}\left[\frac{N_0(x)}{J_0(x)}\right] \tag{2-19}$$

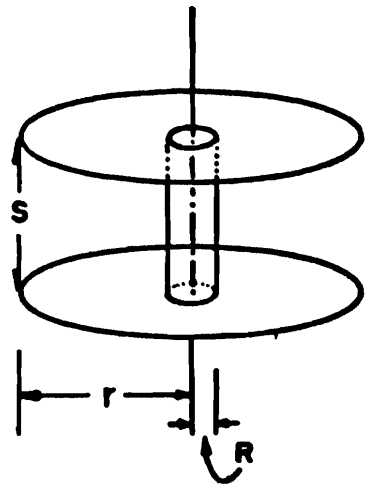

Figure 2-22: Radial line transmission line

$$\psi(x) = tan^{-1}\left[\frac{J_1(x)}{-N_1(x)}\right] \tag{2-20}$$

$$Z_0(x) = \sqrt{\mu/\epsilon}\,\frac{G_0(x)}{G_1(x)} \tag{2-21}$$

$$G_0(x) = \sqrt{J_0^2(x) + N_0^2(x)} \tag{2-22}$$

$$G_1(x) = \sqrt{J_1^2(x) + N_1^2(x)} \tag{2-23}$$

with

$k = \omega\sqrt{\mu\epsilon}$

$J_\nu(x)$ and $N_\nu(x)$ are Bessel functions of the first and the second kind respectively (with order ν). The subscript, i or L, represents the value of a function calculated at the input or load position. For example, Z_{0L} is the characteristic impedance, $Z_0(kr)$, at the location of the load.

In figure 2-22, the central column with radius R represents the shorting spark with finite diameter. Therefore Z_L can be replaced by zero if we assume E_z=0 at r equal to R. Equation 2-18 can be rewritten as (r and R are defined in figure 2-22)

$$Z_i(kr) = jZ_0(kr)\,\frac{\sin[\theta(kr)-\theta(kR)]}{\cos[\psi(kr)-\theta(kR)]} \tag{2-24}$$

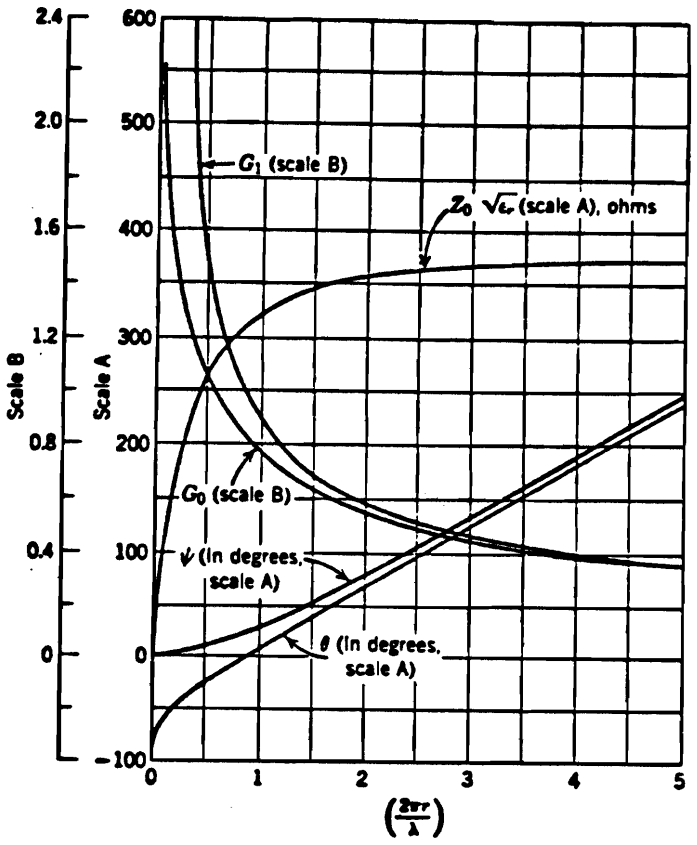

Figure 2-23: Plots of Z_0, G_0, G_1, ψ and θ as functions of kr

A plot of the functions Z_0, G_0, G_1, θ and ψ vs kr is given in figure 2-23 which is reproduced from Ref. [93]. In this plot we can see that the Z_0 stays approximately constant only when $kr > 3.5$. At small values of kr, the value of Z_0 changes rapidly. This is far from the property of a uniform line.

Equation 2-24 also shows the inductive property of the radial line. Figure 2-24 (from Ref. [98], P.6) illustrates the value of $Z_i(kr)/Z_0(kr)$ as a function of kr. (Where kR is taken as 0.02.) As we can see from this plot the radial line starts out inductively at $r > R$ and reaches to infinity at kr equal to 0.817, 4.21 and 7.39 etc. These poles correspond to the resonant frequencies $f_0=0.817c/2\pi r$, $f_1=4.21c/2\pi r$ and $f_2=7.39c/2\pi r$ etc. These resonances are not harmonically related to each other as the case of the

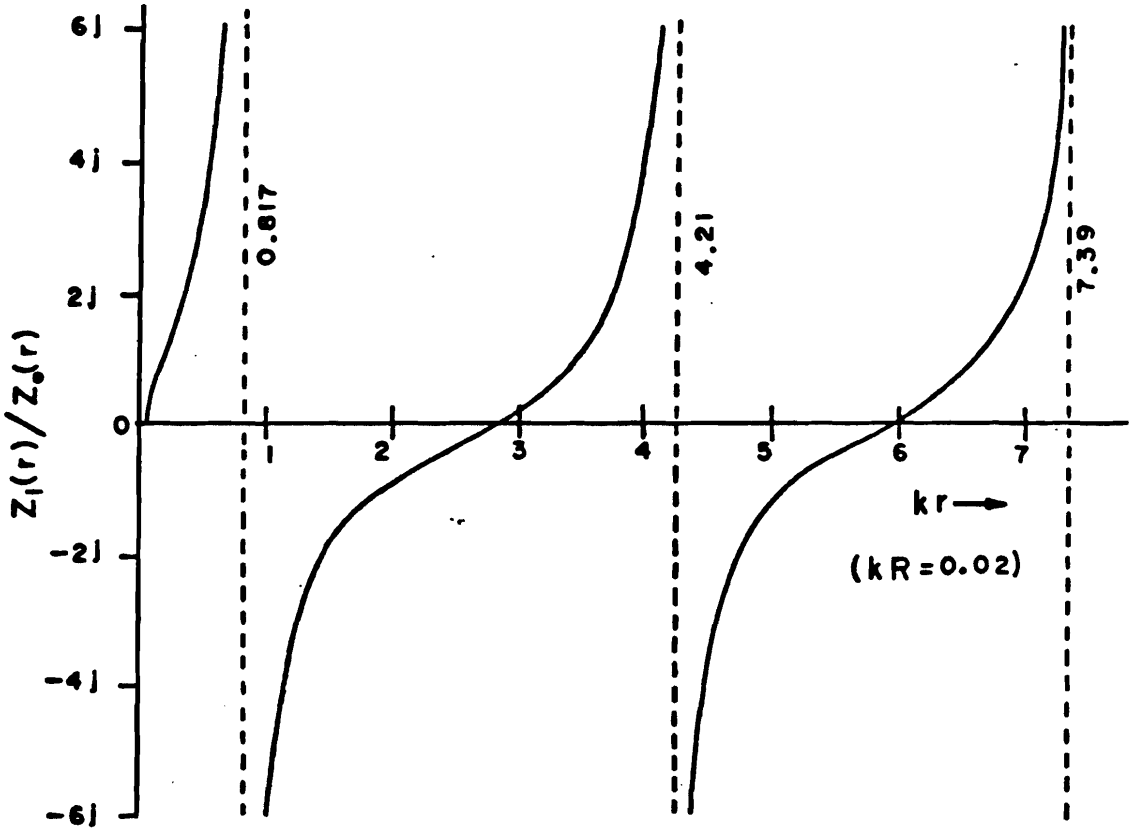

Location of poles in $Z_i(r)$ as a function of $2\pi R/\lambda$

$2\pi R/\lambda$	$2\pi r/\lambda_0$	$2\pi r/\lambda_1$	$2\pi r/\lambda_2$
0.0001	0.510	4.01	7.19
0.0005	0.565	4.04	7.22
0.001	0.596	4.06	7.24
0.005	0.686	4.12	7.30
0.01	0.742	4.16	7.34
0.02	0.817	4.21	7.39
0.05	0.94	4.31	7.48
0.10	1.08	4.42	7.59
1.00	2.33	5.55	8.70

Figure 2-24: Plot of $Z_i(r)/Z_0(r)$ vs kr and the list of poles in $Z_i(r)$

uniform line (equation 2-16. Therefore a radial line does not provide the *right* normal mode frequencies for a rectangular pulse.

The inductive property of the radial line described above comes from the geometric property of the central column (the ***spark***) in figure 2-22. The inductance of this *spark* can be estimated as

$$L = \frac{\mu s}{2\pi} ln(\frac{r}{R}) \tag{2-25}$$

where, again, r is the radius of the line, R is the radius of the spark and s is the spacing of the line. We can immediately see that the inductance of a spark depends strongly on the distance of the gap and the diameter of the spark.

Equation 2-24 is in fact a ***wave impedance***, to calculate the ***total*** impedance we have to take into account the relationship $V=-E_z \cdot s$ and $I=2\pi\, r \cdot H_\phi$. Hence the total input impedance

$$Z_{total} = j\,\frac{s}{2\pi r}\, Z_0(kr)\, \frac{sin[\theta(kr)-\theta(kR)]}{cos[\psi(kr)-\theta(kR)]} \tag{2-26}$$

In the limit $kr \ll 1$, $J_0(kr) \approx 1.0$, $J_1(kr) \approx kr/2$, $N_0(kr) \approx -\frac{2}{\pi} ln\frac{2}{\gamma\, k\, r}$ with $\gamma=1.78107\cdots$, $N_1(kr) \approx -\frac{2}{\pi x}$, $\psi(kr) \approx 0$. Then

$$Z_{total} = js\sqrt{\mu/\epsilon}\,\frac{1}{\lambda}\, ln\frac{r}{R} = j\omega\,\frac{\mu s}{2\pi}\, ln\frac{r}{R} = j\omega Ls \tag{2-27}$$

Equation 2-27 clearly explains the inductive property of $Z_i(kr)$ in figure 2-24.

After realizing this radial line problem, let us go back to our Blumlein. Since the parallel-plate structure of our Blumlein system was so much closer to the case of a shorted radial line, we might as well consider it as an RLC circuit, a combination of a inductive switch L, capacitive parallel plates C and resistive load $2Z_0$. As a mater of fact, the output pulse of our Blumlein (figure 2-25) was indeed very similar to the wave form of a lumped RLC circuit (figure 2-26) where the current can be expressed as:

$$I(t) = -\,V_0\,\frac{\omega_0^{\,2}\,C}{2\alpha_d}\, e^{-\alpha t}\,[e^{\alpha_d t} - e^{-\alpha_d t}] \tag{2-28}$$

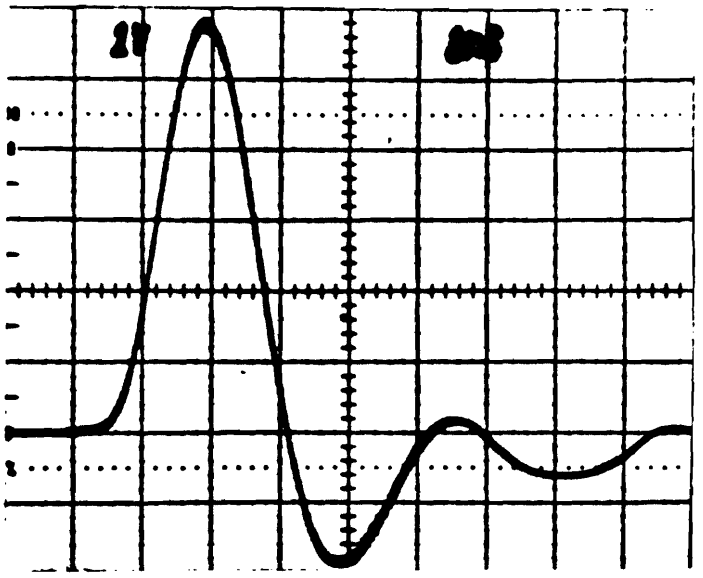

Figure 2-25: The single gap Blumlein output pulse FWHM ~ 1.4 ns; amplitude ~ 150 KV

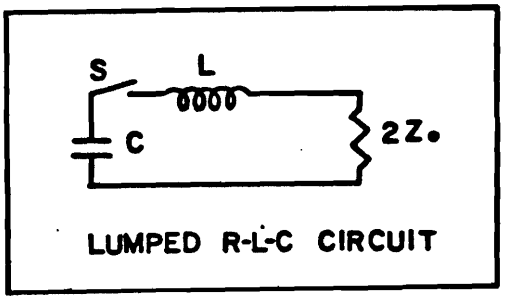

Figure 2-26: Lumped R–L–C circuit

By comparing Figure 2-25 with Eq. 2-28, we estimate that the inductance of the Blumlein switch is about 8×10^{-9} henry

where $\alpha = Z_0/L$, $\omega_0 = \sqrt{1/LC}$ and $\alpha_d^2 = \alpha^2 - \omega_0^2$. The risetime of this simple RLC circuit is $\tau = L/Z_0$. By comparing the risetime of the pulses in figure 2-25, the inductance of the spark gap can be estimated to be on the order of 9 nh.

We concluded that in order to make a faster risetime and shorter duration pulse from our Blumlein, we had to make the inductance of the spark smaller. (note: decreasing the capacitance was not a solution since this would lower the total amount of energy stored inside the capacitor initially)

In reference [94], Rohrbach reported on the improvement of the risetime of Blumlein pulses with multiple spark gaps switched together. This is equivalent to lowering the effective inductance of the switches. (The problem of multi-gap synchronism was not as serious in his application as it is to us since the output pulse of his Blumlein was on the order of 10 to 20 ns.)

In our case, we finally chose to keep only one spark gap and make the gap distance as small as possible. The central electrode plate of the Blumlein was modified and attached to the HV charging lead from the Marx generator. The Blumlein box was pressurized with either dry air or nitrogen. We found that the pulse stability and risetime are slightly better with air than nitrogen (this indicates that the spark switching time is slightly faster in dry air than in nitrogen).

The dry air inside the Blumlein box was constantly flushed. The pressure of the box was carefully adjusted to ensure that the spark gap fires on the peak of the Marx pulse (figure 2-27). The spark gap was made of stainless steel. The radius of curvature of the surface of the spark gap electrode was about 17 mm and the gap distance was about 2.6 mm. Figure 2-28 shows the output pulses of the Blumlein system with 30 traces overlapped. The Blumlein box pressure was 780 psia with dry air and the Marx output voltage (figure 2-27) was 250 KV. The amplitude in figure 2-28 was 165 KV.

The *lifetime* of the the spark gap was about 200,000 breakdowns on the spark gap electrodes. (This corresponded to about 2 weeks continuous operation for the Fermilab E-630 experiment.) By replacing the spark gap every 2 weeks and continuously adjusting

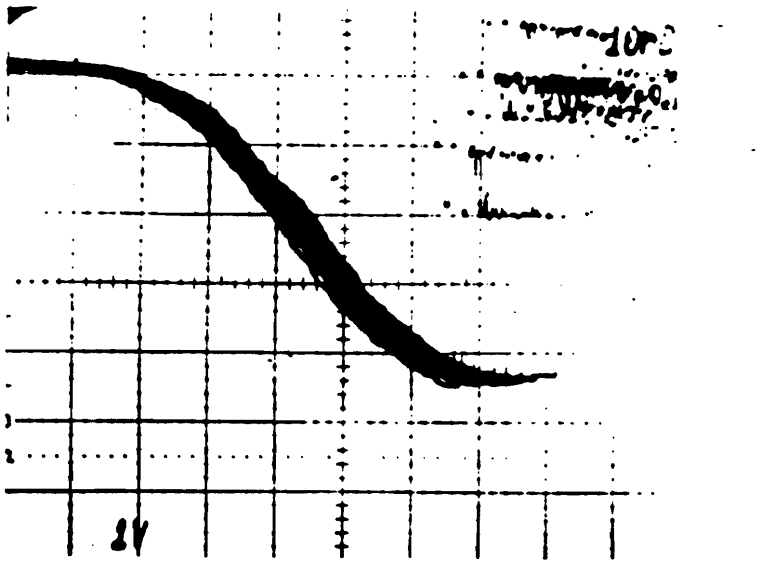

Figure 2-27: Marx output pulse; amplitude ~ 250 KV; rise time ~ 50 ns

The Blumlein box pressure is adjusted such that the spark gap breaks down at the peak of the Marx output voltage

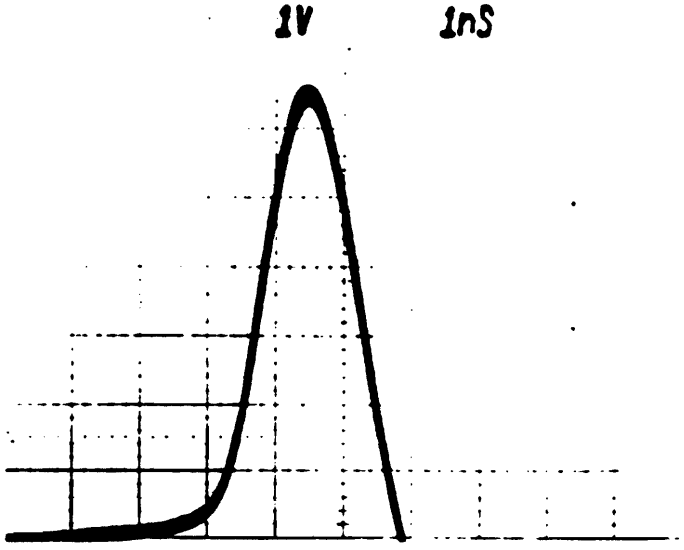

Figure 2-28: Blumlein output pulse; 30 overlapped traces; amplitude ~ 163 KV

Both figure 2-27 and figure 2-28 were taken at the same conditions. The Blumlein box pressure was set at 780 psia with dry air. The spark gap distance was set at 2.6 mm. These pictures were taken with Tektronic 7104 scope with ~ 0.38 ns risetime.

the Blumlein box pressure, the output pulses were adequately stable during the whole data-taking period of E-630 in the spring of 1982.

Before leaving this section, I consider that it is worthwhile to mention the beautiful work of Professor R. Beringer on the calculation of the Blumlein system with inductive switch [100].

The behavior of the Blumlein output pulse can be calculated with the technique of Laplace transformation. Figure 2-30 schematically shows a Blumlein system in the four-terminal network convention. L represents the inductance of the switch and l is the length of the switching lines. The characteristic impedance of the switching line is Z_0 and the load (i.e. main line impedance) is $2Z_0$.

Using the four-terminal network transformation matrix, the transfer equations for a ***transmission line*** (figure 2-29) can be expressed as [117]

$$\begin{bmatrix} \mathcal{E}_2 \\ I_2 \end{bmatrix} = \begin{bmatrix} \cosh j\omega\frac{l}{c} & -Z_0 \sinh j\omega\frac{l}{c} \\ -\frac{1}{Z_0}\cosh j\omega\frac{l}{c} & \cosh j\omega\frac{l}{c} \end{bmatrix} \begin{bmatrix} \mathcal{E}_1 \\ I_1 \end{bmatrix} \tag{2-29}$$

where l and Z_0 are the length and the characteristic impedance of the transmission line. Defining $a \equiv l/c$ and $s \equiv j\omega$, the input impedance of an open-end uniform transmission line can be calculated by letting $\mathcal{E}_2/I_2 \rightarrow \infty$ or $I_2/\mathcal{E}_2 \rightarrow 0$. We thus have, according to equation 2-29, $\mathcal{E}_1/I_1 = Z_0 \coth sa$.

For the Blumlein diagram of figure 2-30, we obtain

$$Z_L = 2Z_0 + Z_0 \coth as \tag{2-30}$$

$$Z_i = \frac{\mathcal{E}_1}{I_1} = Z_0 \frac{Z_L \cosh as + Z_0 \sinh as}{Z_L \sinh as + Z_0 \cosh as} \tag{2-31}$$

$$\mathcal{E}_3 = 2I_2 Z_0 = 2\mathcal{E}_1 \frac{\sinh as}{(\cosh as + \sinh as)^2} \tag{2-32}$$

and

$$\mathcal{E}_0 = \mathcal{E}_1 + j\omega L \cdot I_1 = \mathcal{E}_1\left(1 + \frac{s \cdot L}{Z_i}\right) = \mathcal{E}_1\left(1 + bs\frac{Z_0}{Z_i}\right) \tag{2-33}$$

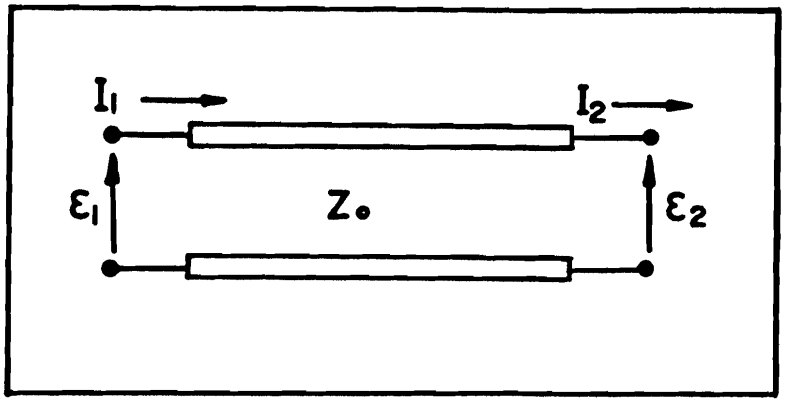

Figure 2-29: Transmission line

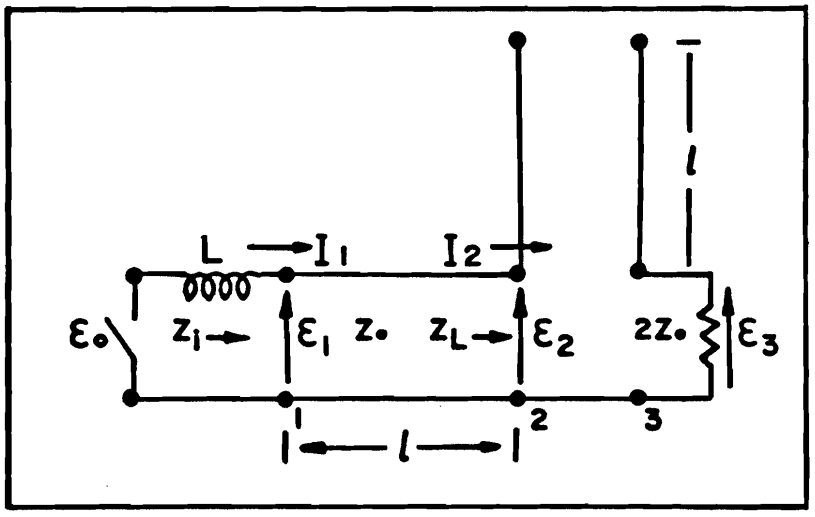

Figure 2-30: Blumlein-line system

(we use the convention $\frac{dI}{dt} = j\omega \cdot I$ here and define $b \equiv L/Z_0$)

After some simple algebra, equation 2-32 can be rewritten as

$$\mathcal{E}_3 = \mathcal{E}_0 \frac{e^{-as}}{bs + \frac{1}{2} + \frac{1}{2}\coth as} \tag{2-34}$$

The transient behavior of $\mathcal{E}_0$ can be expressed as $\mathcal{E}_0(t) = -V_0 \mathcal{U}(t)$, where $\mathcal{U}(t)$ is a step function. The Laplace transform of $\mathcal{E}_0(t)$ is

$$\mathcal{E}_0(s) = \mathcal{L}[\mathcal{E}_0(t)] = -\frac{V_0}{s}$$

and the Laplace transform of $\mathcal{E}_3(t)$ will be

$$\mathcal{E}_3(s) = -V_0 \frac{e^{-as}}{s(bs + \frac{1}{2} + \frac{1}{2}\coth as)} \equiv -V_0 \frac{e^{-sa}}{s\,B(s)} \tag{2-35}$$

where

$$B(s) = bs + \frac{1}{2} + \frac{1}{2}\coth as$$

$$= \frac{1 - e^{-2as}}{(1 + bs)\{1 - [bs/(1+bs)]e^{-2as}\}}$$

Therefore

$$\mathcal{E}_3(s) = -V_0 \frac{e^{-as}(1 - e^{-2as})}{s(1 + bs)\{1 - [bs/(1+bs)]e^{-2as}\}}$$

$$= -V_0 \frac{e^{-as} - e^{-3as}}{s(1 + bs)} \left\{1 + \left(\frac{bs}{1 + bs}\right) e^{-2as} + \left(\frac{bs}{1 + bs}\right)^2 e^{-4as} + \cdots\right\}$$

$$= -V_0 \left\{ \frac{e^{-as}}{s(1 + bs)} - \frac{e^{-3as}}{s(1 + bs)^2} - \frac{b\,e^{-5as}}{(1 + bs)^3} - \frac{b^2\,s\,e^{-7as}}{(1 + bs)^4} \cdots \right\}$$

$$= -V_0 \left\{ f_1(s)e^{-as} - f_3(s)e^{-3as} - f_5(s)e^{-5as} - f_7(s)e^{-7as} \cdots \right\} \tag{2-36}$$

Using the relationship

$$\mathcal{L}^{-1}[f(s)] = F(t) \Rightarrow \mathcal{L}^{-1}[f(s)e^{-As}] = \begin{cases} F(t-A) & \text{for } t \geq A \\ 0 & \text{for } A > t > 0 \end{cases} \tag{2-37}$$

we can immediately recognize that the first term in equation 2-36 represents the main

wave which takes time t=a to propagate from terminal 1 to terminal 3. The following terms in equation 2-36 represent the successive reflections in the switching lines. For example, $f_7(s)$ contributes only after $t \geq 7a$.

For the case of perfect switch (L=0), b=0. Therefore

$$\begin{aligned}\mathcal{E}_3(t) &= \mathcal{L}^{-1}[\mathcal{E}_3(s)] \\ &= -V_0\mathcal{L}^{-1}\left[\frac{e^{-as}-e^{-3as}}{s}\right] \\ &= -V_0\{\mathcal{U}(t-a) - \mathcal{U}(t-3a)\}\end{aligned}$$

where $\mathcal{U}(t)$ is, again, a step function. Hence $\mathcal{E}_3(t)$ is a rectangular pulse as shown in figure 2-14.

For the case of inductive switch, $b \neq 0$, we have

$$\begin{aligned}F_1(t) &= \mathcal{L}^{-1}[f_1(s)] = 1 - e^{-t/b} \\ F_3(t) &= \mathcal{L}^{-1}[f_3(s)] = 1 - (1 + \frac{t}{b})e^{-t/b} \\ F_5(t) &= \mathcal{L}^{-1}[f_5(s)] = \frac{1}{2}(\frac{t}{b})e^{-t/b} \\ F_7(t) &= \mathcal{L}^{-1}[f_7(s)] = [\frac{1}{2}(\frac{t}{b})^2 - \frac{1}{6}(\frac{t}{b})^3]e^{-t/b} \\ F_9(t) &= \mathcal{L}^{-1}[f_9(s)] = [\frac{1}{2}(\frac{t}{b})^2 - \frac{1}{3}(\frac{t}{b})^3 + \frac{1}{24}(\frac{t}{b})^4]e^{-t/b} \\ F_{11}(t) &= \mathcal{L}^{-1}[f_{11}(s)] = [\frac{1}{2}(\frac{t}{b})^2 - \frac{1}{2}(\frac{t}{b})^3 + \frac{1}{8}(\frac{t}{b})^4 - \frac{1}{120}(\frac{t}{b})^5]e^{-t/b} \\ &\vdots\end{aligned}$$

And

$$\mathcal{E}_3(t) = -V_0\,[\,F_1(t-a) - F_3(t-3a) - F_5(t-5a) - F_7(t-7a) - \cdots\,] \tag{2-38}$$

Figure 2-31 shows the plots of $\mathcal{E}_3(t)$ with time scale expressed in the unit of a ($a = l/c$). It is clear from these plots that the output pulse of the Blumlein system with inductive switch will behave like a *ideal Blumlein pulse* only when $b \leq a/4$ (or $L \leq Z_0 l/4c$).

The leading edge of the Blumlein pulse follows the current rise through the inductance L in series with a resistance equal to the impedance, Z_0, of the switching line.

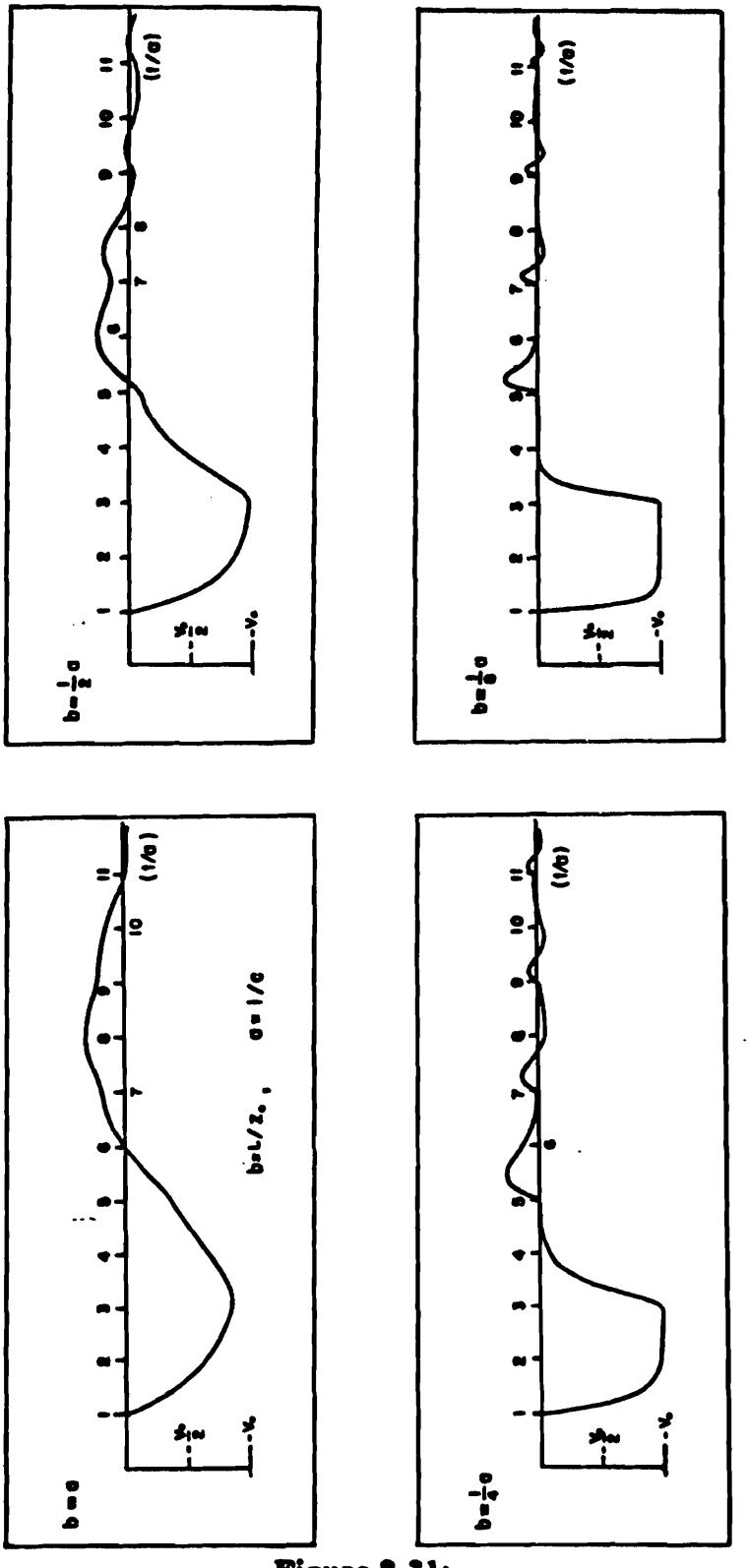

Figure 2-31:
Calculated output pulse shape from a Blumlein system with inductive switch
$a \equiv l/c$ and $b \equiv L/Z_0$

The formula for the leading edge can be expressed [100] as

$$\mathcal{E}_3^{L.E.}(t) = -V_0\left[\, 1-e^{-(Z_0/L)\cdot(t-l/c)} \,\right] \tag{2-39}$$

The risetime in equation 2-39 is equal to L/Z_0 (= b). In our case, the risetime of the Blumlein pulse (b) was about 700 ps (figure 2-25) and a = $l/c \sim 230$ ps. Therefore the pulse shape was worse than the first first drawing of figure 2-31 (where b equals a).

2.4 THE WIRE ELECTRODES AND THE TERMINATOR

The output pulses from the Blumlein system were carried to the wire electrodes of the streamer chamber through a parallel plate transmission line. This transmission line was essentially an extension of the top and bottom electrode plates of the Blumlein system (figure 2-15(b) and figure 2-32). The first section of this transmission line had polystyrene inside the line as dielectric material (60 cm long). The characteristic impedance of the transmission line was designed to be around 26 Ω (Sec.2.3). The actual measured value was about 24 Ω.

As discussed in Sec.2.3, the cut-off frequency for the non-TEM waves inside the transmission line can be calculated as

$$f_c = \frac{c}{\sqrt{\epsilon}} \frac{n}{2s} = 4.0 \times 10^9 \text{ Hz} \tag{2-40}$$

where s=2.5 cm (the spacing of the first section transmission line), $\sqrt{\epsilon}$=2.25 (polystyrene) and n=1. Hence

$$\gamma = \frac{2\pi\sqrt{\epsilon}}{c} \sqrt{(f_c/f)^2 - 1}$$

for f=3.5 x 10^9 Hz (c.f. $f_{max}=0.35/\tau$ and $\tau \sim 0.1$ ns), γ=0.608 cm^{-1}. The attenuation factor $e^{-\gamma z}$ is equal to 1.4 x 10^{-16} for z=60 cm.

Thus after this section, the non-TEM waves in the transmission are basically negligible.

The second section of the transmission line was a transition section to convert the dielectric material from polystyrene to gas. The key point in the design was to keep the line impedance constant. This was accomplished by gradually decreasing the spacing of the line and the effective thickness of the polystyrene. After this section, there was an another section of uniform line (line spacing is 1.6 cm) which extended for about 41 cm and then the spacing and width of the line were both decreased linearly, without changing the value of the line impedance, such that the transmission line joined the chamber smoothly.

The body of the chamber was a pair of transparent electrodes which were two

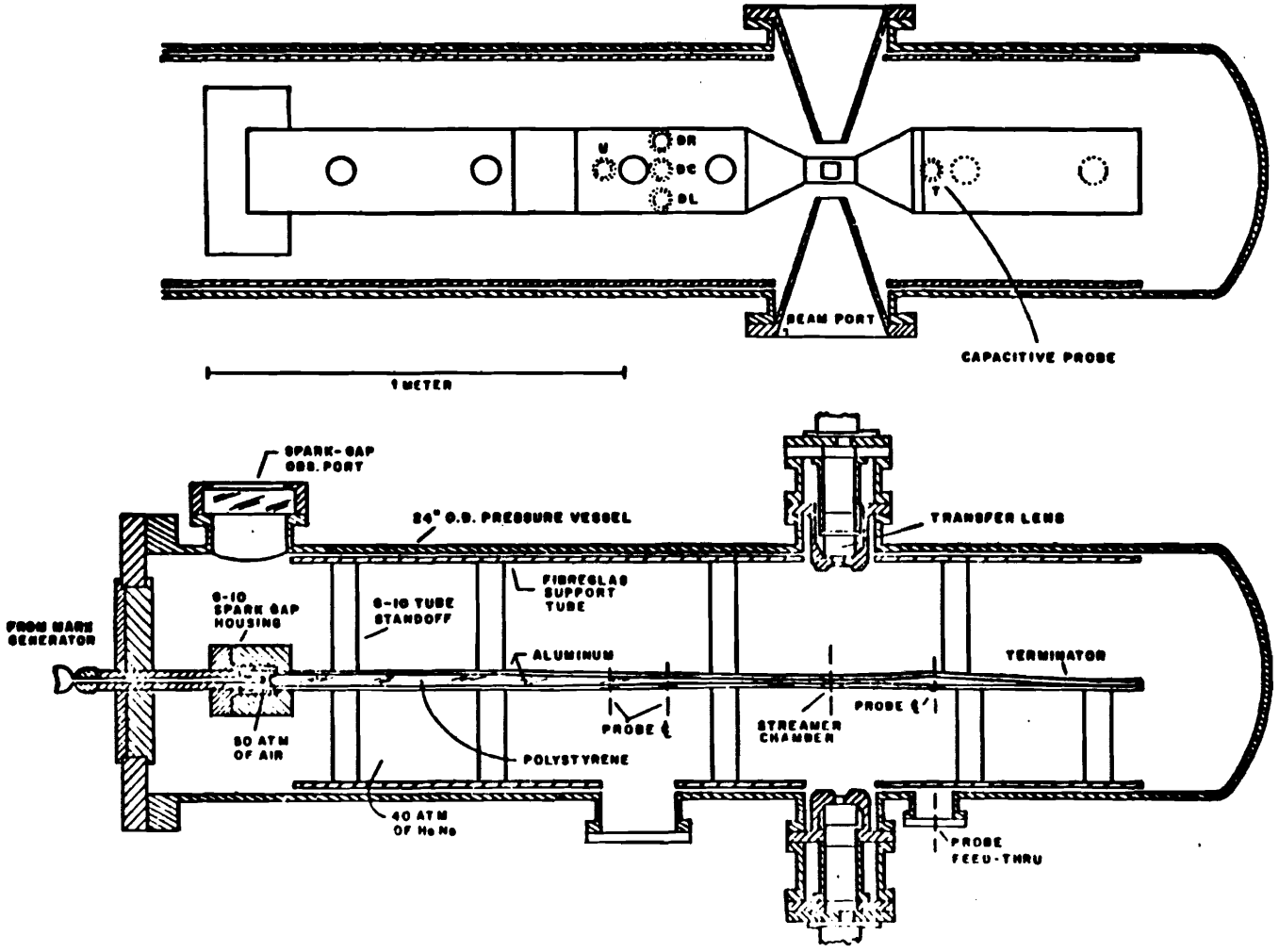

Figure 2-32: The Yale High Resolution Streamer Chamber

identical wire planes. Each wire plane was made of 50 micron diameter stainless steel wire wound on a stainless steel frame with 150 micron wire spacing. The wire direction was parallel to the direction of current flow on the transmission line. (In E-490, the wire diameter was 25 microns with 100 micron wire spacing.) Figure 2-33 shows schematically the structure of the wire plane.

In order to keep the electric field uniform over the whole fiducial volume of the chamber, the two electrodes must be kept parallel. This was achieved by using a set of Lucite clamps which surround the transmission line and were attached to the stainless steel frame. The distance between the two wire planes was fixed to 4.5 mm giving an effective depth of the uniform field of about 4 mm. The fiducial area of the transparent region was 4 cm along the beam direction by 3 cm along the direction of the current flow on the transmission line. Therefore the effective fiducial volume was 4 x 3 x 0.4 cm^3.

Because of the high surge current on the transparent electrodes (about 6000 amperes), the question of how to make a good electrical and mechanical contact between the stainless steel wires and the chamber frame is not trivial. Various methods of soldering and several conducting epoxies were tried yet none of these conventional methods succeeded. In the final solution, indium wires were placed inside triangular grooves at the edges (the junction between the wire chamber and the transmission line) of the stainless steel frames. The stainless steel wires were wound over the indium and glued onto the chamber frame, the indium wires were then pressed flat to let the indium flow around the stainless steel wires (figure 2-33). With this method, we have not observed any trouble at the junction between the wires and the chamber frames.

In the early stage of developing this streamer chamber, at the upstream and downstream (current flow) sides of the transparent region, the edges of the metal frames were shaped with a small radius of curvature to avoid sparking due to field concentration on sharp edges. However discharges at these rounded edges of the frames, especially at the side close to the terminator were observed. We believe that these discharges were initiated by the small voltage difference between the wires and the metal frame. This

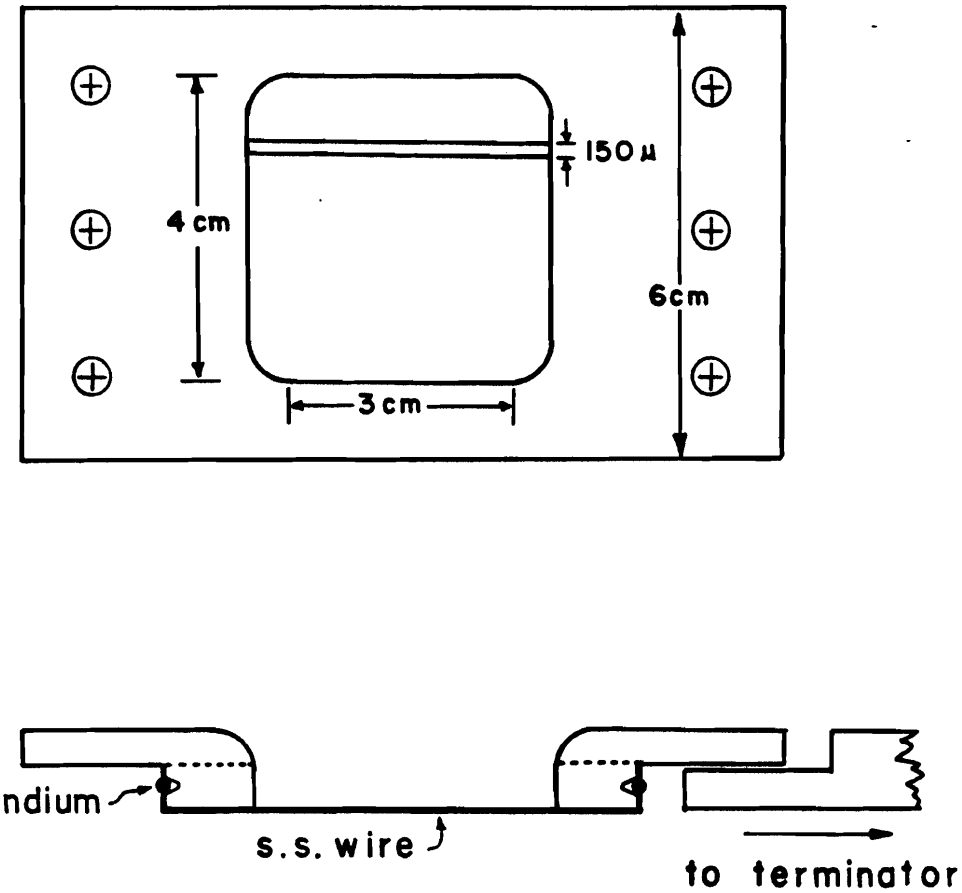

Figure 2-33: The wire electrode section of the Streamer Chamber

problem was finally corrected by making the wire-frame junctions as 90 degree edges. No indication of spurious discharge at these sharp edges has been observed.

After the chamber section, the spacing and the width of the transmission line were both increased linearly again. In this way the highest electric field appeared only in the vicinity of the wire electrodes. This configuration minimized the possibility of spurious breakdown outside the chamber region.

The last section of the transmission line was a wedge-shaped matched terminator (see figure 2-34). The key point in the design was to have the tapered plate carry uniform surface resistance which compensates the decrease in the line impedance due to the decrease of the line spacing. It can be shown (see reference [101]; the discussion on

wedge-shaped load of reference [101] is also included in appendix II.) that this type of wedge-shaped load is reflectionless for an incident TEM wave if

$$Z_0 = R_s \frac{L}{W} \tag{2-41}$$

where Z_0 is the characteristic impedance of the transmission line, R_s, L and W are the surface resistance, length and width respectively of the tapered plate (figure 2-34). In our case W = 20 cm and L = 40 cm. The thickness of the surface resistor must be small enough compared to the skin depth of this material at any frequency under consideration. In this way the surface resistance, R_s , is independent of the wave frequency.

Our first attempt at manufacturing the uniform surface resistance plate was to deposit a thin layer (about 2000 Å) of nichrome on a dielectric surface. This method failed due either to mechanical or electrical damage during repeated pulsing.

A more satisfactory method of making the terminator uses the ***thick film resistor*** (Cermet on Al_2O_3 substrate) which is commonly used in integrated circuit manufacture. The thick film resistors were commercially manufactured (about 25 μm thick and about 12 ohm/square)[10]. Because of the limitation on the maximum size available for such resistors, our terminator consisted of eight rectangular pieces of the thick film resistors (figure 2-35). This kind of terminator has been used for about 5 years. However it is still not perfect. After a considerable amount of pulsing, we did observe damage, especially at the corner and edges of the rectangular resistors. The problem is probably due to the difficulties in making a smooth-surface connection between the resistors.

Figure 2-36 shows the picture of the pulses on the transmission line monitor when the terminator functioned normally (the capacitive monitor will be discussed below). Figure 2-37 was taken when the terminator was damaged seriously. Both pictures were taken from the same monitor (the ***U-pickoff***; U means upstream, close to the Blumlein box. See figure 2-32). The pulse amplitude was about 170 KV for both cases. It is obvious

---

[10] $\sigma = 1/(R_s \cdot t)$, and skin depth $\delta = 1/[\pi f \mu \sigma]^{1/2}$. Therefore $\delta \sim 138$ μm at $f = 4 \times 10^9$ Hz. This is larger than the thichness ($t = 25$ μm) of the resistor.

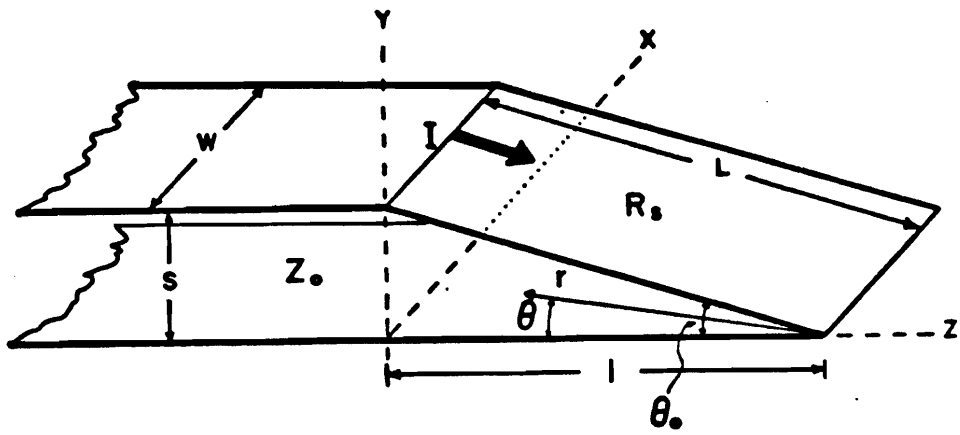

Figure 2-34: The wedge-shaped terminator

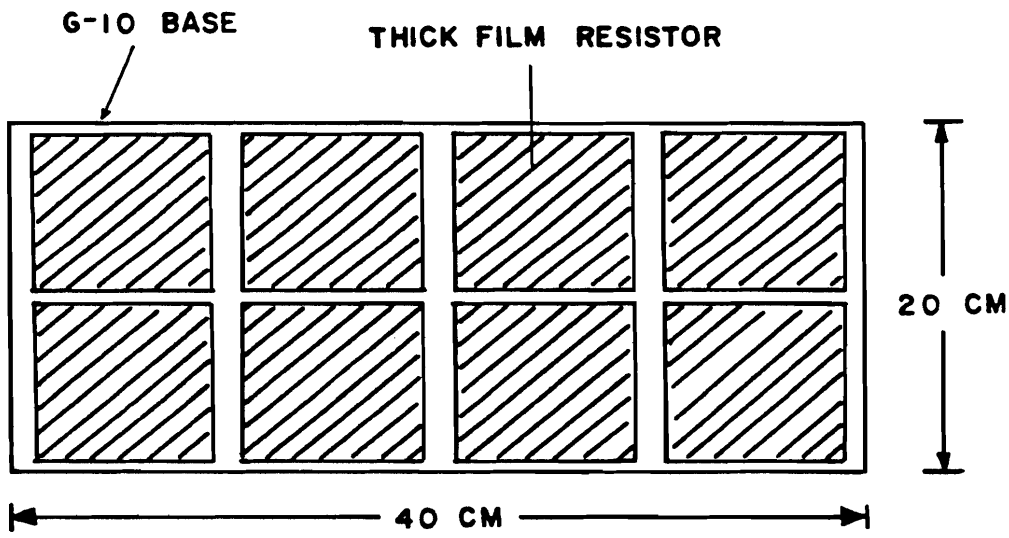

Figure 2-35: 8 thick film resistors are used to make up the terminator

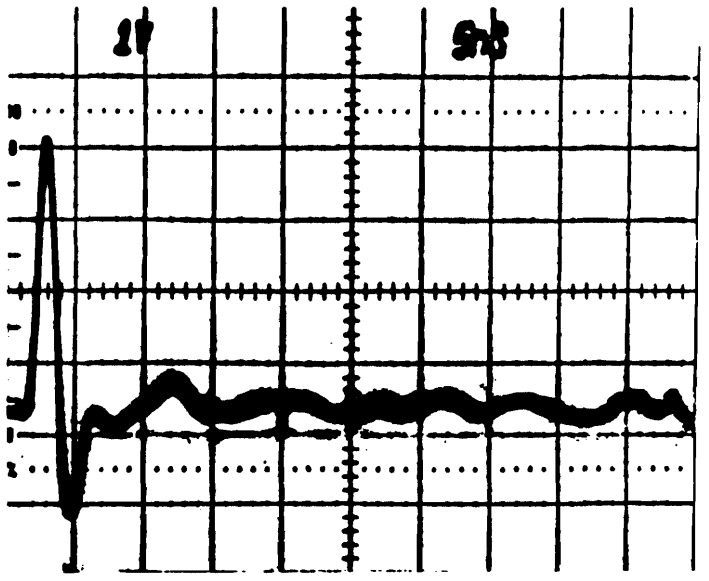

Figure 2-36: Blumlein output pulse; terminator functions normally.
amplitude ~ 170 KV, 5 ns/Div

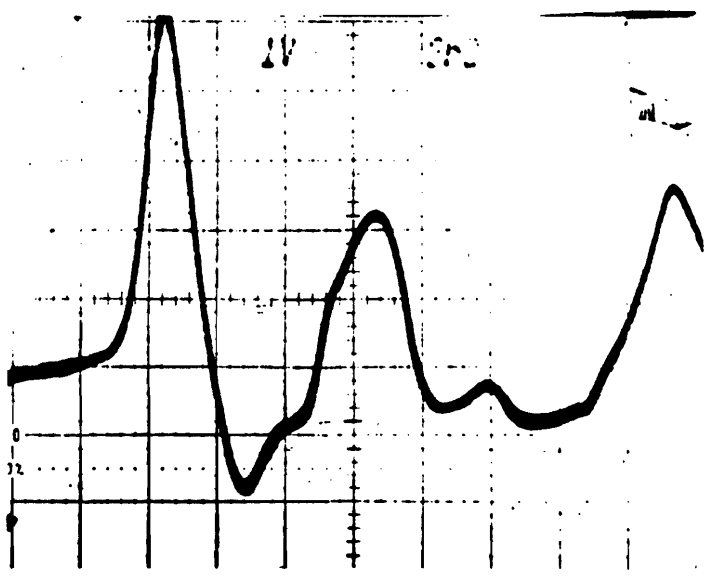

Figure 2-37: Blumlein output pulse; terminator damaged.
amplitude ~ 170 KV, 2 ns/Div

that an enhanced reflection from the damaged terminator appears in figure 2-37 .

Now let us describe the Blumlein/transmission-line pulse monitors (Ref. [109]). Before and after the chamber section, there were several capacitive pickoffs (figure 2-32) which were built into the grounded plate of the transmission line for monitoring the high voltage pulses on the transmission line. These capacitive pickoffs were made of a 700 Å gold layer evaporated on a 25 micron mylar spacer 25 mm in diameter. This mylar piece was glued on a coaxial fixture and a central pin was inserted through the mylar. This pin was therefore connected to the gold layer after the gold was deposited on to the mylar. This coaxial fixture was then threaded into the ground plate of the transmission line and the capacitively coupled signal was transmitted through a 50 Ω cable with a pressure sealed feed-through to the outside of the streamer chamber vessel.

Since the thickness of the gold layer was small compared to the skin depth[11] of the waves with frequency in the range of interest ($f_{max} \sim 3.5 \times 10^9$ Hz). The pickoff capacitive division factor can be estimated by the ratio of the thickness of the mylar spacer to the spacing of the transmission line multipled by the dielectric constant of the mylar($\sim$ 2.8 at 1 GHz frequency). The measured values ranged from 1:1000 to 1:1600 for different pickoffs.

The calibration of the division factor was done together with the measurement of the transmission line impedance. The central conductor of a 50 Ω BNC cable was connected, through a resistor, to one electrode plate of the transmission line and the ground shield of the cable was connected to the other plate. Square pulses from a mercury relay pulser were fed into the BNC cable. By varying the value of the resistor until no reflection was observed, the impedance of the transmission line was thus determined. The best match was obtained by using two 51 Ω resistors connected in parallel, this gave the estimated value of the transmission line impedance to be 24.5 Ω. The division factor of the pickoff was also measured in the same time. Figure 2-38 shows the picture of the ***U-pickoff***

---

[11]For gold, $\sigma = 4.1 \times 10^7$ mhos/m, the skin depth $\delta = 1/[\pi f \mu \sigma]^{1/2} = 0.0786/[f]^{1/2} = 1.33 \times 10^4$ Å for $f = 3.5 \times 10^9$ Hz.

response to a 500 V square pulse from the mercury pulser.

Figure 2-39 shows a scope picture of the Blumlein pulse taken from the ***T-pickoff***. (T means close to the terminator. See figure 2-32). Comparing figure 2-36 and figure 2-39, we see no major difference in the pulse shape between the ***U-pickoff*** and the ***T-pickoff*** when the terminator works normally. However, figure 2-40 and figure 2-41 were taken when the terminator was damaged and the reflection wave was observable. Figure 2-40 is the ***DC-pickoff*** picture (***DC*** means downstream and central with respect to the ***U-pickoff***) and figure 2-41 is the T-pickoff picture. Comparing with figure 2-37 we see that the reflection wave contributed differently to these pictures due to the different locations of the pickoffs.

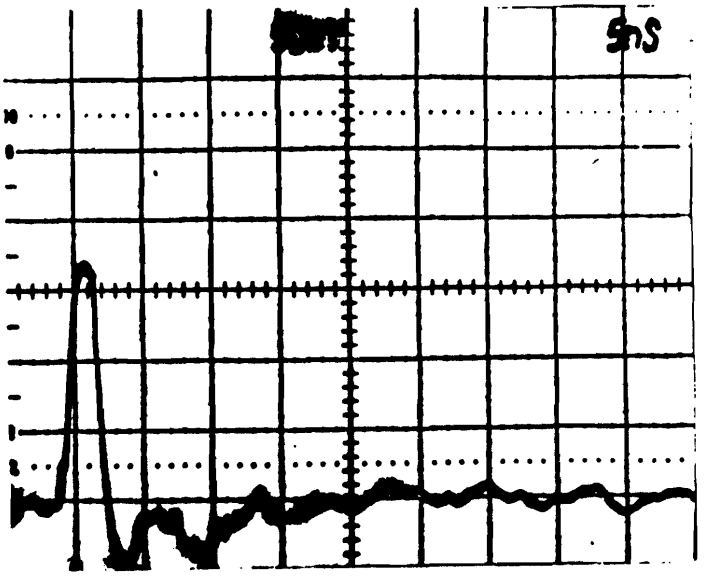

Figure 2-38: U-pickoff response to a square pulse from mercury pulser
The measured division factor $\approx$ 1000

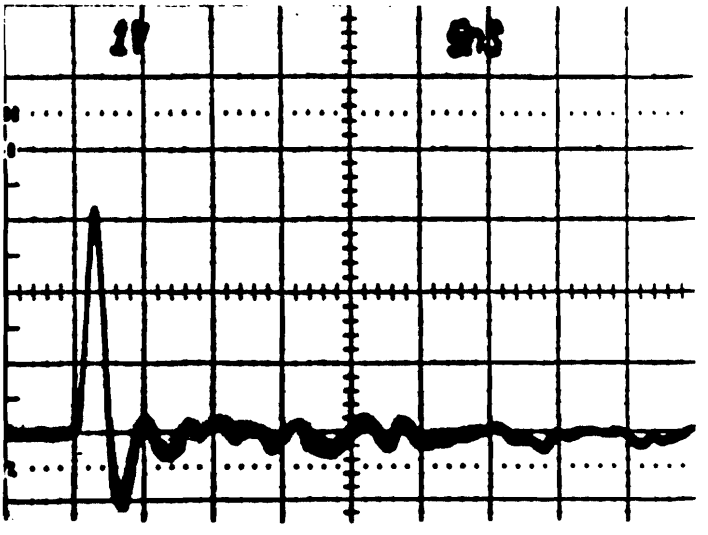

Figure 2-39: Pulse shape at T-pickoff monitor
(Real Blumlein output pulse)

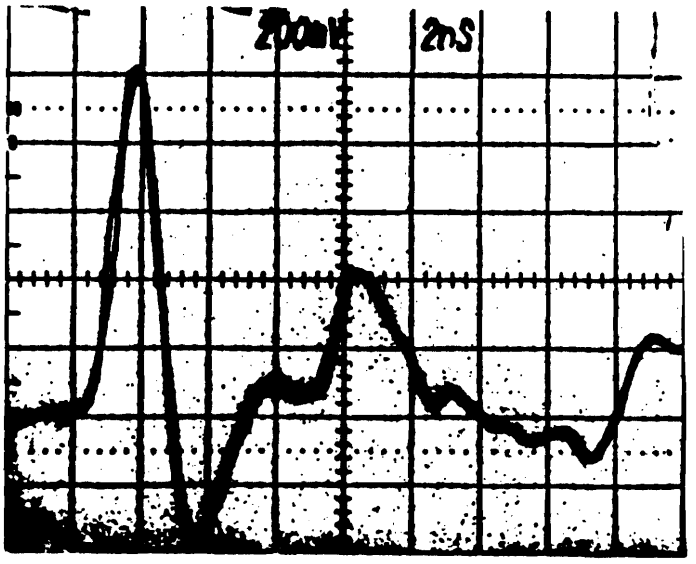

Figure 2-40: Pulse shape at DC-pickoff when the terminator was damaged

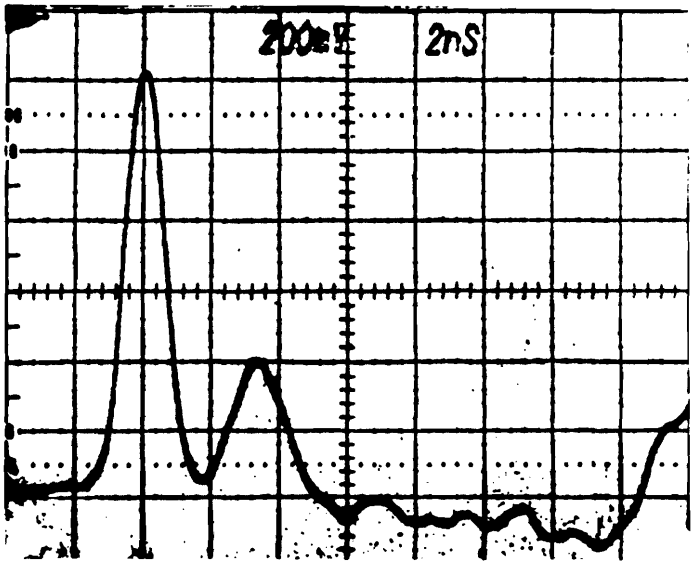

Figure 2-41: Pulse shape at T-pickoff when the terminator was damaged

2.5 THE PERFORMANCE OF THE YALE HIGH PRESSURE STREAMER CHAMBER

The performance of the Yale streamer chamber in the early stage of development has been reported elsewhere (Ref. [108] and Ref. [109]). I will only summarize briefly the results here.

Many of the tests for the Yale streamer chamber were done with a Ru^{106} β source (especially in the early stage of development of this chamber). Figure 2-42 shows a picture taken at the initial testing period. The chamber was filled with 150 psia of conventional spark chamber gas (90%Ne+10%He) and the picture was taken without an image intensifier. The HV pulse on the chamber was about 140 KV with about 0.5 ns width (FWHM). The effective electric field across the chamber was about 300 KV/cm. We see many small bright streamers accompanied by many large bright spots which are essentially over-grown streamers originating from several seed electrons within one single avalanche (due to the Landau fluctuation in the ionization loss).

To solve this problem, the chamber was operated at a slower avalanche and streamer growth rate by increasing the chamber pressure (i.e. decrease the E/P value). Higher chamber pressure also suppressed the diffusion of the seed electrons but the streamer brightness was sacrificed. Image intensifiers were therefore required. Figure 2-43 shows a picture of a 200 Gev/c π^- interaction in the chamber. The picture was taken with a proximity-focused diode image intensifier which has an optical gain of about 80 and resolution of about 50 lines per mm. This image tube (type F4109) was produced by the Electro-Optical Product Division of ITT. The test was set up in the M1 beam line of the Fermilab Meson Laboratory (Feb. 1978). The chamber pressure was 250 psia and the pulse was about 150 KV with 0.5 ns width (field intensity ~330 KV/cm). It can be seen from this picture the big bright streamers along the tracks are much suppressed. However, in the interaction region, there is still a large flare. Also we see a brush-like strip originating from the flare area and extending out along the beam direction. This *mustache*, we believe, is due to the light scattered from the wire electrode into the camera.

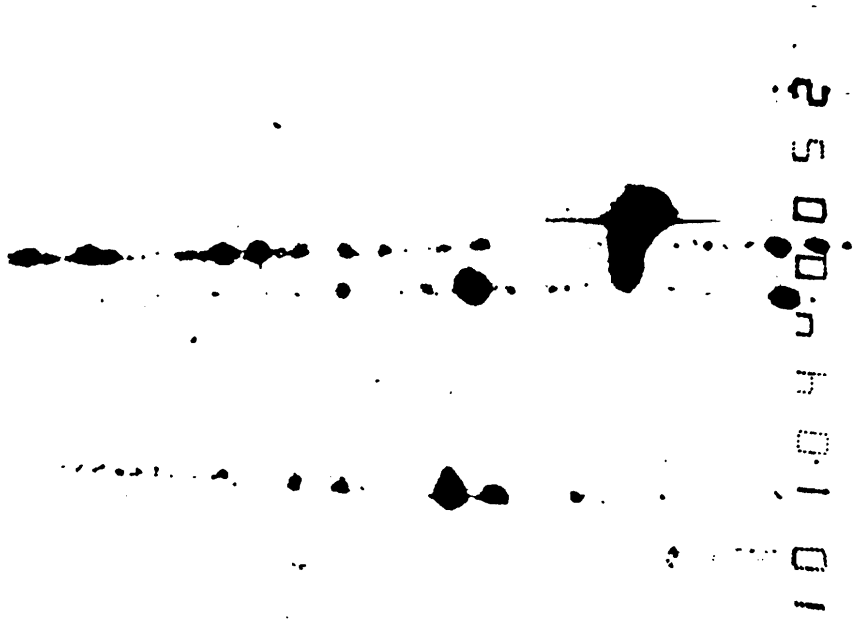

Figure 2-42: 150 psia 90%Ne+10%He; Pulse ~ 140 KV and 0.5 ns
picture was taken without image intensifiers

Figure 2-43: 200 Gev/c π^- interaction
250 psia 90%Ne+10%He; Pulse ~ 150 KV and 0.5 ns
image intensifiers gain ~ 80

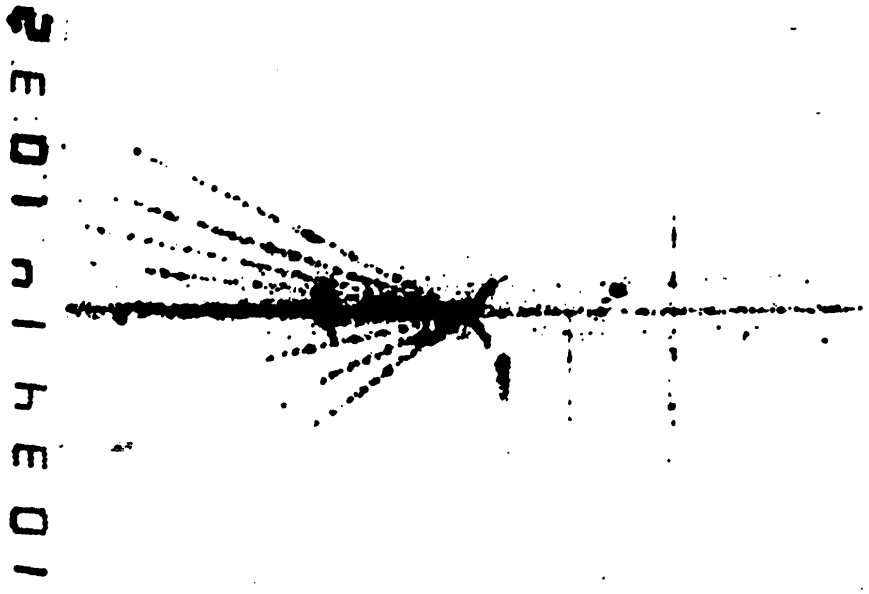

Figure 2-44: 350 Gev/c P^+ interaction
370 psia 90%Ne+10%He; Pulse ~ 150 KV and 0.5 ns
image intensifiers gain ~ 2500

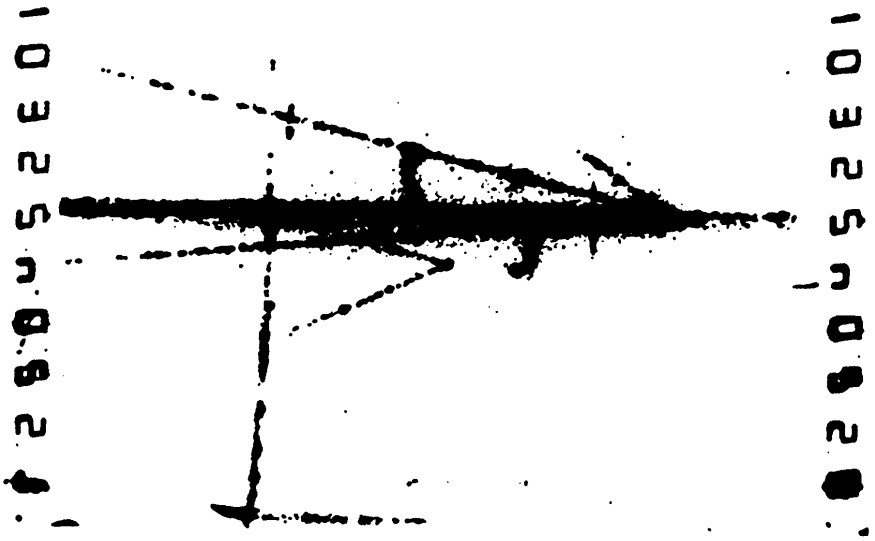

Figure 2-45: 350 Gev/c P^+ interaction
370 psia 90%Ne+10%He; Pulse ~ 150 KV and 0.5 ns
image intensifiers gain ~ 2500

In order to solve the flare problem, we obtained a set of *subspecification* 25 mm micro-channel plate image intensifiers (ITT, type F4112). This type of tube has a full optical gain of about 10,000 and a resolution of about 26 line per mm. Because these tubes were subspecification they were operated at optical gain of about 2500. Figure 2-44 and figure 2-45 are the pictures taken with this kind of image tubes. The chamber was operated at 370 psia Ne-He and with a 150 KV pulse. The incident particles were 350 Gev/c protons from the same M1 beam line. These are basically the running conditions of the streamer chamber for the Fermilab EXP-490 experiment [108, 109, 110]. The track width (full width) of figure 2-44 and figure 2-45 is about 150 μm on the film. (About 225 μm in space.) The individual streamer diameter is about 50 μm which is just about the limit of the resolution of the optical system. The track width is largely due to the diffusion of the seed electrons. This phenomenon can be best illustrated by the picture in figure 2-46. In this picture, the track on the top is from the beam particle which triggered the chamber and the track on the bottom is from an accidental beam track which passed through the chamber after the triggering but before the high voltage pulse. (The time delay between the passage of triggering particle and the arrival of high voltage pulse was about 500 ns for the E-490 setup.) At this stage, the problem of the vertex flare was only relatively improved. A substantial number of E-490 pictures were obscured in the vertex region due to the existence of *flares*.

As is mentioned in section 2.3, there were four spark gaps in the Blumlein system then. Because of the synchronism problem among the four gaps, the output pulses were very unstable. Also, we wanted to increase the chamber pressure in order to further suppress the diffusion of the primary electrons. Consequently, we wanted to raise the Marx voltage. However, the orignal Marx generators[12] used in the E-490 experiment had a lifetime of only about 6 hours under continuous pulsing condition at charging voltage of about 30 KV. Any attempt to increase the Marx charging voltage would end up with breakdowns inside the capacitors or a free-running behavior of the Marx generator. Thus

[12]These were not the one described in section 2.2.

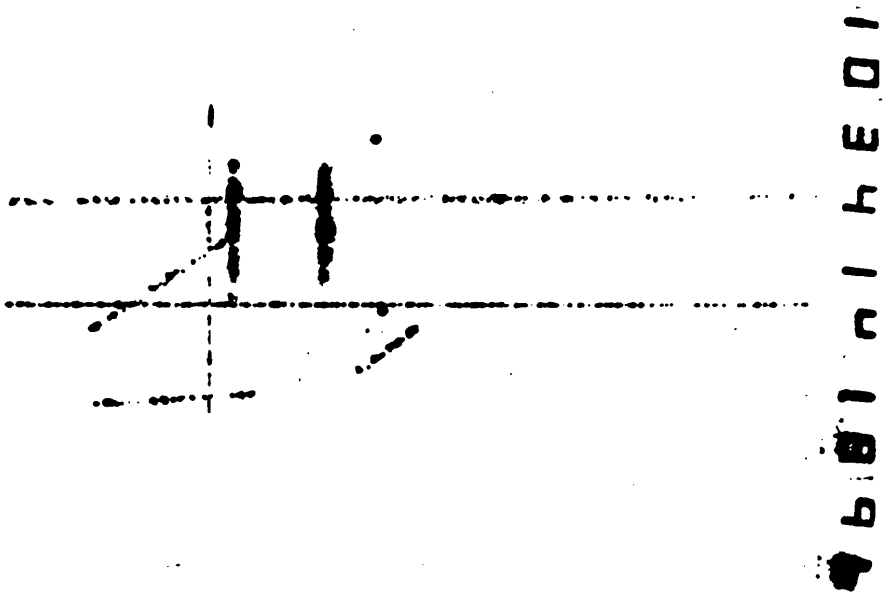

Figure 2-46: 350 Gev/c P^+ beam tracks
The *thinner* track on the bottom is a *younger* track.

to improve the track resolution, we had to have a better Marx generator and a more stable pulsing system.

Following the E-490 experiment, we made many modifications. The new Marx generator, the Marx pulse monitor, the modification of the Blumlein system, the new *full-specification* image intensifiers, a higher bandwidth scope (TEKTRONIC 7104; ~ 1GHz and risetime ~ 0.38 ns) for monitoring the high voltage high frequency pulse and the laser triggered Blumlein system (as mentioned in section 2.3) ··· etc. were all results of this painstaking *learning* period.

The chamber pressure was finally set at 600 psia, which is the maximum allowed by the vessel pressure, and different gas mixtures for the chamber were tried to suppress the thermal diffusion of the seed electrons. The primary electrons created by the ionization of the gas atoms by charged particles will, before the arrival of high voltage pulse, drift away from their original location and collide with gas atoms. As it was mentioned in section 2.1, the fractional energy loss of these electrons can be estimated by the formula

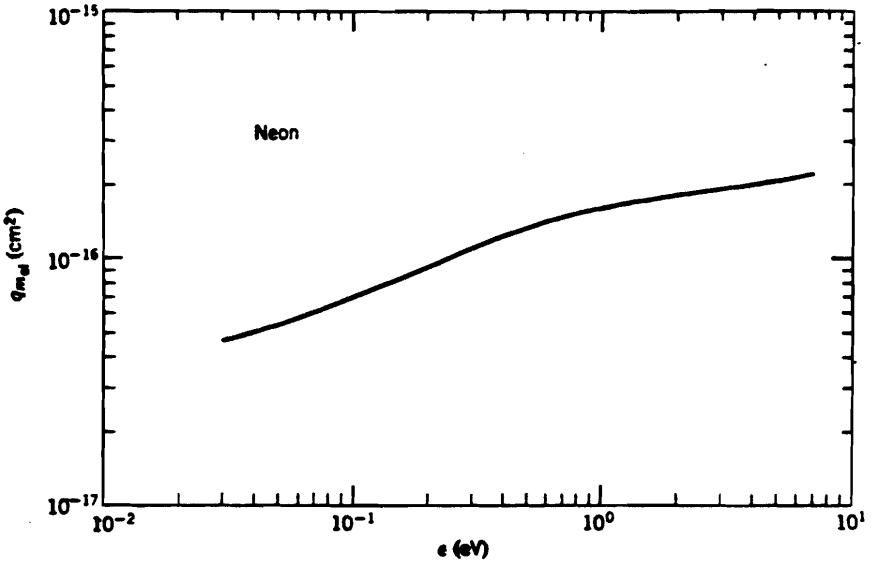

Figure 2-47: The elastic scattering cross section for electron in Ne

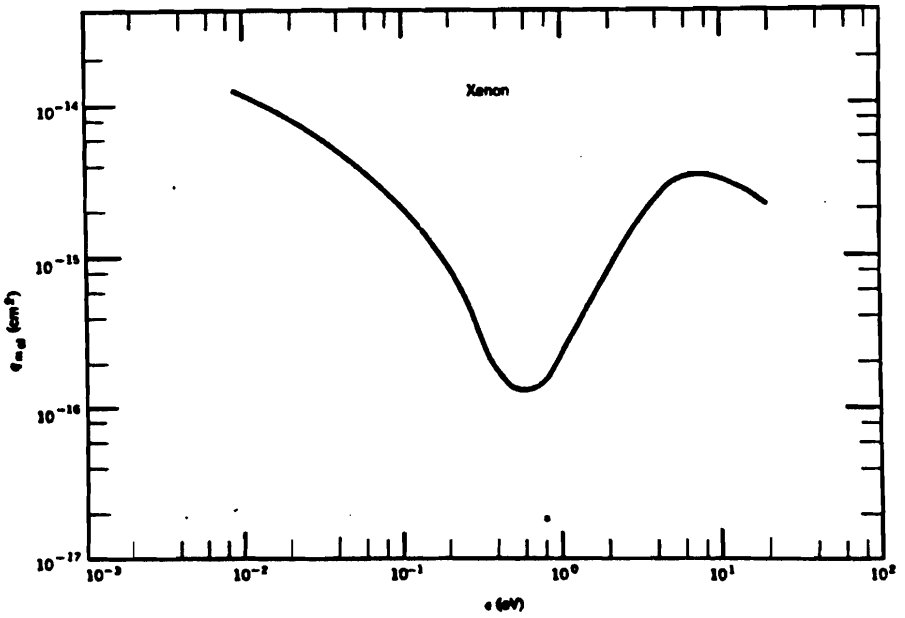

Figure 2-48: The elastic scattering cross section for electron in Xe

$\Delta = 2m_e/M$ (Eq. 2-1) where m_e is the electron mass and M is the mass of the gas atom. In the case of Ne, $2m_e/M_{Ne} = 5.44 \times 10^{-5}$. Let us take a 5ev electron as an example (see Ref. [110]). The electron-atom elastic scattering cross section in Ne is about 10^{-16} cm^2 (figure 2-47; [103]). At 40 atm, this cross section corresponds to a collision mean free path of about 9.3×10^{-6} cm or a collision frequency of about 1.4×10^{13} Hz. This implies that it only takes about 18 ns for the electron energy to drop to 1/e of its initial value. For an electron with higher initial energy, the cross section is larger, therefore the electron looses energy at a higher rate.

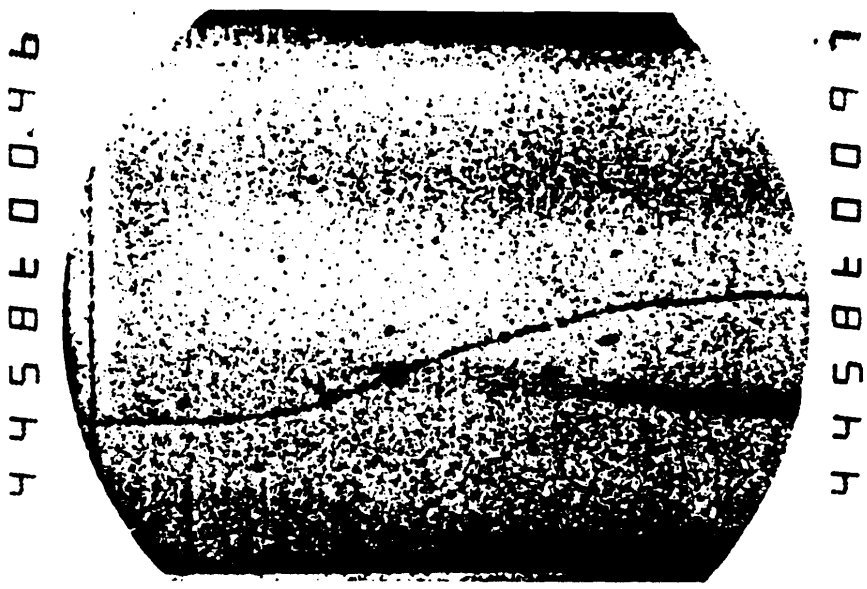

Figure 2-49: Ru^{106} β source track
600 psia 99%(Ne−He)+1%Xe; pulse ~ 110 KV

From this example, we can easily perceive that the primary electrons thermalized in a short time, compared with the time delay of the high voltage pulse (about 500 ns in E-490 and 700 ns in E-630). In order to suppress the thermal diffusion of these primary electrons, we need a gas (or mixture of gases) which has a large electron elastic scattering cross section in the low electron energy range.

We first tried Xe (figure 2-48; [103]) and surprisingly found frequent spurious sparking inside the chamber. The streamers looked over-grown and a lot of individual streamers were found even at few mm from the track center (figure 2-49). To explain this

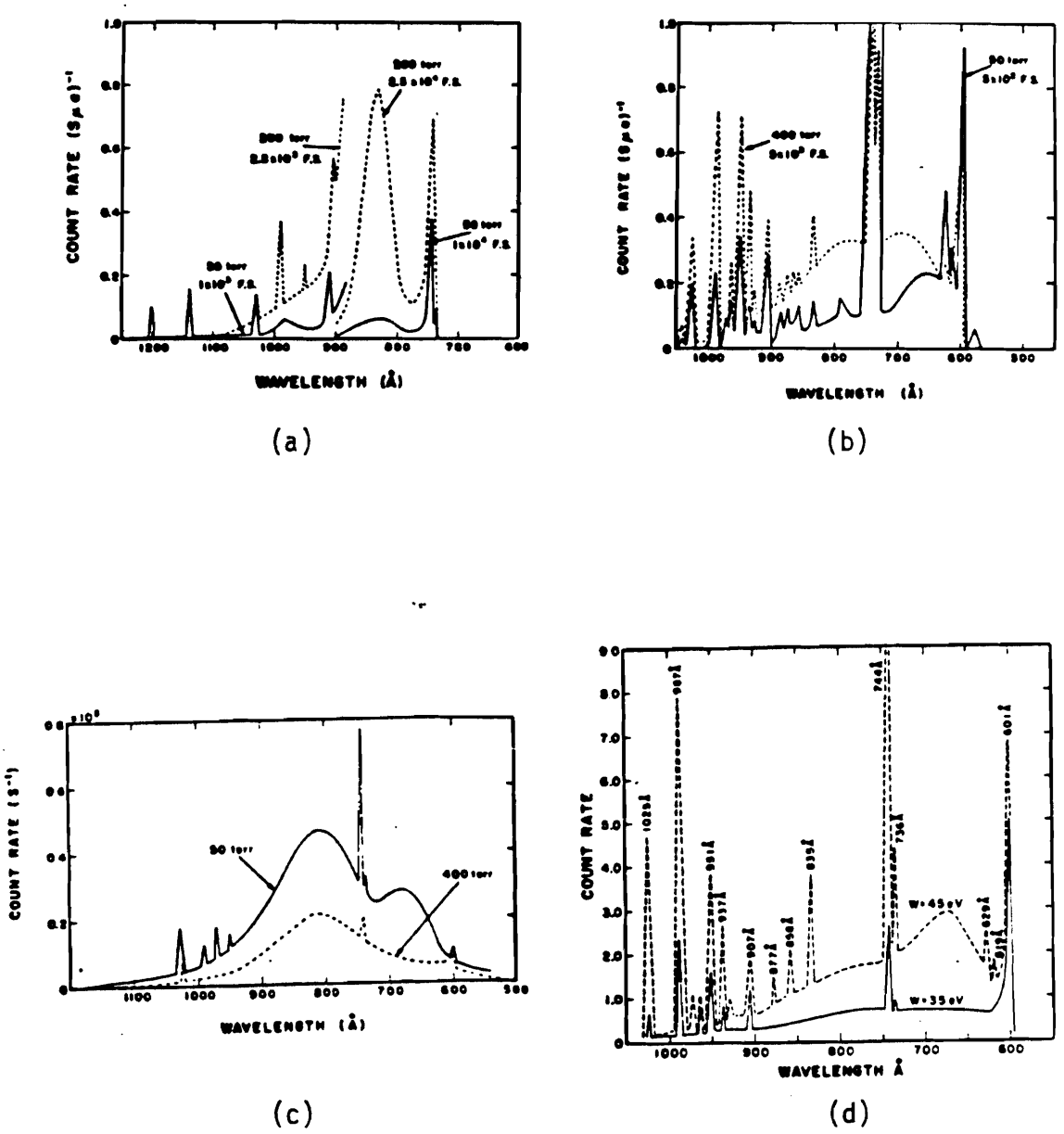

Figure 2-50: Emission spectra for helium and neon

(a) Emission spectra for neon excited by protons. (b) Emission spectra for helium excited by protons. (c) Emission spectra for helium excited by gas discharge. (d) Photon emission spectra of pure helium excited by gas discharge.

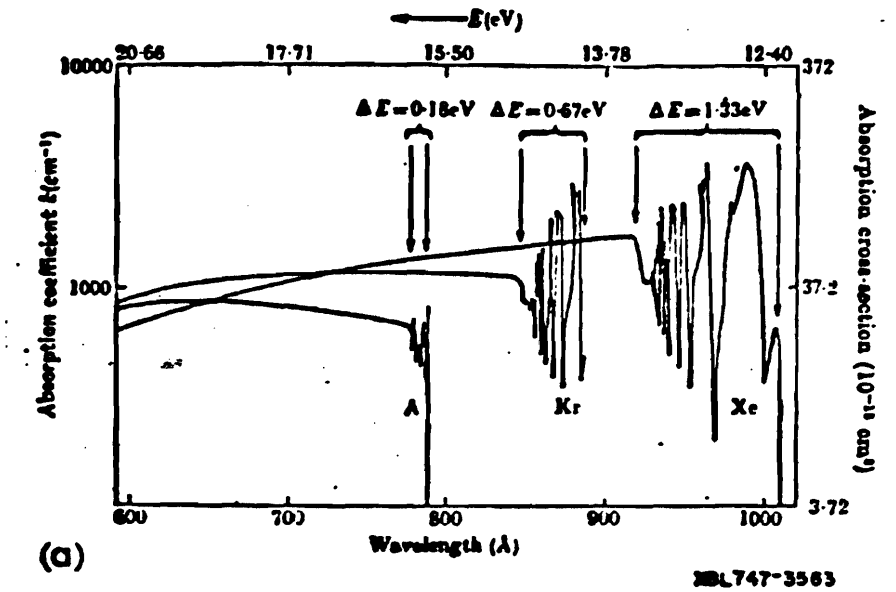

Figure 2-51: Absorption coefficients of UV light in the heavy noble gases

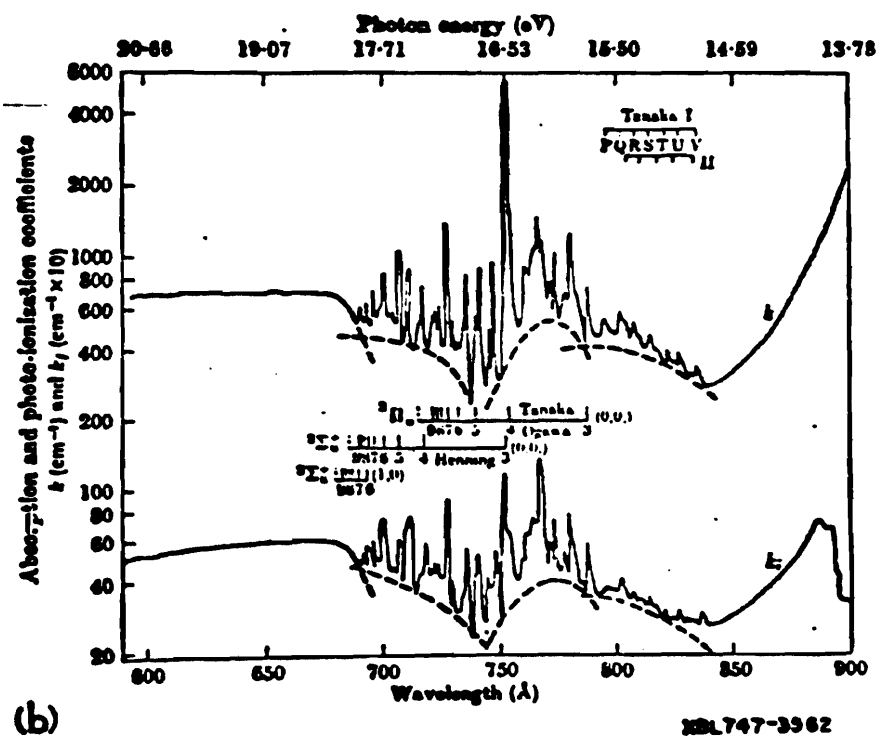

Figure 2-52: Absorption coefficients k and photo ionization coefficient k_i of UV light in CO_2

phenomenon, the following ***hypothesis*** is proposed:

Referring to figure 2-50 [105], the UV emission spectra from excited Ne and He have a peak in the region 700 nm to 1000 nm. On the other hand, Xe has a large photo-absorption cross section (figure 2-51; [104]) in this wavelength range. Since Xe is a monoatomic element, the energy absorbed contributes essentially to the ionization of the Xe atom (photo-ionization).

Based on this argument, we next tried CO_2. Again let us look at figure 2-52 [104]. The photo-absorption cross section of CO_2 in the wavelength range between 700 nm and 1000 nm is only slightly smaller than that of Xe. However for the CO_2 molecule, there are many vibrational, rotational etc. excitation levels available. The photo-absorption cross section is no longer dominated by the photo-ionization process. Moreover, CO_2 also has a large electron elastic scattering cross section (figure 2-53; [103]).

At the level of 2.5% CO_2 concentration, if we keep the pulse duration at the range of 0.5 ns, in order to obtain satisfactory picture quality, we have to substantially increase the pulse voltage. This leads to the risk of breaking the wires on the chamber electrodes. Therefore instead of raising the high voltage, the Blumlein pulse width (FWHM) was increased to about 1.4 ns. With the full gain (10,000 X) of image intensifiers, we were able to operate the chamber with about 110 KV pulse for 600 psia 90%Ne-10%He gas. As one may already see, the required electric field is effectively lower than the previous 370 psia case (where the pulse width was about 0.5 ns and optical gain was about 2500). With optical gain of 10000, the chamber was essentially operated as an ***avalanche*** chamber rather than a ***streamer*** chamber. Figure 2-54 is a picture of a β source track in the standard Ne-He mixture plus 2.5% of CO_2. The chamber pressure was 600 psia and pulse amplitude was about 160 KV with 1.4 ns width. The overall track width was about 80 μm on the film (120 μm in space).

The final gas mixture used during the data taking period of E-630 was CO_2(2.5%)+H_2(200ppm)+Ne-He(9/1;balance). The reason for adding a small amount of hydrogen is discussed below.

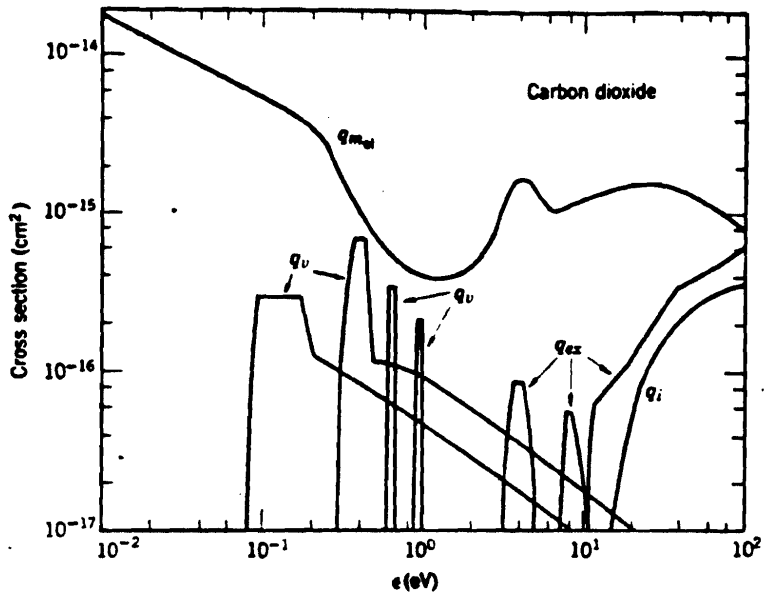

Figure 2-53: Electron elastic and inelastic scattering cross section in CO_2

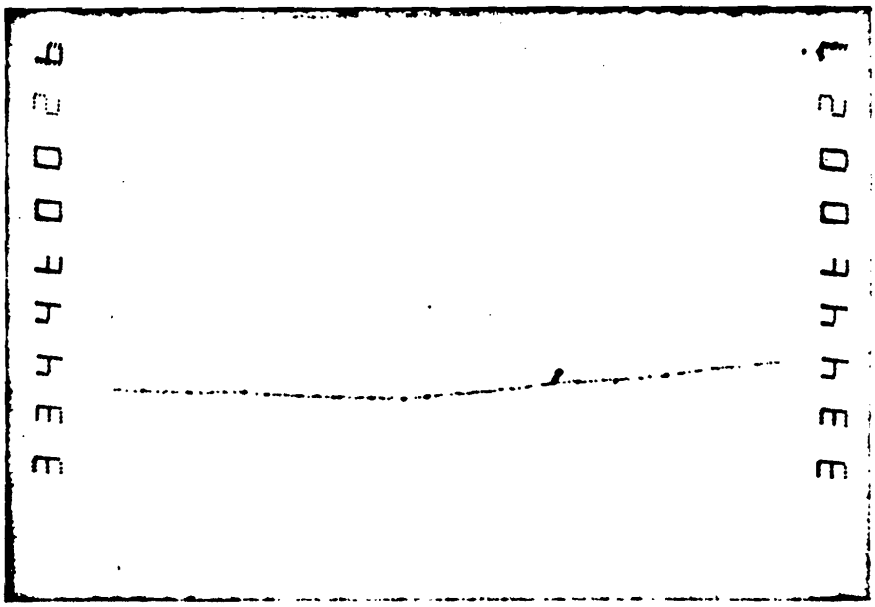

Figure 2-54: Ru^{106} β source track
600 psia 97.5%(Ne–He)+2.5%CO_2; pulse ~ 160 KV

The process

$$e^- + CO_2 \rightarrow e^- + (CO\text{-}O) \rightarrow CO + O^-$$

has a resonance like cross section (figure 2-55; [106]) of about 5×10^{-19} cm^2 at an electron energy of about 7.8 ev (Ref. [79]; p.39). For a primary seed electron with this energy, the average time for the electron to be captured by the CO_2 is only about 0.5 ns at 40 atm with 2.5% of CO_2. Hence some of the primary electrons, in the process of thermalization, passing through this energy might possibly be captured by the CO_2 molecules. However, according to Ref. [107], the negative ion O^- is known to react readily with hydrogen in an associative detachment reaction :

$$O^- + H_2 \rightarrow H_2O + e^-$$

and liberate the electron. This consideration lead us to add 200 ppm of H_2 to the chamber gas. Actually, we did not observe any significant difference in the track streamer density with or without the hydrogen even up to 0.2% level of hydrogen concentration.

At this point we did some studies on the chamber memory time and the thermal diffusion effect by varying the delay time of the high voltage pulse. The test was done with a Ru^{106} β source again. The pictures of the β source tracks were projected on a scanning table and the individual streamers were traced on a piece of paper. Taking into account of the magnification factor of the scanning table, the *full* width of the track can be determined. In order to clearly see tracks at long delay time, the chamber high voltage was slightly higher than normal. Also, the definition of *full width* here means, conservatively, the *extreme edges* of the track. Due to the multiple scattering of β source electrons inside the chamber, it is very difficult to determine unambiguously the *full width* of the tracks. The data presented here are only a crude estimation of the relationship between the track width (on the film, the demagnification factor is about 2/3) and the square root of the overall delay time (c.f. equation 2-6)

Figure 2-56(a) shows the result with [Ne-He(9/1)] + CO_2(2.5%) + H_2(0.2%). The high voltage pulses were about 170 KV. Figure 2-56(b) is the result with [Ne-He(9/1)] + CO_2(3.7%) + H_2(0.2%). The high voltage pulses were about 185 KV. For both cases,

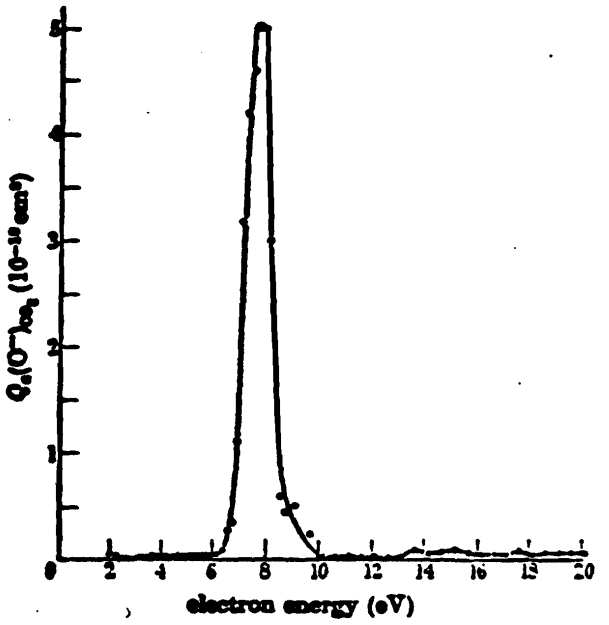

Figure 2-55: Electron attachment cross section in CO_2

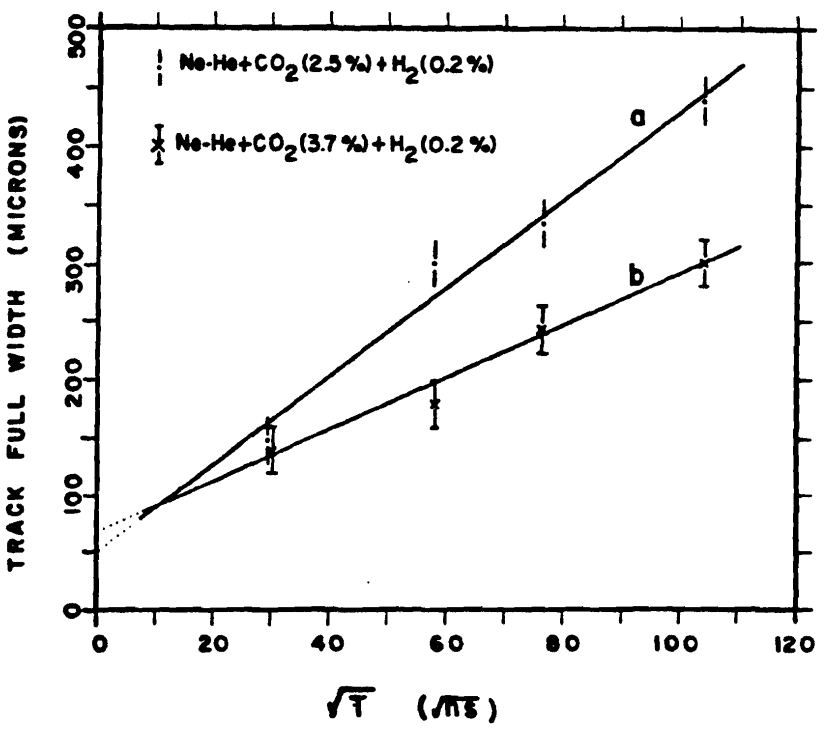

Figure 2-56: Diffusion and memory time study

the tracks were not visible at a delay of 15μs. At a delay of 10μs, the streamer density was very low and the tracks were barely recognizable. Figure 2-57 and figure 2-58 are two typical pictures from the E-630 experiment. Table 2-1 summarizes the operating parameters of the Yale streamer chamber.

It is important to note that in the running condition of E-630, the diffusion of the primary seed electrons contributes substantially to the measured track width. Another important parameter which affects the *true* resolution of the streamer chamber picture is the minimum distance required to unambiguously separate two tracks. Due to the variation in the brightness of the streamers in a picture, the chamber and its optical system had to be tuned in a way such that the faint streamers can be recorded on the film. Therefore the brighter (or bigger) streamers might be slightly overexposed. The consequence of this optical fluctuation together with the *halation* problem on the film cause the area between two close tracks to be filled with small streamer-like dots (like a continuous grey background). Hence for most of the pictures, when two tracks are very close to each other, one can tell that there are *two* tracks but the tracks are not measurable (or can not be measured well). The minimum distance required to separate two tracks in the E-630 pictures is about 150 μm (on the film). This is the number we will use as the *two-track resolution* for analyzing the pictures from E-630 experiment in the following chapters. (Also see the description of the measurement monte-carlo in appendix-I.)

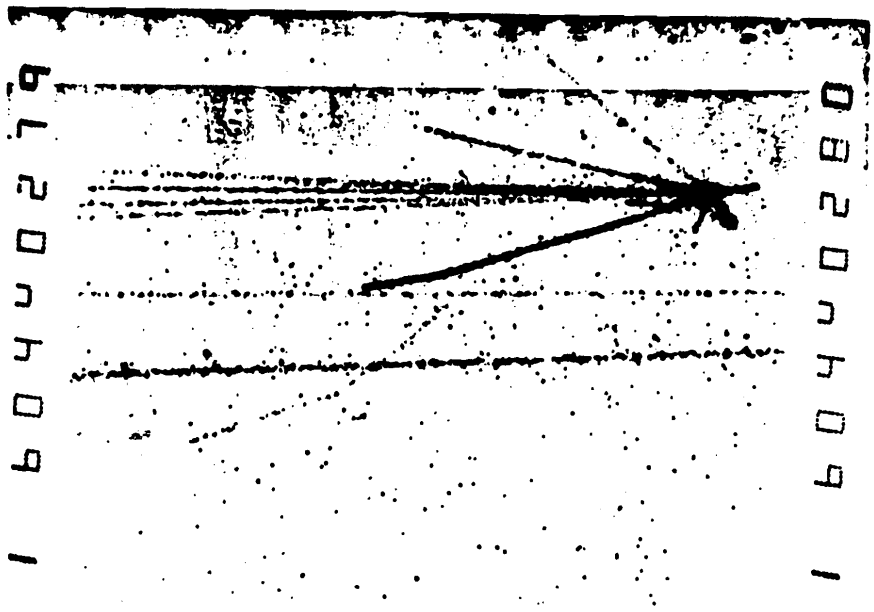

Figure 2-57: Picture from E-630; pulse ~ 160 KV and 1.4 ns FWHM 600 psia Ne–He(9/1)+CO_2(2.5%)

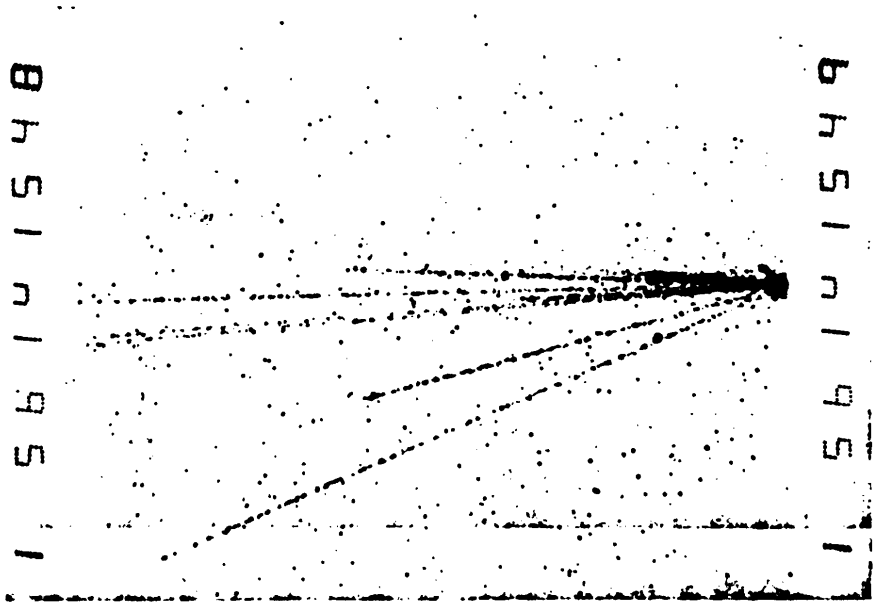

Figure 2-58: Picture from E-630; pulse ~ 160 KV and 1.4 ns FWHM 600 psia Ne–He(9/1)+CO_2(2.5%)

	E-490	E-630
chamber gas and pressure	Ne-He(9/1) 370 psia	Ne-He(9/1)+CD_2(2.5%) 600 psia
optical gain of image intensifier	2500	10000
high voltage pulse amplitude and width	~ 150 KV 0.5 ns	~ 160 KV 1.4 ns
fiducial region of chamber	3 x 4 x 0.45 cm^3	3 x 4 x 0.45 cm^3
Blumlein spark gaps and gas	~ 800 psia Ar 4 gaps	~ 750 psia Air single gap
streamer diameter and track width(space)	~ 50 μm 225 μm (diffusion dominate)	~ 50 μm 120 μm (diffusion dominate)
overall delay time	500 ns	700 ns

Table 2-1: Operating parameters of the Yale high resolution streamer chamber

Chapter 3

THE NEUTRON BEAM LINE, THE MUON SPECTROMETER AND THE TRIGGERS

We have already mentioned, in chapter 1, that a neutron beam was chosen for this experiment in order to allow a higher interaction rate without the obscuring effect on the streamer chamber pictures of the non-interacting beam particles. The structure and operation of the Yale streamer chamber were discussed in chapter 2. In this chapter, the neutron beam line will be discussed in section 1. In section 2, we will briefly discuss the structure of the muon spectrometer and the various triggers. We will also introduce some terminology related to the triggers that will be used frequently in the following chapters when we discuss the data analysis.

3.1 THE NEUTRON BEAM LINE

The neutron beam line for this experiment was located in the Fermilab Proton-Center area. The requirements for the incident neutron beam included a 1 cm by 1 mm beam size, a high neutron intensity ($\sim 10^7$ neutrons/spill) with small photon contamination and a minimum muon background. These requirements were quite stringent given the space available in the P-Center experimental area. Figure 3-1 shows schematically the layout of

the whole beam line from the charged particle sweeping magnet to the streamer chamber. The 35 kilogauss charged particle sweeping magnet, M, was originally designed for the Fermilab hyperon beam [120]. However, the curved channel for the hyperon beam was replaced by a straight brass channel for the neutron beam (figure 3-2 and figure 3-3). The size of the channel is listed in table 3-1.

The 400 Gev Fermilab P-Center proton beam was focused and directed onto a beryllium target in the front section of the beam channel. The effective size of the target was 1 mm^2 in cross section and 30 cm in length corresponding to 1 interaction length for 400 Gev incident protons. In order to suppress the photon component in the neutron beam, 15 lead foils (each 3.2 mm thick and 12.2 cm apart) were installed in the second section of the beam channel. The e^+e^- pairs from photon conversions in these lead foils were swept away from the channel by the magnetic field of the dump magnet.

Following the dump magnet was a muon spoiler [121] to further sweep away the background muons. After the spoiler, there was a vacuum beam pipe followed by three steel collimators, C_1, C_2 and C_3. The first collimator defined the neutron beam pointing at the streamer chamber. The second and the third collimators were shadow collimators to eliminate the beam halo. These collimators subtended a vertical angle of about 12 μr and a horizontal angle of about 120 μr with the central beam line. The sizes of the openings in these collimators are listed in table 3-1 (also, see figure 3-2 and figure 3-3). Three dipole magnets were installed in between the collimators to sweep away the charged particles generated inside the collimators.

Because of the small size of the collimator openings, the alignment of the collimators with respect to the beam channel was very critical. Precision stepping motors allowed us to remotely adjust the positions of the collimators. The alignment was done by maximizing the neutron beam intensity detected in the beam monitors (BM2 to BM4 of figure 3-1). The profile of the collimated neutron beam could be *observed* by placing a piece of the Polaroid film in the beam line for a few beam spills.

Figure 3-4 is a photocopy of the Polaroid film which shows the beam profile at the

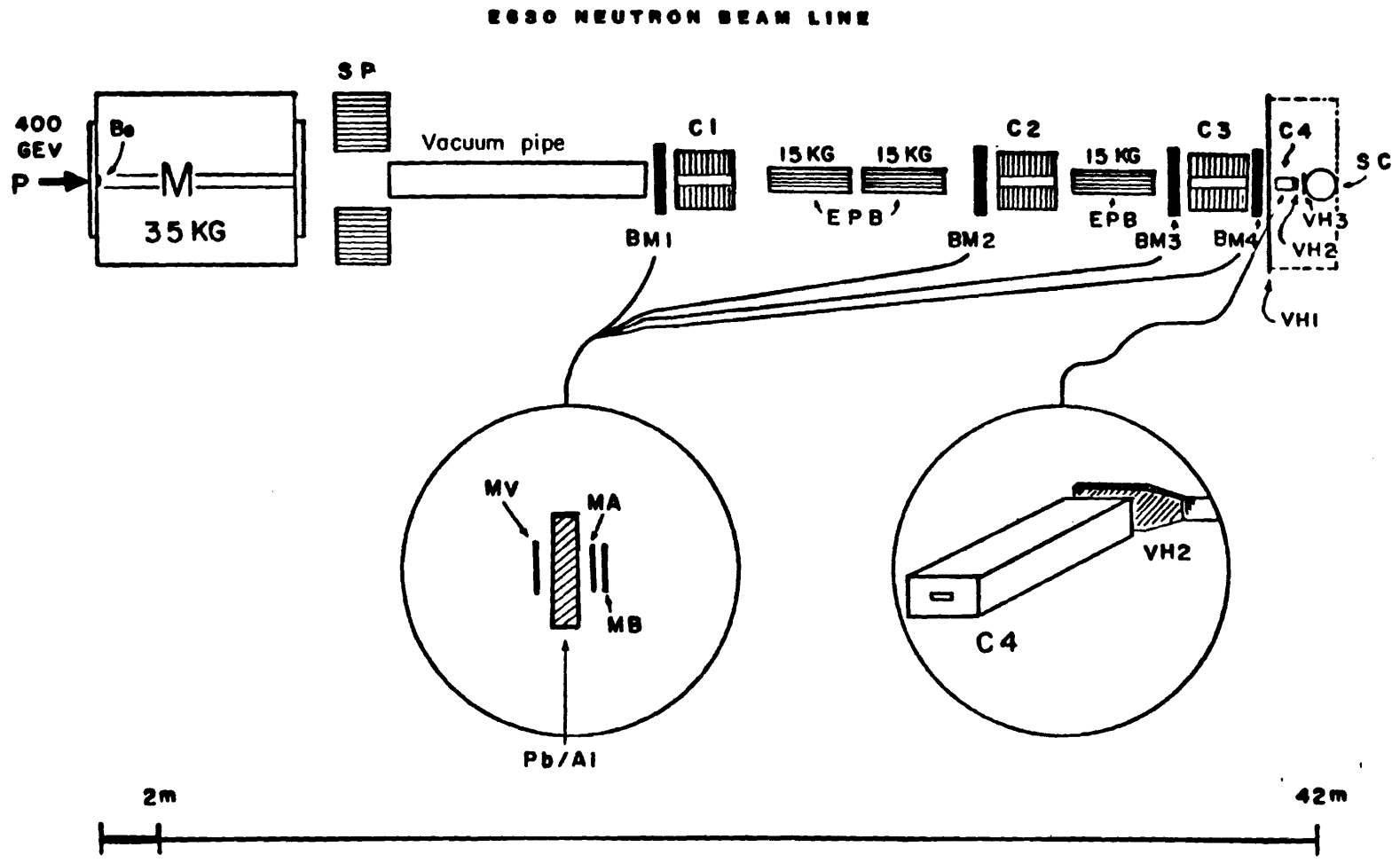

Figure 3-1: E-630 neutron beam line

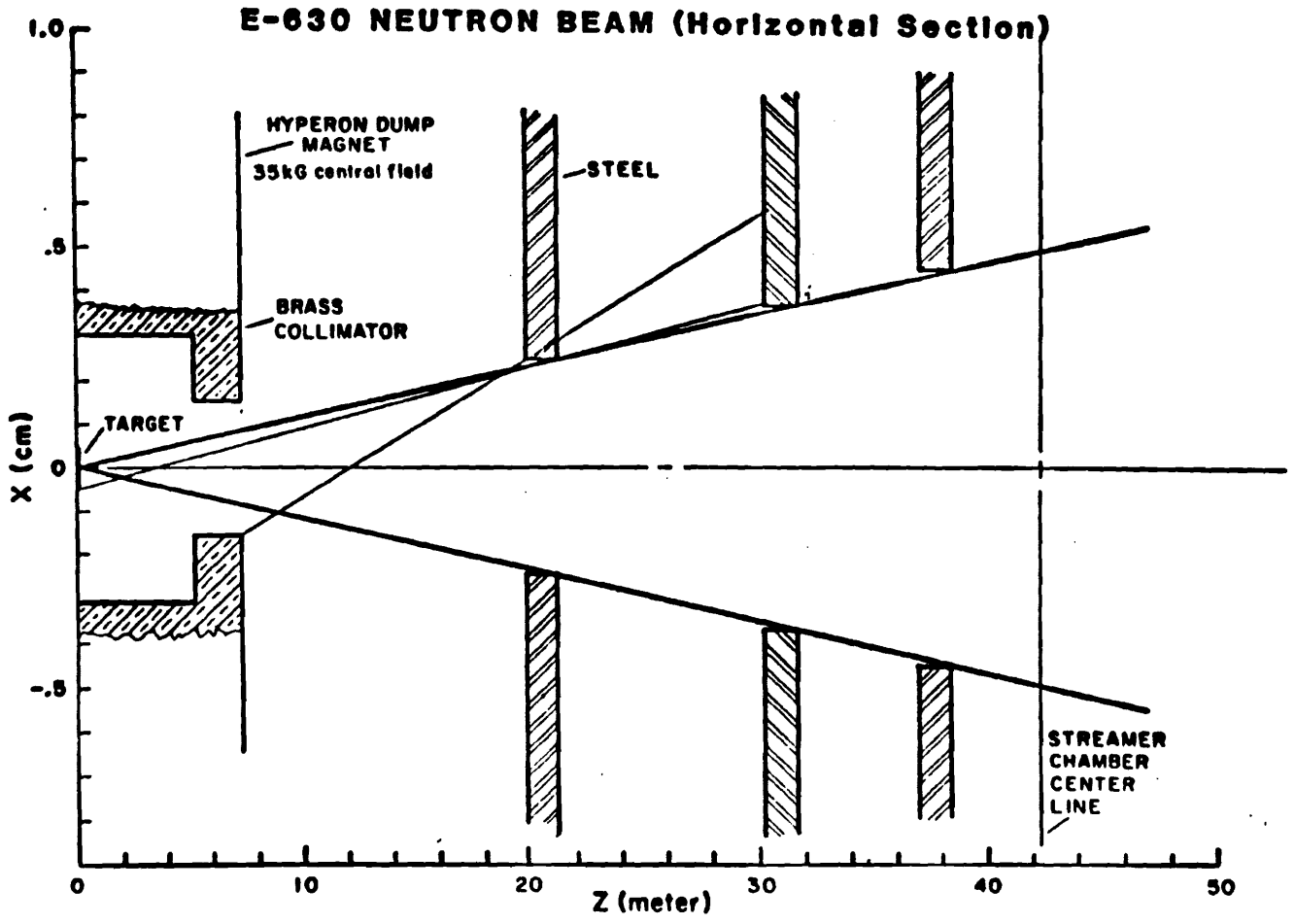

Figure 3-2: Neutron beam line (horizontal section)

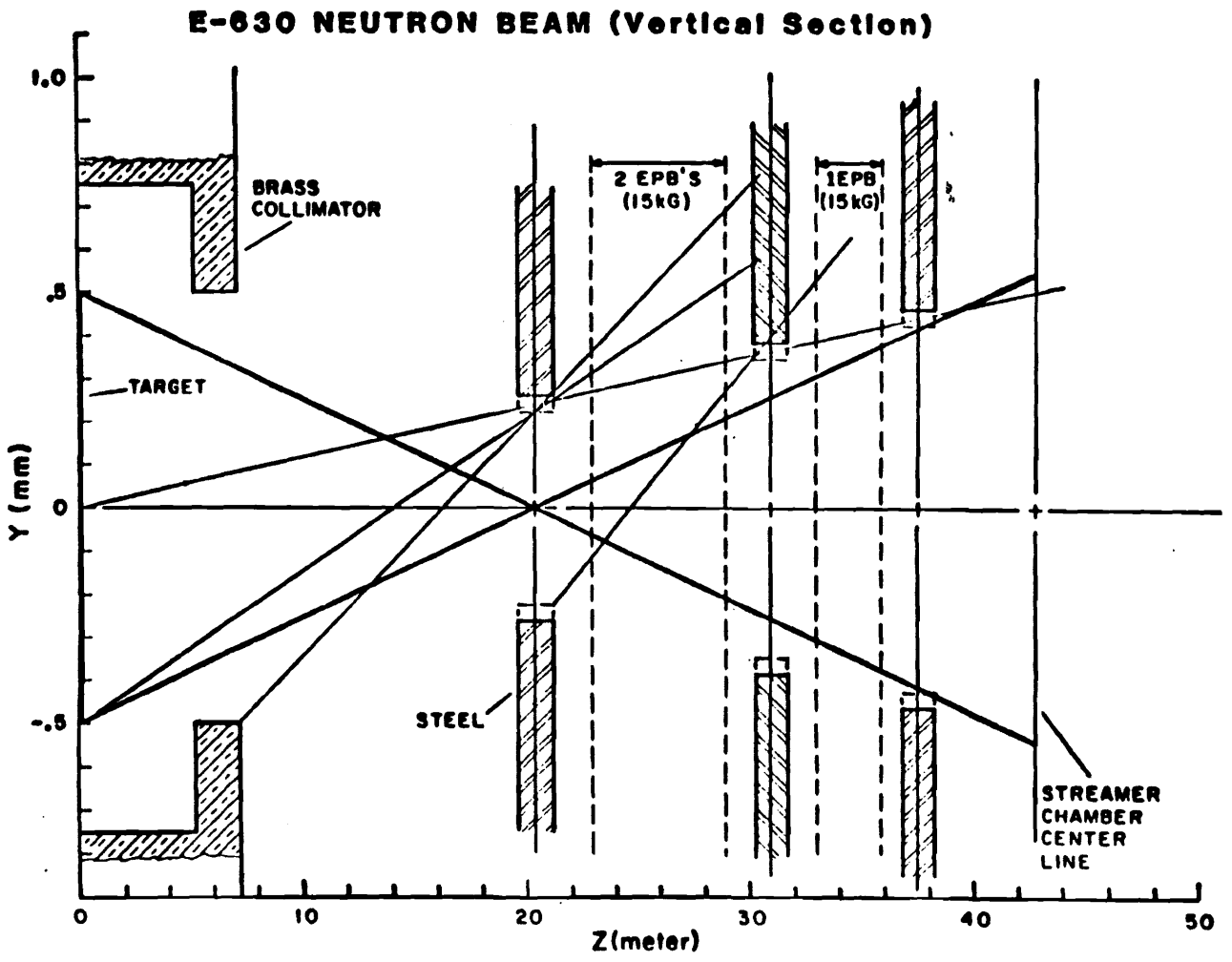

Figure 2-8: Neutron beam line (vertical section)

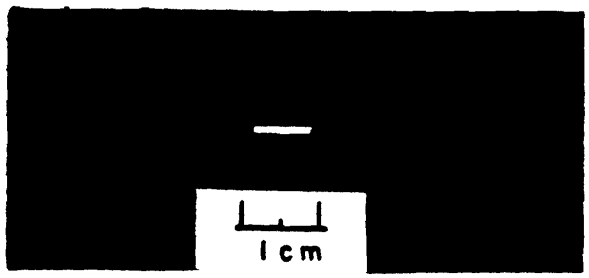

Figure 3-4: Neutron beam profile in front of the streamer chamber

front of the streamer chamber. The size of the beam profile was approximately equal to 1 cm by 0.1 cm. Examining the picture carefully, one can see an extraneous *wing* extending from the right edge of the rectangular beam profile. This was due to the imperfections in the collimators. Each collimator consisted of two parts. The top half was simply a flat piece of steel whereas the lower half has a rectangular groove on the surface. Small flaws in machining the surface left small cracks along the edges of the collimator opening.

The fourth collimator, C_4, was a copper block of about 40.6 cm in length, 7.2 x 8.0 cm^2 in cross section, with a rectangular channel in the center (the cross section of this channel was 2.4 x 14.3 mm^2). This block, together with a set of hole veto counters (VH2 and VH3), was mounted immediately in front of the entrance beam window of the streamer chamber to reduce the number of extraneous triggers due to the beam halo or upstream interactions. A veto wall (VH1) with a hole veto counter at the center was placed just upstream of the RF house containing the streamer chamber. The main purpose of this veto wall was to veto the background muons from upstream.

Also shown in figure 3-1 are four beam monitor stations (BM1 through BM4; there was another monitor station, BM5, located at the end of the downstream muon spectrometer as shown in figure 3-7). These beam monitors were used for aligning the collimators and estimating the neutron/photon ratio of the beam contents. Each monitor consisted of a veto counter (MV) to select neutral incident particles, several converting materials and two coincidence counters (MA and MB). There were seven converting

	Distance from target (meter)	Size of channel Horizontal	vertical
Beam channel (first section)	0 to 3.35	0.60 cm	1.50 mm
Beam channel (second section)	3.35 to 5.33	0.60 cm	1.50 mm
Beam channel (third section)	5.33 to 7.32	0.30 cm	1.00 mm
1st collimator	19.74 to 21.26	0.48 cm	0.45 mm
2nd collimator	30.24 to 31.76	0.72 cm	0.69 mm
3rd collimator	36.89 to 38.41	0.88 cm	0.85 mm
Streamer chamber	42.40		
Muon shield (A section)	42.49 to 43.35	(30 mr inner cone)	
Muon shield (B section)	43.49 to 44.32	(30 mr inner cone)	
PWC-B	44.41		
Muon shield (C section)	44.50 to 45.75	(30 mr inner cone)	
Concrete blocks (D section)	46.20 to 46.66	(30.5 cm square central hole)	
PWC-D	47.12		
1st Toroid	47.40 to 48.33	(30 mr inner cone)	
2nd Toroid	48.81 to 49.74	(30 mr inner cone)	
PWC-T2	49.93		

Table 3-1: E-630 neutron beam line and muon spectrometer setup

materials for each monitor (i.e. *empty space*, 0.127 mm Pb, 0.254 mm Pb, 0.381 mm Pb, 4.76 mm Al, 9.53 mm Al and 19.05 mm Al). The converting materials were mounted on a rotating wheel which could be remotely controlled via a stepping motor. The three counters were also mounted on a stepping motor. They were raised up to the beam level only during the beam tuning period. Now, let us see how the beam monitors were used to estimate the N_n/N_γ ratio.

Define:

$$R_s = 1 - \exp(-l_s/r_s)$$

$$A_s = 1 - \exp(-l_s/a_s)$$

where l_s is the effective thickness of the scintillation counter. r_s and a_s are the radiation length and absorption length respectively of the scintillator.

Similarly, for material x, let us define:

$$R_x = 1 - \exp(-l_x/r_x)$$

$$A_x = 1 - \exp(-l_x/a_x)$$

Let

N_γ = number of photons in the beam

N_n = number of neutrons in the beam

When no converting material is inserted in the monitor, the counts from the monitor (i.e. $\overline{MV}\cdot MA\cdot MB$) will be

$$N_0 = R_s\cdot N_\gamma + A_s\cdot N_n$$

with material x in the beam, the monitor countes

$$N_x = N_0 + R_x\cdot N_\gamma + A_x\cdot N_n$$

Define

$$I_x = N_x - N_0 = R_x \cdot N_\gamma + A_x \cdot N_n$$

Then

$$I_x/R_x = N_\gamma + (A_x/R_x) \cdot N_n \tag{3-1}$$

or

$$I_x/A_x = N_n + (R_x/A_x) \cdot N_\gamma \tag{3-2}$$

Plotting the ratio (I_x/R_x) versus (A_x/R_x) for different materials, we obtain the number N_γ as (A_x/R_x) approaches 0. Similarly, N_n could be found in the plot of (I_x/A_x) versus (R_x/A_x) as the latter approaches 0. When the beam was well tuned, the measured N_n/N_γ ratio was about 80 at monitor station BM4.

The neutron flux at the streamer chamber is calculated in reference [126] by using the Fermilab neutron production data [122] :

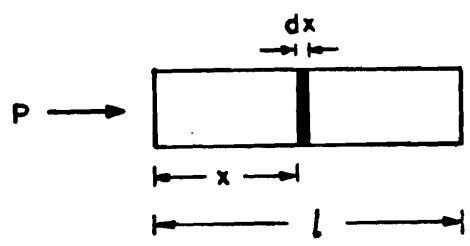

Define

$\frac{d\sigma}{d\Omega}$ ≡ Neutron production cross section per unit solid angle at zero degrees for 400 Gev/c incident protons.
≈ 0.75×10^6 mb (estimated from [122])

$\Delta\Omega$ ≡ The solid angle covered by the beam line.
= $(0.1 \times 1.0)/(4240.5)^2$.

λ ≡ Interaction length of beryllium.

ρ ≡ Number of target particles per unit volume.
~ $(1.848/9.01) \cdot 6.02 \times 10^{23}$ for Be target.

l ≡ Target length.

N_0 ≡ Number of incident protons.

Then

$N_p(x)$ $\equiv$ Number of protons at distance x inside the target.
$= N_0 \cdot e^{-x/\lambda}$

$dN_n(x)$ $\equiv$ Number of neutrons produced by dx of Be at distance x inside the target.

$$= N_p(x) \cdot \frac{d\sigma}{d\Omega} \cdot \Delta\Omega \cdot dx \cdot \rho$$

$dN_l(x)$ $\equiv$ Number of neutrons from $dN_n(x)$ that survive to l.

$$= dN_n(x) \cdot e^{(l-x)/\lambda}$$

Therefore, the total number of neutrons produced is

$$N_n = \int_0^\lambda dN_l(x) dx$$

or

$$N_n = N_0 \cdot \frac{d\sigma}{d\Omega} \cdot \Delta\Omega \cdot l \cdot \rho \cdot e^{-l/\lambda}$$

for $l = \lambda = 30$ cm

$$N_n = 5.68 \times 10^{-6} \cdot N_0 \tag{3-3}$$

Thus for an incident proton intensity of 1.0×10^{12} per beam spill, equation 3-3 implies a neutron intensity of (5.7×10^6) per spill.

In this experiment, the neutron flux was monitored by a neutron calorimeter[1] located behind the downstream muon spectrometer (figure 3-7). Using a special neutron calorimeter run (Run-642), with a proton beam intensity of 2.3×10^{10} protons per spill, the measured neutron intensity was 1.3×10^5 neutrons per spill which was reasonably close to the calculated value from equation 3-3. Figure 3-5 shows the measured neutron spectrum from this run compared to the result from an ISR experiment [124]. The neutron data from the ISR experiment are fitted to a function

$$E\frac{d^3\sigma}{dP^3}(X_F) = e^{C_1 + C_2 X + C_3 X^2} \cdot (1 - X_F)^{C_4} \tag{3-4}$$

[1]The neutron calorimeter was made of layers of scintillation counters sandwitched between layers of steel plates

with C_1=3.03, C_2=−2.65, C_3=9.50 and C_4=2.32

The contamination of neutral strange particles in the neutron beam was not measured directly in this experiment. The flux ratios Λ^0/N, $\overline{\Lambda^0}/N$ and K^0/N are estimated in reference [125] by using the neutron data from reference [124] (figure 3-5) and the strange particle data from the Fermilab neutral hyperon experiment [124]. From this calculation, the ratio of Λ^0/N_n is about 0.001 at the location of the streamer chamber. Both the K^0/N_n and $\overline{\Lambda^0}/N_n$ ratios are far smaller than 10^{-4}. Therefore the contamination of the strange particles can be neglected at the location of the streamer chamber.

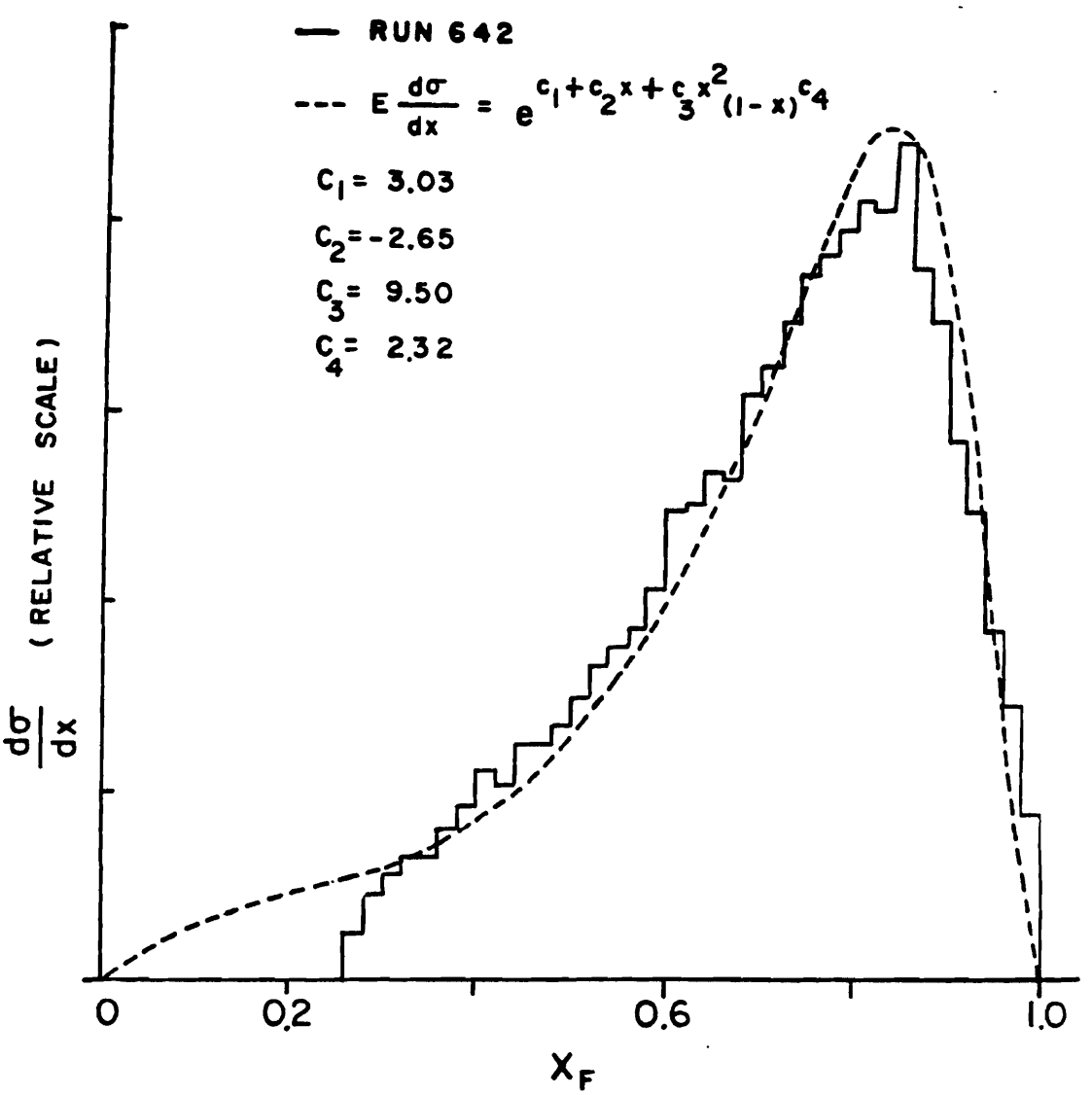

Figure 3-5: Neutron spectrum from Run-642

The solid line histogram is the neutron spectrum measured with the neutron carolimeter. To calibrate the carolimeter, we assume that the end point of the spectrum corresponds to 400 Gev neutron energy. The dashed line curve is obtained by fitting the data of Ref. [123] to Eq. 3-4 with C_1=3.03, C_2=−2.65, C_3=9.50 and C_4=2.32.

3.2 THE MUON SPECTROMETER AND THE TRIGGERS

The main consideration in designing the muon spectrometer was to choose a relatively simple system which would have a good acceptance for the muons from the decays of the charmed particles. In order to provide a clean selection for the muons, the system should also have a good rejection for punch-through hadrons and decays of the hadrons inside the spectrometer.

The layout of the muon spectrometer is shown in figure 3-7 (the locations of the various counters, chambers and shields are listed in table 3-1). The collimated neutron beam was directed into the streamer chamber. The hole veto counters in front of the streamer chamber (figure 3-1) were installed to detect the unwanted particles from upstream interactions. Neutron induced interactions inside the streamer chamber were detected by requiring 2 or more hits in the *interaction hodoscope* located right behind the exit beam window of the streamer chamber. This interaction hodoscope (illustrated in figure 3-6) was made of 8 small scintillation counters arranged in a pie shape configuration with a rectangular hole at the center to avoid background signals generated by the beam particles. Let us label this neutron induced interaction as NI and

$$\mathrm{NI} \equiv \overline{\mathrm{VH1}}\cdot\overline{\mathrm{VH2}}\cdot\overline{\mathrm{VH3}}\cdot(\geq 2 \text{ hits in the I-counters}) \tag{3-5}$$

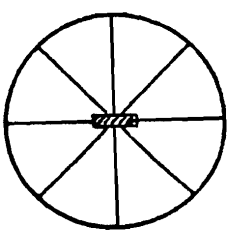

Figure 3-6: Interaction hodoscope

Following the interaction hodoscope, there were four sections of *hadron filter* (section A through D in figure 3-7) and two toroids (T1 and T2, each with 15 kilogauss magnetic field and reversible polarity). The central inner holes inside the hadron filter and the

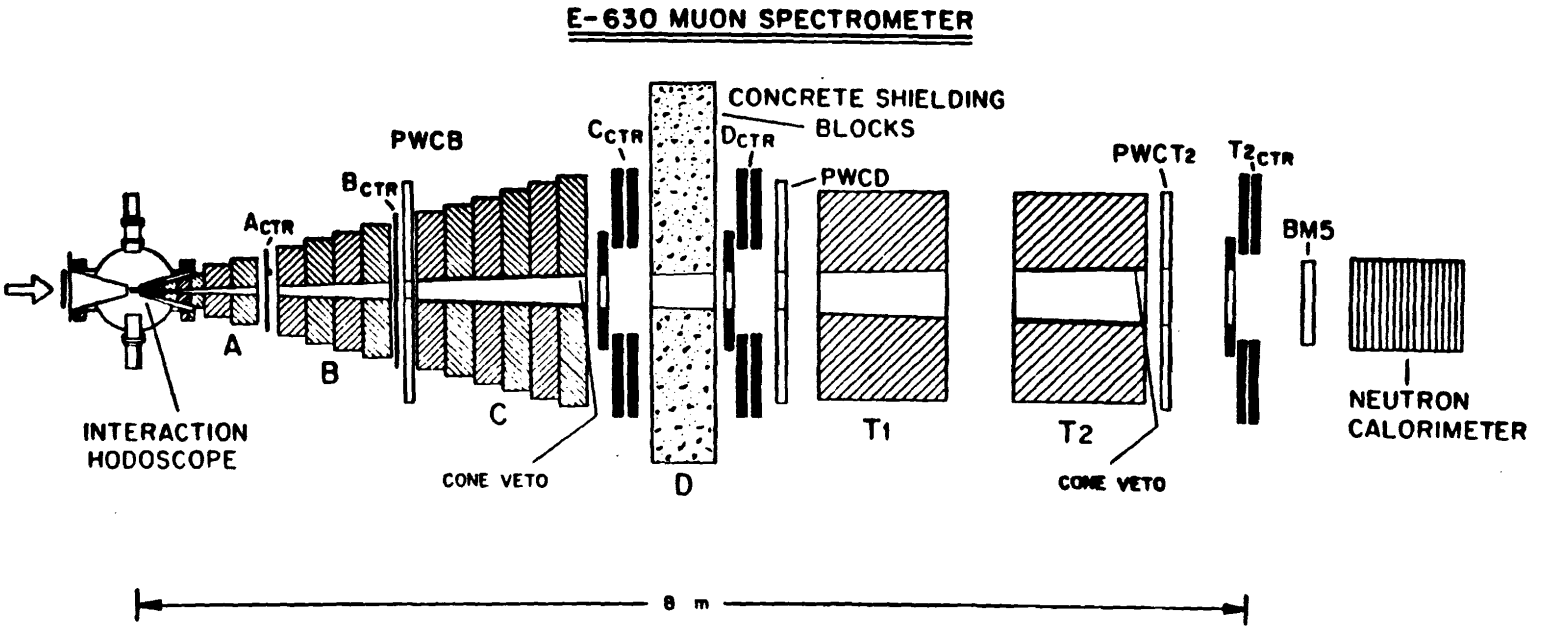

Figure 2-7: E-630 muon spectrometer

toroids subtended an angle of 30 mr with respect to the beam line. The first three sections of the hadron filter were made of steel and covered a polar angle range between 30 mr to 250 mr. The D-section was a stack of concrete blocks with a square hole at the center. The outer radii of both toroids were equal to 91.4 cm (equivalent to a maximum angular acceptance of 182 mr for muons from the streamer chamber). The minimum energy required for a muon to travel through this hadron filter was about 6 Gev.[2]

Behind every section of the hadron filter and the second toroid, there was a layer of scintillation counters. Again a hole with appropriate size was cut out at the center of these counter walls. These holes together with the central holes of the hadron filter provided a passage for the beam particles and the particles in the forward jet from the hadron interactions. The *A-counter layer* (the counter layer behind the A-section hadron shield) was simply a 61 x 61 cm^2 scintillation counter. The *B-counter layer* was made out of four 114 x 28 cm^2 rectangular counters. These four counters allowed us to determine whether a muon track was pointing up or down, assuming that the muon came from the streamer chamber. The *C-counter layer* was a 1.8 x 1.8 m^2 counter wall consisting of six pieces of 91 x 61 cm^2 counters at the two sides (east and west) and one 61 x 61 cm^2 counters (with a circular hole cut out at the center) in the middle. Two phototubes were attached to this middle counter to provide up/down information for the track direction. The configuraton of both the *D-counter layer* and the *T2-counter layer* were the same as that of the C-counter layer. Muon tracks were detected by a suitable tracking requirement among the first four layers of the muon counters with the additional requirement that at least 1 hit be detected in the T2-counter (the latter requirement was implemented to utilize the toroids for the muon momentum analysis). Detailed descriptions of the spectrometer and the trigger logic will be reported in reference [78].

There were three sets of proportional wire chambers installed in this experiment (PWC-B, PWC-D, and PWC-T2 in figure 3-7). The size of each PWC was about 160 cm

---

[2]The spectrometer has a maximum acceptance for muons with energy greater than 8 Gev, polar angle greater than 30 mr and less than 120 mr.

by 160cm with 2 mm wire spacing and every 5 wires ganged together for the anode wire plane. The resolution of the PWC was estimated to be on the order of 6 mm. Detailed description of the PWC's and the related electronics will be given in another thesis [78]. Briefly speaking, the three coordinate planes (X, Y, and U) of each PWC were contained in a single chamber (i.e. an anode wire plane and two cathode planes) with central area desensitized. The momentum resolution and the angle resolution of the muon tracks measured with these PWC's, basically limited by the multiple scattering and the energy loss of the muon tracks inside the shields and the toroids, were estimated to be on the order of 15% (i.e. $\frac{\delta P}{P} \sim 15\%$ and $\frac{\delta\theta}{\theta} \sim 15\%$).

Two cone shaped veto counters were installed one inside the inner hole of the C-section and the other inside the second toroid (figure 3-7). The first cone veto counter eliminated events with hadrons exiting and re-entering the hadron shield (i.e. to enhance the rejection efficiency for the punch-through hadrons). The second veto counter inside the toroid removed muons which curved into the central holes of the toroids.

Now, let us define the ***muon trigger*** associated with the neutron induced interactions inside the streamer chamber as follows:

Let

$$\begin{aligned} NI &\equiv \text{Neutron induced interaction} \\ &\quad\ \text{(defined in equation 3-5)} \\ \overline{CV} &\equiv \text{No } \textit{hit} \text{ at the cone-veto counters} \\ MU &\equiv \text{(Tracking between A, B, C and D counters)} \\ &\quad\ \bullet\ (\geq 1 \text{ hit at T2-counter}) \end{aligned} \tag{3-6}$$

then

$$\textbf{Muon trigger} \equiv \mathbf{NI} \bullet \overline{\mathbf{CV}} \bullet \mathbf{MU} \tag{3-7}$$

Since the hadron filter could not stop completely all of the hadrons, undoubtly a non-negligible portion of the *muon trigger* events would be the ordinary inelastic interactions. In order to prepare an unbiased sample of events to study the backgrounds, interaction triggers without the muon tracking requirement, the NI·$\overline{CV}$ triggers, were mixed with the

full muon triggers (equation 3-6) during the experiment. Figure 3-8 illustrates the relationships between the trigger gates and the triggers for this experiment. The Fermilab beam spill spreaded over a time period of about 1 second. Within about the last 10 ms[3] of the beam spill, the muon tracking function in the trigger electronics was disabled (i.e. enable the NI·$\overline{CV}$ trigger gate). Both the NI·$\overline{CV}$·MU and the NI·$\overline{CV}$ triggers were used to trigger the Marx generator and advance the film inside the streamer chamber cameras. After every trigger, a 200 ms gate (the *Marx dead-time*) was started to inhibit the Marx trigger such that the Marx generator would be fully charged up before the next trigger.

In this way, two different kinds of scalars for each trigger type were accumulated during each beam spill. They were the *gated* scalars and the *ungated* scalars. The *gated* scalars accumulated the number of triggers taken within the corresponding trigger gates. For example, the *gated* NI·$\overline{CV}$·MU scalar counted the number of pictures taken with the NI·$\overline{CV}$·MU trigger and the *gated* NI·$\overline{CV}$ counted the number of pictures associated with the NI·$\overline{CV}$ trigger. On the other hand, the *ungated* scalars accumulated the number of the triggers occuring during the whole beam spill, with or without the streamer chamber pictures. Therefore, the *ungated* NI·$\overline{CV}$·MU scalar counted the total number of events which satisfied the NI·$\overline{CV}$·MU trigger requirements in the whole beam spill including the time slots when the Marx trigger was inhibited. The *ungated* NI·$\overline{CV}$ scalar counted the total number of events which satisfied the NI·$\overline{CV}$ trigger definition in the whole beam spill (not necessarily confined in the last 10 ms NI·$\overline{CV}$ enable gate). It is obvious that the *ungated* NI·$\overline{CV}$ triggers included the *ungated* NI·$\overline{CV}$·MU triggers.

[3]This time length changed according to the condition of the experiment and the variation of the spill structure.

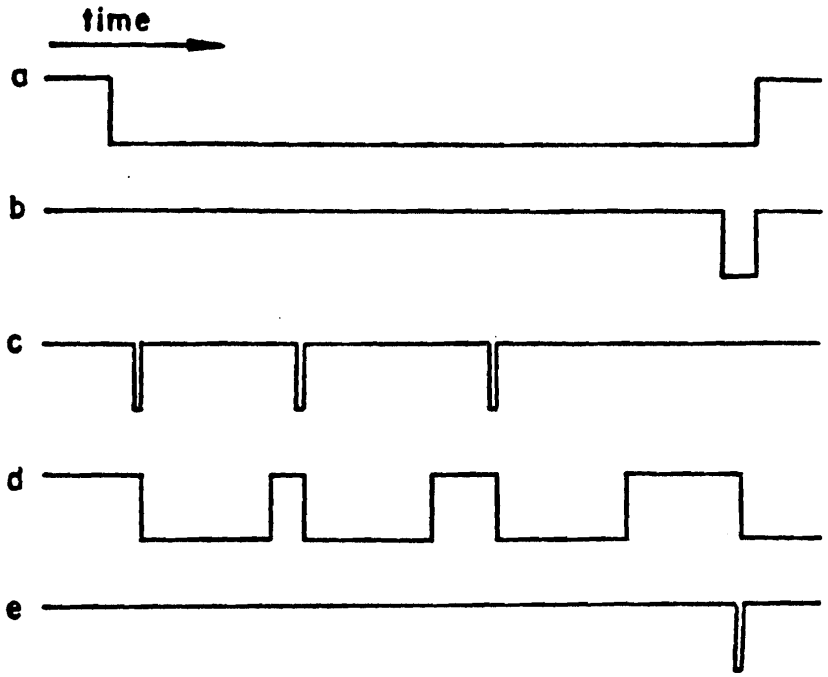

Figure 3-8: E-630 triggers

[a] Beam gate (~1 s). [b] NI·$\overline{\text{CV}}$enable gate (~10 ms). [c] NI·$\overline{\text{CV}}$·MU triggers. [d] Marx dead time (~200 ms). [e] NI·$\overline{\text{CV}}$ triggers.

Chapter 4

MUON RECONSTRUCTION AND PICTURE MEASUREMENT

The data collected in this experiment can be classified into two different categories namely the *streamer chamber pictures* and the *on-line computer information* which includes the data from the counter latches, ADC's, PWC readouts and the beam line control devices. In measuring the streamer chamber pictures, in principle, only those events with at least one muon detected in the downstream spectrometer had to be measured since this experiment was set up to trigger on the muonic decay of the charmed particles. However, in order to study the backgrounds, we also measured a sample of events which do not have any muon detected in the spectrometer. Thus the picture measurement list was generated according to the off-line muon reconstruction program. The muon selection criterion for the measurement list was chosen to be very generous to minimize the loss of charm events. The fiducial interaction pictures were then selected and measured according to this measurement list. The basic procedures for the reconstruction of the muon track will be briefly[1] discussed in the first section of this chapter and the measurement of the streamer chamber pictures will be discussed in the second section. In section 3, we will discuss the three dimensional reconstruction of the

[1]Detailed discussions on the muon reconstruction program will be reported in another thesis [78].

streamer chamber tracks and the alignment between the streamer chamber and the muon spectrometer.

4.1 MUON TRACK RECONSTRUCTION

The muon tracks were determined by the information from the PWC's and the muon counters (figure 3-7). Each muon track was divided into two sections: a straight section from the streamer chamber (e.g. from the decay of a charmed particle) to the front end of the first toroid and a curved section where the muon traversed the toroids.

The straight section was constructed by using the coordinates of the hits[2] in the PWC-B and the PWC-D together with the event vertex determined from the streamer chamber picture[3]. The basic limitations on the precision of fitting this straight section came from the multiple scattering and energy loss of the muon tracks inside the hadron filter. Measurement of the muon momentum was therefore necessary for the estimation of the effects of the multiple scattering. The muon momentum was measured, basically, from the angle of the muon track entering the first toroid and the position where the muon track hit the PWC-T2. Therefore, to determine the momentum of a muon track, we had to locate the point where the muon track hit the PWC-T2.

The direction (angle) of a candidate muon track was first estimated by using only the center of the streamer chamber and the location of the hit in the PWC-D. As it is shown in figure 4-1, the three points, O, D and T2 represent the center of chamber, the hit in the PWC-D and the hit in the PWC-T2 respectively. These three points are expected to fall on a line if they are associated with a real muon track traversed the spectrometer without multiple scattering. However, because of the multiple scattering, the point T2 might have a ϕ angle different from that of the front section. The difference between the

[2]The detailed definition for the hits on the PWC's will be given in reference [78].

[3]As a matter of fact, because of the small size of the streamer chamber and the resolution of the PWC's (chapter 3, section 2), the results would not change (within the limits of our resolution) if the center of the streamer chamber ([0, 0, 0]) was used instead of the true vertex of the event.

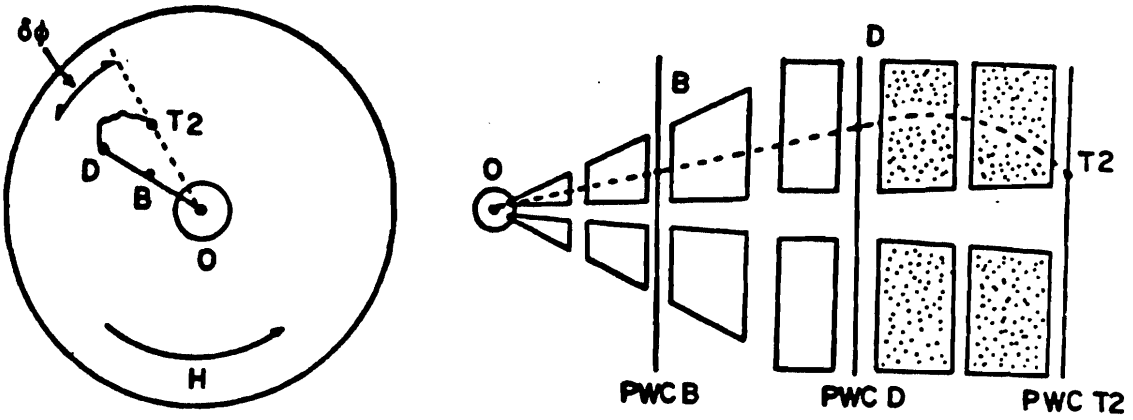

Figure 4-1: $\delta\phi$ of muon track
Left: beam-direction view. Right: elevation view

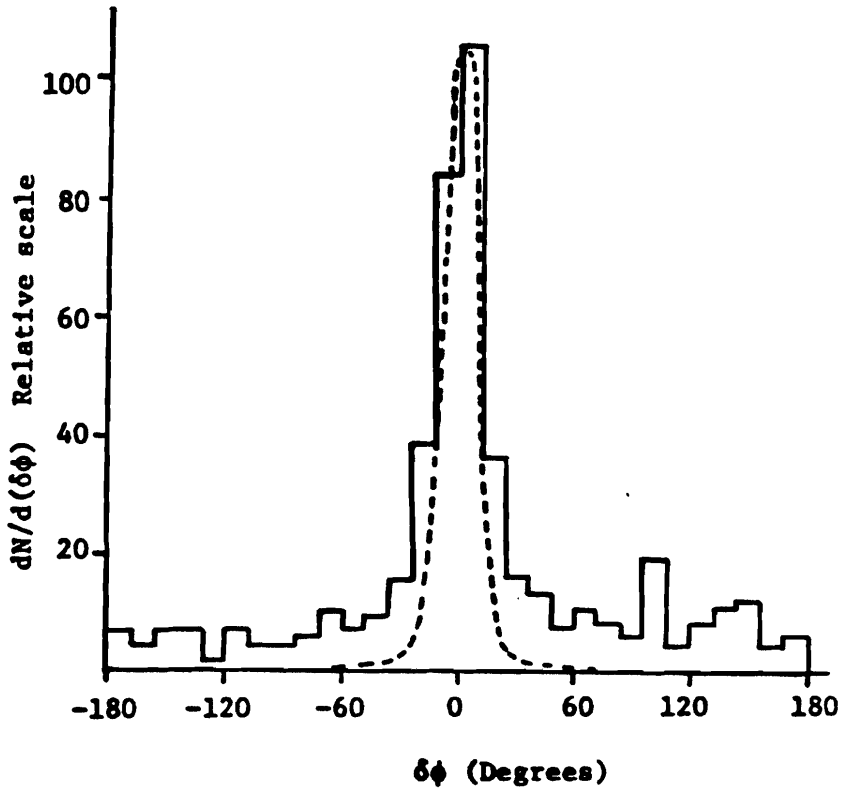

Figure 4-2: Distribution of $\delta\phi$

Solid line: real events. Dashed line: monte-carlo distribution with perfect PWC resolution.

ϕ angles of point D and point T2, $\delta\phi$, is expected to have a distribution centered at $\delta\phi$=0. In figure 4-2, the $\delta\phi$ distribution obtained from a sample of 442 events is compared with a predicted distribution from a monte-carlo simulation. It should be noted that the monte-carlo distribution is slightly narrower than that of the real events since the monte-carlo assumed a perfect resolution for the three PWC's. From this figure, a clear signal of *real tracks* can be easily identified. Thus the quantity $\delta\phi$ provided a means of selecting the corresponding hits between PWC-D and PWC-T2. The selection criterion was that the quantity $|\delta\phi|$ for a candidate muon track should be less than 40 degrees.

Based on this $\delta\phi$ cut, we selected the candidate muon track with known track angle and exit location in the PWC-T2. A look-up table generated by a monte-carlo program was used to find out the most probable momentum for each candidate track. The front straight section of the candidate muon track, with the additional point from PWC-B, was then fitted with appropriate errors due to the multiple scattering and the resolution of the PWC's. A cut on the chi-squared for this linear fit was set at χ^2=10. This fitting procedure was applied to all of the possible combinations from the hits in the three PWC's. Any event with at least one muon track satisfying all of the fitting criteria was labeled as a ***good-muon*** event and events without any *good-muon* track were labeled as ***bad-muon*** events.

The streamer chamber picture measurement list was generated according to this good-muon selection procedure. In addition to the good-muon events, a sample of $NI\cdot\overline{CV}$ (interaction-trigger) pictures of about the same size as the *good-muon* sample and a sample of *bad-muon* events of about one-tenth the size of the *good-muon* sample were also included in the measurement list for the purpose of the background study, as discussed in the introduction of this chapter.

The good-muon measurement list only provided a very generous selection of the muon tracks. The main purpose was to identify the *bad-muon* events and to exclud most of them from the measurement list (hence to speed up the picture measurement process). Tighter criteria on the muon track selection are therefore necessary for the final analysis

of the measured events. An intermediate step in refining the reconstruction procedures of the muon track included the following requirements. First, a better estimation of the PWC resolution[4] was obtained. Second, comparisons between the effective PWC fiducial regions and the the coordinates of the hits in the PWC's were performed to ensure that the candidate track stayed inside the spectrometer[5]. Finally, for the hits of a candidate track in the three PWC's, a set of matched muon-counter latch bits was required to ensure that the hits were not caused by the noise of the PWC's. Events selected with these additional criteria were labeled as ***better*** muon events. Again, details on the various cuts, fitting criteria are given in reference [78].

The estimation of the ***error*** associated with the measurement of the muon momentum from the muon fitting method discussed above was however very poor. A more sophisticated method of determining the muon momentum was applied to the measured muon events in the final analysis. Briefly speaking, we can consider the problem as following. Given a muon track with known momentum and direction, we can calculate (with the effects of multiple scattering, energy loss and magnetic field inside the spectrometer and toroids) the probability function of actually measuring this track at certain positions in the three PWC's. Once the probability function was evaluated, given the measured coordinates of the hits in the three PWC's, with a maximum likelihood method, we can obtain the most probable values for the muon momentum, direction and the errors. The muon events selected with this method were labeled as ***best-muon*** events. Details for the evaluation of the likelihood function and the minimization procedures will also be reported in reference [78].

It should also be mentioned here that a momentum cut of 7 Gev/c was applied to the best-muon selection procedure. The range of a muon in our spectrometer was about 6 Gev. Below 7 Gev, the best-muon fitting procedure can not accurately determine the

---

[4]The studies on the properties of the muons inside the spectrometer and the characteristics of the PWC's proceeded in parallel with the streamer chamber picture measurement.

[5]The size of the active regions of the PWC's were slightly different from that of the steel shields and toroids.

muon momentum. From the monte-carlo study, the possibility for a muon with energy less than 7 Gev from the decay of a charm particle to satisfy the trigger requirement is negligibly small. Therefore by applying the 7 Gev/c momentum cut to the best-muon selection procedure, we expect to eliminate more background with a minimum loss of charm events.

4.2 FILM MEASUREMENT

The streamer chamber pictures were selected for measurment according to the muon track information as discussed in the previous section (i.e. good-muon events + $N1 \cdot \overline{CV}$ events + bad-muon events with the ratio $\sim$ 1:1:0.1). All of the fiducial pictures in the measurement list were measured with the same measurement rules. Two measurement machines were used to measure the E-630 data. Most of the first measurements were done at the Fermilab film analysis facility with an image-plane digitizer[6]. A small portion of the first measurements and all of the remeasurements were done at Yale with a Vanguard film-plane digitizer[7]. Both machines had a least-count resolution of $\sim$ 2.5 μm and a magnification factor of about 25.

The following measurement rules were applied to the film measurement process at both places:

Fiducial interaction

Only fiducial interaction events were measured. A fiducial interaction is defined as an event with the primary vertex located between −20 mm and +12 mm, along the beam direction in space coordinate, with respect to the center of the streamer chamber. (Remember that the chamber size was 40 mm along the beam direction and the space to film demagnification factor was about 2/3.) Therefore, if an event had a vertex too close to the downstream edge of the chamber frame, we did not measure it since the tracks are usually short and not measurable. On the other hand, if an event vertex is not visible in the picture because it is slightly upstream toward the front end of the chamber region, the tracks are usually long and well separated from each other. In this case, it is possible to measure these tracks well enough to find the vertex by extrapolation.

[6]The average number of scanners assigned to this machine at Fermilab is 1.5.

[7]With 1 scanner.

Picture quality

Each event has pictures (view 1 and view 2) taken with the two cameras of the streamer chamber (section 2.1). Events are considered as not measurable if either (or both) of the pictures are too faint due to the fluctuation of the streamer chamber high voltage pulse. Pictures with a dark background due to the discharge between the two wire electrodes of the streamer chamber were also not measured. (Sometimes a single discharge would affect several frames due the *memory* of the image intensifier.)

A track is measurable only if it is well separated from the rest of tracks in either view. The minimum distance between two separated tracks was determined empirically to be on the order of 150 μm on the film. Tracks with the measurable length less than 1 mm on the film were not measured.

Events with less than three measurable tracks are not considered as useful. These events were not measured.

Track measurement

At least three measurement points are required for each measurable track. The minimum distance between two consecutive measurement points is about 0.4 mm on the film. For longer tracks, the maximum number of measurement points per track is 15. On average, 7-8 points were measured per track. On the Yale Vanguard measurement machine, tracks were measured with a *centroid measurement* method which will be described below.

Nuclear fragments

Nuclear fragments are identified as fat and dark (heavily ionized) tracks associated with the interaction vertices (primary or secondary interactions). The nuclear fragments are usually short (stopped inside the streamer chamber) and sometimes heavily multiple scattered. In this case, only the front straight sections of the nuclear fragment were measured. All measured nuclear fragments were

assigned a special track label.

Non-primary vertex tracks

Non-primary vertex tracks were labeled according to their characteristics such as *vee*, *kink* or *short decay*. *Vees* and *kinks* are defined as the secondary tracks from the decays of the neutral or charged particles respectively (when the decay vertex is clearly visible). *Short decays* are defined as the tracks which visibly do not come from the primary vertex but whose decay vertex is not visible (i.e. obscured).

Background tracks and obscured regions

δ-rays, low energy tracks with visible multiple scattering, tracks from upstream interactions or stray tracks due to the beam particles hitting the wire electrodes or the chamber frames are all considered as the background tracks. These background tracks together with the vertex flare and the obscured forward jet (overlapping tracks in the forward direction) were treated as parts of the obscured regions. The contours of the obscured regions were traced by the measurer on the measurement machines and stored as part of the data from the picture measurement.

Old events

Old events (due to the memory time of the streamer chamber, which was $\sim$ 10 μs) are identified by comparing the track width with the ordinary events. If an old event is overlaid on the top of an ordinary event, the tracks of the old event will be treated as obscured regions.

Since the film measurement was expected to be the most time consuming process in analyzing the data, at the beginning of developing the analysis strategy, the measurers were instructed to measure everything on the film even if it did not exactly satisfy the measurement rules. The main purpose was to unload the film measurement effort as soon as possible. As a result, some events which should not have been measured (such as faint events) were measured. Additional clean-up and remeasurement procedures were

Item	Quantity
1. Total number of runs	75
2. Ungated interaction triggers	447798691
3. Gated interaction triggers	44801
4. Ungated muon triggers	221277
5. Gated muon triggers	116073
6. Total number of triggers	160874
7. Number of good-muon events (in measurement list)	20138
8. Number of bad-muon events (in measurement list)	9144
9. Number of interaction trigger events (in measurement list)	18460
10. Number of good-muon events (actually measured)	1807
11. Number of bad-muon events (actually measured)	1116
12. Number of interaction trigger events (actually measured)	1612
13. Number of measured better-muon events (A sub-sample of item 10)	1492
14. Number of matched best-muon events (A sub-sample of item 13)	769

Table 4-1: E-630 data summary

Interaction trigger $\equiv$ NI·$\overline{\text{CV}}$ trigger and muon trigger $\equiv$ NI·$\overline{\text{CV}}$·MU trigger (defined in section 2 of chapter 3). The definitions for ***bad-muon***, ***good-muon***, ***better-muon*** and ***best-muon*** events have been discussed in the previous section. Also, see text for the definition of the ***matched-muon*** events. Note that the ratio of item 10 to item 7 ($\sim$9%) is approximately equal to the ratio of item 12 to item 9.

anticipated. Another reason for this measurement strategy was to minimize the scanning biases.

In this experiment, the data were separated into many runs. Each run contained about 2500 streamer chamber pictures. The 75 runs included in the analysis for this thesis (from Run 542 to Run 667) were selected with the requirement that the trigger electronics and the streamer chamber functioned correctly for these runs. Table 4-1 lists a summary of the various summed scalar numbers from the on-line data collection system and the total number of scanned and measured pictures in these 75 runs.

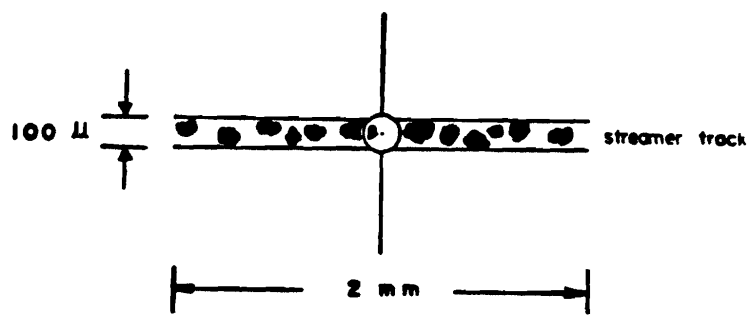

Figure 4-3: Centroid measurement

Let us now discuss the ***centroid measurement*** method mentioned above for the track measurement. Figure 4-3 illustrates schematically a section of streamer track. Because of the irregular shape of the streamer dots on the pictures, it is very difficult to define their central points for measurement. However, with two parallel lines separated by 0.1 mm (on the film) and projected onto the screen of the measurement machine, it is possible to connect several streamer dots together and estimate the center of the track. Therefore, instead of measuring the center of an individual streamer, the centroid measurement averages over several streamers and measures the center of the sections of a track. The centroid measurement method was used on the Yale measurement machine. For the Fermilab measurement machine, only the central circle of figure 4-3 was projected on tha table.

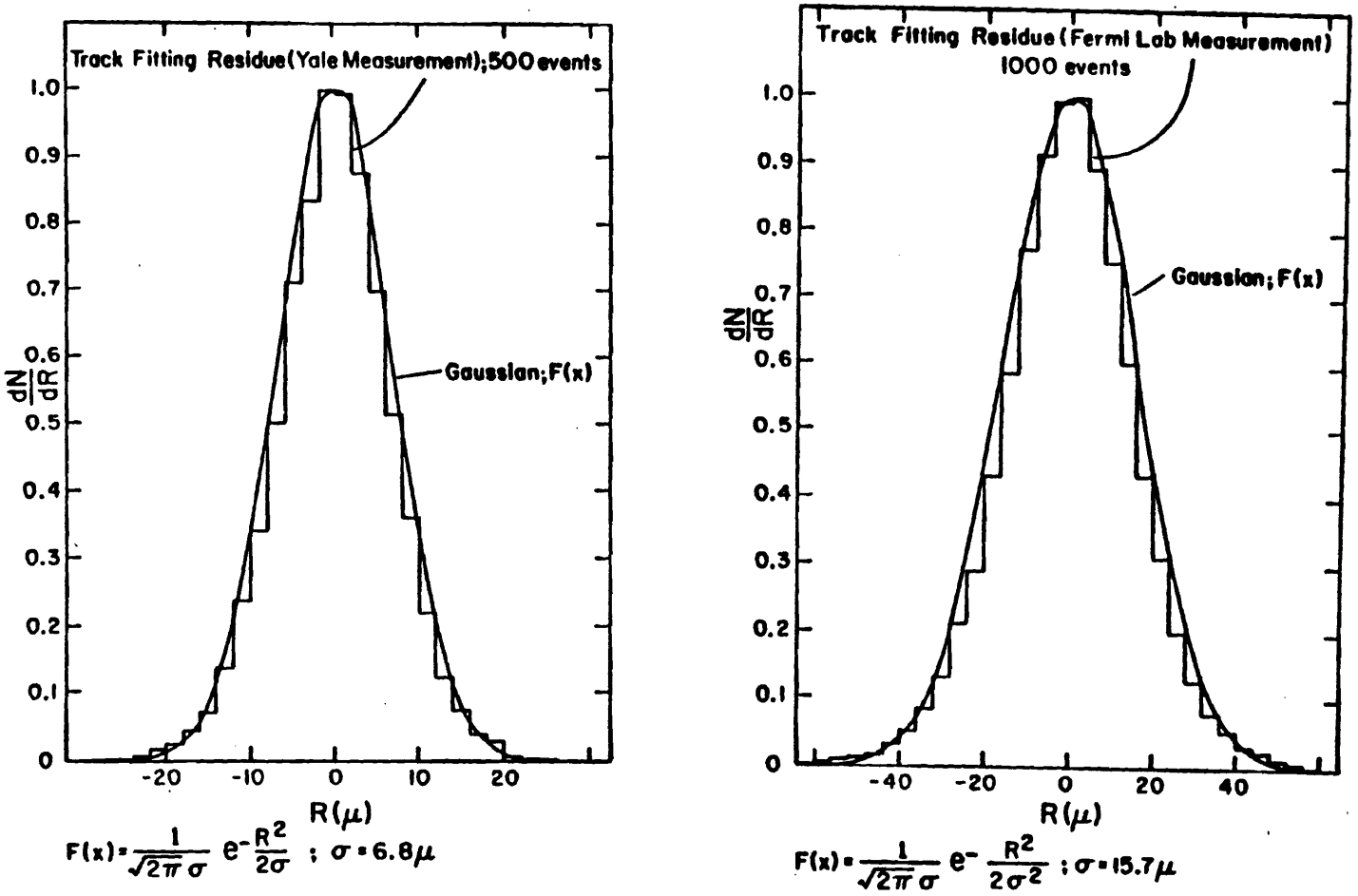

Figure 4-4: Track fitting residue

If we fit a line to the measurement points of a track and plot the distribution of the residual distances between the points and the fitted line, we get the distributions shown in figure 4-4. In this figure, the distributions are compared to a Gaussian functions with standard deviations equal to 6.8 μm and 15.7 μm for the Yale measurements and the Fermilab measurements respectively. However, these numbers should not be used directly as the *setting errors* for the measurement points.[8] The *true* errors for the measurement points can be determined statistically by examining the distribution of the reduced chi-squared of the event vertex fitted for a sample of single vertex events.

A sample of interaction trigger pictures were measured. All of the non-primary vertex tracks were labeled and excluded from the vertex-fitting calculation. The reduced chi-squared of a fitted vertex can be calculated as

$$\frac{\chi^2}{\nu} = \frac{1}{\nu} \sum_{i=1}^{N} \left(\frac{S_i}{DS_i} \right)^2 \tag{4-1}$$

where N is the number of tracks used to fit the vertex, ν is the degrees of freedom (ν=N−2), S_i is the distance from the fitted vertex to the ith track. The error associated with the calculation of S_i is labeled as DS_i and depends directly on the choice of the setting error for the measurement points. If we define $X = \frac{\chi^2}{\nu}$, and h=$\nu/2$ for fixed ν, the distribution of X should follow the function (if the setting errors were appropriately selected)

$$\Phi(X,\nu) = [\nu^h \cdot X^{h-1} \cdot e^{-hX}] \;/\; [2^h \cdot \Gamma(h)] \tag{4-2}$$

For a sample of M events, the ensemble distribution of the quantity X will be

$$\Psi(X) = \frac{1}{M} \sum_{j=1}^{M} [\nu^{h_j} X^{h_j - 1} e^{-h_j X}] \;/\; [2^{h_j} \Gamma(h_j)] \tag{4-3}$$

with

$$\int \Psi(X) dX = 1$$

[8]For example, the centroid measurement did not measure each point independently, every measurement point was strongly correlated to its neighboring points if these consecutive measurement points were covered inside the two parallel lines of figure 4-3.

$$\int X\Psi(X)dX = 1$$

where the subscript j stands for the jth event.

By varying the setting errors and comparing the distribution of the reduced chi-squared with equation 4-3 (figure 4-5), we determined empirically the appropriate errors for our measurement procedures. The setting errors used for the E-630 analysis are :

σ(Ordinary tracks, Yale machine) = 0.014 mm
σ(Nuclear fragments, Yale machine) = 0.060 mm
σ(Ordinary tracks, Fermilab machine) = 0.022 mm
σ(Nuclear fragments, Fermilab machine) = 0.060 mm

To prevent accidental malfunction of the the measurement machines such as loss of vacuum or electronic noise etc., the following checks on all of the measured pictures were performed. First, the chi-squared for every measured track was checked. Track with a reduced chi-squared for the linear track fit greater than 5 was considered as a signature of bad measurement and the event was remeasured.

Another check was the measurement of the fiducial marks. There were four groups of circular fiducial marks located at the four corners of each frame of the streamer chamber picture. These fiducial marks were made of 12 optical fibers ($\sim$100 μm diameter) divided in four groups of three fibers. One end of the group was attached perpendicularly onto the surface of the image intensifier plate (which held the image intensifier and provided housing for the protection circuit of the image intensifier). The other end of the group was illuminated with light from LED's. These 12 fiducial marks were located very close to the outer rim of the image intensifier. For every measured picture, the coordinates of the 12 measured fiducial marks were compared with a standard set of fiducial mark coordinates. After rotational and translational adjustment between these two coordinate sets[9], the distances between the corresponding fiducial marks

[9]Magnification or demagnification factors were allowed to compensate any possible minor distortion of the film introduced during the developing process

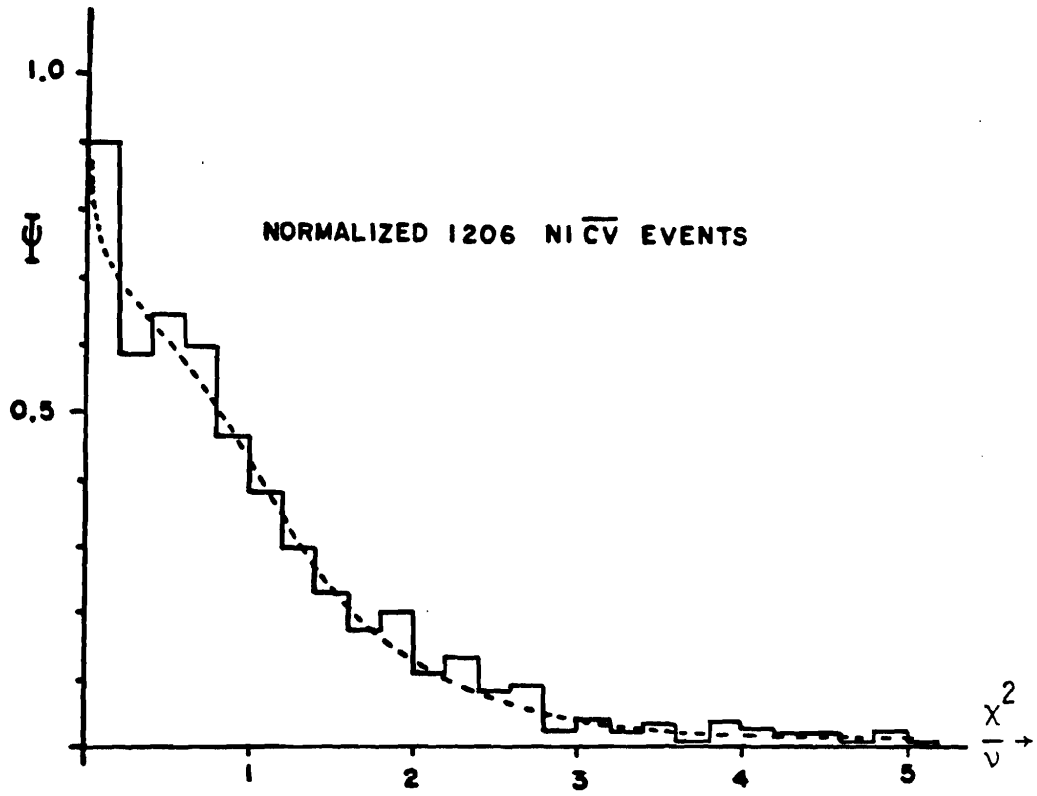

Figure 4-5: Distribution of the vertex chi-squared per degree of freedom

Solid line: From 1206 interaction trigger events. Dashed line: Ψ function of equation 4-3. The point measurement errors are discussed in the text.

(i.e. the residuals) were calculated. These residuals were required to be less then 20 μm otherwise the event was remeasured. These fiducial marks also provided a means of fixing the relative orientation between the pictures and the streamer chamber coordinate system. This coordinate adjustment was important for the three dimensional reconstruction of the streamer chamber tracks and the alignment between the streamer chamber and the downstream muon spectrometer. We will discuss these subjects in the next section.

The output of the picture measurement (digitized data) was combined with the on-line computer information (see the introduction of this chapter) and stored on a computer disk and magnetic tapes. Most of the analysis was done in a PDP-10 computer. A fortran program, <MAPP>,[10] was developed to handle most of the analysis processes such as linear track fitting, three dimensional reconstruction, vertex fitting and the downstream muon reconstruction. This program also provided facilities such as displaying the fitted events and their obscured regions on a graphic terminal.

[10]The <MAPP> program was developed by Professor Peter S. Cooper.

4.3 THREE DIMENSIONAL RECONSTRUCTION AND THE ALIGNMENT OF THE APPARATUS

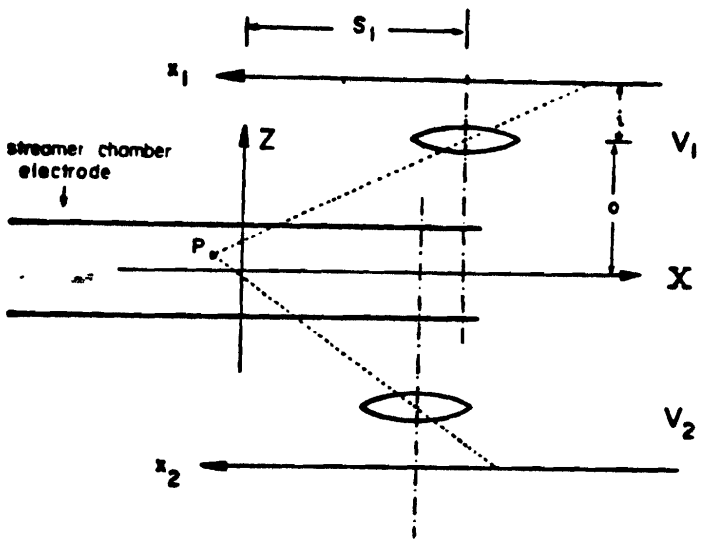

Figure 4-6: Illustration of the streamer chamber optical system. (Not according to the true scale; beam direction along X axis)

The optical system of the streamer chamber consisted of two lenses which subtended a stereo angle of about 7 degrees with the center of the chamber. This small stereo angle is the major limitation on the resolution of the three dimensional reconstruction. This is especially true for the vertical angle.

Figure 4-6 shows schematically a two dimensional view of the streamer chamber optical system. We define 3 coordinate systems here: The [X, Y, Z] system represents the 3-D space system which will ultimately be aligned with the downstream spectrometer. The V_1 ($[x_1, y_1]$) and V_2 ($[x_2, y_2]$) systems are the 2-D coordinate systems on the view 1 film and view 2 film respectively. All measured points are in the V_1 or V_2 system. Let the coordinate of the point P inside the chamber be [X, Y, Z][11] and its images on view 1

[11] $\hat{X}$ is the beam direction and $\hat{Z}$ points upward

and view 2 be $[x_1, y_1]$ and $[x_2, y_2]$ respectively. S_1 is the off-set in the $\hat{X}$ direction between the origin of the view 1 coordinate system and the origin of the space coordinate system. With $Z \ll o$ ($o > 250$ mm and $Z < 2.5$ mm), then the relationship between x_1 and X can be expressed as

$$\frac{-x_1}{S_1-X} = \frac{i}{o-Z} \sim \frac{i}{o}(1+\frac{Z}{o}) \tag{4-4}$$

or

$$x_1 = -\frac{i}{o}S_1 + \frac{i}{o}X + \frac{i}{o^2}XZ - \frac{iS_1}{o^2}Z \tag{4-5}$$

where o is the distance between the Z=0 plane to the primary principle plane of the view 1 lens; i is the distance from the secondary principle plane of the view 1 lens to the view 1 film.

Similiar relationship between x_2 and X can be obtained. In general (from equation 4-5), we have the following relationships:

$$x_1 = a_1 + b_1X + c_1XZ + d_1Z$$

$$x_2 = a_2 + b_2X + c_2XZ + d_2Z$$

$$y_1 = A_1 + B_1Y + C_1YZ + D_1Z$$

$$y_2 = A_2 + B_2Y + C_2YZ + D_2Z$$

Where the subscripts 1 and 2 refer to view 1 and view 2 respectively. Since $b_1=B_1=\frac{i}{o}$ and $c_1=C_1=\frac{i}{o^2}$ (from equation 4-5; so are $b_2=B_2$ and $c_2=C_2$), we may rewrite these equations as

$$x_1 = a_1 + B_1X + C_1XZ + d_1Z \tag{4-6}$$

$$x_2 = a_2 + B_2X + C_2XZ + d_2Z \tag{4-7}$$

$$y_1 = A_1 + B_1Y + C_1YZ + D_1Z \tag{4-8}$$

$$y_2 = A_2 + B_2Y + C_2YZ + D_2Z \tag{4-9}$$

where B_1 and B_2 are simply the demagnification factors of view 1 and view 2. Therefore

the major job for the three dimensional reconstruction is to determine the 12 optical constants in equations 4-6 to 4-9.

If we can obtain a set of points with known values of space coordinates, $[X^i, Y^i, Z^i]$, and known values of the image coordinates, $[x_1^i, y_1^i]$ and $[x_2^i, y_2^i]$, the 12 optical constants can be found by fitting the 4 equations mentioned above to the measured values. For example, use the points in the plane[12] Z=0 and plot the value of x_1^i versus X^i (equation 4-6), we will have a line

$$x_1 = a_1 + B_1 X \tag{4-10}$$

The slope of the line is equal to the demagnification factor B_1 and the intersection of the line with the x_1 axis is equal to the optical constant a_1. For the points in the plane with $Z \neq 0$, equation 4-6 can be written as

$$x_1 = (a_1 + d_1 Z) + (B_1 + C_1 Z)X \tag{4-11}$$

Again, Eq. 4-11 is a line equation. From the slope of the line, with B_1 determined from equation 4-10 and the known value of Z, we get the value of C_1. From the intersection of the line with the x_1 axis, we obtain the value of d_1. The same procedures can be used for both views and for both X and Y coordinates and all of the 12 optical constants will therefore be determined.

Figure 4-7 is an illustration of the three-dimensional grid used to provide a set of points with known values of $[X^i, Y^i, Z^i]$. The grid was made of a thin emulsion film sandwiched in between two emulsion plates. Each emulsion plane was divided into 16 squares. Some of the squares were exposed to a pattern as illustrated in figure 4-7 and the rest of squares were left blank (unexposed). The exposed areas on the three planes were displaced from each other such that all 16 exposed squares, distributed in three planes with different Z coordinates, could be seen from either side of the grid. In

[12]The Z=0 plane can be arbitrarily chosen inside the chamber. We can always shift this plane back to the center of the chamber after reconstruction

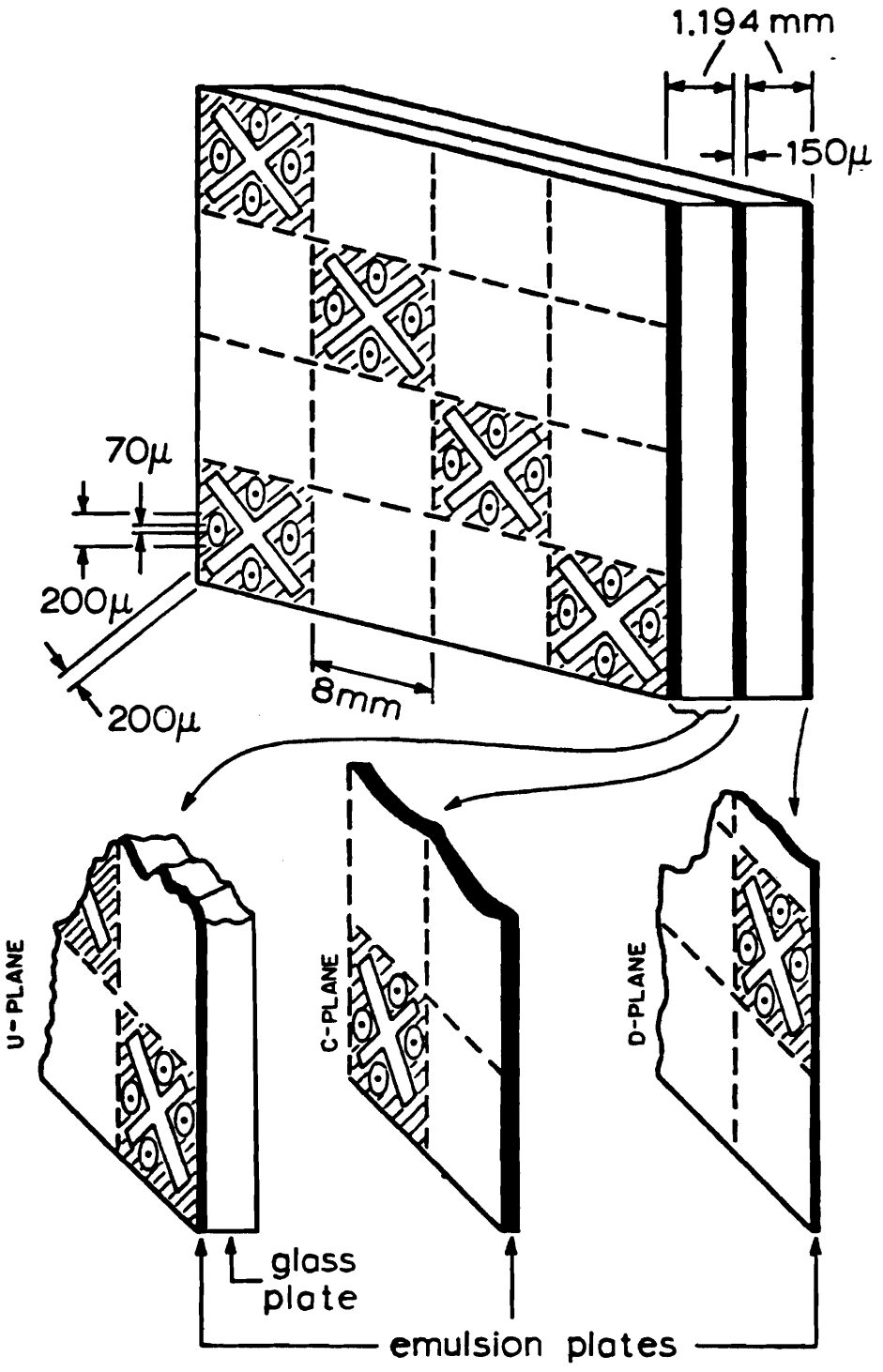

Figure 4-7: 3-D grid for the space reconstruction

The C-plane is a thin emulsion film sandwitched in between two emulsion coated glass plates (the U and D planes). The shaded area represents the exposed emulsion. The inner diameter for all of the *rings* on the sides of the crosses is 70 μm. The centers of these rings are used as the corresponding points in equations 4-6 to 4-9

calculating the Z coordinate of the emulsion planes, we used the true optical length of the glass plates. Corrections however were included when applying these optical constants to the reconstruction of the streamers since there was no glass between the streamers and the lenses. The grid was inserted in between the two wire planes of the streamer chamber before the chamber was pressurized. Pictures of the grid were taken (with the image intensifiers) for both views by illuminating the 3-D grid with LED light. The positions of the 12 fiducial marks (the fiducial marks were discussed in section 4-2) were also recorded at the same time.

The fiducial marks allowed us to fix the relative orientation between the grid pictures and the space coordinate system. This was achieved by using the points on the C-plane (Z=0) of the grid. According to equations 4-6 and 4-8, with Z=0

$$x_1 - a_1 = B_1 X$$

$$y_1 - A_1 = B_1 Y$$

the relationship between the points and their images includes only a demagnification factor, B_1. Therefore by applying the transformations

$$x' = \alpha x + \beta y$$

$$y' = -\beta x + \alpha y$$

$$(\alpha^2 + \beta^2 = B_1^{\,2})$$

to all of the image points and mapping the images to their corresponding values of X's and Y's in space coordinates (which were measured directly from the grid), with a simple fitting procedure, we obtained the values of α and β (the rotation angles). With this transformation, we also had a set of *standard* fiducial-mark coordinates. The optical constants obtained henceforth (according to equation 4-10 and equation 4-11), were applicable only to the film coordinate system defined by these standard coordinates. Appropriate transformations were therefore necessary to bring every measured streamer chamber picture to the standard V_1 or V_2 coordinate orientation for the three dimensional reconstruction. Table 4-2 lists the values and the associated errors of the 12 optical

constants determined in this way. The reason we had two sets of optical constants was becuase the two lenses of the streamer chamber were disassembled once during the experiment and hence the relative positions between the chamber and the fiducial marks changed.

Items	1st set (before run 546)	2nd set (after run 546)
a_1	− 3.9161±0.0023 (mm)	− 3.8584±0.0021 (mm)
a_2	− 6.1663±0.0034 (mm)	− 6.0951±0.0014 (mm)
A_1	7.9415±0.0031 (mm)	8.2959±0.0030 (mm)
A_2	9.5263±0.0032 (mm)	9.6690±0.0025 (mm)
B_1	0.6139±0.0002	0.6142±0.0002
B_2	0.6641±0.0002	0.6635±0.0002
C_1	0.0023±0.0001 (1/mm)	0.0023±0.0001 (1/mm)
C_2	− 0.0018±0.0001 (1/mm)	− 0.0018±0.0001 (1/mm)
d_1	0.0051±0.0070	0.0001±0.0085
d_2	0.0201±0.0062	0.0131±0.0075
D_1	− 0.0221±0.0078	− 0.0222±0.0084
D_2	0.0107±0.0060	0.0027±0.0076

Table 4-2: Optical constants of the E-630 streamer chamber

For convenience in the following discussions, let us make another translation on the coordinates of view 1 and view 2 such that

$$x_1 \rightarrow x_1 - a_1$$

$$y_1 \rightarrow y_1 - A_1$$

$$x_2 \rightarrow x_2 - a_2$$

$$y_2 \rightarrow y_2 - A_2$$

equations 4-6 to 4-9 can be rewritten as

$$x_1 = B_1X + C_1XZ + d_1Z \tag{4-12}$$

$$x_2 = B_2X + C_2XZ + d_2Z \tag{4-13}$$

$$y_1 = B_1Y + C_1YZ + D_1Z \tag{4-14}$$

$$y_2 = B_2Y + C_2YZ + D_2Z \tag{4-15}$$

The line equations for a track inside the streamer chamber can be expressed as

$$\begin{cases} Z = \mathcal{A}_z + \mathcal{M}_zX \\ Y = \mathcal{A}_y + \mathcal{M}_yX \end{cases} \tag{4-16}$$

and the measured line equations for the images of this track on view 1 and view 2 can be expressed as

$$y_1 = m_1x_1 + b_1 \tag{4-17}$$

and

$$y_2 = m_2x_2 + b_2 \tag{4-18}$$

Substituting equations 4-12 to 4-15 into equations 4-17 and 4-18, after some simple algebra, we have

$$\mathcal{A}_y = \frac{1}{\Delta}(AY1 - AY2) \tag{4-19}$$

$$\begin{cases} AY1 = b_1(m_2d_2 - D_2 - b_2C_2/B_2)/B_1B_2 \\ AY2 = b_2(m_1d_1 - D_1 - b_1C_1/B_1)/B_1B_2 \end{cases}$$

$$\mathcal{M}_y = \frac{1}{\Delta}(BY1 - BY2) \tag{4-20}$$

$$\begin{cases} BY1 = m_1(m_2d_2 - D_2 - b_2C_2/B_2)/B_2 \\ BY2 = m_2(m_1d_1 - D_1 - b_1C_1/B_1)/B_1 \end{cases}$$

$$\mathcal{A}_z = \frac{1}{\Delta}\{\frac{b_1}{B_1} - \frac{b_2}{B_2}\} \tag{4-21}$$

$$\mathcal{M}_z = \frac{1}{\Delta}\{m_1 - m_2\} \tag{4-22}$$

where

$$\Delta = D1 - D2$$

$$\begin{cases} D1=(m_2d_2-D_2-b_2C_2/B_2)/B_2 \\ D2=(m_1d_1-D_1-b_1C_1/B_1)/B_1 \end{cases}$$

and the errors associated with these four coefficients can be estimated according to the formula

$$\sigma_{\mathcal{A}}^2 = \sum_{i=1}^{16} [\frac{\partial \mathcal{A}}{\partial u_i}\sigma(u_i)]^2 \tag{4-23}$$

where $u_i(i=1,\cdots,16)$ are the 16 parameters including m_1, m_2, b_1, b_2 and the 12 optical constants. The projection angle θ and the dip-angle η of the track in space (figure 4-8) can be calculated as

$$\theta = tan^{-1}M_y \tag{4-24}$$

$$\eta = tan^{-1}(M_z cos\theta) \tag{4-25}$$

The resolution of the dip-angle depends strongly on the stereo angle of the optical system. This can be easily understood from the following example. In the limit of zero degree stereo angle (S_1 in figure 4-6 approaches 0), equation 4-6 to 4-9 can be written as

$$x_1 = (B_1+C_1Z)X \tag{4-26}$$

$$y_1 = (B_1+C_1Z)Y \tag{4-27}$$

$$x_2 = (B_2+C_2Z)X \tag{4-28}$$

$$y_2 = (B_2+C_2Z)Y \tag{4-29}$$

A track passing through the origin of the space coordinate system will have line equations $\{Y=M_yX,\ Z=M_zX\}$. From equation 4-26 and 4-27, we have

$$y_1 = M_y x_1\ (= m_1x_1)$$

$$y_2 = M_y x_2\ (= m_2x_2)$$

Therefore the slopes of the two image lines on view 1 and view 2 are both equal to M_y. The calculated dip-angle will always equal to 0 (Eq. 4-22) even if $M_z \neq 0$. In our system,

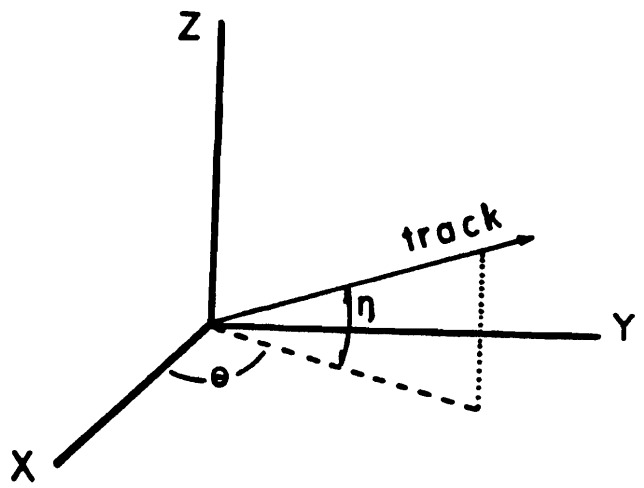

Figure 4-8: Definition of the projection angle and the dip-angle

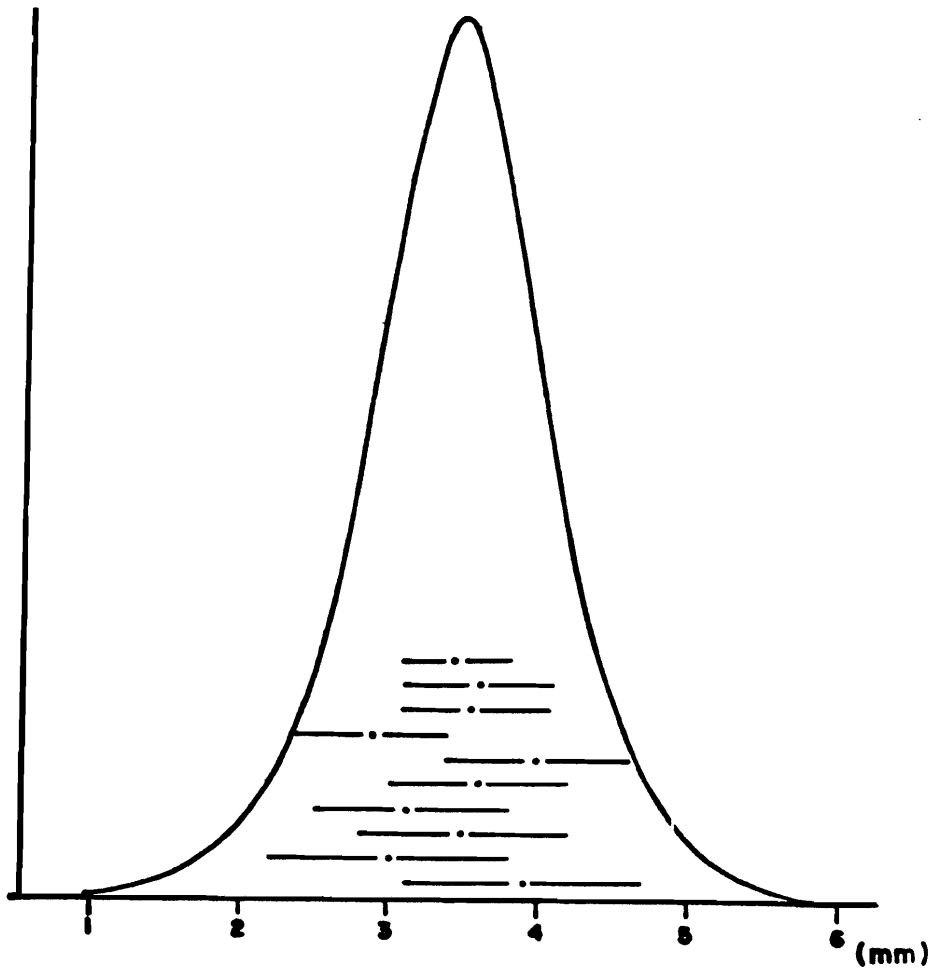

Figure 4-9: Estimation of the effective field region of the streamer chamber

The solid line curve: Gaussian ideogram. The dots and error bars: measured results from 3-D reconstruction.

with about a 7 degree stereo angle, we estimate that the resolution of the track dip-angle is about on the order of 2° (or $\sigma_M \sim 0.036$) for the forward tracks.

Two tests were performed to check the 3-D reconstruction procedures. The first one was to reconstruct several *fake* tracks made out of the measured points from the C-plane of the 3-D grid. Since all of the points lie on a plane, the value of M_z for these tracks were expected to be zero. The five measured values (after reconstruction) were:

M_z
− 0.0128±0.0825
0.0120±0.0455
− 0.0041±0.0384
− 0.0046±0.0513
0.0139±0.0601

The mean value was consistent with 0 (although with huge errors). Another test of the reconstruction process was to measure the chamber width from real streamer tracks of particles which were generated by upstream interactions and traveled through both wire planes of the chamber. The distance between the two wire planes was calculated with the dip-angle and the track length which were measured from the 3-D reconstruction. The major uncertainty in this test was the determination of the track length since the *end points* of these stray tracks were not well defined on the pictures. The distance between the two wire planes of the streamer chamber was 4.5 mm. Assuming that the uniform electric field region started from a distance of about 1.5 wire-spacing from the wire plane, thus the effective uniform field region was approximately equal to 4.2 mm. Given a streamer density of about 6 streamers per mm, naively, one would expect the first streamer to be visible at $\sim$ 0.1 mm inside the uniform field region. So, taking into account the uncertainty of measuring the *end points* of the tracks, the measured value for the chamber width was anticipated to be on the order of 3.8 mm. Figure 4-9 is a plot of the ideogram for the results of the reconstruction from 10 stray tracks. The mean value is about 3.5 mm which is close to our estimate.[13]

[13]The center of the chamber can be determined from the reconstruction of the end points of these stray tracks.

After fixing the coordinate system for the streamer chamber, the next thing we did was to match this coordinate system with the downstream muon spectrometer which was carefully surveyed before and after the experiment. At the end of the E-630 data taking period, the three PWC's were purposely moved 15 inches toward one side (west) of the spectrometer such that the central hole areas of the hadron filter were covered by the active regions of the PWC's. (Each PWC had a central circular region desensitized.) The idea was to find events with only one or two reconstructable forward tracks that traveled through the central hole inside the hadron filter. The direction of these tracks, free from multiple scattering, can be well determined with the information from the three PWC's. Some of these tracks might also be clear and measurable on the streamer chamber pictures. Using the 3-D reconstruction results for these events we can then align the streamer chamber with respect to the muon spectrometer.

Eight events from Run-680 and Run-681 were selected and measured for this alignment procedure. Figure 4-10 shows one of the eight events. The bottom two pictures show the film measurement points and the corresponding fitted tracks in the streamer chamber fiducial volume. The solid tracks are projections of the measured tracks on the film. The area enclosed by dotted lines around the vertex region indicates the obscured region in the vicinity of the interaction vertex, as discussed in the measurement rules of the previous section. The first plot on the top is an vertical view of the whole event together with the positions and scales for the hadron filter and toroids. The dashed line overlapping track-D indicates the track detected by the three PWC's. The second plot is the horizontal view. Again, the same PWC track is overlapping with the track-D. This plot also shows that the three PWC's were shifted 15 inches toward west. The four solid lines in these two plots are the measured streamer chamber tracks, extrapolated through the whole apparatus.

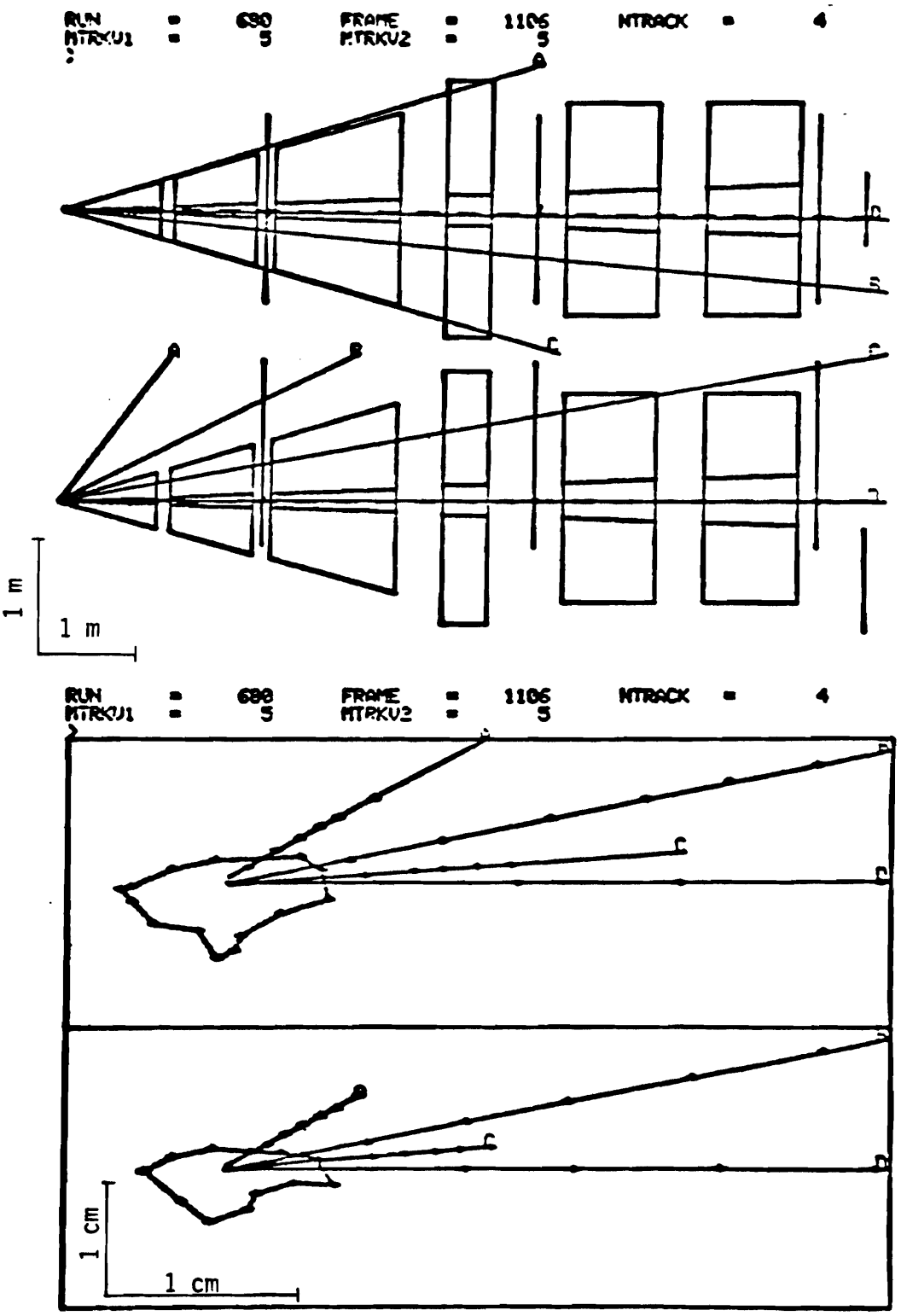

Figure 4-10: Alignment of the streamer chamber and the muon spectrometer (see text)

Chapter 5

THE MISS-DISTANCE ANALYSIS

In chapter 1, equation 1-13, we estimate that in order to clearly observe the charmed particles with a visual detector, the detector should have a resolution of about 40-50 μm or less. At the end of chapter 2, we report that in our streamer chamber pictures, the streamer size is about 50 μm (limited by the resolution of the image intensifiers) and the *full track width* is about 80-90 μm on the film mainly due to the diffusion effect of the primary seed electrons. We also mentioned that this full track width is however not the only limitation on the true two-track resolution of the streamer chamber pictures. In fact, the pictures suffer from the characteristics of the self-luminous streamers such as fluctuations in the brightness of the streamers and the halation problem on the film etc. Empirically we determined that two close tracks are measurable only if they are separated from each other by more than 150 μm. Taking this 150 μm as the true track resolution on the film, the efficiency for visual identification of short lived particles from our streamer chamber pictures will be very small. We therefore developed a different method to extract the charm signal.

One way of finding the charm signal is to look for events with tracks which miss the primary vertex (tracks from the decays of short lived particles). First of all, let us take a look at the first picture of figure 5-1 where we schematically define several event topology parameters, S, L, θ_B and θ_d. The miss-distance, S, is the most sensitive parameter to test

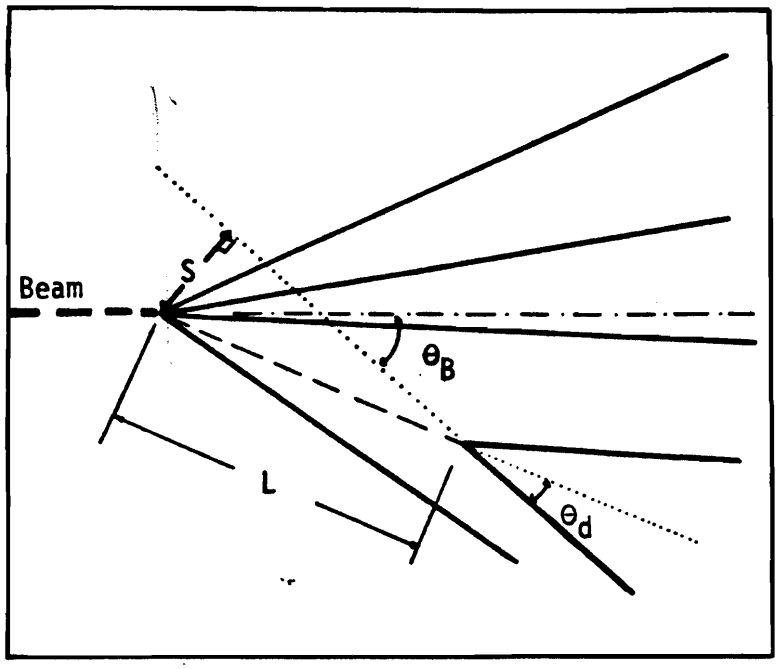

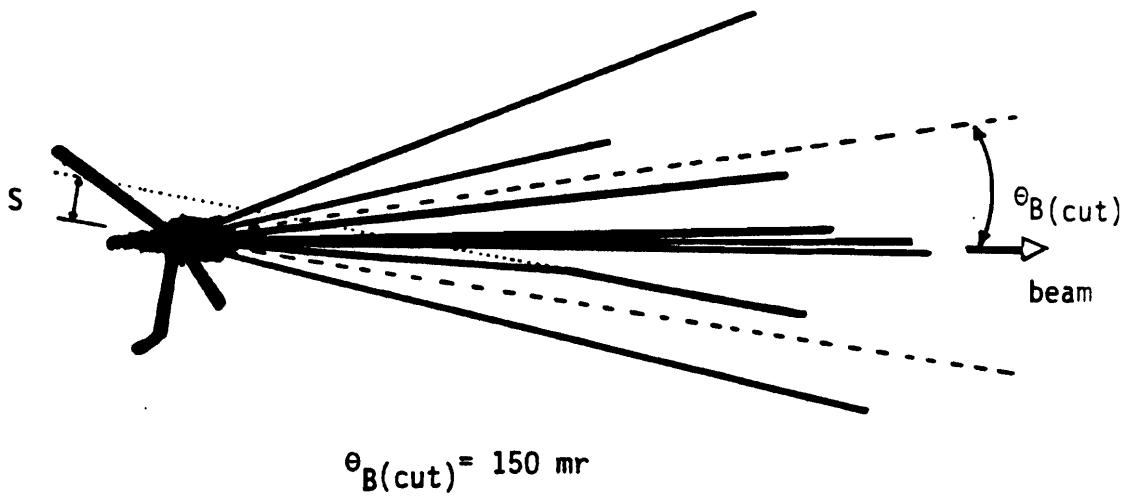

Figure 5-1: Definition of event topology parameters

For the top figure: (a)S - the miss-distance, the distance between a track and the primary vertex. (b)L - decay length. (c)θ_B - the track angle measured w.r.t. the beam direction. (d)θ_d - the angle between the *daughter* track and the *parent* track. All parameters are measured on the streamer chamber pictures.
For the bottom figure: all *visible* non-primary vertex tracks with θ_B greater than 150 mr are considered as the *daughter* tracks from strange particles.

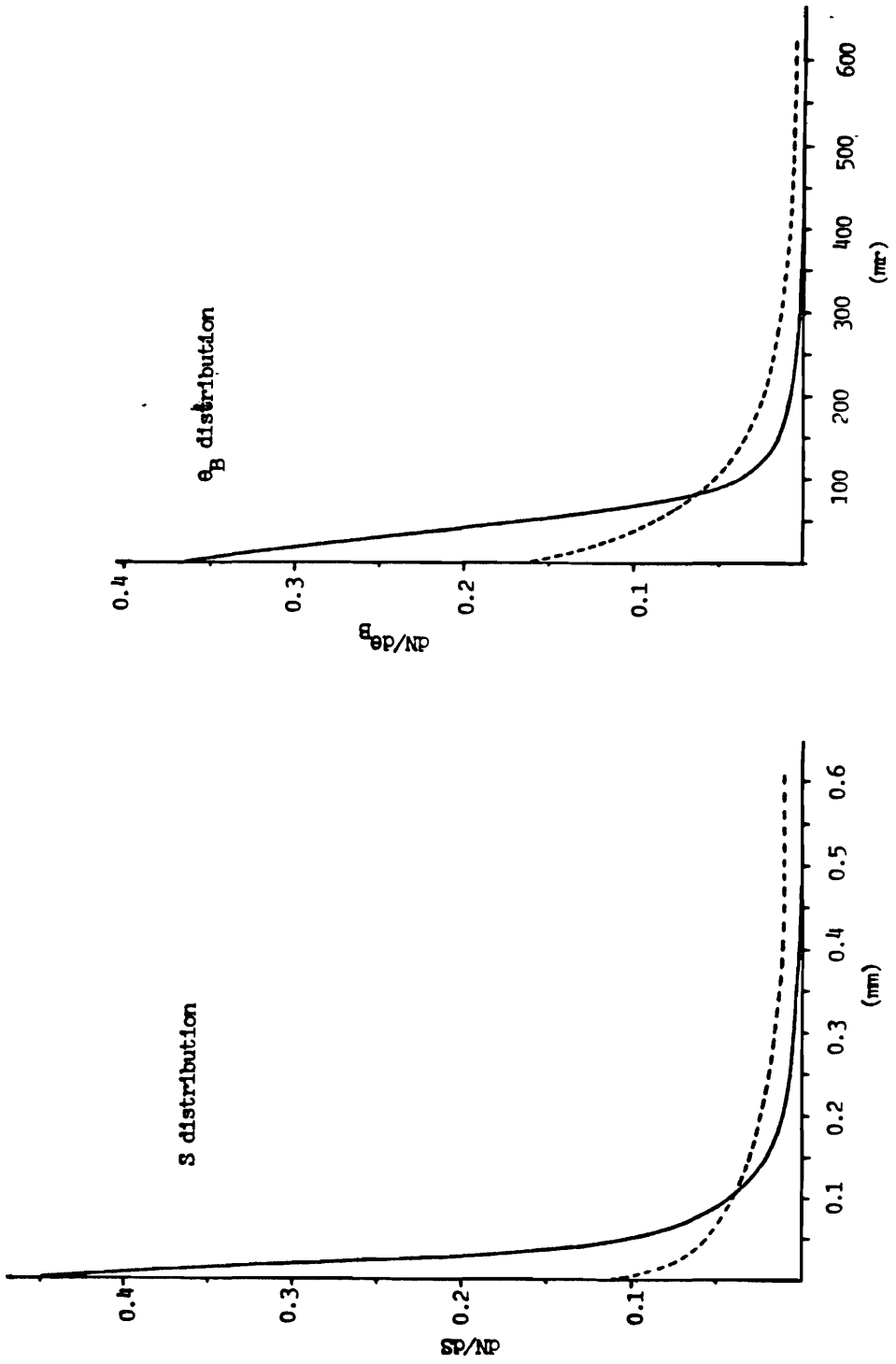

Figure 5-2: S and θ_B distributions

Solid line: from charm monte-carlo. Dashed line: from strange particle monte-carlo. In these plots, we assume that the streamer chamber had a perfect resolution and all charged particle tracks are measurable.

whether or not a track comes from the primary vertex. The sensitivity depends, of course, on the resolution of the streamer tracks. In our case, we found that to tell visually that a track misses the primary vertex, the minimum value for S is about 200 μm on the film[1].

A potentially serious background in this way of defining the charm signal is the decay tracks from strange particles such as K^0_s, Σ^+ etc. To see how we can suppress this strange particle contamination, let us first compare the kinematic characteristics of the charmed particle events and strange particle events. Figure 5-2 shows S and θ_B distributions for tracks from charmed and strange particles generated by a monte-carlo program. The basic algorithm of this monte-carlo will be described in appendix-I. For charmed particle events, figure 5-2 includes the generation of D-$\bar{D}$ pairs with the following distribution for the inclusive production cross section of D particles (see equation 7-1):[2]

$$\frac{d\sigma}{dX_F dP_t^2} = C(1-|X_F|)^{\beta}\exp(-2.5P_t) \quad \text{with } \beta=5 \tag{5-1}$$

From these monte-carlo studies, we have the following probabilities:

$$\theta_B \geq 150 \text{ mr}: \begin{cases} \sim 7\% & \text{for tracks from charmed particles} \\ \sim 45\% & \text{for tracks from strange particles} \end{cases} \tag{5-2}$$

$$S \geq 200\ \mu\text{m}: \begin{cases} \sim 9\% & \text{for tracks from charmed particles} \\ \sim 61\% & \text{for tracks from strange particles} \end{cases} \tag{5-3}$$

and the probability for $S \geq 200\ \mu$m and $\theta_B \geq 150$ mr:

$$\begin{cases} \sim 1\% & \text{for tracks from charmed particles} \\ \sim 34\% & \text{for tracks from strange particles} \end{cases} \tag{5-4}$$

---

[1]All of the values concerning the four topology parameters are referred to the values measured on the film unless otherwise mentioned.

[2]These distributions are not very sensitive to the value of β of equation 5-1 in the range $1 \leq \beta \leq 7$.

If we define a *kinematic cut* such that *all of the visible non-primary vertex tracks with $\theta_B \geq$ 150 mr are considered as the secondary tracks from strange particles* we will at most loose ~1% of charm events and considerably reduce the strange particle background. Conversely, tracks with $\theta_B \geq$ 150 mr are in general not from charm and can be used to define the primary vertex.

Based on these considerations, we set up the ***miss-distance*** analysis for the measured events as follows (see figure 5-1) :

- Remove all of the tracks which visually miss the primary vertex and have $\theta_B \geq$ 150 mr from the measured events. In the case of the **vee** tracks, if one of them has θ_B greater than or equal to 150 mr, remove both tracks from the event.
- Assign all of the measurable nuclear fragments and ordinary tracks with $\theta_B \geq$ 150 mr to the primary vertex.
- Fit the primary vertex.
- Calculate the value S and the error, DS, for tracks with θ_B less than 150 mr.[3]
- Calculate the quantity S/DS.
- Find the largest value of S/DS, from both views, for each event.
- Tag the events with the largest value of S/DS greater than or equal to 3.

From the monte-carlo study[4], we estimate that the probability for a charm event, which satisfies the *topology requirements*[5] of the miss-distance analysis, to have the quantity S/DS greater than 3 is ~ 38% (see table 6-1). On the other hand, the probability for a

---

[3]Note that tracks that visually miss the vertex and are not removed bythe kinematic cut are treated exactly the same as tracks that do not visually miss the vertex.

[4]See appendix-I, the monte-carlo takes the measurement process into account.

[5]At least two measurable tracks with $\theta_B \geq$ 150 mr to make up the primary vertex and at least one measurable track with $\theta_B <$ 150 mr for the S/DS calculation.

single vertex event which satisfies the topology requirements of the miss-distance analysis to have S/DS greater than 3 is $\sim$ 4%. Figure 5-3 illustrates the S/DS distributions of charm events and single vertex events. Also shown in figure 5-3 is the histogram of the quantity S/DS cauculated from 892 interaction trigger (NI·$\overline{CV}$) pictures. The majority of these interaction events were expected to be single vertex events. The monte-carlo distribution for single vertex events adequately reflects the overall shape of the histogram.

In principle, there are three possible causes for a big value of S/DS. They are 1) a real charm event, 2) strange particles and 3) the statistical tail in the distribution of the quantity S/DS. Presumably, only a certain fraction of our muon-trigger events (see section 3.2 and section 4.2) contains charmed particles. If we want to apply this miss-distance analysis to the measured muon-trigger events, we have to estimate the backgrounds due to the strange particles and statistical fluctuations. The best and most unbiased way of doing this is to use the interaction-trigger events.

The off-line muon analysis has already been discussed in chapter 4. The total number of events in the various categories for the purpose of this analysis is also listed in table 4-1. The ***matched-muon*** events included in item 14 of table 4-1 were selected according to the requirement that the reconstructed muon track should have the potential to match with one of the tracks inside the streamer chamber. The match-up criterion is

$$\chi^2 = (\theta_\mu - \theta_t)^2 \,/\, (\delta\theta_\mu{}^2 + \delta\theta_t{}^2) < 4.0$$

where θ_μ and θ_t are the horizontal angles of the muon track and the streamer track respectively. In general, there are three possible classes of events:

Case 1 The muon track matches with one of the measurable tracks in the streamer chamber picture.

Case 2 The muon track falls inside the obscured region of the streamer chamber picture due to a group of tracks which are very close to each other.

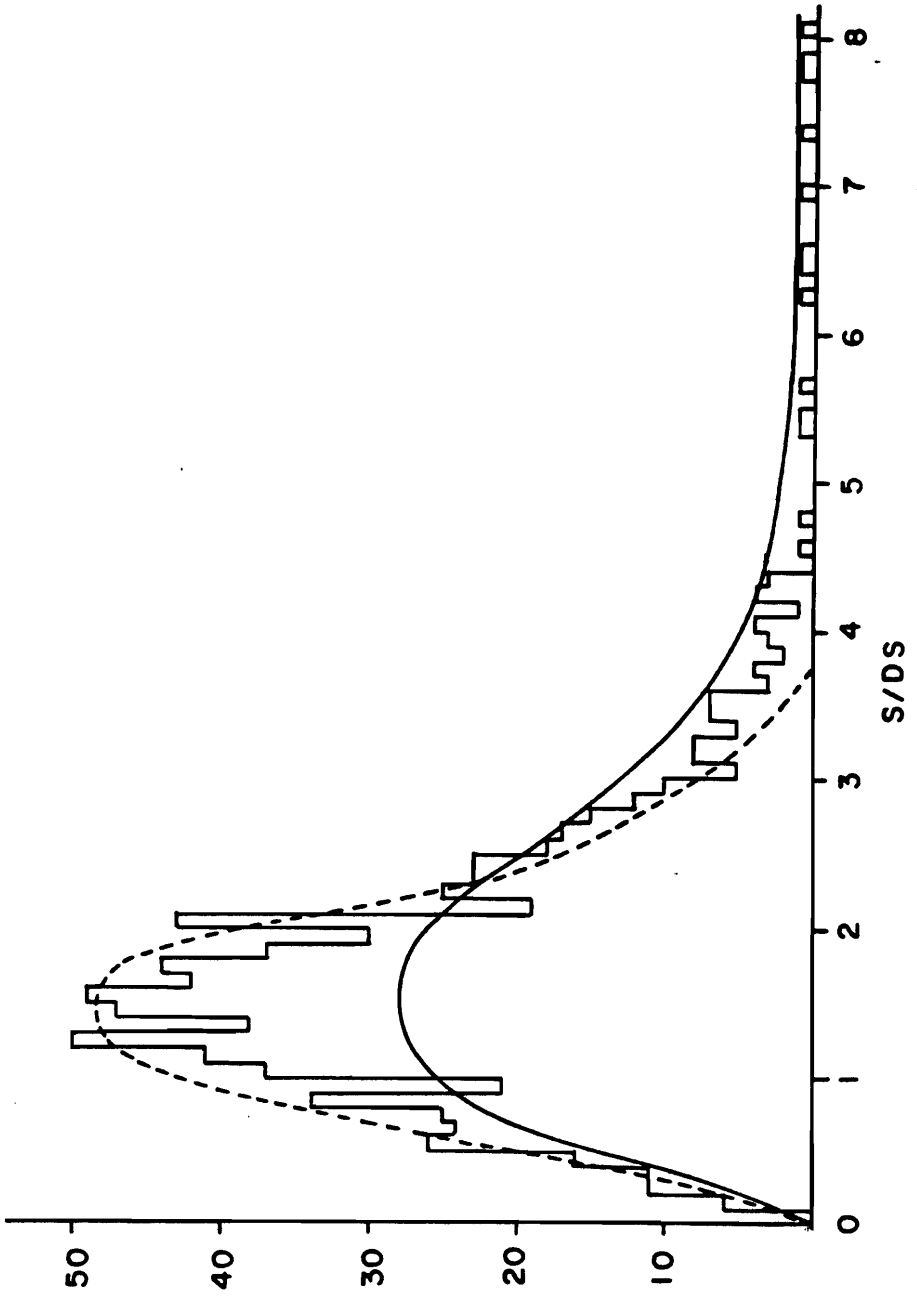

Figure 5-3: S/DS distributions

Solid line : from monte-carlo charm (D-$\bar{D}$) events. Dashed line : from monte-carlo single vertex events. The monte-carlo includes the picture quality simulation and the film measurement process (see appendix-I). The histogram is the S/DS distribution calculated from 892 NI-$\overline{CV}$ pictures.

Case 3 The muon track can not possibly match up with any track inside the streamer chamber.

For events belonging to case 3, the reconstructed muon-tracks are considered as not originating inside the streamer chamber and therefore should not be included in the final analysis for extracting the charm signal.

What we will eventually do is compare the result from the miss-distance analysis for the *best-matched-muon* sample (769 events; item 14 of table 4-1) to the result for the interaction-trigger sample (1612 events; item 12 of table 4-1). However, due to historical reasons, the whole analysis started from the sample of 1492 *better-muon* events (item 15, table 4-1). From this better-muon sample, 831 events satisfied the topology requirements for the miss-distance analysis and 120 events had at least one track with S/DS $\geq$ 3 in either view 1 or view 2. From the interaction-trigger sample, 892 events satisfied the topology requirements and 88 events had at least one track with S/DS $\geq$ 3 in either view 1 or view 2[6]. Events with S/DS $\geq$ 3 were then rescanned twice, by a scanner and a physicist independently. The reason for this rescanning process has already been mentioned in section 4.2. In the first measurement of the streamer chamber pictures, the measurers were instructed to measure whatever was visible and at all measurable on the film. As a result, many events which were not really measurable or did not satisfy all of the measurement rules were included in the first measurement.

During the rescanning process, the following classes of events or tracks were removed from the measurement data:

- Events which are too faint to be measured.
- Events which have too big an obscured region or a dark background due to the discharge inside the streamer chamber in the previous frames.

[6]From now on, for the simplicity of discussion, when we say an event with S/DS $\geq$ 3 we mean that this event has at least one track with S/DS $\geq$ 3 in either view 1 or view 2.

- Charged particle interaction events.

- Events which are really stray tracks due to particles striking the metal frames of the streamer chamber.

- Tracks too close to each other.

- Faint tracks. Usually, faint tracks are associated with faint events. However, there is a small fraction of the tracks that are faint because of small streamer density or possibly due to the fluctuation in the local field inside the chamber.

- Mislabeling of tracks. For example, the nuclear fragments were sometimes mistakenly labeled as ordinary tracks. In this case, we simply corrected the mistakes and kept the tracks.

In the process of rescanning the pictures, events from the muon sample are mixed with events from the interaction-trigger sample to avoid psychological bias. After rescanning, 34 events from the muon sample have the quantity S/DS greater than 3 and 14 events from the interaction-trigger sample have S/DS greater than 3.

One inefficiency factor which should be discussed here is the loss of events due to the picture quality or the event track topology. For an event to be included in the final miss-distance analysis, the event must have at least two *measurable* tracks with θ_B greater than 150 mr and one *measurable* track with θ_B less than 150 mr. Thus the overall probability for an event to be included in this analysis is a combination between the event topology and the picture quality. The topology efficiency was estimated with the ratio of the 831 events, which satisfy the topology requirements, to the original 1492 better-muon events. That is

$$\mathcal{E}_{\text{topology}} = \frac{831}{1492} = 0.56 \pm 0.02 \tag{5-5}$$

To estimate the picture quality efficiency, 184 events were randomly selected from the *better-muon* sample and rescanned. After rescanning, there were 148 events which

still satisfy the topology requirements of the miss-distance analysis. Hence the overall picture efficiency can be estimated as

$$\mathcal{E}_{pix} = \mathcal{E}_{topology} \times \mathcal{E}_{picture\ quality}$$

or

$$\mathcal{E}_{pix} = (0.56 \pm 0.02)\,(148/184) = 0.45 \pm 0.04 \qquad (5\text{-}6)$$

Here the symbol $\mathcal{E}_{pix}$ represents the ***probability for an event to be included in the miss-distance analysis.***

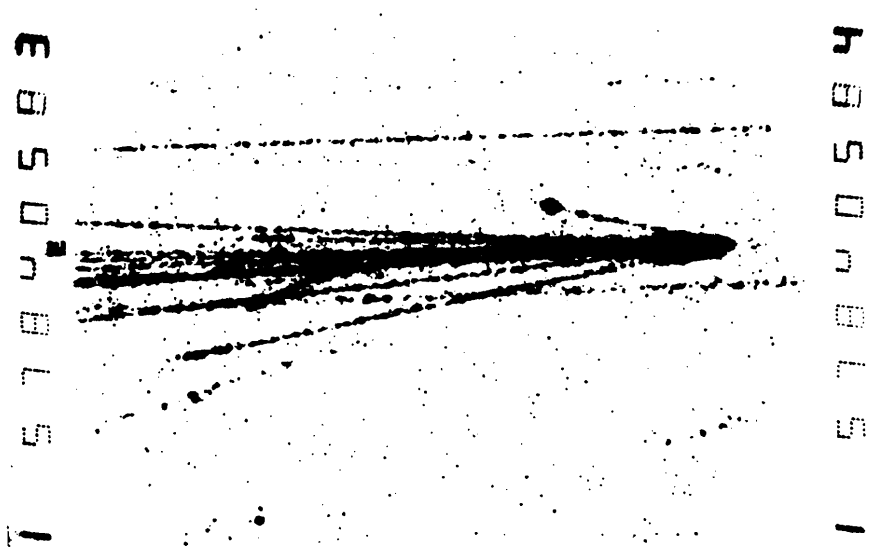

Figure 5-4: An event picked up by the miss-distance analysis

An interesting point for this analysis method is that events like the one shown in figure 5-4, which was picked up by the miss-distance calculation, could very likely be missed if the event-selection depends completely on the visual scanning of the pictures. Examining figure 5-4 carefully (by viewing the picture at a shallow angle with respect to the surface of the paper), one will find that track-E misses the primary vertex (S = 400μ and S/DS = 5.39). This example shows that although the miss-distance method sacrifices a lot of events (because of the topology requirements), the method is however free from scanning losses which occur in the traditional analysis procedures for bubble

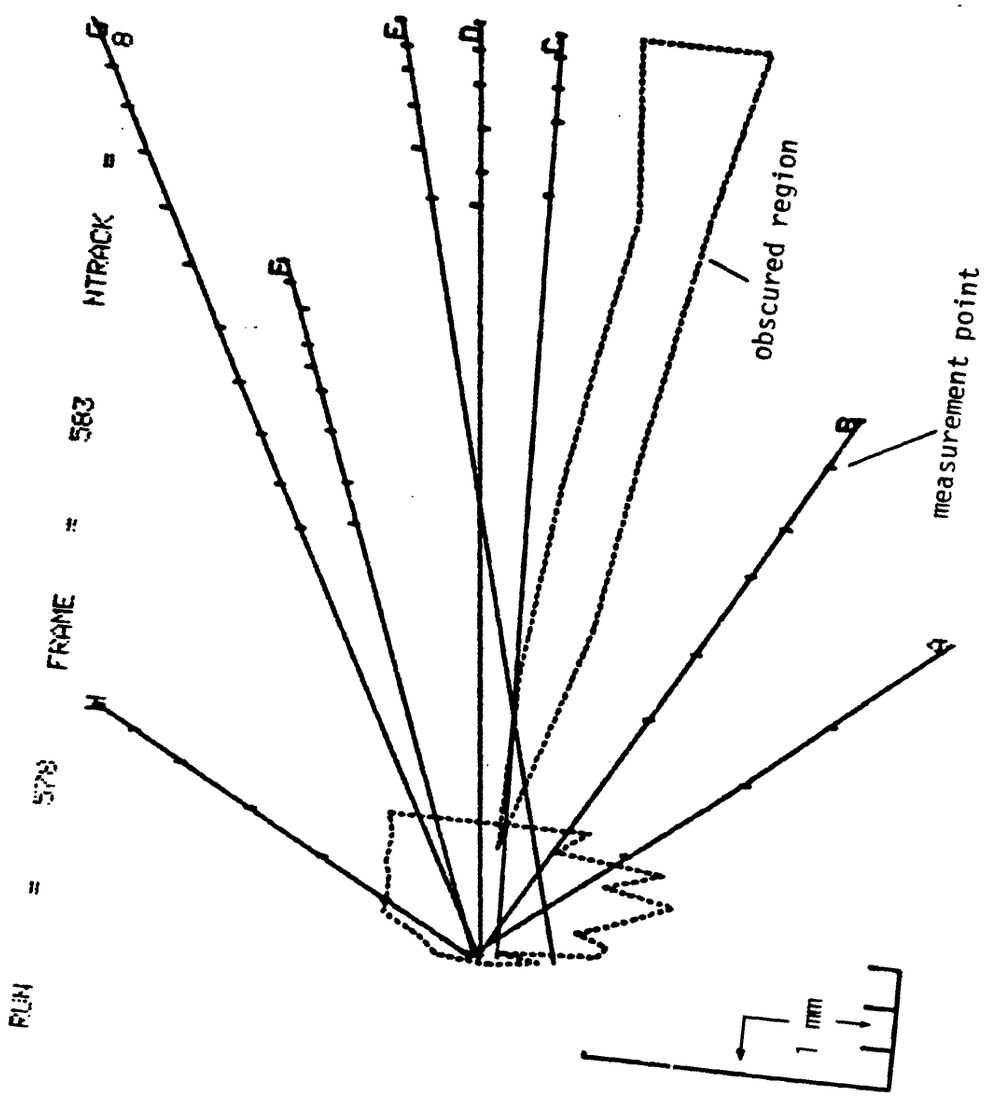

Figure 5-5: Graphic display of the measurement output for the event in figure 5-4

chamber experiments. Figure 5-5 shows the measurement points, the point measurement error bars and the fitted line for this event. Track A and track H are both with $\theta_B \geq 150$ mr and are therefore assigned to the primary vertex.

So far, the miss-distance calculation is applied to the sample of better-muon events and a comparable sample of interaction-trigger events. We now apply more stringent muon selection requirements, the ***best-muon*** criterion, and the ***matched-best-muon*** criterion (see section 4.1, and table 4-1 for details). With tighter muon selection criteria, we expect to remove more background events but still keep most of the *real* muon events from charm decay. Table 5-1 summarize this clean-up process. Let us now concentrate on the *matched-best-muon* sample and the *interaction-trigger* sample. From the *interaction-trigger* sample, there are 892 events included in the miss-distance analysis and 14 events have S/DS greater than 3 after the rescanning procedures. From the *matched-best-muon* sample, there are only 362 events included in the miss-distance analysis and 23 events, after rescanning, have S/DS greater than 3. Therefore the expected number of background events which have S/DS greater than or equal to 3 can estimated as

$$14 \times (362/892) = 5.68 \text{ events} \tag{5-7}$$

Figure 5-6 shows the histograms of the quantity S/DS from both the 23 muon events and the 5.68 normalized background events. By subtracting these two numbers directly, the charm signal is estimated as

$$23 - 5.68 = 17.32 \pm 4.73 \text{ events} \tag{5-8}$$

Before concluding this chapter, let me point out an interesting (self-consistent) check between the data and the monte-carlo predictions. From the monte-carlo study, the possibility for a detected charm event (i.e. at least one track with S/DS $\geq$ 3) to have two tracks with S/DS $\geq$ 3 is about 19%. The possibility to have three tracks with S/DS $\geq$ 3 is about 6%. These probabilities imply that out of the 23 detected events in our data (17.32 events are charm events), we should expect to have 3 events with two tracks

having S/DS $\geq$ 3 and 1 event with three tracks having S/DS $\geq$ 3. In our data, within these 23 events, 2 events have two tracks with S/DS greater than 3 and 1 event has three tracks with S/DS greater than 3. Even though the statistics are low, the results are however consistent with the monte-carlo predictions.

Samples	Total number of events	Number of events included in the miss-distance analysis	Nmuber of events with S/DS ≥ 3	Number of events with S/DS ≥ 3 (after rescanning)
Better muon	1492	831	120	34
"Matched" Best muon events	640	362	66	23
Interaction-trigger events	1612	892	88	14

Table 5-1: Summary of the miss-distance analysis

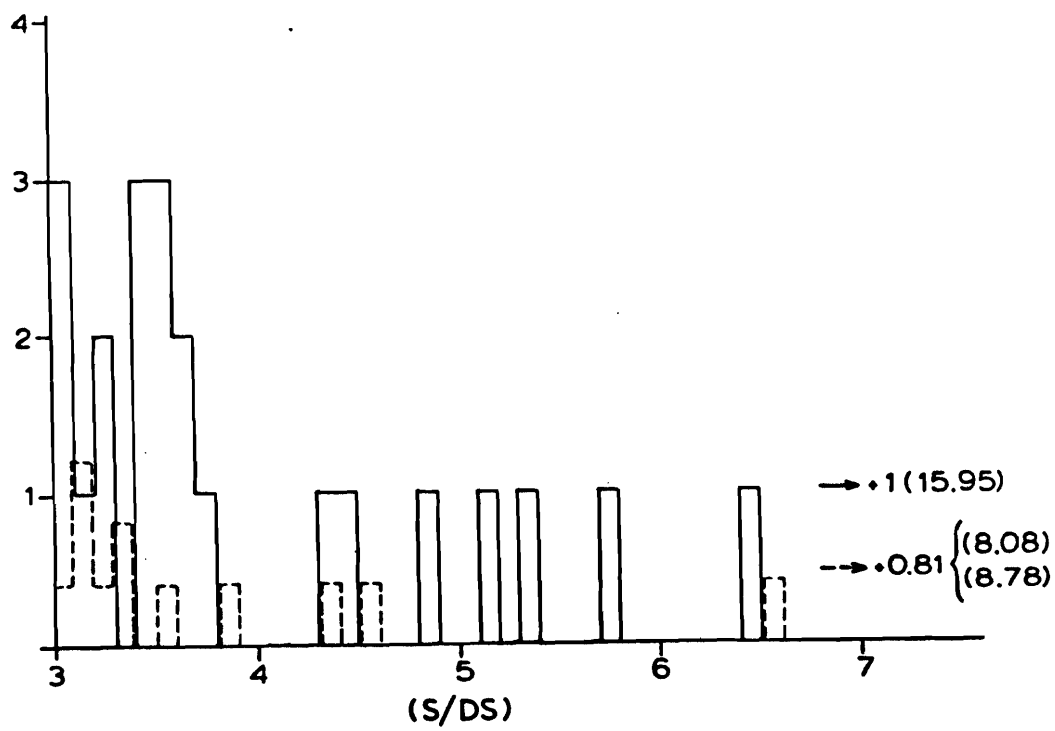

Figure 5-6: Histogram of S/DS for events with S/DS ≥ 3

Solid line: from the *matched-best-muon* sample. Dashed line: from the normalzed *interaction-trigger* sample.

Chapter 6

RESULTS AND DISCUSSIONS

6.1 CALCULATION OF THE CHARM PRODUCTION CROSS SECTION

First of all let me introduce the following symbols which will be used as either superscripts or subscripts to indicate certain categories of quantities when we calculate the charm production cross section.

p: Primordial production. In our experiment, this symbol corresponds to the number of ***ungated trigger*** events.

t: The ***gated trigger*** events[1]. By *trigger*, we mean either muon-trigger or interaction-trigger. Also note that a streamer chamber picture was taken with every ***gated*** trigger in our experiment.

mf: Measurable fiducial interaction events. For example, the miss-distance analysis includes only measurable fiducial interaction events.

c: Charm production events.

[1]See section 3.2 for the definitions of gated triggers and ungated triggers.

μ: Muon-trigger (NI·$\overline{\text{CV}}$·MU), gated or ungated.

int: Interaction-trigger (NI·$\overline{\text{CV}}$), gated or ungated.

det: Detected events. That is the number of events detected as the signature of charm production events according to the S/DS analysis (chapter 5).

G/UG: Quantities associated with *gated* or *ungated* triggers such as the gated muon triggers, ungated interaction triggers etc. See the last paragraph of section 3.2 for examples.

There are two basic assumptions implicitly included in the calculation of the ratio of the hadronic charm production cross section to the hadronic inelastic interaction cross section:

Assumptions

1. As is mentioned in the measurement rules of section 4.2, the miss-distance analysis includes only measurable fiducial interactions events. We assume that the fiducial and measurable requirements do not distinguish between charm production events and ordinary inelastic interaction events. In fact, this assumption is consistent with the ratios between item 7, 10 and item 9, 12 of table 4-1 (section 4.2).

2. We also assume that the loss of the events due to the existence of the cone-shaped veto counter inside the hadron filter and the second toroid is the same for both the charm production events and the ordinary inelastic interaction events.

Now as a first step to calculate the ratio of the hadronic charm production cross section to the hadronic inelastic interaction cross section, let us suppose our experiment was capable of identifying all of the primordial charm production events and all of the ordinary hadronic inelastic interaction events. In this case, the ratio of the production cross sections would be

$$\frac{\sigma_c}{\sigma_{int}} = N_c^p \,/\, N_{int}^p \tag{6-1}$$

where N_c^p is the total number of charm events produced and N_{int}^p is total number of inelastic interaction events[2]. If we further suppose that we took pictures for all of these primordial production interactions, from the first assumption above, we have

$$\frac{\sigma_c}{\sigma_{int}} = N_c^{p,mf} / N_{int}^{p,mf} \tag{6-2}$$

In our experiment, we did not collect all of the primordial charm events (nor did we take pictures for every interaction). Instead, we collected a fraction of $N_{c,\mu}^p$ charm events which satisfy the muon-trigger requirement. Let us define $\mathcal{E}_\mu^c$ as the *probability for a charm event to satisfy the muon-selection requirements* (including the on-line muon-trigger and the off-line muon clean-up processes), then

$$N_{c,\mu}^p = N_c^p \cdot \mathcal{E}_\mu^c$$

or

$$N_{c,\mu}^{p,mf} = N_c^{p,mf} \cdot \mathcal{E}_\mu^c \tag{6-3}$$

and

$$\frac{\sigma_c}{\sigma_{int}} = N_{c,\mu}^{p,mf} / (N_{int}^{p,mf} \cdot \mathcal{E}_\mu^c) \tag{6-4}$$

So far, we always use the primordial production numbers (the superscript p) which correspond to the *ungated* scalars in our experiment. However, the charm signal can only be established through the *gated* muon-trigger events since the streamer chamber was triggered on the gated triggers only. Statistically, the values of $N_{c,\mu}^{p,mf}$ and $N_{int}^{p,mf}$ can be expressed as

[2]Since both N_{int}^p and N_c^p are accumulated in the same experiment over the same period of time, the factors concerning the beam flux and the target density can be neglected here.

$$N^{p,mf}_{c,\mu} = N^{t,mf}_{c,\mu} \, [\, (N^{scalar}_{\mu})_{UG} \, / \, (N^{scalar}_{\mu})_{G} \,] \tag{6-5}$$

$$N^{p,mf}_{int} = N^{t,mf}_{int} \, [\, (N^{scalar}_{int})_{UG} \, / \, (N^{scalar}_{int})_{G} \,] \, [\, (N^{scalar}_{int})_{G} \, / \, N^{t,scan}_{int} \,]$$

or

$$N^{p,mf}_{int} = N^{t,mf}_{int} \, [\, (N^{scalar}_{int})_{UG} \, / \, N^{t,scan}_{int} \,] \tag{6-6}$$

where $(N^{scalar}_{\mu})_{UG}$ and $(N^{scalar}_{\mu})_{G}$ are the total numbers of ungated muon-trigger events and gated muon-trigger events respectively. Obviously, $(N^{scalar}_{\mu})_{G}$ is a sub-sample of $(N^{scalar}_{\mu})_{UG}$ and only events in this sub-sample are associated with the streamer chamber pictures. $N^{t,mf}_{c,\mu}$ is the total number of *measurable charm events* satisfying the on-line muon trigger requirements. This number will be obtained from the results of the miss-distance analysis. $(N^{scalar}_{int})_{UG}$ corresponds to the total number of interaction-trigger events. $N^{t,scan}_{int}$ is the number of interaction-trigger events included in the measurement list. $N^{t,mf}_{int}$ is the number of fiducial and measurable events from the sample of $N^{t,scan}_{int}$. The ratio of $N^{t,mf}_{int}$ to $N^{t,scan}_{int}$ is simply the effect of the *measurable and fiducial requirements* of the first assumption mentioned above.

Now, let us apply the miss-distance analysis to a sample of $N^{t,mf}_{\mu}$ muon-trigger events and a comparable sample of $N^{t,mf}_{int}$ interaction-trigger events. Let us also assume that there are $N^{t,mf}_{c,\mu}$ *charm events* in the $N^{t,mf}_{\mu}$ muon-trigger sample[3]. As we have already discussed in the previous chapter, only a portion of the $N^{t,mf}_{c,\mu}$ events will be included in the calculation of the quantity S/DS due to the picture quality requirement and event topology requirement (this fraction is represented by the symbol $\mathcal{E}_{pix}$ in equation 5-6). As a result of the miss-distance analysis, there is a certain probability for a charm-event to contribute to an entry with S/DS greater than 3.0. Let us call this probability $\mathcal{E}_{D}$ and the

[3]The sequential logic is: Within $(N^{scalar}_{\mu})_{G}$ events, $N^{t,mf}_{\mu}$ are measurable. Within this $N^{t,mf}_{\mu}$ events, there are, presumably, $N^{t,mf}_{c,\mu}$ charm events. The value of $N^{t,mf}_{c,\mu}$ is what we are eventually interested at.

total number of detected charm-events N_c^{det}, we then have

$$N_c^{det} = N_{c,\mu}^{t,mf} \cdot \mathcal{E}_{pix} \cdot \mathcal{E}_D \tag{6-7}$$

and equation 6-5 can be rewritten as

$$N_{c,\mu}^{p,mf} = [\,(N_\mu^{scalar})_{UG} \,/\, (N_\mu^{scalar})_G\,]\,[\,N_c^{det} \,/\, \mathcal{E}_D \cdot \mathcal{E}_{pix}\,] \tag{6-8}$$

We can now put equations 6-4, 6-6 and 6-8 together. The ratio of the cross sections can be calcualted as:

$$\frac{\sigma_c}{\sigma_{int}} = N_c^{det}\{\,[(N_\mu^{scalar})_{UG}\, N_{int}^{t,scan}] \,/\, [(N_{int}^{scalar})_{UG}\, (N_\mu^{scalar})_G\, N_{int}^{t,mf}\, \mathcal{E}_{total}]\,\} \tag{6-9}$$

where $\mathcal{E}_{total} = \mathcal{E}_\mu^c \cdot \mathcal{E}_D \cdot \mathcal{E}_{pix}$ (6-10)

Some of the quantities in equation 6-9 are included in table 4-1, they are

$(N_\mu^{scalar})_{UG} = 221277$

$(N_{int}^{scalar})_{UG} = 447798691$

$N_{int}^{t,scan} = 18460$

$(N_\mu^{scalar})_G = 116073$

$N_{int}^{t,mf} = 1612$

Thus let us rewrite equation 6-9 as

$$\frac{\sigma_c}{\sigma_{int}} = N_c^{det}\,\frac{4.88\text{x}10^{-8}}{\mathcal{E}_{total}} \tag{6-11}$$

The quantity $\mathcal{E}_{total}$ is the multiplication of three efficiencies, $\mathcal{E}^c_\mu$, $\mathcal{E}_D$ and $\mathcal{E}_{pix}$. The value of $\mathcal{E}_{pix}$ has been estimated in chapter 5 (equation 5-6) as

$$\mathcal{E}_{pix} = 0.45 \pm 0.04 \tag{6-12}$$

$\mathcal{E}_D$, the detection efficiency, is the *probability for a charm event, which satisfies the topology criterion for the S/DS analysis method, to have at least one track with S/DS greater than* 3. This efficiency is estimated with a monte-carlo program (appendix-I) and its value depends basically on the lifetimes of the charmed particles. Table 6-1 lists the values of $\mathcal{E}_D$ versus various different charmed particle production models.

The charm muon-trigger efficiency, $\mathcal{E}^c_\mu$, has been defined in equation 6-3. This efficiency is a combination of the on-line charm-trigger efficiency, $\mathcal{E}_{trig}$, and the off-line muon selection efficiency, $\mathcal{E}_{pwc} \cdot \mathcal{E}_{software}$. Hence

$$\mathcal{E}^c_\mu = \mathcal{E}_{trig} \cdot \mathcal{E}_{pwc} \cdot \mathcal{E}_{software} \tag{6-13}$$

where $\mathcal{E}_{software}$ is the software efficiency for the muon-selection program to detect a muon from the semileptonic decay of the charmed particle. This number is estimated, from the monte-carlo study, as

$$\mathcal{E}_{software} = 0.89 \pm 0.03 \tag{6-14}$$

$\mathcal{E}_{pwc}$ is the overall efficiency for the three PWC's to detect a muon which traverses the muon spectrometer. This number has been estimated as (the combined efficiency for the three PWC's [78])

$$\mathcal{E}_{pwc} = 0.74 \pm 0.04 \tag{6-15}$$

The on-line trigger efficiency, $\mathcal{E}_{trig}$, for a charm event is also estimated with the monte-carlo program of appendix-I. This efficiency represents the *probability for a charm-anticharm pair to satisfy the muon-trigger requirements described in section* 3.2. Again, $\mathcal{E}_{trig}$ depends on the production model and the semileptonic branching ratios of the

charmed particles. Table 6-1 shows the values of $\mathcal{E}_{trig}$ versus various production models.

Let us subsititute the values of $\mathcal{E}_{pix}$, $\mathcal{E}_{pwc}$ and $\mathcal{E}_{software}$ into equation 6-11, the ratio of the cross sections is

$$\frac{\sigma_c}{\sigma_{int}} = N_c^{det} \frac{(1.65 \pm 0.18) \times 10^{-7}}{\mathcal{E}_{trig} \cdot \mathcal{E}_D} \tag{6-16}$$

where the error represents the overall systematic error introduced in estimating the various efficiencies.

In the last chapter, as a result of the miss-distance analysis, we stated that there are 23 events with S/DS > 3.0 (indicating charm production signal) from the *matched-best-muon* sample. Presumably, these 23 events include real charm events and background events due to statistical fluctuation and strange particle contamination. The number of background events is estimated (equation 5-7) as 5.68 events from the normalized interaction-trigger sample. Therefore by subtracting these two numbers directly, we have

$$N_c^{det} = 17.32 \pm 4.73 \text{ events} \tag{6-17}$$

Table 6-1 lists the values of σ_c/σ_{int} (the ratio of the nucleon-nucleus charm production cross section to the nucleon-nucleus inelastic interaction cross section) versus various production models. Also listed in this table are the absolute values of the nucleon-nucleon charm cross section, σ_c, calculated with either A^1 or $A^{2/3}$ dependence for the production cross section. The value of nucleon-nucleon inelastic interaction cross section for this calculation is taken as 32 mb. The charmed particle production models used in this table follow the distribution [11, 15, 20] (see Appendix-I, equation 7-1)

$$\frac{d\sigma}{dX_F dP_t^2} = C(1-|X_F|)^{\beta} \exp(-\alpha P_t) \tag{6-18}$$

(with $\alpha = 2.5$)

with each charmed particle produced independently. The value of β is taken as a variable of the production model. The parameter α is fixed to 2.5 since the P_t distribution has been measured by several different experiments and the results are consistent with the distribution $\exp(-2.5P_t)$ (see, for example, reference [11, 14, 74]).[4]

For the semileptonic branching ratios of the charmed particles, we use the relationships (see Eq. 1-6, Eq. 1-7 and reference [38])

$$r(D^+)/r(D^0) = BR(D^+)/BR(D^0) = 2.1$$

and $[BR(D^+)+BR(D^0)]/2 = 8\%$

hence

$$BR(D^+ \rightarrow \mu) = 11\% \tag{6-19}$$

$$BR(D^0 \rightarrow \mu) = 5\% \tag{6-20}$$

and [18]

$$BR(\Lambda_c^+ \rightarrow \mu) = 5\% \tag{6-21}$$

The trigger efficienfy, $\mathcal{E}_{trig}$, of table 6-1 was calculated according to the weighted sum of the monte-carlo estimations for two different magnetic field polarities in the toroids. During the experiment, the magnetic field polarity of the toroids was frequently reversed. One polarity focused positive charged particles and the other one focused negative charged particles. In either one of the toroid polarities, the trigger efficiency for the positive muons was expected to be different from the trigger efficiency for the negative muons. For example, if the toroids were set to focus positive charged particles, positive muons would have a higher possibility than negative muons to curve into the central holes of the toroids and thus to fail the muon-trigger requirements.[5] The total number of

---

[4]Some groups fit the P_t distribution to a form like $\exp(-1.1P_t^2)$. From the monte-carlo study, our trigger efficiency is not sensitive to which distribution form are used. The trigger efficiency is also not very sensitive to the exact value of α within the range between 2.25 and 2.5.

[5]Most of the tracks from the charm decay were confined in a small angular region with respect to the beam direction (see figure 5-2).

ungated interaction triggers included in this analysis was 447798691 (item 2 of table 4-1). Within this amount, 241403041 triggers were taken with the toroids set to focus positive charged particles and 206395650 triggers were taken with the toroids set to focus negative charged particles. Therefore, in calculating the overall trigger efficiency, we included the weight factors of 0.54 and 0.46 for positive focusing toroid polarity and negative focusing toroid polarity respectively.

Generally speaking, for production mechanisms with the same distribution for the charmed and anticharmed particles (such as the D-$\bar{D}$ production with the same β value), the difference in the toroid polarty should not affect the overall trigger efficiency. For production models such as the Λ_c^+-$\bar{D}$ production, the event trigger efficiency depends on the toroid polarty if the β value of the charmed particle is different from the β value of the anti-charmed particle. For production models with small value of β (such as $\beta \sim 1$), most of the charmed particles are produced in the forward and backward direction (i.e. high $|X_F|$ value) in the center of mass system. Muons from the forward produced charmed particles were likely to fall into the central holes of the hadron filter and would be rejected by our muon-trigger requirements. Muons from the backward produced charmed particles were likely to be stoped inside the hadron filter because of low energy. Therefore, the smaller the β value, the smaller the trigger efficiency.

The values of the cross section listed in table 6-1 are calculated according to the various assumptions the charm production mechanism. The first error for all of the values in this table is the statistical error and the second one is the systematic error which comes from the uncertainties in estimating the efficiencies for equation 6-9. The values of $\sigma_c(A^{2/3})$ were calculated directly from the ratios of the cross sections $\frac{\sigma_c}{\sigma_{int}}$ (with $\sigma_{int} = 32$ mb). Since the gas inside the streamer chamber was Ne(90%)+He(10%), the A value was approximately equal to 19. The relationship between the nucleon-nucleon cross sections calculated according to A^1 and $A^{2/3}$ dependence assumptions can be expressed as

$$\sigma_c(A^1) = 0.38\ \sigma_c(A^{2/3}) \tag{6-22}$$

It should be noted that the systematic errors in table 6-1 do not include the errors due to the uncertainties of the charmed particle lifetimes and the semileptonic branching ratios. Generally speaking, the detection efficiency, $\mathcal{E}_D$, depends linearly on the average lifetime of the charmed particles. The trigger efficiency, $\mathcal{E}_{trig}$, depends linearly on the average semileptonic branching ratio of the charmed particles. The average lifetime and branching ratio used in table 6-1 are (see equations 1-6 to 1-9 and equations 6-19 to 6-21)

$$<\text{D lifetime}>_{av} = 6.1 \times 10^{-13} \text{ sec.}$$

$$<\text{D branching ratio}>_{av} = 8\%$$

If different average lifetime or average branching ratio should be used, the corresponding value of the cross section can be calculated by using equation 6-16, equation 6-17 and equation 6-22.

Charm pair	β	$\mathcal{E}_{trig}$	$\mathcal{E}_D$	σ_c/σ_{int} ($\times 10^{-4}$)	σ_c (A^1) (μb)	σ_c ($A^{2/3}$) (μb)
D	1	0.0089 ± 0.0005	0.4013 ± 0.0174	$8.00 \pm 2.19 \pm 1.04$	$9.75 \pm 2.66 \pm 1.27$	$25.67 \pm 7.01 \pm 3.34$
$\bar{D}$	1					
D	2	0.0112 ± 0.0005	0.3972 ± 0.0173	$6.42 \pm 1.75 \pm 0.81$	$7.81 \pm 2.13 \pm 0.98$	$20.56 \pm 5.61 \pm 2.58$
$\bar{D}$	2					
D	3	0.0136 ± 0.0005	0.3893 ± 0.0175	$5.40 \pm 1.47 \pm 0.67$	$6.56 \pm 1.79 \pm 0.81$	$17.27 \pm 4.72 \pm 2.13$
$\bar{D}$	3					
D	5	0.0163 ± 0.0005	0.3836 ± 0.0178	$4.57 \pm 1.25 \pm 0.56$	$5.56 \pm 1.52 \pm 0.68$	$14.63 \pm 3.99 \pm 1.79$
$\bar{D}$	5					
D	7	0.0184 ± 0.0005	0.3887 ± 0.0178	$4.00 \pm 1.09 \pm 0.49$	$4.86 \pm 1.33 \pm 0.59$	$12.79 \pm 3.49 \pm 1.55$
$\bar{D}$	7					
D	5	0.0149 ± 0.0005	0.3977 ± 0.0180	$4.82 \pm 1.32 \pm 0.59$	$5.86 \pm 1.60 \pm 0.72$	$15.43 \pm 4.21 \pm 1.89$
$\bar{D}$	3					
D	7	0.0136 ± 0.0005	0.3834 ± 0.0178	$5.48 \pm 1.50 \pm 0.68$	$6.66 \pm 1.82 \pm 0.83$	$17.54 \pm 4.79 \pm 2.18$
$\bar{D}$	1					
Λ_c	1	0.0094 ± 0.0005	0.2452 ± 0.0179	$12.40 \pm 3.39 \pm 1.76$	$15.08 \pm 4.12 \pm 2.14$	$39.68 \pm 10.84 \pm 5.62$
$\bar{D}$	3					
Λ_c	1	0.0102 ± 0.0005	0.3000 ± 0.0176	$9.34 \pm 2.55 \pm 1.24$	$11.36 \pm 3.10 \pm 1.51$	$29.89 \pm 8.16 \pm 3.98$

Table 6-1: Estimation of charm production cross sections versus various production models

For example, the first row in this table lists the values of $\mathcal{E}_{trig}$, $\mathcal{E}_D$, σ_c/σ_{int} and σ_c if all of the charm and anticharm quarks hadronized into D or $\bar{D}$ particles and both the D and $\bar{D}$ were produced with the same distribution $(1-|X_F|)^1$.

6.2 DISCUSSIONS AND CONCLUSIONS

Table 6-1 lists the ratios of the hadronic charm production cross section to the hadronic inelastic interaction cross section and the absolute values of the nucleon-nucleon charm production cross section. These values were calculated according to the various different production models. Since we did not have a fixed energy incident neutron beam and since the muon spectrometer was not capable of identifying hadrons such as pions and kaons etc., we can not measure directly the X_F dependence for the produced charmed particles in this experiment[6].

It is interesting to note that the cross sections calculated with the Λ_c^+-$\bar{D}$ production models are obviously larger than the results based on the the D-$\bar{D}$ production models. The reasons are partially because of the low trigger efficiency for muons from the Λ_c^+-$\bar{D}$ events (since these models use flatter X_F distributions for the production cross section; as discussed in the previous section) and partially because of the low detection efficiency due to the short life time of the Λ_c^+. In this experiment, we tried to compare the relative importance between the D-$\bar{D}$ production models and the Λ_c^+-$\bar{D}$ production models according the following probability analysis.

Within the 23 charm signal events, some of them were taken with the toroids set to positive charged particle focusing mode and some of them were taken with the opposite toroid mode. (The two toroid polarities are discussed in the previous section.) If we classify these event acording to the signs of the muons and the polarities of the toroids, we get:

$$n_1 \equiv n^{++} = 11 \tag{6-23}$$
$= $ Number of positive muon events detected with positive focusing toroids.

$$n_2 \equiv n^{-+} = 3 \tag{6-24}$$
$= $ Number of negative muon events detected with positive focusing toroids.

---

[6]We tried to use the distribution of the muon pseudo-rapidity as a means of distinguishing between models with different X_F dependence. However, this method failed because the statistics of the data is not high enough for us to make sensitive comparisons.

$$n_3 \equiv n^{+-} = 5 \tag{6-25}$$
= Number of positive muon events detected with negative focusing toroids.

$$n_4 \equiv n^{--} = 4 \tag{6-26}$$
= Number of negative muon events detected with negative focusing toroids.

and

$$N = n_1 + n_2 + n_3 + n_4 = 23 \tag{6-27}$$

Now suppose we know the probabilities for an event to be in n_1, n_2, n_3 or n_4, we can calculate the probability, P_0, for us to observe the event distribution as described in equation 6-23 to equation 6-26. Suppose we repeat the experiment many times, the value of N in equation 6-27 is expected to follow a Poisson distribution with mean value ν=23.

The problem is actually a combination between the multinomial distribution and the Poisson distribution:

Define

R_1 = Probability for an event to be in the n_1 category.

R_2 = Probability for an event to be in the n_2 category.

R_3 = Probability for an event to be in the n_3 category.

R_4 = Probability for an event to be in the n_4 category.

(These probabilities will be estimated from the monte-carlo study)

Then the probability P of having n_1, n_2, n_3 and n_4 can be calcualted as (see reference [78] for detailed discussion)

$$P = \prod_{i=1}^{4} \frac{1}{n_i!}(\nu R_i)^{n_i}\exp(-\nu R_i) \tag{6-28}$$

Define

$P_0 = P(n_1=11,\ n_2=3,\ n_3=5,\ n_4=4 \text{ and } \nu=23)$

The probability, P_{sum}, to observe a set of $\{n_i\}$ values which has the P value less than or equal to P_0 can be calculated by summing equation 6-28 through all of the possible values of N with all of the possible combinations of n_i's (with the condition $P \leq P_0$). A detailed

discussion of the calculation of P_0, P_{sum} and the estimation of the R_i values will be given in reference [78]. The results are summarized in table 6-2. As can be seen from this table, the values of P_{sum} for the Λ_c^+-$\bar{D}$ production models are much smaller than the values for D-$\bar{D}$ production models. The reason can be explained as follows.

As suggested by Halzen in reference [15], for the Λ_c^+-$\bar{D}$ production models, since the Λ_c^+ contains two valence quarks and the $\bar{D}$ contains only one, the production distribution for Λ_c^+ is expected to be flatter[7] than the distribution for $\bar{D}$. In this case, the positive muon from the decay of the forward produced Λ_c^+ would have higher probability than the negative muon from the $\bar{D}$ to fall into the certral hole of the muon spectrometer. On the other hand we would also have a higher probability to get a low energy (less than 6 Gev) positive muon from the backward produced Λ_c^+ than the low energy negative muon from the backward produced $\bar{D}$. Our apparatus would therefore have a higher probability to be triggered by the negative muons. This difference in the positive and negative muon trigger efficiency would be even enhanced when the toroids were set to focus positive muons. Therefore we should have detected more negative muons than positive muons. This is however inconsistent with our data, in particular when one compares the value of n_1 (11) to the value of n_2 (3). Equation 6-23 to equation 6-26 indicate that we observed more positive muons than negative muons within our final detected charm signal events. Even though the statistics are limited, our results do indicate that the charm production process can not possibly be completely dominated by the Λ_c^+-$\bar{D}$ production mechanism in which the Λ_c^+ baryons are more diffractively produced than the $\bar{D}$ mesons.

Suppose the produced charm-anticharm quarks are always hadronized into D-$\bar{D}$ mesons. The D meson consists of a charm quark and an anti-light quark ($\bar{u}$ or $\bar{d}$), neither one of them are from the valence quarks of the interacting hadrons. Contrarily, the $\bar{D}$ meson contains one valence quark from the interacting hadrons. Therefore one may expect that the D meson will be produced more centrally than the $\bar{D}$ meson. The positive

[7]Small value of β in table 6-1.

Charm pair	β	i	R_i	P_o	P_{SUM}
D	1	1	0.2052	5.01×10^{-6}	0.03
		2	0.3301		
$\bar{D}$	1	3	0.3160		
		4	0.1487		
D	3	1	0.1916	3.22×10^{-6}	0.02
		2	0.3286		
$\bar{D}$	3	3	0.3152		
		4	0.1646		
D	5	1	0.2371	1.88×10^{-5}	0.10
		2	0.3013		
$\bar{D}$	5	3	0.2992		
		4	0.1624		
D	7	1	0.1979	4.63×10^{-6}	0.03
		2	0.3250		
$\bar{D}$	7	3	0.3005		
		4	0.1766		
D	5	1	0.2015	5.25×10^{-6}	0.03
		2	0.3104		
$\bar{D}$	3	3	0.3260		
		4	0.1621		
D	7	1	0.2625	2.61×10^{-5}	0.12
		2	0.2251		
$\bar{D}$	1	3	0.3955		
		4	0.1169		
Λ_c^+	1	1	0.1036	7.40×10^{-9}	0.68×10^{-4}
		2	0.4308		
$\bar{D}$	3	3	0.2342		
		4	0.2314		
Λ_c^+	1	1	0.1149	1.30×10^{-8}	0.12×10^{-3}
		2	0.4501		
$\bar{D}$	5	3	0.2033		
		4	0.2317		

Table 6-2: Values of R_i, P_o and P_{sum} for different production models

The value of R_i were calculated from charm monte-carlo together with the estimation of background events. 140 events with $1.0 < S/DS < 2.0$ from the matched-best-muon sample were used to estimate the background distribution. For this background sample, $n_1=30$, $n_2=38$, $n_3=51$ and $n_4=21$.

muon from the decay of the D meson will thus have a higher possibility for being accepted by our muon spectrometer. Two production models of this type are also included in both table 6-1 and table 6-2.

Now let us compare our cross section values (table 6-1) to the result from the high resolution bubble chamber experiment. The average value of the cross section measured in this experiment (for the case of $A^{2/3}$ dependence and from the D-$\bar{D}$ production models of table 6-1) can be estimated to be on the order of 17.69±6.81 μb (the error was calculated as a combined error including the systematic error due to the various different production models.) The inclusive D or $\bar{D}$ production cross section in 360 Gev pp interactions was measured by the LEBC EHS Collaboration [37] as 56 (+25; −12) μb. From this inclusive cross section, they estimate (with assumptions on the production models) the event cross sections as $\sigma(D\bar{D}) = 24$ (+9; −5) μb and $\sigma(\Lambda_c^+\bar{D}) = 8$ (+10; −8) μb. Since our data were collected over the whole neutron spectrum, the cross section calculated with equation 6-16 (and the values of table 6-1) are actually the average values weighted by the neutron spectrum (let us use the symbol $<\sigma_c>$ to indicate the *averaged value* from now on). Thus we can not compare our cross section values listed in table 6-1 directly to the LEBC values.

The dashed line of figure 6-1 shows the distribution of the interaction center of mass energy calculated according to the E-630 neutron spectrum as discussed in section 1 of chapter 3 (figure 3-5). The three solid lines in this figure are the theoretical predictions for the charm production cross section as functions of the center of mass energy (see figure 1-5 of chapter 1). These curves are reproduced from reference [69] and [11]. Let functions $\sigma(S^{1/2})$ and $E(S^{1/2})$ represent the cross section and the center of mass energy distribution respectively, the value of the average cross section measured in our experiment will be

$$<\sigma_c> = \int \sigma(S^{1/2})E(S^{1/2})d(S^{1/2}) \;/\; \int E(S^{1/2})d(S^{1/2}) \qquad (6\text{-}29)$$

and (with numerical integration)

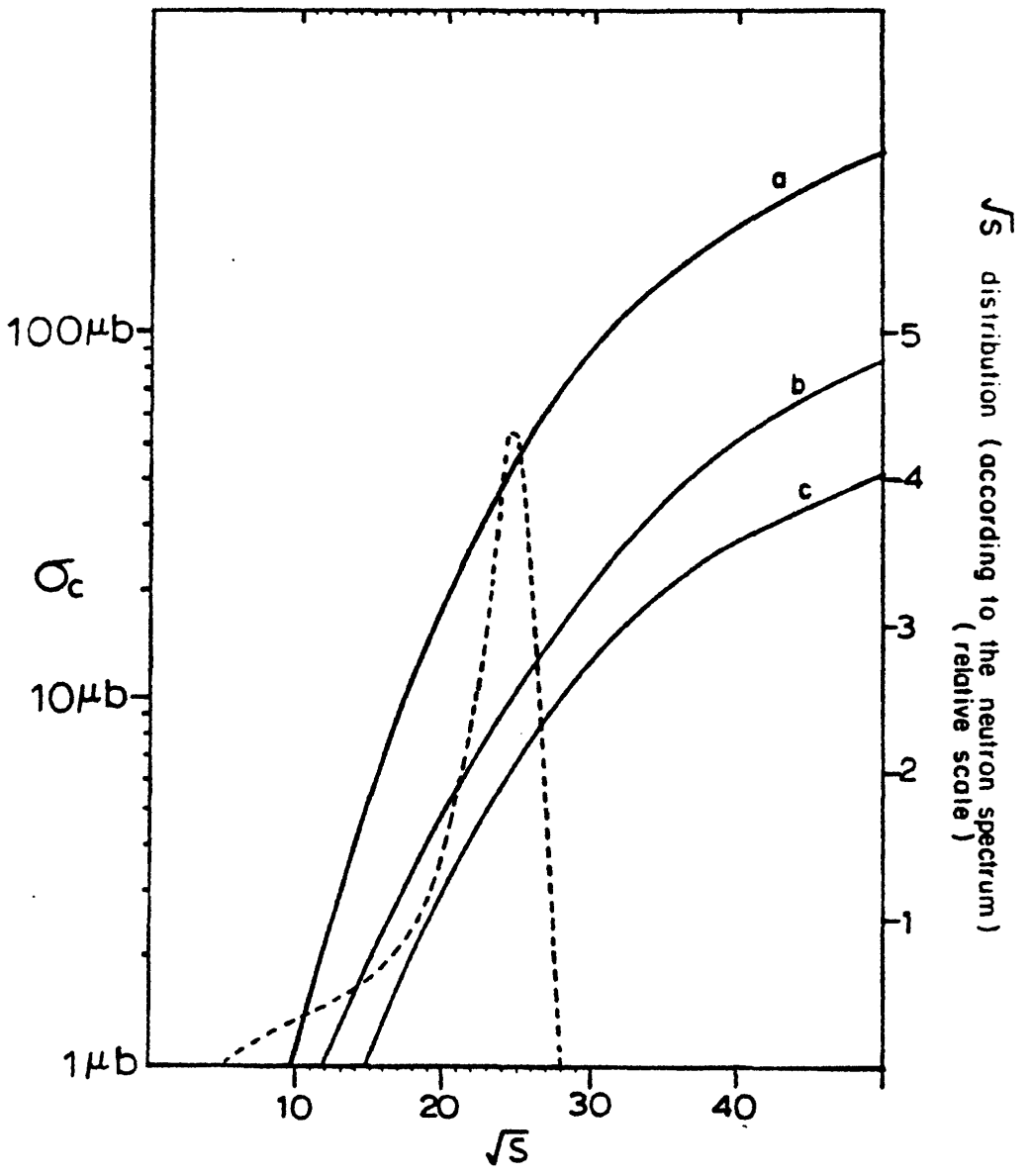

Figure 6-1: Charm production cross section and the distribution of the center of mass energy (see text)

$$<\sigma_c(\text{for curve a})> \sim 30.7\ \mu b \tag{6-30}$$

$$<\sigma_c(\text{for curve b})> \sim 8.0\ \mu b \tag{6-31}$$

$$<\sigma_c(\text{for curve c})> \sim 5.0\ \mu b \tag{6-32}$$

On the plot of figure 6-1, the value of the event cross section of LEBC ($\sim$ 24-32 μb), at $\sqrt{S}$=26 Gev, will fall in between curve a and curve b. Taking into account the effect of our neutron spectrum, the corresponding average cross section (equation 6-29) estimated from the LEBC value will be

$$<\sigma_c>_{\text{from LEBC}} \sim 15 - 22\ \mu b$$

This value is reasonably close to our cross section values in table 6-1, for the D-$\bar{D}$ production models and assuming an $A^{2/3}$ dependence. Since the data of LEBC was collected from the proton-hydrogen interactions, their value is the absolute value for the nucleon-nucleon interaction cross section. Therefore, in order to be consistent with the LEBC result, our data favors the $A^{2/3}$ cross section dependence for the hadronic charmed particle production.

CONCLUSIONS

In this thesis, I report the experiments in which a triggerable streamer chamber was used as a visual vertex detector for studying the hadronic production of charmed particles. We achieved a streamer size of 50 μm, a full track width of 80μm and a two track resolution of 150 μm. Even though we consider the performance of the streamer chamber is technically successful, the resolution (150 μm on the film) is marginal for the study of charm physics. Utilizing the triggerability of the streamer chamber, out of about 45 million hadronic interactions, 1807 muon trigger pictures were selected and measured. With a special miss-distance analysis, we obtained 17.32±4.73 events as the charm production signal. With various assumptions for the D-$\bar{D}$ production mechanism, the nucleon-nucleon charm production cross section, averaged over the neutron spectrum, can be estimated according to the assumption of either A^1 or $A^{2/3}$ dependence for the cross section (see table 6-1) :

$<\sigma_c> \sim$ 5-8 μb For A^1 dependence

and

$<\sigma_c> \sim$ 13-20 μb For $A^{2/3}$ dependence

Our result is consistent with the analysis of the LEBC Collaboration if the $A^{2/3}$ dependence is chosen.

Appendix I. MONTE-CARLOS

I.1 THE CHARM MONTE-CARLO - <MONTED>

A Fortran monte-carlo program, <MONTED>, has been developed to simulate the hadronic charm production interactions. In this section, the algorithm of the program will be described step by step.

• Neutron spectrum generator - <NEUTRN>

The incident neutron energy is generated according to the neutron spectrum of equation 3-4 and figure 3-5 with the minimum value of X_F set at 0.3. The center of mass energy, S_{cm}, for the neutron induced interaction is calculated according to the generated neutron momentum.

• Selection of charm pair - <DPAIR>

The charmed particles are always produced in pairs. For the case of Λ_c^+-$\bar{D}$ production, the D particles are chosen equally between D^- and $\bar{D}^0$. For the case of D-$\bar{D}$ production, the charm pairs are chosen equally among (D^+-D^-), (D^+-$\bar{D}^0$), (D^0-$\bar{D}^0$) and (D^--D^0).

• Production mechanisms

Two different production mechanisms are included in this monte-carlo:

(A) <DGENTR>

Charmed and anti-charmed particles are produced independently according to the following distribution

$$\frac{d\sigma}{dX_F dP_t^2} = C(1-|X_F|)^{\beta}\exp(-\alpha P_t) \tag{7-1}$$

where $\alpha = 2.5$ (see discussions for equation 6-18 of section 6.1) and the value of β is chosen between 1 and 7 [15] according the the various production models. In our data analysis, we used this production mechanism (see section 6.1).

(B) <MASSDS>

The mass of the composite D-$\bar{D}$ system is generated according to the distribution [20]:

$$M^3 dN/dM = e^{-0.55M} \tag{7-2}$$

with α and β of equation 7-1 equal to 2.23 and 2.96 respectively.

- **Selection of charm decay mode - <DMODE>**

The decay of a charmed particle is considered only if it decays before the front end of the first hadron filter[1]. The decay position is calculated according to the lifetime (Eq. 1-6 to Eq. 1-9) and the momentum of the decaying particle (subroutine <DECAYP>).

Only Cabibbo favored decay modes are currently included in this program. That is the charm quark always decays via the process

$$c(\bar{c}) \rightarrow s(\bar{s}) + l^+(l^-) + \nu \tag{7-3}$$

or

$$c(\bar{c}) \rightarrow s(\bar{s}) + q + \bar{q} \tag{7-4}$$

Equation 7-3 leads to the semileptonic decay mode (subroutine <SMILEP>) and equation 7-4 leads to the hadronic decay mode (subroutine <HADRON>). For D particle decay, the s quark is assumed to hadronize into a K meson or a K^* meson with equal probability (the K^* subsequently decays to $K\pi$) according to the spectator diagrams. Therefore

$$D^+ \rightarrow \bar{K}^0(\bar{K}^{0*}) + X \tag{7-5}$$

$$D^0 \rightarrow K^-(K^{-*}) + X \tag{7-6}$$

and so on

For Λ_c^+ decay, we assume that the s quark hadronizes equally into Λ^0 and (K+p) channels.

---

[1]Most of the charmed particles will decay inside the chamber.

We also assume that the ratio of the semileptonic branching ratios is equal to the ratio of the lifetimes:

$$BR(D^+)/BR(D^0) = \tau(D^+)/\tau(D^0) \tag{7-7}$$

with $BR(D\rightarrow\mu) = BR(D\rightarrow e) \equiv BR(D)$ and

$[BR(D^0)+BR(D^+)]/2 = 8\%$ (world average)

For Λ_c^+, we assume that $BR(\Lambda_c^+\rightarrow\mu)=5\%$

For the hadronic decay mode of the D particles, we assume that the D particles always decay to $K\pi\cdots$ system. The number of pions is chosen to be equal to 1+n where n is generated according to the Poisson distribution with a mean value equal to 1.7 (DHMEAN). For Λ_c^+, we assume that Λ_c^+ decays into $\Lambda\pi\cdots$ or $Kp\pi\cdots$ systems. Where again, the number of pions is equal to 1+n with <n>=0.5. (In the process of choosing the type of pions, charge conservation is always considered in the subroutine <PIONS>)

Once the decay mode is chosen, the decay mechanism follows a uniform phase space distribution. The subroutines <THREEB>, <DALITZ> and the program <SAGE>[2] are used as the uniform phase space generator for this monte-carlo.

After selecting the decay modes for the charm-anticharm pair, the program requires the existence of at least one muon among all of the final state particles. If not, a new pair of charmed particles will be generated.

- **Strange particle decay**

The subroutine <KAONS> takes care of the decays of the K mesons. Subroutine <SBRYON> handles the decays of the strange baryons Σ^+, Σ^-, Λ^0 and $\bar{\Lambda}^0$. The various decay modes and branching ratios are chosen according to the particle data book [144].

- **Generate tracks for the primary vertex - <PRIMRY>**

In order to simulate the neutron induced interactions inside the streamer chamber, pions

---

[2]Jerry Friedman, LBL Group A Programming Note No. P-189, 1971

are generated together with the charm pair for each event. The number of charged pions is chosen according to the relationships

$$<N(\pi^+)> = <N(\pi^-)> = \frac{1}{2}<N_{ch}> \tag{7-8}$$

and [140]

$$<N_{ch}> = 2.12 + 0.179(ln S_{eff}) \tag{7-9}$$

where <N> is the mean value of a Poisson distribution and S_{eff} is the effective center of mass energy. In reference [140], S_{eff} was calculated by subtracting the energy of the leading particles (both forward and backward) from the total center of mass energy. In our case, S_{eff} is calculated by subtracting the energy of the charm-anticharm pair from the total center of mass energy.

These pions are then generated according to the distribution [130]

$$\frac{d\sigma}{dY_{cm}dP_t^2} = A \exp(-7.0P_t+0.5P_t^2) \exp(-0.14Y_{cm}^2) \tag{7-10}$$

where Y_{cm} is the rapidity of the pions

- **Charged particle track generator** - <TRACK>

All charged particle tracks inside the streamer chamber[3] are converted into the film images (view 1 and view 2). This space to film conversion follows the algorithm of the three dimensional reconstruction discussed in chapter 4. At this step, all measurement points are generated at the center of the track image. This monte-carlo measurement output is arranged in a format suitable for the E-630 analysis program - <MAPP>.

- **Trigger requirement** - <CONDTN> and <PROPAG>

The muons from each monte-carlo event are propagated through the muon spectrometer. If none of the muons satisfys the muon trigger requirements as described in chapter 3, the event is aborted and a new charm-anticharm pair will be generated.

[3]the effective field region inside the chamber is chosen as 3.5 mm as discussed in section 4.3

• **Track "blocking" simulation** - <REMEAS>

In chapter 2 and chapter 5, we mentioned that although the full width of the streamer chamber track is about 80 μ on the film, we can not measure the regions where two tracks are closer than 150 μm. In order to simulate this track overlapping effect, a set of measurement points are generated for events which satisfy the trigger requirements. This monte-carlo measurement procedure should have a net result statistically similar to that of the real measurement of the streamer chamber pictures. The measurement points are generated according to the following guides:

1. The distances between the measurement points and the center of a track follow a Gaussian distribution with standard deviation equal to 0.014 mm (see section 4.2).

2. If a track is shorter than 1.5 mm, this track is not measurable.

3. The distance between two successive measurement points, DL, is equal to the maximum value between 1 mm and one eighth of the track length. If the track length is shorter than 2 mm, DL ranges randomly between 0.5 to 0.7 mm.

4. A point is measurable only if no other track is within a distance of 150 μm from this point.

5. Some tracks might have to be divided into two or three measurable sections (for example, two tracks crossing over each other). In this case the minimum length for a measurable section is chosen as 1 mm.

6. If a track misses the primary vertex by greater than 0.2 mm, the program labels this track as a *non-primary-vertex track*. Otherwise the program labels the tracks as if they are associated with the primary vertex.

Figure 7-1 to figure 7-4 are comparisons between the monte-carlo and the real data. It is fair to say that the monte-carlo reflects the the overall character of the E-630 data very well. This is very important since we use the monte-carlo to estimate the detection efficiency of the charm signal in our S/DS analysis (chapter 5).

I.2 STRANGE PARTICLE MONTE-CARLO - <STRNGE>

In order to study the problems of the strange particle backgrounds and to provide a corresponding monte-carlo program for the interaction-trigger events (section 3.2), the charm monte-carlo <MONTED> was modified such that instead of generating the charm pairs the following strange particles are generated by the neutron induced interactions. References [128] to [145] are particularly useful for this strange particle monte-carlo.

1. K mesons

The K mesons are generated with the assumptions

$$<N(K^+)>=<N(K^-)>=2<N(K^0_s)>=2<N(K^0_L)> = NK \qquad (7\text{-}11)$$

where <N> is the average number of particles per event.

and [130]

$$\frac{d\sigma}{dY_{cm}dP_t^2} = A\, e^{-4.9P_t}e^{-1.0Y_{cm}^2} \qquad (7\text{-}12)$$

The value of $<N(K^{+/-})>$ is estimated as 0.3 from reference [129] and $<N(K_s)>=0.15$ from reference [138]. Reference [138] is based on data from 147Gev/c π-p interactions. Our incident neutron beam had an average momentum of about 280 Gev/c. Hence, to avoid under estimating the background, we choose the value NK=0.5 for this monte-carlo.

2. Σ^+ and Σ^- hyperons

According to table 3 and appendix of reference [135] (p-BeO interactions), the particle multiplicities in the forward hemisphere of the center of mass system are $<N(\Sigma^+)>\sim0.030$ and $<N(\Sigma^-)>\sim0.014$. Therefore, for this monte-carlo, we use

$$<N(\Sigma^+)>=0.060 \;\; ; \;\; <N(\Sigma^-)>=0.028 \qquad (7\text{-}13)$$

For the production mechanism, we use

$$\frac{d\sigma}{dX_F dP_t^2} = A\,(1-|X_F|)^{\beta} e^{-7.0P_t} \tag{7-14}$$

$\beta = -0.24$ for $|X_F| < 0.9$

(we assume that the distribution for $|X_F| > 0.9$ is the same as the distribution for X_F=0.9)

The value of β is estimated from the results of the Fermilab hyperon (p-Be interactions) experiment [145]. However, in the hyperon experiment, with 400 Gev/c incident protons, the leading particle effect for the production of the Σ^+ particles is expected. In our case, with 280 Gev average energy neutrons as incident particles, the β values for the Σ hyperons are anticipated to be larger than -0.24. However, in the monte-carlo, we use the same distribution for both Σ^+ and Σ^- in both forward and backward directions.

3. Λ^0 and $\bar{\Lambda}^0$

Again, the particle muliplicities are taken from reference [135] (multiplied by 2 for both forward and backward hemispheres):

$$<N(\Lambda^0)>=0.126 \text{ and } <N(\bar{\Lambda}^0)>=0.026 \tag{7-15}$$

and the production models [132]

$$\frac{d\sigma}{dX_F dP_t^2} = A \exp\{-F(P_t)-G(X_F)\}\,(1-X_F)^{S(P_t)} \tag{7-16}$$

with

$$F(P_t)=\begin{cases} 3.79(P_t^2+0.304)^{1/2} & \text{for } \Lambda^0 \\ 2.45P_t^2 & \text{for } \bar{\Lambda}^0 \end{cases}$$

$$G(X_F)=\begin{cases} 1.65(X_F-0.866)^2 & \text{for } \Lambda^0 \\ 12.2X_F & \text{for } \bar{\Lambda}^0 \end{cases}$$

and

$$S(P_t) = 0.804 + 0.999 P_t^2 \qquad \text{for } \Lambda^0$$

$$S(P_t) = 0 \qquad \text{for } \bar{\Lambda}^0$$

After generating the strange particles, pions associated with the primary vertex are generated as in the charm monte-carlo. The decay modes and lifetimes of the strange particles are again processed by the subroutines <KAONS> and <SBRYON>. The track "blocking" and measurement simulations are handled in the same way as the charmed monte-carlo.

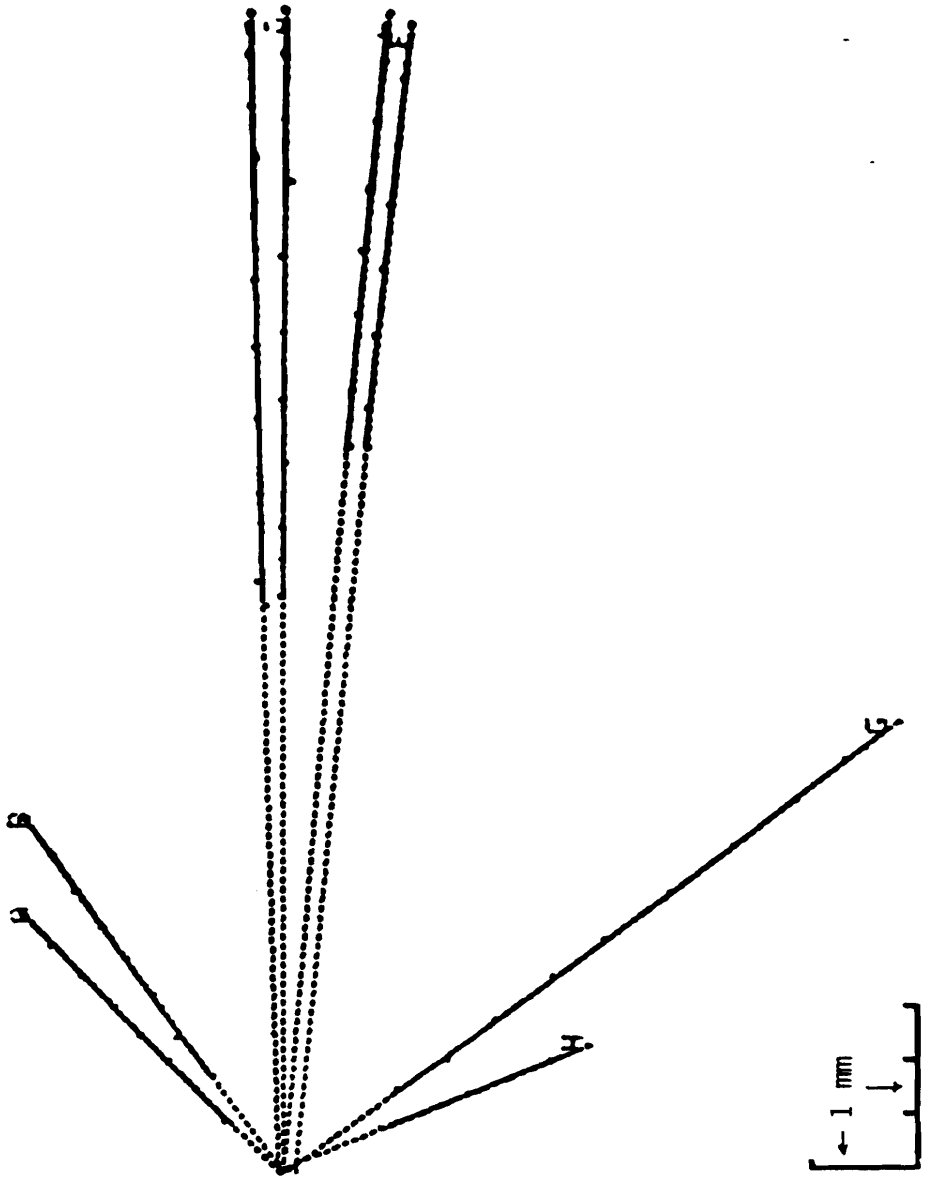

Figure 7-1: Comparison of the monte-carlo film measurement procedure with a real event from E-630 data

The dashed lines and measurement points are from real data, 598-906 (V1). The first measurement point on a track can be regarded as the beginning of the measurable section as determined by the scanner. The darker lines are the measurable sections determined by the monte-carlo (see text). It can be seen that the beginnings of these sections are very close to the first measurement points of the tracks. (The scale at the lower left corner represents 1 mm/Div.)

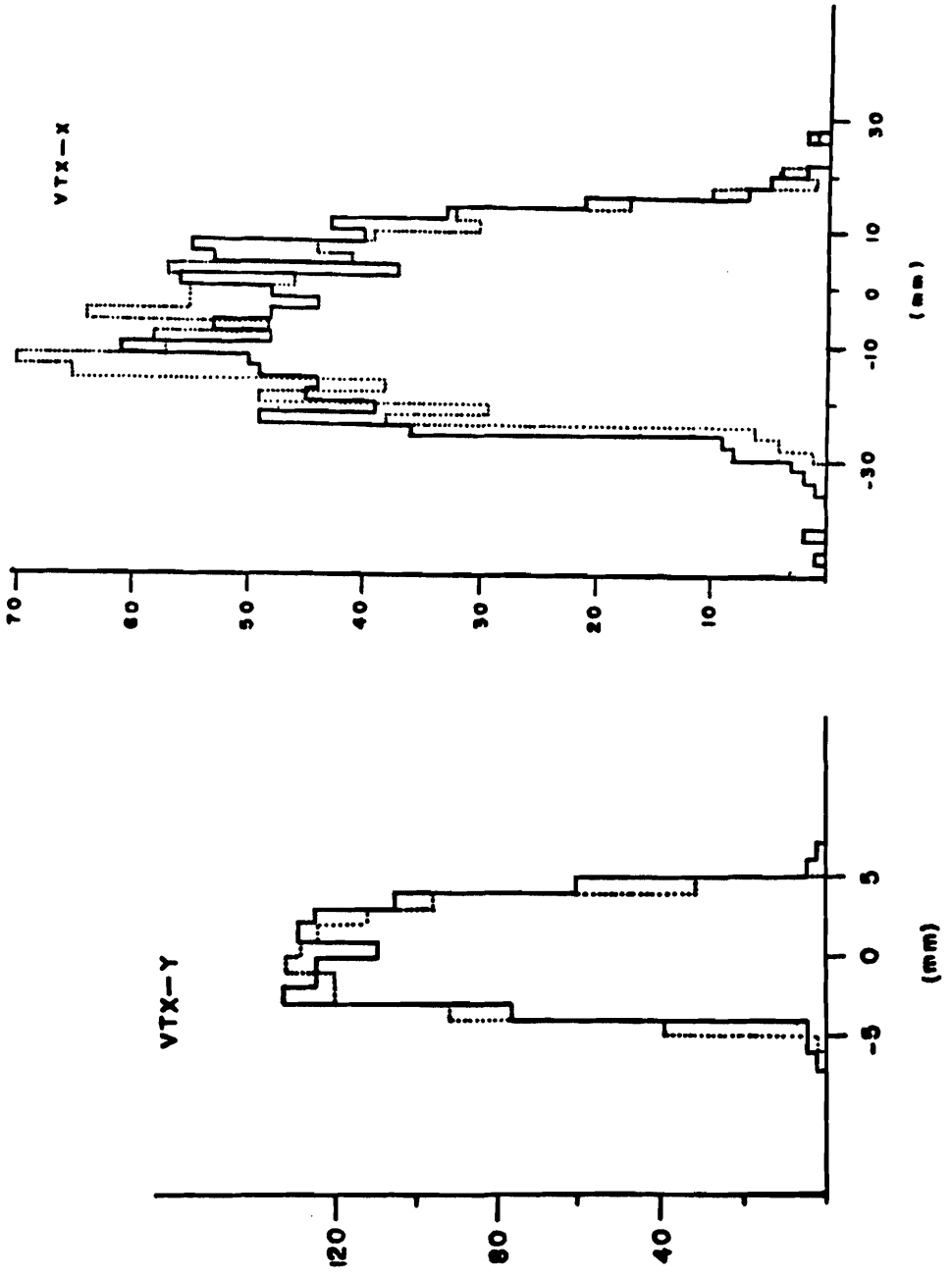

Figure 7-2: Distribution of fitted vertices
Solid line: from real data. Dotted line: from monte-carlo.

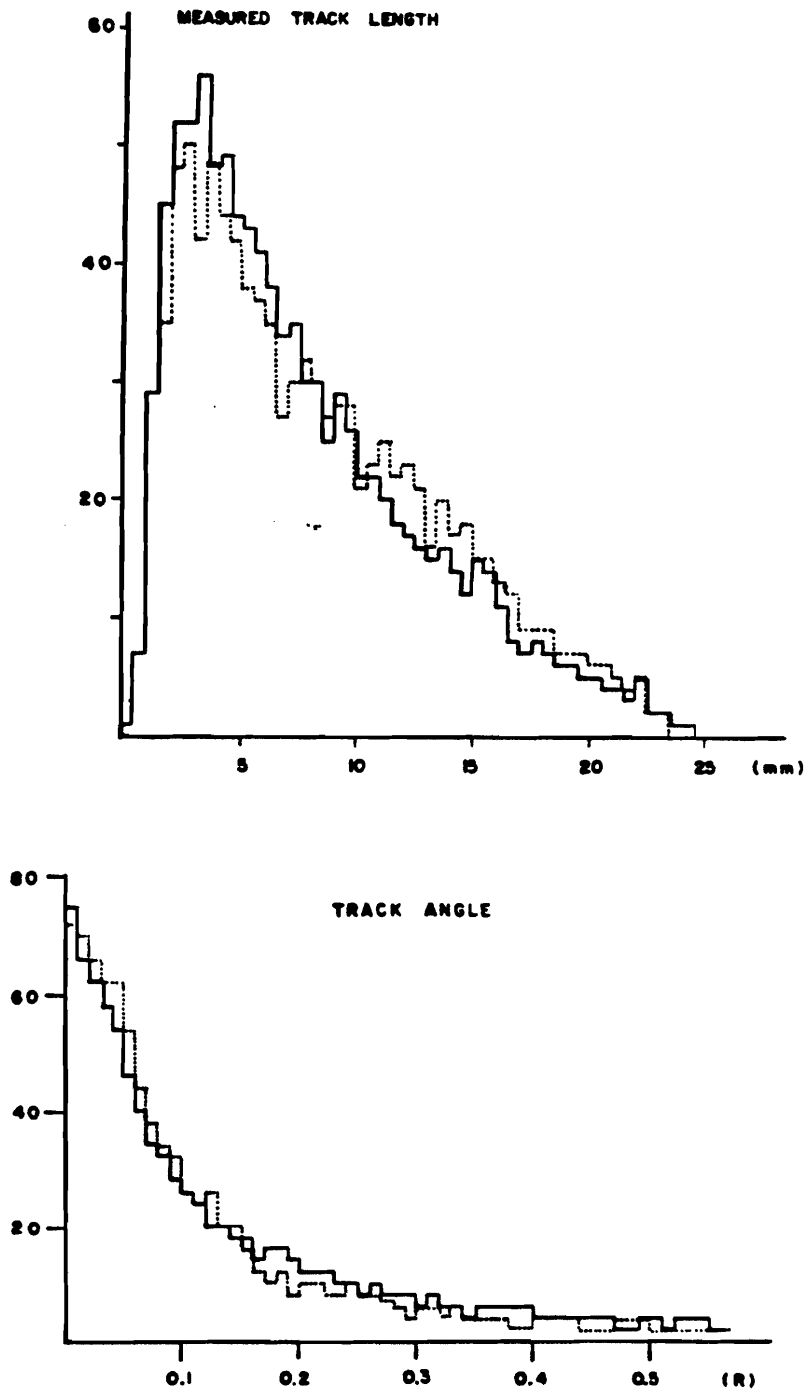

Figure 7-3: ***Measurable track length*** **distribution and** ***measurable track angle*** **distribution**

Solid line: from real data. Dotted line: from monte-carlo. The track angles are measured with respect to the beam direction

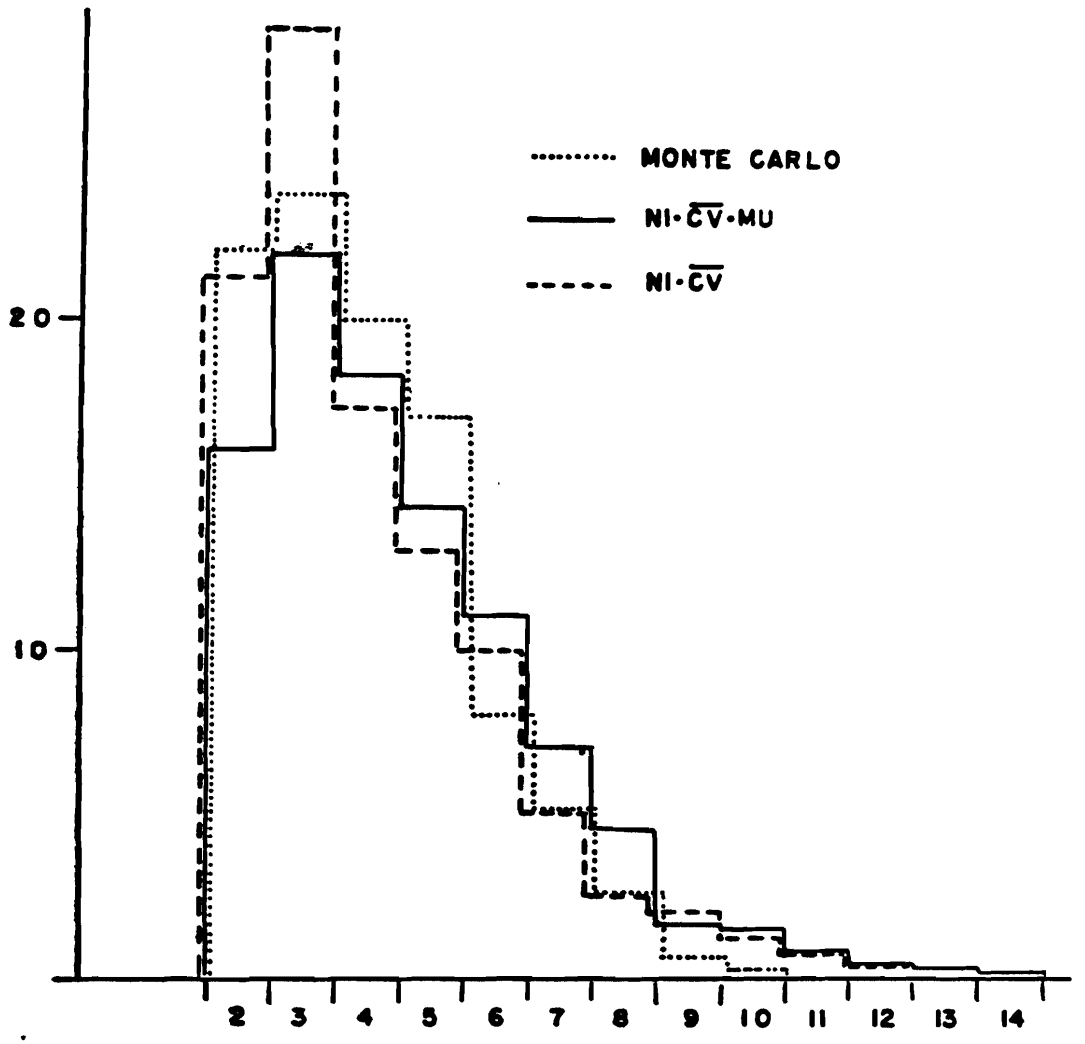

Figure 7-4: Number of measurable tracks per event

Solid line: from muon-trigger events. Dashed line: from interaction-trigger events. Dotted line: from monte-carlo.

Appendix II. THE WEDGE-SHAPED TERMINATOR

The behavior of the wedge-shaped terminator is discussed in detail in reference [101]. Some interesting points which result from solving the Maxwell's equation inside the wedge are summarized here.

Using cylindrical coordinates (figure 2-34), the Laplace equation inside the wedge can be written as

$$\nabla^2 V = \frac{1}{r}\frac{\partial}{\partial r}\left(r\frac{\partial V}{\partial r}\right) + \frac{1}{r^2}\frac{\partial^2 V}{\partial \theta^2} + \frac{\partial^2 V}{\partial x^2} = 0 \tag{8-1}$$

Letting $V = P(r)Q(\theta)X(x)$ and $X(x) =$ constant, equation 8-1 becomes

$$\frac{1}{r}\frac{d}{dr}\left(r\frac{dP}{dr}\right) - \frac{n^2}{r^2}P = 0 \tag{8-2}$$

and

$$\frac{\partial^2 Q}{\partial \theta^2} = -n^2 Q \tag{8-3}$$

The general solution for equation 8-2 and equation 8-3 is

$$V = \sum_{n=1}^{\infty} (A_n r^n + B_n r^{-n})(C_n \sin n\theta + D_n \cos n\theta) \tag{8-4}$$

with the boundary conditions

$$V = 0 \qquad \text{for } \theta = 0 \tag{8-5}$$

$$V = I\frac{R_s}{W}r \qquad \text{for } \theta = \theta_0 \tag{8-6}$$

where I is the current on the plate. Therefore, $B_n = D_n = 0$ and $n = 1$, equation 8-7 becomes

$$V = \frac{I \cdot R_s}{\sin\theta_0 \cdot W} r \sin\theta \tag{8-7}$$

The Maxwell's equation, $\nabla \cdot H = 0$, implies a uniform magnetic field inside the wedge :

$$H_x = \frac{I}{W} \tag{8-8}$$

Thus we have

$$E_r = -\frac{I \cdot R_s}{\sin\theta_0 \cdot W} \sin\theta$$

$$E_\theta = -\frac{I \cdot R_s}{\sin\theta_0 \cdot W} \cos\theta$$

$$H_x = \frac{I}{W}$$

These expressions can be rewritten in Cartesian coordinates :

$$E_y = -\frac{I \cdot R_s}{\sin\theta_0 \cdot W} \tag{8-9}$$

$$E_z = 0 \tag{8-10}$$

$$H_x = \frac{I}{W} \tag{8-11}$$

Equation 8-9 to equation 8-11 are exactly in the form of a TEM wave. Therefore the wedge is reflectionless over an infinite[1] bandwidth if the incident TEM waves satisify the boundary conditions of the wedge (i.e. the relationships between the impedance of the transmission line and the surface resistance and dimension of the wedged plate). The impedance of the transmission line with line spacing equal to S (figure 2-34) can be calculated according to equation 8-9 and equation 8-11 ($\sin\theta_0 = S/L$):

$$V = -E_y \cdot S = \frac{I \cdot R_s \cdot L}{W}$$

and

$$Z_0 = V/I = R_s \cdot \frac{L}{W}$$

[1]If the surface resistance is independent of the wave frequency. See chapter 2 section 2.4

References

[1] Elliot Leader & Enrico Predazzi.
An Introduction To Gauge Theories And The New Physics.
Cambridge University Press, 1982.

[2] E. G. Cazzoli et al.
Evidence for $\Delta S = -\Delta Q$ currents or charm-baryon production by neutrinos.
Physical Review Letters 34(17):1125, 1975.

[3] G. Goldhaber et al.
Observation in e^+e^- annihilation of a narrow state at 1865Mev decaying to $K\pi$ and $K\pi\pi\pi$.
Physical Review Letters 37(5):255, 1976.

[4] J. Kirkby.
Review of e^+e^- reactions in the energy range 3 to 9 Gev.
In T.B.W. Kirk and H.D.I. Abarbanel (editor), *Proceedings of the 1979 International symposium on lepton and photon interactions at high energy*, pages 107. Fermilab, 1979.

[5] Anne Kernan.
Observation of charmed baryon production at the CERN ISR.
In T.B.W. Kirk and H.D.I. Abarbanel (editor), *Proceedings of the 1979 International symposium on Lepton and Photon interactions at high energy*, pages 535. Fermialb, 1979.

[6] Horst Wachsmuth.
Recent data on prompt single lepton production in hadron-nucleus collisions.
In T.B.W. Kirk and H.D.I. Abarbanel (editor), *Proceedings of the 1979 International symposium on Lepton and Photon interactions at high energy*, pages 541. Fermilab, 1979.

[7] Don D. Reeder.
Observation of short lifetime particles in track chamber.
In T.B.W. Kirk and H.D.I. Abarbanel (editor), *Proceedings of the 1979 International symposium on Lepton and Photon interactions at high energy*, pages 553. Fermilab, 1979.

[8] J. D. Prentice.
The Neutrino production and weak decay of charmed hadrons.
In T.B.W. Kirk and H.D.I. Abarbanel (editor), *Proceedings of the 1979 International symposium on Lepton and Photon interactions at high energy*, pages 563. Fermilab, 1979.

[9] L. Voyvodic.
A review of recent measurements of charmed particle lifetimes using emulsions.
In T.B.W. Kirk and H.D.I. Abarbanel (editor), *Proceedings of the 1979 International symposium on Lepton and Photon interactions at high energy*, pages 569. Fermilab, 1979.

[10] R. J. N. Phillips.
Phenomenology of new particle production.
In L. Durand & L. G. Pondrom (editor), *Proceeding of international conference on high energy physics, Madison*, pages 1471. AIP, 1981.

[11] D. Treille.
Photon and hadron production of open heavy flavours.
In W. Pfeil (editor), *1981 International Symposium On Lepton And Photon Interactions at High Energy*, pages 750. Bonn, 1981.

[12] George H. Trilling.
The properties of charmed particles.
Physics Reports 75(2):57-124, 1981.

[13] D. Haidt.
Summary of the session on lepton-hadron physics.
In P. Petiau & M. Porneuf (editor), *21st international conference on high energy physics*, pages C3-5. Paris, 1982.

[14] C. M. Fisher.
New experimental results on the hadroproduction and photoproduction of charmed particles.
In P. Petiau & M. Porneuf (editor), *21st international conference on high energy physics*, pages C3-146. Paris, 1982.

[15] F. Halzen.
Production of heavy quarks.
In P. Petiau & M. Porneuf (editor), *21st international conference on high energy physics*, pages C3-381. paris, 1982.

[16] G. Kalmus.
Weak decays of new particles.
1982.
Rutherford Appleton Laboratory, RL-82-090, Talk at XXI International Conference on High Energy Physics, Paris, 1982.

[17] Sheldon Stone.
Weak decays of heavy quarks.
In D. G. Cassel and D. L. Kreinick (editor), *1981 International Symposium On Lepton And Photon Interactions at High Energy*, pages 203. Cornel University, 1983.

[18] N. W. Reay.
Heavy quark and lepton lifetimes.
In D. G. Cassel and D. L. Kreinick (editor), *1981 International Symposium On Lepton And Photon Interactions at High Energy*, pages 244. Cornel University, 1983.

[19] Thomas Nash.
Recent results on D decays and lepton, photon, (and hadron) production of charm.
In D. G. Cassel and D. L. Kreinick (editor), *1981 International Symposium On Lepton And Photon Interactions at High Energy*, pages 329. Cornel University, 1983.

[20] K. W. Brown et al.
Observation of prompt single-muon production by 400-Gev protons.
Physical Review Letters 43(6):410, 1979.

[21] D. Drijard et al.
Observation of charmed D meson production in pp collisions.
Physics Letters 81B(2):250, 1979.

[22] T. Hansl et al.
Results of a beam dump experiment at the CERN SPS neutrino facility.
Physics Letters 74B(1,2):139, 1978.

[23] A. Chilingarov et al.
On the production of charmed mesons in high energy proton-proton collisions.
Physics Letters 83B(1):136, 1979.

[24] H. Fuchi et al.
Direct observation of a pair decay of neutral charmed particles produced in 400 Gev/c proton interaction.
Physics Letters 85B(1):135, 1979.

[25] K. L. Giboni et al.
Diffractive production of the charmed baryon Λ_c at the CERN ISR.
Physics Letters 85B(4):437, 1979.

[26] W. Lockman et al.
Evidence for Λ_c in inclusive pp$\rightarrow(\Lambda^0\pi^+\pi^+\pi^-)$+X and pp$\rightarrow$(K$^-\pi^+$p)+X at $\sqrt{s}$=53 and 62 Gev.
Physics Letters 85B(4):443, 1979.

[27] M. Calicchio et al. (BEBC TST collaboration).
First observation of the production and decay of the $\Sigma^+{}_c$.
Physics Letters 93B(4):521, 1980.

[28] J. Sandweiss T. Cardello, P. Cooper, R. Kellogg, D. Ljung, T. Ludlam, R. Majka, P. Mcbide, P. Nemethy, L. Rosselet, A.J. Slaughter, H.D. Taft, L. Teig, L. Tzeng, S. Ecklund and M. Johnson.
Observation of Hadronic Charm Production in A High Resolution Streamer Chamber Experiment.
Phys. Rev. Lett. 44:1104, 1980.

[29] M. Jonker et al. (CHARM collaboration).
Experimental study of prompt neutrino production in 400 Gev proton-nucleus collisions.
Physics Letters 96B(3,4):435, 1980.

[30] V. L. Fitch et al.
Measurement of D^* production in pion-nucleon interactions at 200 Gev/c.
Physical Review Letters 46(12):761, 1981.

[31] W. Allison et al.
Direct evidence for associated charm production in 340 Gev π^-p interactions.
Physics Letters 93B(4):509, 1981.

[32] M. Basile et al.
Measurement of associated charm production in pp interactions at $\sqrt{s}$=62 Gev.
Il Nuovo Cimento 63A(2):230, 1981.

[33] M. Basile et al.
Measurement of associated production of $D^0\overline{D}$ in pp interactions at $\sqrt{s}$=62Gev.
Il Nuovo Cimento 65A(4):457, 1981.

[34] M. Basile et al.
Measurement of $(D_+\overline{D})$ charm mson pair production in (pp) interactions at $\sqrt{s}$ =62Gev.
Il Nuovo Cimento 67A(1):40, 1982.

[35] N. Usida et al.
Measurement of the lifetimes of the charmed D^+, D^0 and F^+ mesons and Λ_c^+ charmed baryon.
1982.
Ohio State University, Fermilab E531 Collaboration.

[36] M. Aguilar-Benitez et al. (LEBC EHS).
Charm D-Meson production in 360 Gev π^-p interactions.
Physics Letters 123B(1,2):98, 1982.

[37] M. Aguilar-Benitez et al. (LEBS EHS).
Charm D-Meson production in 360 Gev pp interactions.
Physics Letters 123B(1,2):103, 1982.

[38] M.Aguilar-Benitez et al.
Lifetime measurement of charm mesons produced in π^-p and pp interactions at 360 Gev/c.
Physics Letters 122B(3,4):312, 1983.

[39] S. R. Amendolia et al. (FRAMM NA1).
Evidence for F meson photoproduction.
1982.
CERN, CERN-EP/82-200.

[40] T. Aziz et al.
Charm production in 400 Gev/c proton-emulsion interactions.
Nuclear Physics B199:424, 1982.

[41] A. Badertscher et al. (BIBC).
Search for charmed particles with the heavy liquid bubble chamber BIBC.
Physics Letters 123B(6):471, 1983.

[42] R. Bailey et al. (ACCMOR collaboration).
Observation of $D^{*\pm}$ and $(\overline{D})^0/D^{\pm}$ production in high energy π^-Be interactions at the SPS.
1983.
CERN, CERN-EP/83-83.

[43] R. Bailey et al. (ACCMOR collaboration).
Production and decay properties of D and D^* mesons in π^-Be interactions.
1983.
CERN, CERN-EP/83-84.

[44] B. Hyams.
A silicon counter telescope to study shrt-lived particles in high-energy hadronic interactions.
Nuclear Instruments and Methods 205:99, 1983.

[45] R. H. Schindler et al.
Measurement of the properties of D-meson decays.
Physical Review D 24(1):78, 1981.

[46] E. N. Vella et al.
Observation of semileptonic decays of charmed baryons.
Physical Review Letters 48(22):1515, 1982.

[47] Mary K. Gaillard, Benjamin W. Lee and Jonathan L. Rosner.
Search for charm.
Reviews of Morden Physics 47(2):277, 1975.

[48] J. Ellis, M.K. Gaillard and D.V. Nanopoulos.
On the weak decays of high-mass hadrons.
Nuclear Physics B100:313, 1975.

[49] S. D. Ellis, M. B. Einhorn and C. Quigg.
Comment on hadronic production of Psions.
Physical Review Letters 36(21):1263, 1976.

[50] C. E. Carlson and R. Suaya.
Hadronic Production of the Ψ/J meson.
Physical Review D 14(11):3115, 1976.

[51] C. E. Carlson and R. Suaya.
Hadronic Production of heavy-quark bound states.
Physical Review D 18(3):760, 1978.

[52] H. Fritzsch.
Producing heavy quark flavours in hadronic collisions - a test of quantum chromodynamics.
Physics Letters 67B(2):217, 1977.

[53] G. Gustafson and C. Peterson.
On the diffractive production of charmed baryons.
Physical Letters 67B(1):81, 1977.

[54] F. Halzen.
CVC for gluons and hadroproduction of quark flavours.
Physics Letters 69B(1):105, 1977.

[55] L. M. Jones and H. W. Wyld.
Hadronic charm production by gluon fusion.
Physical Review D 17(7):1782, 1978.

[56] J. Babcock, D. Sivers and S. Wolfram.
Quantum-chromodynamic estimates for heavy-particle production.
Phsical Review D 18(1):162, 1978.

[57] M. Gluck and E, Reya.
Duality prediction for the production of heavy quark system in QCD.
Physics Letters 79B(4,5):453, 1978.

[58] C.E. Carlson and R. Suaya.
Hadronic charm production in QCD.
Physics Letters 81B(3,4):329, 1979.

[59] B. L. Combridge.
Associated production of heavy flavour states in pp and $p\bar{p}$ interactions: some QCD estimates.
Nuclear Physics B151:429, 1979.

[60] A. B. Carter and C. H. Llewellyn Smith.
Perturbative QCD in a covariant gauge.
Nuclear Physics B162:397, 1980.

[61] H. Fritzsch and P. Minkowski.
Test of the quark annihilation hypothesis for D and F decays.
Nuclear Physics B171:413, 1980.

[62] H. Fritzsch and P. Minkowski.
The puzzle of nonleptonic decays and its resolution.
Physics Letters 90B(4):455, 1980.

[63] H. Fritzsch and P. Minkowski.
Flavordynamics of quarks and leptons.
Physics Reports 73(2):67-173, 1981.

[64] S. J. Brodsky, P. Hoyer, C. peterson and N. Sakai.
The intrinsic charm of the proton.
Physical Letters 93B(4):1980, 1980.

[65] S. J. Brodsky and C. Peterson.
Intrinsic heavy-quark states.
Physical Review D 23(11):2745, 1981.

[66] D. P. Roy.
Intrinsic-charm contribution to scale breaking at large x.
Physical Review Letters 27(4):213, 1981.

[67] R. Winder and C. Michael.
Some QCD estimates of the production of heavy flavours in hadron-hadron collisions.
Nuclear Physics B173:59, 1980.

[68] V. Barger, F. Halzen and W.Y. Keung.
Central and diffractive components of charm production.
Physical Review D 25(1):112, 1982.

[69] R. Odorico.
Hadronic production of charm via flavour excitation.
Nuclear Physics B209:77, 1982.

[70] S. N. Ganguli and M. Schouten.
Correlation of charm particles from gluon-gluon fusion in hadronic collisions.
1982.
CERN, CERN/EP 82-213.

[71] L. Montanet.
Hadronic production of heavy flavours.
In P. Carison and W. P. Trower (editor), *Physics in Collision, Vol. 2*, pages 369. Plenum Publishing Co., 1983.

[72] R. Ruckl.
The Λ_c and its inclusive nonleptonic decay.
Physics Letters 120B(4,5,6):449, 1983.

[73] F. Muller.
Hadroproduction of Heavy Flavours.
1983.
CERN, CERN-EP/83-67, Lectures given at the 20th Course of the International School of Subnuclear Physics, Erice, Sicily, 1982.

[74] J. L. Ritchie et al.
Forward production of charm states and prompt single muons in 350 Gev p-Fe interactions.
Physics Letters 126B(6):499, 1983.

[75] J. L. Ritchie et al.
Forward production of charm states and prompt single muons in 278 Gev π^--Fe interactions.
1983.
University of Rochester, UR-829/C00-3065-388.

[76] J. L. Ritchie.
Hadronic charm production by protons and pions on iron.
PhD thesis, University of Rochester, 1983.

[77] P. Cooper.
Misdistance distribution.
1981.
Yale University, Internal Report, AUG-5.

[78] P. L. McBride.
Ph.D thesis, Yale University.
1984.

[79] Peter Rice-Evans.
Spark, Streamer, Proportional and Drift Chambers.
The Richelieu Press., 1974.

[80] J.M. Meek and J.D. Craggs.
Electrical Breakdown of gases.
John Wiley & Sons, 1978.

[81] Sanborn C. Brown.
Introduction To Electrical Discharges in Gases.
John Wiley & Sons, 1966.

[82] E. D. Lozanskii.
Photoionization Radiation In The Streamer Breakdown Of A Gas.
Soviet Physics-Technical Physics 13(9):1269, 1969.

[83] E.D. Lonzanskii and O.B. Firsov.
Qualitative Streamer Theory.
Soviet Physics JETP 29(2):367, 1969.

[84] G. Charpak.
Evolution of the Automatic Spark Chamber.
Annu. Rev. Nucl. Sci. 20:195, 1970.

[85] F. Sauli.
Principle Of Operation OF Multiwire Proportional And Drift Chamber.
1977.
CERN, CERN 77-09.

[86] H. Reather.
Electron Avalanche And BreakDown in Gases.
Bitterworth, London, 1964.

[87] G. E. Chikovani, V. A. Mikhailov and V. N. Roinishvili.
A Track Spark Chamber.
Physics Letter 6(3):254, 1963.

[88] G. E. Chikovani, V. N. Roinishvili and V. A. Mikhailov.
Operation Mechanism of the Track Spark Chamber.
Nucl. Instr. and Meth. 29:261, 1964.

[89] B. A. Dolgoshein, B. U. Rodionox and B. I. Luchkov.
Streamer Chamber.
Nucl. Instr. and Meth. 29:270, 1964.

[90] G. N. Glasoe and J. V. Lebacqz; Editors.
MIT Radiation Laboratory Series Vol.5 ; Pulse Generator.
McGraw-Hill, 1948.

[91] E. Gigy and F. Schneider.
CERN REPORT.
1964.
CERN, CERN 64-46.

[92] Jack Sandweiss.
Notes On The Design of the High Resolution Streamer Chamber.
1974-1975.
Yale University, Internal Reports.

[93] S. Ramo, J. R. Whitnnery and T. Van Duzen.
Field And Waves In Communication Electronics.
John Weily & Sons, 1965.

[94] F. Rohrbach.
Multiple firing of a streamer chamber conical Blumlein line.
In *Proc. Intern. Conf. On Instrumentation For High Energy Physics.* Frascati, 1973.
Frascati.

[95] F. Bulos, A. Odian and D. Yount.
Streamer Chamber Development.
Technical Report SLAC-74 UC-28, SLAC, 1974.
Particle Accelerator And High Voltage Machine TID-4500.

[96] R. Littauer.
Pulse Electronics.
Mcgraw-Hill, 1965.

[97] R. Beringer.
Parabolic Parallel-Plate Transmission Line.
1980.
Yale University, Internal Report, June-26.

[98] R. Beringer.
Measurement With A Parabolic Parallel-Plate Blumlein.
1980.
Yale University, Internal Report. Aug-14.

[99] R. Beringer.
Theory Of Resistive Voltage Divider With Coaxial Return.
1980.
Yale university, Internal Report. Oct-29.

[100] R. Beringer.
On The Theory Of Blumlein Pulses.
1981.
Yale University, Internal Report. May-26.

[101] R. Beringer.
On Wave Guide With Resistive Wall.
1982.
Yale University, Internal Report. Mar-15.

[102] M. J. Druyvesteyn and F. M. Penning.
The Mechanism of Electrical Discharges in Gases of Low Pressure.
Rev. of Morden Physics 12(2):87, 1940.

[103] L. G. Huxley and R. W. Crompton.
The Diffusion And Drift of Electrons In Gases.
John Wiley & Sons, 1974.

[104] V. Palladino and B. Sadoulet.
Application of The Classical Theory of Electrons In Gases To Multiwire Proportional And Drift Chamber.
1974.
LBL publication.

[105] T. E. Stewart, G. S. Hurst, T. E. Bortner, J. E. Parks, F. W. Martin and H. L. Weidner.
Proton Excitation of Continuous Emission in the Noble Gases.
Journal of Optical Society of America 60(10):1290, 1970.

[106] J. D. Craggs and B. A. Tozer.
The attachment of slow electrons in carbon dioxide.
In *Proc. Roy. Soc. A254*, pages 229. The royal society of London, 1960.

[107] D. A. Price, J. Lucas and J. L. Moruzzi.
Ionization in Oxygen-Hydrogen Mixtures.
J. Phys. D: Appl. Phys. 5:1249, 1972.

[108] J. Sandweiss.
The High Resolution streamer chamber.
Physics Today 31(10):40, 1978.

[109] R. Majka, T. Cardello, S. Dhawan, A. Disco, R. Kellogg, T. Ludlam, P. Nemethy, J. Sandweiss, A.J. Slaughter, L. Tzeng and I. Winter.
Design and Performance of A High Resolution Streamer Chamber.
Nucl. Instr. and Meth. 192:241, 1982.

[110] J. Sandweiss.
High Resolution Streamer Chamber for Heavy Quark Spectroscopy.
Physics Report 83(1):39, 1982.

[111] A. H. Guenter and J. R. Bettis.
The Laser Triggering of High-Voltage Switches.
J. Phys. D: Appl. Phys. 11:1577, 1978.

[112] H. C. Harjes.
Laser Triggered Spark Gap Using Fiber Optic Transmission.
Technical Report LLL 2257509-1, Texas Tech. University, 1979.

[113] D. K. Koopman and K. A. Saum.
Formation and guiding of high-velocity electrical streamer by laser-induced ionization.
J. Appl. Phys. 44(12):5328, 1973.

[114] W. R. Rapoport, J. Goldhar and J. R. Murray.
KrF Laser-Triggered SF_6 Spark Gap for Low Jitter Timing.
Technical Report UCRL-82697, UC Lawrence Livermore Laboratory, 1980.

[115] S. H. Khan and D. Walsh.
Effect of cathode material in a laser triggered spark gap.
J. Phys. D: Appl. Phys. 4:344, 1971.

[116] J. R. Vaill, D. A. Tridman, T. D. Wilkerson and D. W. Koopman.
Propagation of high-voltage streamers along laser-induced ionization trails.
Appl. Phys. Lett. 17(1):20, 1970.

[117] L. A. Pipes.
Applied Mathmatics For Engineers and Physics.
McGraw-Hill, 1958.

[118] N.Z. Anisimova et al.
Eight meter streamer chamber operating on the IHEP proton synchrotron.
In *Proc. Intern. Conf. On Instrumentation For High Energy Physics.* Frascati, 1973.
Frascati.

[119] G.A. Vardenga et al.
The JINR 2 m streamer chamber.
In *Proc. Intern. Conf. On Instrumentation For High Energy Physics.* Frascati, 1973.
Frascati.

[120] T. Cardello.
A charge hyperon beam for Proton Center.
Technical Report TM 964, Fermilab, 1980.

[121] A. T. Visser.
A short approach to the electrical design of a muon spoiler magnet.
Technical Report TM 978 6013.000, Fermilab, 1980.

[122] M. R. Whalley et al.
Inclusive neutron production.
1979.
Fermilab report. UM HE 79-14.

[123] W. Flauger and F. Monnig.
Measurement of inclusive zero-angle neutron spectra at the CERN ISR.
Nuclear Physics B109:347-356, 1976.

[124] P. Skubic et al.
Neutral-strange-particle production by 300-Gev protons.
Physical Review D 18(9):3115, 1978.

[125] P. Cooper.
Neutral strange particle fluxes.
Yale University, internal report.

[126] J. Sandweiss.
E-630 neutron beam design, Recalculate N flux from UM HE 79-14.
Nov. 5, 1980.
Yale University, internal report.

[127] J. Sandweiss.
E-630 neutron beam design, Photon background and Lead Filter.
Nov. 20, 1980.
Yale University, internal report.

[128] P. Capiluppi et al.
Charge Particle Production In Proton-Proton Inclusive Reaction At Very High Energy.
Nuclear Physics B79:189, 1974.

[129] R. Slansky.
High Energy Hadron Production And Inclusive Reactions.
1973.
Yale University, 3075-50.

[130] B.Alper et al.
Production spectra of π, K, P at large angles in proton-proton collisions in the CERN intersection storage rings.
Nuclear Physics B100:237, 1975.

[131] J. Whitmore.
Multiparticle Production In The Fermilab Bubble Chambers.
Physics Reports 27(5):187, 1976.

[132] P. L. Skubic.
Neutral Strange Particle Production from Nuclear Targets by 300 Gev protons.
PhD thesis, The Univ. of Michigan, 1977.

[133] J. Kalinowski et al.
Probablistic Quark-Model Approach to Proton Fragmentation.
Z. Physik C2:85, 1979.

[134] M. Bourquin et al.
Particle and antiparticle production by 200 Gev/c protons in the charged hyperon beam at the CERN SPS.
Nuclear Physics B153:13, 1979.

[135] M. Bourquin et al.
Charge Baryon and Antibaryon Production in the Fragmentation region by 240 Gev Protons.
Z. Physik C5:275, 1980.

[136] D. Fong et al.
Cross section and charged multiplicity distributions for π^-p and K^-p interactions at 147 Gev/c.
Nuclear Physics B102:386, 1976.

[137] D. Brick et al.
Average charge-particle multiplicities in π^-p inclusive reactions at 147 Gev/c.
Physical Review D 19(3):743, 1979.

[138] D. Brick et al.
Neutral-particle production in π^-p interactions at 147 Gev/c and comparison to charged-particle production.
Physical Review D 20(9):2123, 1979.

[139] D. Brick et al.
Inclusive production of neutral strange particles by 147 Gev/c $\pi^+/K^+/p$ interactions in hydrogen.
Nuclear Physics B164:1, 1980.

[140] D. Brick et al.
The effective-energy dependence of the charged particle's multiplicity in $p/\pi^+/K^+$ interactions on protons at 147 Gev/c.
Physics Letters 103B(3):241, 1981.

[141] D. Brick et al.
Inclusive strange-resonance production in pp, π^+p, and K^+p interactions at 147 Gev/c.
Physical Review D 25(9):2248, 1982.

[142] D. Bricket al.
Topological, total and elastic cross sections for K^+p, π^+p and pp interactions at 147 Gev/c.
Physical Review D 25(11):2794, 1982.

[143] D. Brick et al.
Measurement of the multiplicities in the collision of hadrons with heavy nuclei at 200 Gev/c.
Nuclear Physics B201:189, 1982.

[144] Particle Data Group.
Review of Particle Properties.
LBL-100 Revised, UC-34d, 1982.

[145] Thomas R. Cardello.
Strange Charged Baryon Production.
PhD thesis, Yale University, 1983.